Stony Brook University

Elucidating lithosphere-mantle coupling by modeling the lithospheric stress field and predicting plate motions

A Dissertation Presented

by

Attreyee Ghosh

to

The Graduate School

in Partial Fulfillment of the

Requirements

for the Degree of

Doctor of Philosophy

in

Geosciences

Stony Brook University

May 2008

Stony Brook University

The Graduate School

Attreyee Ghosh

We, the dissertation committee for the above candidate for the
Doctor of Philosophy degree, hereby recommend
acceptance of this dissertation.

William E. Holt - Dissertation Advisor

Professor, Department of Geosciences

Daniel M. Davis - Chairperson of Defense

Professor, Department of Geosciences

Lianxing Wen - Co-advisor

Associate Professor, Department of Geosciences

Timothy Glotch

Assistant Professor, Department of Geosciences

Paul Silver

Staff Scientist, Department of Terrestrial Magnetism, Carnegie Institute of Washington

This dissertation is accepted by the Graduate School

Lawrence Martin
Dean of the Graduate School

Abstract of the Dissertation

Elucidating lithosphere-mantle coupling by modeling the Earth's lithospheric stress field and plate motions

by

Attreyee Ghosh

Doctor of Philosophy

in

Geosciences

Stony Brook University

2008

Even after the establishment of the plate tectonic theory nearly four decades ago, some fundamental questions have still not been satisfactorily answered. What drives the Earth's plates? Are plates and mantle coupled, and if so, what is the nature of that coupling? What is the role of density buoyancy-driven flow in driving the plates? These are some of the questions we try to address in our study through a joint modeling of lithosphere dynamics and mantle convection. If the initial coupling model is correct, the predicted stresses will match the observed deformation along the plate boundary zones and the predicted velocities will match the observed plate motions. We model the lithospheric deviatoric stress field from gravitational potential energy (GPE) differences and compare our modeled stress tensor field with velocity gradient tensor field along the Earth's deforming plate boundary zones (from GSRM). The deviatoric stresses due to active basal tractions acting at the base of the lithosphere, arising from density buoyancy-driven mantle convection, are also compared with the strain rate tensor dataset from GSRM. We find that the combined stresses from lithosphere and mantle buoyancies yield the best fit to the deformation indicators, especially in areas of continental deformation. This is most likely due to driving shear tractions induced by the surrounding mantle, related to the history of subduction in those areas. We also generate plate motions in our convection models by incorporating lateral viscosity variations generated by major geological features of the Earth, such as the continent-ocean divide, the presence of cratonic roots as well as age differences in the oceanic lithosphere. For each structure, we predict the deviatoric stress field, the pattern of poloidal and toroidal flow and the partitioning ratio between toroidal/poloidal velocities. The predicted deviatoric stress field is added to the deviatoric stresses generated by lithosphere buoyancies and

the total stress field is compared with strain rate tensor information from GSRM. The best-fit model has to satisfy both the constraints of matching the plate motions and the deviatoric stress field simultaneously. By using both these constraints, we are able to eliminate several types of models and narrow down significantly the set of models that fit the observations.

Contents

List of Figures

List of Tables

Acknowledgements

I would take this opportunity to express my gratitude to all the people without whom this thesis would not have been possible.

Foremost, I would like to thank my advisor, Dr. William Holt for his inspiration, encouragement and constant guidance that has led to this work. His efforts at explaining problems clearly and simply have made it possible for me to learn, understand and appreciate this subject, which was completely new to me when I started graduate school. Special thanks to my co-advisor Dr. Lianxing Wen for his sound advice, teaching, and ideas. I am also grateful to Lucy Flesch of Purdue University, our collaborator and my advisor's former student, for her constant support and encouragement. I also thank our collaborator from University of Cambridge, Dr. John Haines, for all his help, support and his mathematical skills that have helped solve problems that had sometimes seemed almost insurmountable. My thesis committee members, Dr. Dan Davis, Dr. Tim Glotch and Dr. Paul Silver from DTM, deserve special mention. I would also like to thank Dr. Teng-fong Wong, former Chair of the department for his encouragement and assistance. I am grateful to the staff of the department, especially Loretta Budd and Owen Evans, for their tremendous help and for taking care of all the bureaucratic issues.

Intellectual discussions with fellow students, Elliot Klein, Wen-che Yu and Yi Wang have been very helpful. Special thanks to Mainak Mookherjee of Yale University for his advice and the intellectually stimulating conversations. Thanks to Stacey Cochiara, Wei Zhu and Daniel Hernandez for their support and friendship.

Thanks to Jorge Cham for his phdcomics, which has helped in making my grad student life a little more colorful. Notwithstanding the procrastination, it has provided a great motivation in finishing my phd.

Most importantly I would like to thank my parents for their love, support and help. Without their support this thesis would not have existed. Finally, I would like to mention my friends, especially my friends in New York, without whom the completion of this work would not have been possible. At times, when things had seemed too difficult, they had lent their ears to my complaint; they had encouraged me to carry on and not give up. They have made me feel at home so far away from home. To my friends, Parul, Reena, Anita, Sanjeev, Anuranjan, Debarati and Sharvari, I owe a lot.

I dedicate this work to my parents and my friends to honor their love and support during all these years.

Chapter 1

Introduction

Introduction

After decades of studies and observations, the plate tectonic theory was finally established by middle to late 1960's. Because of its power in explaining a diverse array of puzzling features on the Earth, it has sometimes been hailed as "the grand unifying theory of the earth sciences". The phenomenon of plate tectonics also distinguishes the Earth from the other planets of the solar system, as none of them are recognized to demonstrate the plate tectonic phenomenon. Although some of the important tenets of the theory, such as rigid plates surrounded by narrow deforming plate boundaries, have been modified to account for more complex phenomena, like the wide, diffuse deformation along the continental margins, the basic theory has endured the test of time. However, there are still certain aspects of the theory that are not fully explained, and one such aspect is the plate-mantle coupling problem, which in turn has important implications in addressing the issue of driving mechanism behind plate tectonics.

The coupling problem, in simpler terms, can be restated as the interaction between plates and the convective mantle. A coupled plate-mantle system would imply that stresses, generated by sub-lithospheric density buoyancies, are transmitted to the overlying lithosphere and influence the motion and deformation of the plates. A decoupled plate-mantle system would prevent transmission of such stresses and the mantle would play no active role in the motion and deformation of the lithosphere. This would imply that the plates are self-driving. Indeed, there have been two different schools of thought regarding the role of mantle in influencing the plate motions and the deformation of the lithosphere. Studies, such as *Forsyth and Uyeda* (1975), *Harper* (1975), *Lister* (1975), *Solomon et al.* (1975), *Richardson et al.* (1979), *Sandiford and Coblentz* (1994), have concluded that mantle convection plays a negligible role in the process of plate tectonics; the most important factor influencing the plate tectonic process is the lithosphere itself. The ridge-push force, arising from gravity acting on density variations in the oceanic lithosphere, and slab-pull force, which is the downward pull of the slabs at subduction zones, are thought to be the dominant forces behind plate tectonics. On the other hand, plate tectonics has been regarded solely as a fluid dynamical process by several authors, starting from *Turcotte and Oxburgh*

(1967), followed by *Zhong and Gurnis* (1996), *Bercovici* (1998), *Tackley* (1998), *Trompert and Hansen* (1998), *Bercovici and Ricard* (2000), *Tackley* (2000) and *Bercovici* (2003), amongst others, who have attempted to model plate tectonics and mantle convection as a single system.

However, none of the above studies have been able to fully explain all the observations predicted by the plate tectonic theory. In recent years, studies have been undertaken that take into account the contribution of both lithosphere dynamics and mantle convection in explaining the various observables (*Bai et al.,* 1992; *Bird*, 1998; *Steinberger et al.,* 2001; *Lithgow-Bertelloni and Guynn*, 2004; *Ghosh et al.*, 2008). Such studies have attempted to evaluate the role of mantle by comparing their model predictions with observations on the Earth.

The various observables that can constrain this coupling issue are the Earth's long wavelength geoid, dynamic topography, plate motions, and the lithospheric stress field. The last two are the most definitive of the above-mentioned constraints. The constraint of plate motions can be subdivided into the poloidal and the toroidal components. The former is the vertical component of the convective flow, responsible for upwelling along the mid-oceanic ridges, and downwelling in subduction zones. The latter causes strike-slip motion along transform fault boundaries. The ratio of the magnitudes of these two types of motion can also provide a significant constraint in addressing this coupling problem. The toroidal/poloidal ratio on Earth has been observed to be close to unity for each degree of spherical harmonic (*Hager and O'Connell*, 1979) and historically it has been extremely difficult to match this observed ratio in models of mantle convection.

In this dissertation I investigate the plate-mantle coupling problem by employing the constraints of lithospheric stress field, plate motions, and the toroidal-poloidal velocity ratio for the first time, through a joint modeling of lithosphere dynamics and mantle convection. I use the velocity gradient tensor field along the Earth's deforming plate boundary zones as a proxy or indicator for the lithospheric stress field. The additional dataset of the earthquake moment tensor field is also used to constrain the modeled stress field. I use both the pattern and magnitude of the poloidal and toroidal velocity fields to constrain the predicted plate motions from our models.

The dissertation is organized in the following way. It consists of an Introduction (Chapter 1) and Conclusion chapters (Chapter 7) and five main chapters that have either been previously published or are to be submitted for publication. Chapter 2 deals with the contributions of lithospheric density buoyancies on the lithospheric stress field. It discusses the method of predicting a global deviatoric stress field from gravitational potential energy differences per unit area (GPE) from the Crust 2.0 dataset and the geoid. Chapter 2 also discusses the significance of using a correct reference level for GPE calculations and gives a quantitative comparison with the velocity gradient tensor field along the plate boundary zones. Additionally, chapter 2 gives the methodology for treating the spherical equations. This work is in preparation to be submitted to the *Journal of Geophysical Research*. Chapter 3 is also related to the contribution of lithospheric density buoyancies to the global deviatoric stress field, but is confined to the analysis of the Indian plate where I demonstrate the need for additional contribution of sub-lithospheric density buoyancies to drive India into Eurasia, and thus explain the excess GPE of the Tibetan Plateau. It is published in *Geology* by *Ghosh et al.* (2006). Chapter 4, submitted to *Geophysical Research Letters*, and currently under revision, deals with the contribution of both lithospheric and sub-lithospheric density buoyancies. However, it concentrates only on the poloidal component of the total flow field. Chapter 4 clearly demonstrates quantitatively the need for lithospheric coupling with deeper mantle density buoyancy-driven flow to explain the lithospheric deviatoric stress field. Chapter 4 also contains important benchmarking exercises, where I show that the thin sheet method that I employ is capable of recovering the lithospheric deviatoric stress field. Chapter 5 investigates a best-fit coupling model by using the additional constraints of plate motions and the toroidal-poloidal velocity ratio. Chapter 6 is essentially related to Chapter 5, in that it details the methodology used in computing the solutions in Chapter 5. These last two chapters are also in preparation for submission to the *Journal of Geophysical Research*.

Chapter 2

Contribution of Gravitational Potential Energy Differences to the Global Stress Field

Contribution of gravitational potential energy differences to the global stress field

Abstract

Modeling the lithospheric stress field has proved to be an efficient means of determining the role of lithospheric vs sublithospheric buoyancies and also of constraining the driving forces behind plate tectonics. Both these sources of buoyancies are important in generating the lithospheric stress field. However, these sources and the contribution that they make are dependent on a number of variables, such as the role of lateral strength variation in the lithosphere, the reference level for computing the gravitational potential energy per unit area (GPE) of the lithosphere, and even the definition of deviatoric stress. For the mantle contribution, much depends on the mantle convection model, including the role of lateral and vertical viscosity variations, the spatial distribution of density buoyancies, and the resolution of the convection model. Because of its importance in the total contribution of stresses to the plates, this study isolates only the contribution of crust and upper mantle buoyancies, from the surface down to a constant reference level (100 km below sea-level). Deficiencies in this contribution provide insight into the necessity and role of deeper mantle density buoyancies in affecting the lithospheric stress field. Buoyancy distributions used to calculate GPE differences within the layer considered are inferred from the Crust 2.0 dataset. We show that the GPE differences within this top layer alone are not sufficient to match all the directions of principal strain rate axes and relative magnitudes of these principal axes (style of faulting), as inferred from the comparison of our depth integrated deviatoric stress tensor field with the velocity gradient tensor field within the Earth's plate boundary zones. The EGM96 geoid dataset is also used as a rough proxy for GPE values in the lithosphere. However, the GPE differences from the geoid fail to yield depth integrated deviatoric stresses than can provide a good match to the deformation indicators. GPE values inferred from the geoid have significant shortcomings when used on a global scale due to the role of dynamic support of topography. Other important factors in estimating the depth integrated deviatoric stresses are (1) use of the correct level of reference in

calculating GPE, where that level of reference must be the base of the layer of depth integration and (2) correct treatment of dynamic topography. We also elucidate the importance of understanding the reference pressure for calculating deviatoric stress and show that overestimates of deviatoric stress may result from either simplified 2-D approximations of the thin sheet equations or the assumption that the mean stress is equal to the vertical stress.

2.1 Introduction

Since the advent of plate tectonics there have existed considerable controversies regarding the nature, magnitude, and source of the forces that drive tectonic plates. The lithospheric stress field serves as an important indicator of these plate-driving forces. Lateral density variations within the lithosphere have been shown to be a major factor influencing the global stress field (*Frank*, 1972; *Artyushkov*, 1973; *Fleitout and Froidevoux*, 1982, 1983; *Fleitout*, 1991; *Coblentz et al.*, 1994; *Coblentz and Sandiford*, 1994; *Sandiford and Coblentz*, 1994; *Coblentz et al.*, 1995). Lithospheric deformation is not confined along narrow plate boundaries. Rather, deformation within many plate boundary zones is distributed (*McKenzie*, 1972; *Molnar and Tapponnier*, 1975; *England and McKenzie*, 1982; *Molnar*, 1988; *England and Jackson*, 1989; *England and Molnar*, 1997b; *Flesch et al.*, 2000), with the bulk of crustal strain accommodated along major fault zones (*Holt and Haines*, 1995; *Holt et al.*, 2000; *Thatcher*, 2007; *Meade*, 2007). In present-day modeling of the tectonic stresses, the notion of rigid plates has been replaced by the notion of the continental lithosphere behaving as a continuous medium (*England and Jackson*, 1989). The importance of this is the recognition that resulting crustal thickening and thinning leads to important internal lateral and vertical density variations; these lateral and vertical variations profoundly influence the deviatoric stress field in the lithosphere. Furthermore, it has also been recognized that horizontal dimensions of deformation far exceed the thickness of the lithosphere, and in this regard lithospheric deformation has been quantified in terms of a thin viscous sheet in order to solve for the depth averaged or depth integrated deviatoric stresses within the lithosphere over large scales (*England and McKenzie*, 1982; *Houseman and England*, 1986; *England and Jackson*, 1989; *England and Molnar*, 1997b; *Flesch et al.*, 2001; *Ghosh*

et al., 2006). The assumption that goes with the thin sheet approximation is that the gradients of shear tractions at the base of the plate are negligibly small compared to the force of gravity acting on density. Hence, the sources of these driving stresses can be divided into two main categories: (1) gravity acting on density variations within the thin sheet and (2) gravity acting on density variations deeper than the thin sheet, related to density buoyancy-driven convective circulation of the mantle. In this paper, we use the thin sheet approximation to quantify the first of these two sources. These lateral density variations mentioned above manifest, in part, as varying crustal thicknesses, which, together with topography, cause variations in gravitational potential energy per unit area (GPE). Differences in GPE contribute to the deviatoric stress field in the lithosphere. This deviatoric stress field is calculated and compared quantitatively with stress observations, such as the World Stress Map (WSM) or strain rate tensor field in the earth's plate boundary zones (this study).

We calculate depth integrated deviatoric stresses, where the depth of integration is from the surface down to a constant reference level of 100 km below sea-level. This incorporates the lithosphere for most parts of the Earth. However, under the assumption that there is no buoyancy-driven mantle convection, no dynamic topography, and hence, equal vertical stress at the depth of the deepest continental keels, one can integrate to a deeper depth in order to account for deeper density buoyancies associated with continental keels. Although neglecting the above factors represents an oversimplified approximation, we nevertheless explore the influence of integrating to the base of the deepest continental keels in order to quantify differences with our standard reference level of 100 km.

We also investigate the role of lateral strength variations in the lithosphere. We calculate the depth integrated deviatoric stresses on a one-plate planet of uniform lithospheric viscosity, in addition to stress calculations on an Earth-like planet with weak plate boundaries. We show how the consideration of laterally variable viscosities in the lithosphere enable the calculated deviatoric stresses to have a better match with stress and strain rate observations.

Calculation of GPE requires a level of reference. When the vertical stress is laterally variable at the base of the depth of integration the choice of reference level has important

dynamic implications. In this paper, we discuss the reference level problem in calculating GPE, and show that for a thin sheet calculation in which the vertical stress varies beneath topography along the base of the depth of integration, there is only one correct level of reference. In particular, we show that for such cases, the shallow density anomalies have a more dominant effect on the depth integrated deviatoric stresses than the deeper anomalies. Another important aspect of our study is to bring forward the substantial changes in stress magnitudes that arise by solving the full 3-D force-balance equations instead of the 2-D equations, and also the importance of using a correct definition of deviatoric stress. Although the total forces driving lithospheric deformation are a combination of the two sources mentioned above, arising from density variations both within and below the thin sheet (*Lithgow-Bertelloni and Guynn*, 2004), our study focuses only on quantification of the lithospheric contribution. Our confidence in the magnitude and distribution of GPE variations far exceeds our confidence in the magnitude and distribution of basal tractions associated with mantle convection. Nevertheless, if the contribution from GPE differences can be correctly quantified, then the misfit of the associated depth integrated deviatoric stress field with stress tensor indicators holds promise for constraining the remaining contribution associated with basal tractions. Therefore, it is important to isolate the contribution of GPE differences to depth integrated deviatoric stresses because they calibrate the absolute magnitudes of deviatoric stresses acting within the lithosphere.

2.2 The Force Balance Equations and Validity of the Thin Sheet Approximation

The force balance equations, which state that gradients of stresses are balanced by the force of gravity per unit volume, are given by

$$\frac{\partial \sigma_{ij}}{\partial x_j} + \rho g_i = 0 \tag{1}$$

(*England and Molnar*, 1997b), where σ_{ij} is the ij^{th} component of the total stress tensor, x_j is the j^{th} coordinate axis, ρ is the density and g_i is the i^{th} component of the acceleration

due to gravity. The above equations use summation notation, where i takes the values of x,y and z and the repeated index j represents the summation over x,y and z. For clarity we show the cartesian form of (1). However, we solve the spherical form of (1) in our global calculations (see Appendix).

We explore next the conditions under which the thin sheet approximation is valid. The basis of the thin sheet approach is that because the horizontal distance scales are large in comparison with the thickness of the lithosphere, we can take depth integrals of the force balance equations down to a constant reference level, and then solve these equations for the depth integrals of deviatoric stress within that layer. Expanding the z-equation from (1) and then integrating from the surface to the base of a uniform reference level, L, yields

$$\frac{\partial}{\partial x}\left[\int_{-h}^{L}\sigma_{xz}(z)dz\right]+\frac{\partial}{\partial y}\left[\int_{-h}^{L}\sigma_{yz}(z)dz\right]+\frac{\partial}{\partial z}\left[\int_{-h}^{L}\sigma_{zz}(z)dz\right]=-\int_{-h}^{L}\rho g_z dz \qquad (2)$$

The approximation in the thin sheet approach is that

$$\frac{\partial}{\partial x}\int_{-h}^{L}\sigma_{xz}(z)dz+\frac{\partial}{\partial y}\int_{-h}^{L}\sigma_{yz}(z)dz << -\int_{-h}^{L}\rho g_z dz, \qquad (3)$$

such that, from (2) we have

$$\sigma_{zz}(z)=-\int_{-h}^{z}\rho g(z')dz' \qquad (4)$$

Assuming that $\sigma_{xz}(z)$ and $\sigma_{yz}(z)$ are linear, from zero at the surface to $\sigma_{xz}(L)$ and $\sigma_{yz}(L)$ at the base, then the question is how large can the gradients of shear tractions be in order for (3) to hold ? Using $3000kg/m^3$ for an average density of the lithosphere and a 100 km thick lithosphere, we find that horizontal gradients in shear tractions applied to the base of the lithosphere at depth 100 km would have to be as high as 6 MPa/10 km in order for the left hand side of (3) to be 1% of the magnitude of the right hand side of (3), the vertical stress at depth L. This is at least an order of magnitude higher than horizontal variations of tractions from large scale mantle circulation (*Steinberger et al.*, 2001; *Becker and O'Connell*, 2001), and is likely to be much larger than the most extreme gradients in tractions that might occur beneath subduction zones. Therefore, the 'thin sheet' approximation in (3) is valid, in which case we can use the relation in (4) for the vertical stress, and use only the two

horizontal force balance equations to investigate depth integrals of horizontal deviatoric stress.

Substituting into (1) for the total stresses via the relationship, $\tau_{ij} = \sigma_{ij} - \frac{1}{3}\sigma_{kk}\delta_{ij}$, where τ_{ij} is the ij^{th} component of the deviatoric stress tensor, δ_{ij} is the Kronecker delta, and $\frac{1}{3}\sigma_{kk}$ is the mean total stress, and integrating (1) over the thickness of the lithosphere, we arrive at the full horizontal force balance equations, neglecting flexure (*England and McKenzie*, 1982; *England and Houseman*, 1986; *England and Molnar*, 1997b; *Flesch et al.*, 2001):

$$\frac{\partial \bar{\tau}_{xx}}{\partial x} - \frac{\partial \bar{\tau}_{zz}}{\partial x} + \frac{\partial \bar{\tau}_{xy}}{\partial y} = -\frac{\partial \bar{\sigma}_{zz}}{\partial x} + \tau_{xz}(L) \tag{5}$$

$$\frac{\partial \bar{\tau}_{yx}}{\partial x} + \frac{\partial \bar{\tau}_{yy}}{\partial y} - \frac{\partial \bar{\tau}_{zz}}{\partial y} = -\frac{\partial \bar{\sigma}_{zz}}{\partial y} + \tau_{yz}(L), \tag{6}$$

where the over bars represent depth integration. The two terms on the right hand sides of equations (5) and (6) constitute body-force-like terms. The first terms on the right side of (5) and (6) represent horizontal gradients in GPE per unit area, whereas $\tau_{xz}(L)$ and $\tau_{yz}(L)$ are the tractions, arising from density buoyancy-driven mantle convection, applied at the base of the thin sheet at depth L. We do not quantify the contributions of $\tau_{xz}(L)$ and $\tau_{yz}(L)$ here, but have addressed them elsewhere (*Ghosh et al.*, 2008).

The thin sheet approximation also implicitly assumes that vertical variations in horizontal velocity are small, or that one of the principal axes of the stress or strain rate tensor is close to vertical. The presence of a basal traction boundary condition in (5) and (6), associated with a deeper mantle density buoyancy contribution, calls for the need to evaluate the validity of this assumption. If one principal axis is close to vertical, then depth integrals of shear stress should be small in comparison with depth integrals of horizontal deviatoric stress. Using 5 MPa for $\sigma_{xz}(L)$, and assuming a linear gradient of $\sigma_{xz}(L)$, such that it is zero at the surface, the depth integrals of $\sigma_{xz}(z)$ are 2.5×10^{11} N/m. This is about 10% of the magnitude of the depth integral of horizontal deviatoric stress in the lithosphere (*Ghosh et al.*, 2008). Therefore, even in the presence of basal tractions of significant magnitude, the assumption that one of the principal axes is near-vertical appears to be valid.

The forcing terms in (5) and (6) are constrained by observations. For example, GPE per

unit area is constrained by topography and seismically-defined crustal thicknesses (Crust 2.0 [G. Laske et al., Crust 2.0: A new global crustal model at 2 × 2 degrees, 2002, available at http://mahi.ucsd.edu/Gabi/rem.html]) and tractions can be constrained by self-consistent circulation models that match plate motion, dynamic topography, and geoid (e.g. *Wen and Anderson*, 1997b). Depth integration over the entire plate thickness is indicated by bars over the total stress and deviatoric stress terms, σ_{ij} and τ_{ij}, respectively. The vertically integrated vertical stress, $\bar{\sigma}_{zz}$, which is the negative of GPE per unit area is given by

$$\bar{\sigma}_{zz} = -\int_{-h}^{L}\left[\int_{-h}^{z}\rho(z')gdz'\right]dz = -\int_{-h}^{L}(L-z)\rho(z)gdz \tag{7}$$

(*Jones et al.*, 1996), based on a reference level of depth L. Here, $\rho(z)$ is the density, L is the depth to the base of the thin sheet, h is the topographic elevation, and g is the acceleration due to gravity.

2.3 Method for Solving the Force Balance Equations

The deviatoric stress field solution that we obtain is the mathematically unique solution that both balances the body force distribution (GPE differences) and provides a global minimum in the second invariant of stress (following *Flesch et al.* (2001)). We also take into account weak plate boundaries and strong plates, as discussed later. Solutions to (5) and (6) for $\bar{\tau}_{ij}$ can be obtained, given distributions of $\frac{\partial\bar{\sigma}_{zz}}{\partial x}$ and $\frac{\partial\bar{\sigma}_{zz}}{\partial y}$ with $\tau_{xz}(L)$ and $\tau_{yz}(L)$ set to zero (e.g. *Flesch et al.*, 2001; *Ghosh et al.*, 2006). Alternatively, solutions can be obtained given distributions of $\tau_{xz}(L)$, $\tau_{yz}(L)$, with gradients in GPE set to zero. The contribution from basal traction can simply be added to the contribution from GPE differences in order to obtain the full stress field. This motivates our study to correctly quantify the global solution associated with GPE distributions in order to better understand the full global solution, which has contributions from density variations at all depths.

Previously, most authors had used the geoid surface (sea-level) as the reference level for calculating GPE (*Fleitout*, 1991; *Coblentz et al.*, 1994; *Jones et al.*, 1996; *Zoback and*

Mooney, 2003), in which case,

$$\bar{\sigma}'_{zz} = \int_{-h}^{L} \rho(z) g z dz = \bar{\sigma}_{zz} + L\sigma_{zz}(L). \tag{8}$$

Thus, for areas in which $\sigma_{zz}(L)$ is a constant, the choice of reference level is irrelevant (*Haxby and Turcotte*, 1978). However, this reference level yields significantly different values from that obtained using (7) when the pressure, $\sigma_{zz}(L)$, at the reference level L is non-uniform, as we discuss in a later section. We use both the Crust 2.0 dataset and the EGM96 geoid model (available from NIMA at http://164.214.2.59/GandG/wgs-84/egm96.html) to calculate GPE. We show that the latter can only be used as a proxy for GPE if the pressure or vertical stress at the base of the layer of integration is uniform globally.

We use a finite element method to solve the three-dimensional force balance equations over a global grid of $2.5^o \times 2.5^o$ for the spherical case, neglecting basal tractions, to quantify the contributions to deviatoric stresses that are intrinsic to the lithosphere. We minimize the functional (after *Flesch et al.* (2001)):

$$I = \int_S \frac{1}{\mu}[\bar{\tau}_{\alpha\beta}\bar{\tau}_{\alpha\beta} + \bar{\tau}^2_{\gamma\gamma}]dS + \int_S 2\lambda_\alpha \Big[\frac{\partial}{\partial x_\beta}(\bar{\tau}_{\alpha\beta} + \delta_{\alpha\beta}\bar{\tau}_{\gamma\gamma}) + \frac{\partial \bar{\sigma}_{zz}}{\partial x_\alpha}\Big] dS, \tag{9}$$

where μ is the relative viscosity, $\bar{\tau}_{\alpha\beta}$ is the vertically integrated horizontal deviatoric stress, $\bar{\tau}_{\gamma\gamma} = \bar{\tau}_{xx} + \bar{\tau}_{yy}$, λ_α is the horizontal component of the Lagrange multiplier for the constraint to satisfy the two force balance differential equations, $\bar{\sigma}_{zz}$ is the vertically integrated vertical stress (GPE per unit area), and S represents area on the entire Earth's surface. In *Flesch et al.* (2001), μ was assigned a value of 1. We assign variable values to μ in order to approximate weak plate boundary zones and strong plates. This is done in two ways. In the first case, an inverse relationship between strain rates (from *Kreemer et al.* (2003)) and relative viscosities, μ, is assumed (Figure 1a). The relative viscosities of the deforming plate boundary regions are obtained by assigning a reference viscosity to the moderately straining region in western North America with a strain rate of 1.5×10^{-7}/yr via the relationship:

$$\frac{1}{\mu} = 1 + \left(\frac{1}{\mu_{ref}} - 1\right)\sqrt{\frac{E^2}{E^2_{ref}}}, \tag{10}$$

where μ_{ref} is the viscosity corresponding to the above-mentioned area, $E^2 = 2(\dot{\varepsilon}_{xx}^2 + \dot{\varepsilon}_{yy}^2 + \dot{\varepsilon}_{xy}^2 + \dot{\varepsilon}_{xx}\dot{\varepsilon}_{yy})$, where $\dot{\varepsilon}_{xx}, \dot{\varepsilon}_{yy}$ and $\dot{\varepsilon}_{xy}$ are the strain rates from *Kreemer et al.* (2003), and E_{ref}^2 is the reference value for E^2, corresponding to the value for μ_{ref}. The lowest viscosities occur along the mid-oceanic ridges, whereas relatively higher viscosities occur in the deforming continental areas (Figure 1a). The rigid plates (blank regions) have the highest viscosities with a μ value of 1. We try different values for the reference viscosity, μ_{ref}, such as 1/3, 1/30, 1/300 and 1/3000, where the reference region in western North America is 3, 30, 300 and 3000 times weaker than the plates, respectively. The viscosity structure giving rise to the deviatoric stress field that matches the deformation indicators best is chosen. Taking into account the above viscosity variations yields a focusing of stresses within the plates and fits well the observed SH_{max} orientations in most places within the plates (*Zoback*, 1992).

The second way takes into account the dependence of effective viscosities on lithospheric thickness in addition to strain rates (Figure 1b). The viscosity, μ', in this case is given by:

$$\mu' = \frac{1}{100}\int_{-h}^{L'} \mu dz = \frac{1}{100}(L' + h)\mu, \tag{11}$$

where $L' + h$ is the thickness of the lithosphere (*Conrad and Lithgow-Bertelloni*, 2006) and μ are the strain rate dependent viscosities. Note that here L' is no longer constant; the variable base of the lithosphere is taken into account. In the case where GPE is calculated with a reference level of 100 km, the maximum value of L' is fixed at 100 km. Therefore, in this case, our depth integrals do not encompass the deeper lithospheric keels, but take into account the variable depths of the oceanic lithosphere. However, we do address a case where $L' = 270$ km, a depth great enough to include the keels. Note, in (11) the lithosphere thickness is normalized by a reference thickness of 100 km. Areas deforming at the same rate will have different viscosities based on lithospheric thickness: thicker lithosphere will be stronger than lithosphere that is less thick.

We minimize (9) with respect to $\bar{\tau}_{\alpha\beta}$ using the variational principle (*Morse and Fesh-*

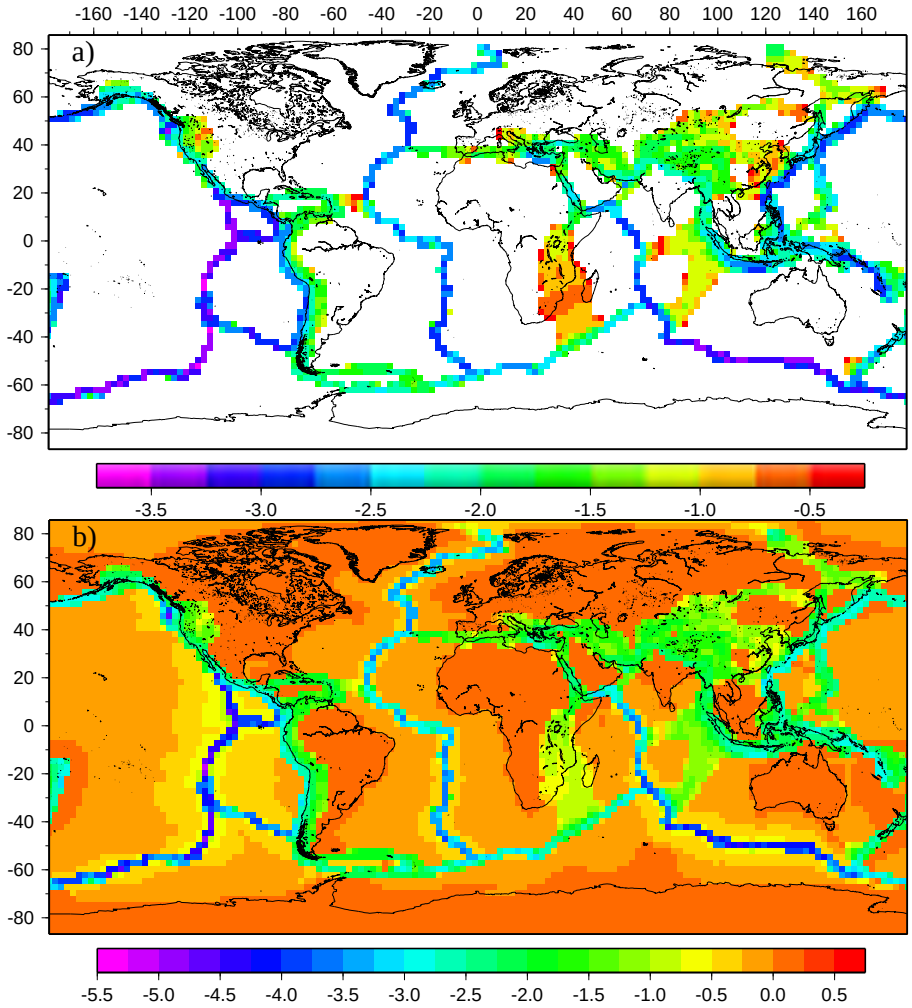

Figure 1: Logarithm of relative viscosity distribution for all the plates based on a) strain rates from GSRM and b) both strain rates and lithospheric thickness. The white areas represent intra-plate regions with relative viscosity 1. A reference viscosity of $\mu_{ref} \sim \frac{1}{30}$ is chosen at the moderately fast straining western North America (1.5×10^{-7}/yr). Areas with higher viscosities than μ_{ref} are deforming at a slower rate.

bach, 1953), which then yields the relation

$$\bar{\tau}_{\alpha\beta} = \frac{1}{2}\left(\frac{\partial \lambda_\alpha}{\partial x_\beta} + \frac{\partial \lambda_\beta}{\partial x_\alpha}\right). \tag{12}$$

Here, $\bar{\tau}_{\alpha\beta}$ has the same relation with the vector of Lagrangian multipliers as does the strain rate, $\dot{\varepsilon}_{\alpha\beta}$, to the velocity vector. Substituting $\bar{\tau}_{\alpha\beta}$ from (12) into the J functional below (*Flesch et al.*, 2001) and then minimizing the functional J with respect to the Lagrange

multipliers yields the force balance equations that the Lagrange multipliers have to satisfy.

$$J = \int_S \left[\begin{pmatrix} \bar{\tau}_{xx} \\ \bar{\tau}_{yy} \\ \bar{\tau}_{xy} \end{pmatrix} - \begin{pmatrix} \Phi_{xx}^{obs} \\ \Phi_{yy}^{obs} \\ \Phi_{xy}^{obs} \end{pmatrix} \right]^T \widetilde{V}^{-1} \left[\begin{pmatrix} \bar{\tau}_{xx} \\ \bar{\tau}_{yy} \\ \bar{\tau}_{xy} \end{pmatrix} - \begin{pmatrix} \Phi_{xx}^{obs} \\ \Phi_{yy}^{obs} \\ \Phi_{xy}^{obs} \end{pmatrix} \right] dS, \qquad (13)$$

where $\bar{\tau}_{xx}$, $\bar{\tau}_{yy}$ and $\bar{\tau}_{xy}$ are the vertically integrated deviatoric stresses that we are solving for, $\widetilde{V}^{-1}$ is the covariance matrix (see Appendix), $\Phi_{xx}^{obs} = \Phi_{yy}^{obs} = -\frac{1}{3}\bar{\sigma}_{zz}$ and $\Phi_{xy}^{obs} = 0$. Minimizing J with respect to the Lagrange multipliers provides a unique solution to the force balance equations that corresponds to the global minimum in the second invariant of deviatoric stress (*Flesch et al.*, 2001).

2.4 GPE from Crust 2.0

We use the crustal thicknesses and densities from the Crust 2.0 dataset to calculate GPE per unit area. For the oceanic regions, we use the cooling plate model based on ocean floor age data (*Müller et al.*, 1997) and with revised parameters from *Stein and Stein* (1992) to define densities there. The densities of the last layer of the crustal model are replaced by an upper mantle density of 3300 kg/m^3 beneath the continental lithosphere. The reference level, L, is chosen as 100 km (after *Jones et al.* (1996)) in this particular case. We also use a deeper reference level in order to take into account the density buoyancies associated with cratonic roots, which we discuss in a later section. Since water and ice are unable to transmit significant tectonic shear stresses, effects of ice and water layers are excluded from our GPE calculation. However, we take into account the pressure exerted by water and ice layers, which constitutes a boundary condition in the computation of the GPE integral (equation (7)). The GPE calculated from crustal thickness estimates of Crust 2.0 show high values occurring at high elevation regions like the Andes, western North America, eastern Africa, Tibetan plateau, as well as at the mid-oceanic ridges, with the maximum GPE at the Tibetan plateau (Figure 2). Lower elevation regions like the ocean basins and topographically low continental areas exhibit low GPE. The resultant depth integrated devi-

Figure 2: Global distribution of vertically integrated horizontal deviatoric stresses and GPE calculated from the uncompensated Crust 2.0 data. Tensional deviatoric stresses are shown by red arrows while compressional deviatoric stresses are shown by black arrows. Length of the arrows are proportional to the magnitude of stresses. Strike-slip regions are indicated by one tensional and one compressional pair of arrows. Areas having high GPE are in deviatoric tension while areas having low GPE are in deviatoric compression. GPE on scalebar is in Newtons/meter and corresponds to the depth integral of σ_{zz} from the Earth's surface to the reference level L at 100 km below sea-level.

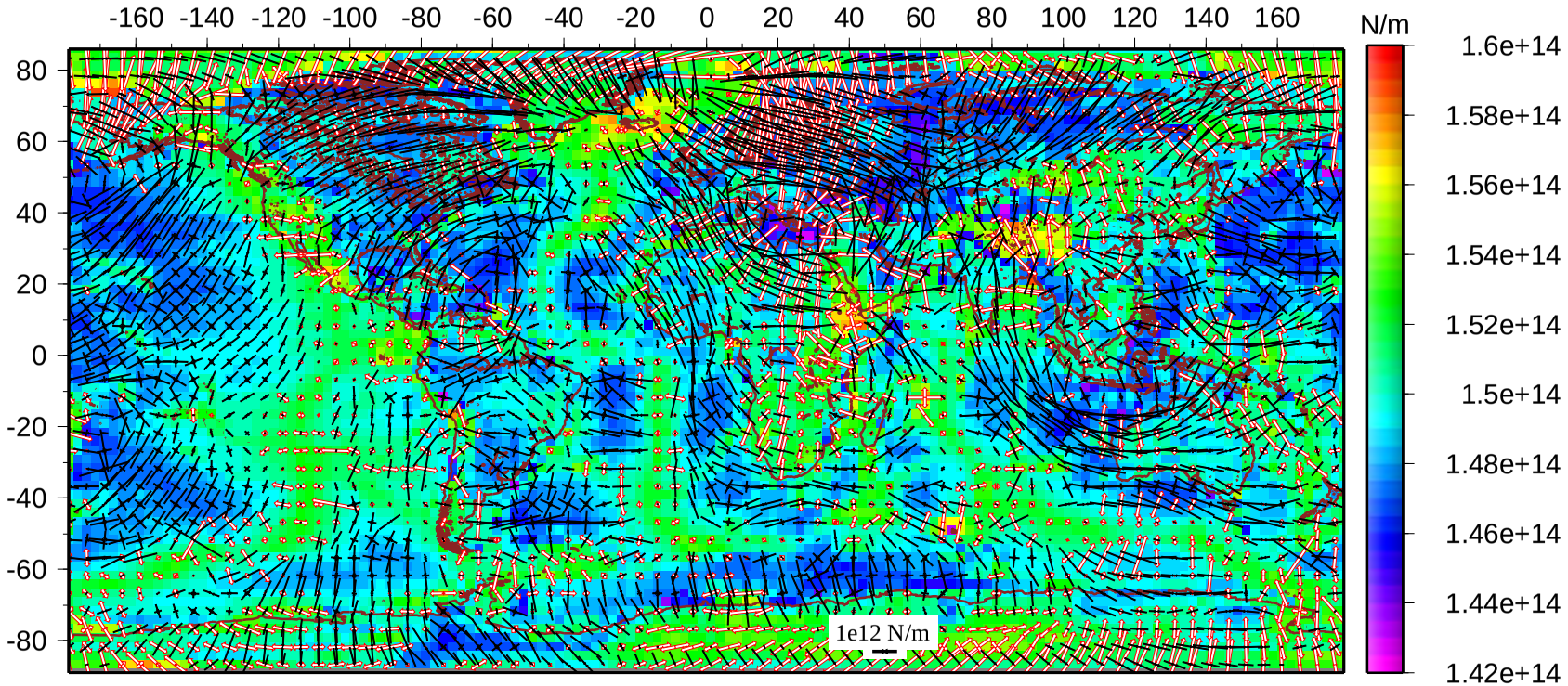
-160 -140 -120 -100 -80 -60 -40 -20 0 20 40 60 80 100 120 140 160
80
60
40
20
0
-20
-40
-60
-80
1e12 N/m
N/m
1.6e+14
1.58e+14
1.56e+14
1.54e+14
1.52e+14
1.5e+14
1.48e+14
1.46e+14
1.44e+14
1.42e+14

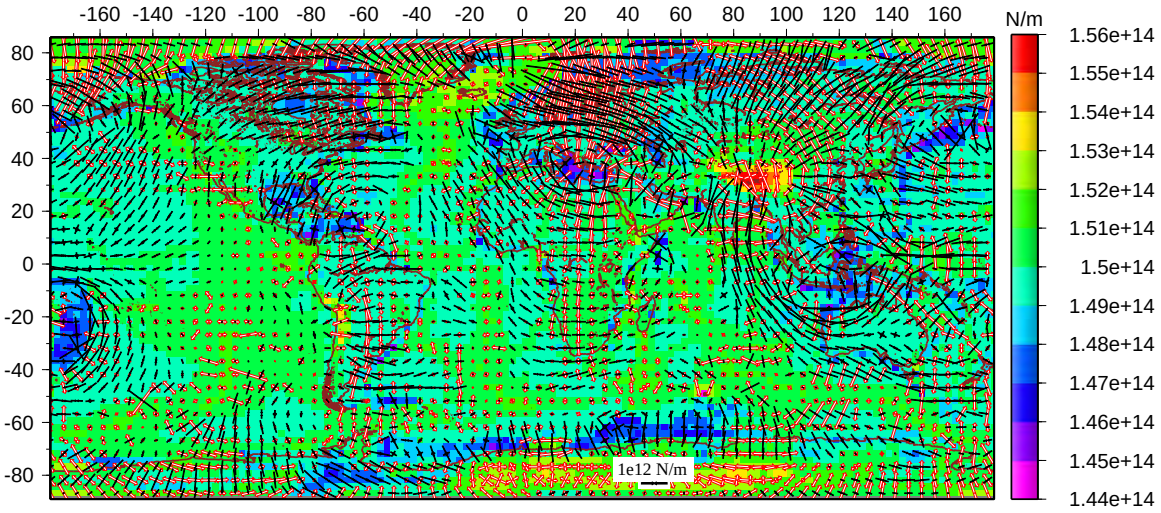

Figure 3: Global distribution of vertically integrated horizontal deviatoric stresses and GPE calculated from Crust 2.0, compensated by elevation adjustment. The range of GPE values, as well as the absolute magnitudes of deviatoric stresses, decrease compared to the uncompensated (in figure 2) as well as the other compensated case (figure 3), but the overall pattern remains similar to that in figures 2 and 3. Because compensation is achieved via elevation adjustment, figure 4 is the theoretical response of lithosphere from internal buoyancies, with the influence of dynamic topography removed.

atoric stress magnitudes (Figure 2) show a maximum depth integrals of deviatoric extension at the Tibetan plateau ($\sim 3 \times 10^{12}$ N/m) and compressional deviatoric stresses in the oceans and low elevation continental regions. The mid-oceanic ridges are in deviatoric extension ($\sim 1 - 1.5 \times 10^{12}$ N/m) as are topographically high areas that have higher GPE values. Moreover, the depth integrated deviatoric stresses for the Indo-Australian plate agree with the SH_{max} directions of the WSM (*Zoback*, 1992; *Reinecker et al.*, 2005) and those derived by *Sandiford et al.* (1995).

The Crust 2.0 model is not compensated. In order to investigate the effect of compensation, an isostatic solution was computed by compensating our model (equal pressure, $\int_{-h}^{L} \rho g dz = \sigma_{zz}(L)$, at the reference level L). The concept of isostatic equilibrium dates back to the 19^{th} century. The Airy model of isostatic compensation (*Airy*, 1855) involves a constant density layer with variable thickness while the Pratt model (*Pratt*, 1855) is based on a constant thickness layer of variable density. What occurs on Earth is perhaps a combination of these two end-members, with different regions exhibiting each mechanism in

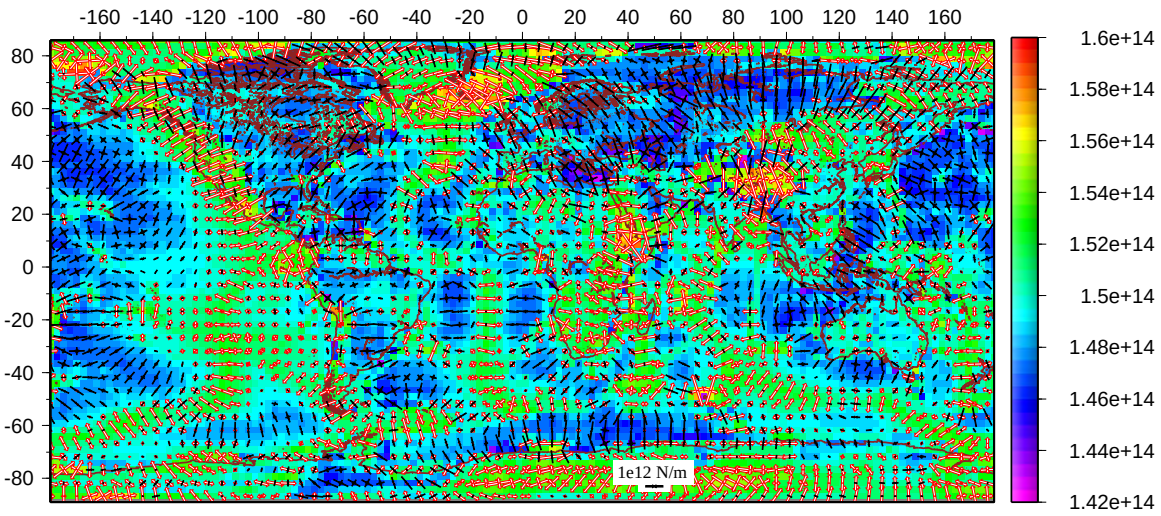

Figure 4: Same as Figure 2, but with laterally uniform lithospheric viscosity. Note that significant changes occur in deviatoric stress orientations in many of the plate boundary zones (western N. America, Mediterranean, southeast Asia) as well as within the Indo-Australian plate region.

varying degrees. The vertical stress at the reference level, L, is given by:

$$\sigma_{zz}(L) = \int_{-h}^{L} \rho(z) g dz \tag{14}$$

can be equilibrated either by adjusting the density of the upper mantle, $\rho(z)$, or by adjusting the elevation, h, of the crustal blocks. In the latter case, the adjustment constitutes the removal of the inferred dynamic topography that has resulted from radial tractions applied at the reference level, L, (which is the inferred source of the variable values of $\sigma_{zz}(L)$).

Upper mantle densities are adjusted with respect to an average vertical stress $\sigma_{zz}(L)$ for the continents and oceans. Although the resultant GPE and deviatoric stress solutions (Figure 3) provide values that are $10-20\%$ lower than the uncompensated case, the overall style of deviatoric tension and compression remain unchanged, with the maximum deviatoric tension ($\sim 2.5 \times 10^{12}$ N/m).

In the second method, compensation is achieved by adjusting the elevations based on an average vertical stress, $\sigma_{zz}(L)$, for the continents and oceans, while keeping the densities of the mantle constant. Thus, elevations of the crustal blocks are lowered or raised according to whether the actual vertical stress at reference level L is greater or less than the average vertical stress there. Both the GPE and deviatoric stress magnitudes show similar

pattern as before (Figure 4), with the maximum deviatoric tension of $\sim 2 \times 10^{12}$ N/m occurring at the Tibetan Plateau. Compensation by density adjustment does not acknowledge the existence of dynamic topography (discussed later), whereas in the later case, the entire deviation from an isostatic solution is attributed to the existence of dynamic topography. The deviatoric stress field in Figure 4, therefore, represents the theoretical contribution of lithosphere buoyancies alone, with dynamic topography removed under the assumption that all variations in vertical stress at the reference level are due to dynamic topography. What occurs on Earth is a combination of these two end-members. On comparing the GPE differences and deviatoric stress magnitudes for the two compensated cases (Figures 3 and 4), we find that magnitudes of both are reduced considerably in the latter case (compensation by elevation adjustment). Due to increasing density moment as a function of mass anomalies considered at increasing distances away from the reference level, L, (discussed in detail in section 2.7), near-surface densities have a greater impact on the change in GPE than do deeper density variations. This means that adjustment of elevation has a greater impact on GPE change, and associated deviatoric stress magnitudes, than the adjustment of density in the mantle. Another way of interpreting this result is that, assuming flexure to be negligible at long wavelengths, if horizontal variations in $\sigma_{zz}(L)$, are inferred to be associated with mantle flow or dynamic support, then the resulting dynamic topography is a major factor contributing to lithospheric GPE differences.

As a way of investigating the role of weak plate boundaries, we also compute deviatoric stresses with a uniform lithospheric viscosity (μ =1 in (9)) based on an uncompensated Crust2.0 model. The resultant deviatoric stresses (Figure 5) have magnitudes similar to those in the uncompensated case. However, the plate boundaries, in this uniform viscosity case, have higher stresses as compared to the plate boundaries in all the other cases (cases with lateral viscosity variations). When compared with the uncompensated result with lateral viscosity variations, the stress patterns appear similar in a few areas, but differ substantially in many regions, particularly in the continents. Furthermore, the arcuate feature of compressive deviatoric stresses throughout the Indo-Australian plate boundary regions (observed in the WSM) is only achieved when lateral viscosity variations in the lithosphere are taken into consideration (refer to Figure 5 and compare with Figures 2-4,

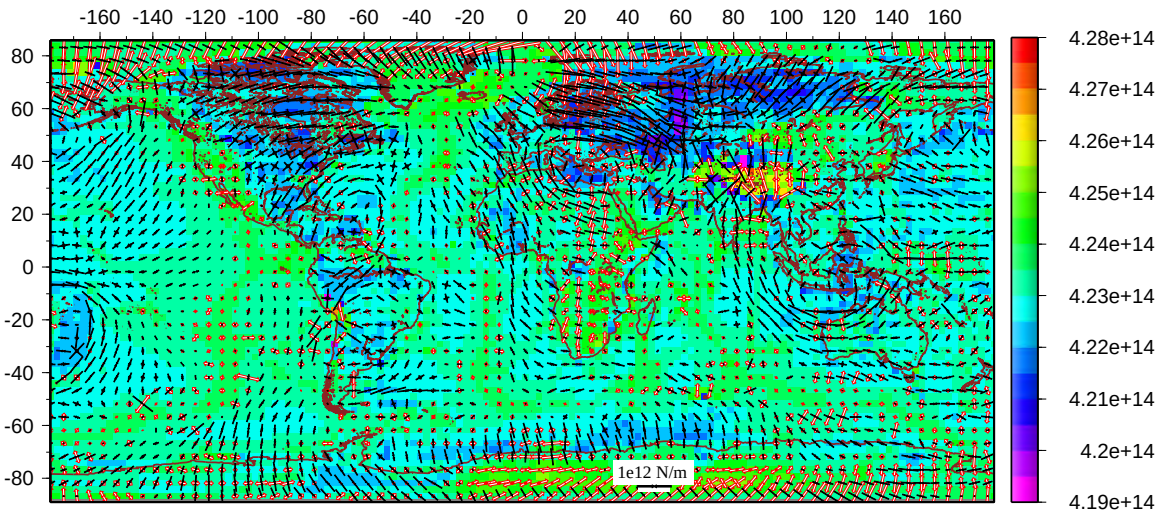

Figure 5: Same as Figure 3, but compensated at the depth of the deepest lithosphere ($\sim$ 270 km).

and 6). Lateral strength variations, with weak zones corresponding to location of today's plate boundary zones, and stronger zones corresponding to position of the plates, therefore, plays a profoundly important role in affecting the deviatoric stress field.

2.5 Deeper Lithospheric Density Buoyancies

As mentioned earlier, we perform depth integrals to 100 km, which is sometimes assumed to approximate the boundary between the non-convecting lithosphere and the convecting mantle. However, the base of the lithosphere is variable in depth due to continental keels, depth variations for different aged oceans, etc. Accounting properly for this variable depth involves sophisticated methods that we do not attempt in this paper. One can approximate the influence of variable bottom lithosphere, however, by integrating down to a constant reference level, equal to the depth of the deepest lithosphere. However, this can only be achieved under the assumption that there is no buoyancy-driven mantle convection acting on the variable base of lithosphere, and no dynamic topography. This implies total compensation; that is, equal vertical stress at the depth of the reference level (bottom of the deepest lithosphere).

In order to take into account the effects of the deeper density buoyancies associated with the lithosphere, the reference level, L, is extended to a greater depth. Based on the

lithospheric thickness model of *Conrad and Lithgow-Bertelloni* (2006), we take L to be at the depth of the deepest lithosphere ($\sim$ 270 km). Integrating to a depth of $\sim$ 270 km captures a significant portion of the asthenosphere. However, a constant asthenospheric density outside of the very deep cratonic areas makes no contribution to the deviatoric stress field.

In order to achieve compensation at L, we adjust the densities of the subcrustal layer (layer between the base of the crust and the base of the lithosphere) with respect to an average vertical stress at 270 km depth for continents and oceans. The asthenosphere layer (layer between the base of the lithosphere and the reference level, L) is assigned a constant density of 3300 kg/m^3. Based on these adjusted densities, the GPE and the corresponding deviatoric stress field are calculated with viscosities varying as a function of both strain rates (Figure 1a) and combined strain rates and lithospheric thickness (Figure 1b).

The absolute GPE values naturally increase when L is at a greater depth (Figure 6). However, the GPE differences, and consequently the deviatoric stress magnitudes, are lower than the corresponding model compensated at 100 km (Figure 3). The overall depth integrated deviatoric stress pattern (Figure 6) is similar to the previous cases (Figures 2-4). The lower deviatoric stress magnitudes may indicate the influence of a lower density (less than 3300 kg/m^3) subcrustal lithospheric layer used in most of the regions to achieve compensation.

2.6 GPE from Geoid

We also calculate GPE from the EGM96 geoid dataset. Geoid anomalies have been used to calculate GPE by *Coblentz et al.* (1994); *Sandiford and Coblentz* (1994); *Flesch et al.* (2000, 2001). *Coblentz et al.* (1994) calculated geoid anomaly as

$$\Delta N = -\frac{2\pi G}{g^2}\Delta U_l \tag{15}$$

(*Turcotte and Schubert*, 1982) where G is the universal gravitational constant, g is the acceleration due to gravity and ΔU is the GPE from geoid given by

$$\Delta U_l = -\int_0^L \Delta\rho(z) g z dz = -\frac{\Delta N g^2}{2\pi G} \tag{16}$$

However, this relationship is true only if isostatic compensation prevails everywhere at the reference level L (*Haxby and Turcotte*, 1978). Otherwise, significant errors will be introduced if the geoid is used to infer GPE and dynamic topography is present. Moreover, the geoid anomalies, and hence the computed GPE values, are also sensitive to the filtering techniques. Note that the integral in (16) is not equivalent to the vertical integral of vertical stress, σ_{zz}, or GPE, which is correctly shown in equation (7). Instead,

$$\int_0^L \rho(z) g z dz = L\bar{\sigma}_{zz} - \int_{-h}^0 \rho(z) z g dz + L\int_{-h}^L \rho(z) g dz \tag{17}$$

(*Flesch et al.*, 2007). Hence, the geoid can only be used as a proxy for GPE if the right most integral in (17) is a constant at reference depth L, meaning there is no dynamic topography (*Flesch et al.*, 2007). Note that if the last term in (17), the pressure at reference depth L, varies over long wavelengths, then the geoid can be used as a proxy for GPE over length scales where those lateral variations in pressure are small. For example, for regional scale models such as North America, it may be appropriate to use the geoid as a proxy for GPE (*Humphreys and Coblentz*, 2007).

For comparison purposes, we evaluate the deviatoric stress field associated with GPE inferred from the geoid in order to quantify the differences from a solution directly inferred from crustal structure. We use the EGM96 geoid model in order to approximate the GPE, with reference to a mid-oceanic ridge column of lithosphere (after *Coblentz et al.* (1994)). Like *Flesch et al.* (2001), and *Jones et al.* (1996) before them, we filter the geoid such that terms below degree and order 7 are removed with a cosine taper to degree and order 11. A constant crustal and mantle density of 2828 kg/m^3 and 3300 kg/m^3 are assumed (after *Flesch et al.* (2001)). The deviatoric stresses are computed in the same way as from the Crust 2.0 dataset.

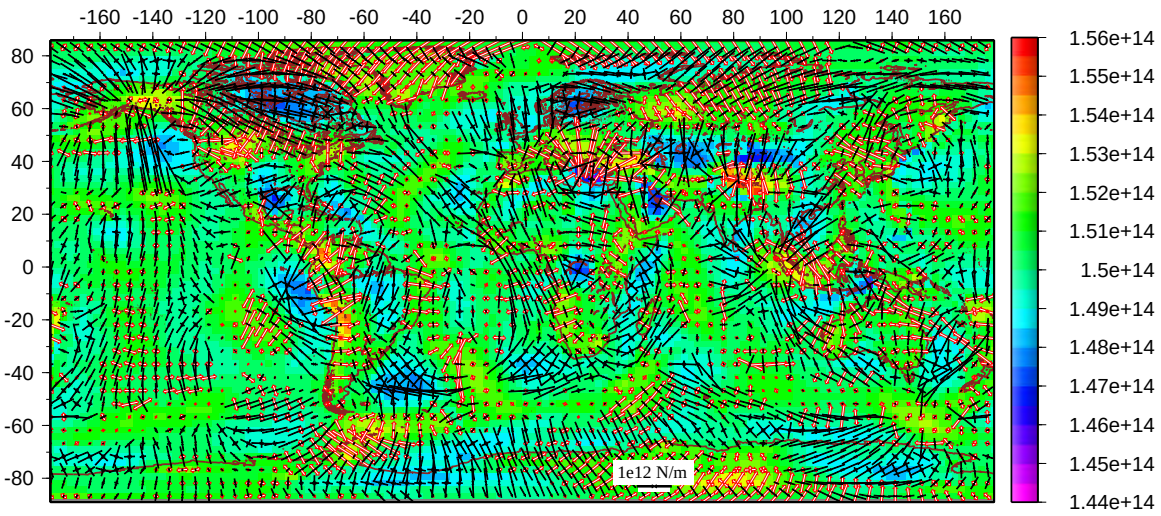

Figure 6: Global distribution of vertically integrated horizontal deviatoric stresses and GPE inferred from the EGM96 geoid dataset.

There are many differences between the deviatoric stresses calculated from the geoid dataset and those from the Crust 2.0 dataset. Both GPE differences and the deviatoric stress field (Figure 7) are in general lower than those from the Crust 2.0 solutions. The deviatoric tension in western North America does not show up in the geoid solution. For the geoid solution, deviatoric compression in northern Europe, the South-east Asian subduction zone, and the North American continent change to deviatoric tension, or strike-slip style of deformation, with the highest deviatoric tension ($\sim 2 \times 10^{12}$ N/m) occurring at the Tibetan plateau. The mid-oceanic ridges in the geoid case constitute a much weaker signal than in the Crust 2.0 solutions. The matching of deviatoric stresses for the Indo-Australian plate with the SH_{max} directions of the WSM is considerably poorer for the geoid case. Similar differences exist between the geoid and uncompensated solution (Figure 2), with the differences in magnitudes being greater.

2.7 Reference Levels

Choice of reference level for the calculation of GPE has significant impact on the inferred deviatoric stresses associated with internal density buoyancy distributions in the lithosphere for the uncompensated case. Gravitational potential energy values must be

computed with respect to some reference level and, depending on which reference level is chosen, the calculated GPE, and the associated deviatoric stresses, will change if the topography is uncompensated. Historically, there has been a precedence of calculating GPE with the surface of the geoid (sea-level) as the reference level (*Fleitout and Froidevoux*, 1982; *Fleitout*, 1991; *Coblentz et al.*, 1994; *Jones et al.*, 1996; *Zoback and Mooney*, 2003). *Fleitout* (1991) gave the "moment law":

$$\int_0^L \Delta\sigma_{zz}(z)dz = \delta mgd, \tag{18}$$

which states that the influence of an intralithospheric mass anomaly is proportional to its moment, the product of its amplitude δmg and depth d. This means that the greater the depth of the mass anomaly, the larger the impact on the GPE and the associated stress field. If the surface is treated as reference level, the above relation can be re-written as

$$\int_0^L \Delta\sigma_{zz}(z)dz = g\int_0^L \Delta\rho(z)zdz \tag{19}$$

However, this moment law is based on treating the sea-level as the level of reference. On the other hand, if we consider a constant depth level of L, which is the maximum depth of integration, as the reference level, then the moment equation will be modified to

$$\int_0^L \Delta\sigma_{zz}(z)dz = \int_0^L \left[\int_0^z \Delta\rho(z')gdz'\right]dz = \int_0^L (L-z)\Delta\rho(z)gdz = \delta mg(L-z) \tag{20}$$

This implies that the near-surface density anomalies will have a greater effect on GPE, and the corresponding deviatoric stress field, than deeper anomalies within the portion of the lithosphere considered in the depth integrals. However, the differences in reference level are only relevant when topography is uncompensated. In the compensated case, the term in (20), $\sigma_{zz}(L)$, is a constant and the remaining term, $\int_0^L z\Delta\rho(z)gdz$ is identical to that in (19), where the reference level is sea-level. Although the inferred value of GPE is different, depending on whether (18) or (20) is used, because deviatoric stress depends only on the gradient in GPE, (18) and (20) yield the same result when $\sigma_{zz}(L)$ is a constant. When vertical stress $\sigma_{zz}(L)$ varies at the reference level, L, however, use of (18) and (20)

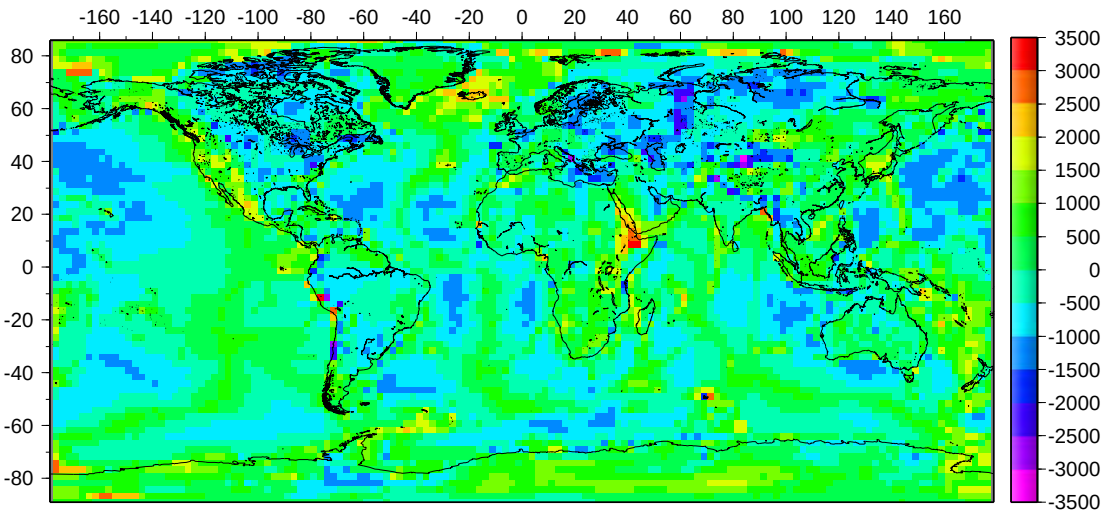

Figure 7: Global distribution of dynamic topography. The red areas indicate positive dynamic topography while the blue areas indicate negative dynamic topography. The maximum dynamic topography $\sim$ 3.5 km occurs in central East Africa. Topography on scalebar is in meters.

will yield different estimates of deviatoric stress. Recall that the thin sheet equations arise from depth integration of the full three dimensional force balance equations, with limits of integration from the surface, down to the reference level, L. The GPE term thus arises from the depth integration of the vertical stress, $\bar{\sigma}_{zz}$. To remain consistent with the thin sheet approach, the only appropriate form for GPE is therefore equation (20), where the reference level is at depth L.

2.8 Dynamic Topography

We define dynamic topography as the topography that arises from sub-lithospheric density anomalies that drive mantle flow. The radial component of mantle flow (τ_{rr}) causes vertical displacements of the lithosphere producing dynamic topography. These kinds of topographical features are in contrast to those created by density variations within the lithosphere, which might be called static topography. The total topography that we observe on the surface of the Earth is the net sum of these static and dynamic parts. Isolation of this dynamic topography provides a constraint on the lithospheric contribution of topography. Thus, one aim of our study is to distinguish between these two types of topographies by estimating the styles and magnitudes of dynamic topography from our crustal solutions. Esti-

mates of global dynamic topography have been provided by *Hager et al.* (1985); *Cazenave et al.* (1989); *Panasyuk and Hager* (2000); *Steinberger et al.* (2001) and *Lithgow-Bertelloni and Guynn* (2004). *Cazenave et al.* (1989) and *Panasyuk and Hager* (2000) calculated dynamic topography by removing the effects of isostatic topography from the observed topography, the same way as we do here. *Steinberger et al.* (2001) and *Lithgow-Bertelloni and Guynn* (2004) used mantle flow field while *Hager et al.* (1985) used geoid anomalies in order to calculate dynamically induced topography.

GPE values from the uncompensated model contain the influence of dynamic topography as well. The weight of the lithospheric column, $\sigma_{zz}(L)$, at reference depth L is given by $\sigma_{zz}(L) = \int_{-h}^{L} \rho(z')g(z')dz' = \sigma_{zz}^{o}(L) + \tau_{zz}(L)$, in the presence of dynamic topography. This formulation ignores any contribution from flexure. Here, $\sigma_{zz}^{o}(L)$ is the reference stress, while $\tau_{zz}(L)$ is the radial traction at reference level L associated with deeper mantle flow that is responsible for producing dynamic topography. In order to remove the dynamic topography contribution, an isostatically compensated solution (uniform vertical stress at depth L) is calculated. One way of compensating our solution, as stated before, is by adjusting the elevations of the crustal blocks. Accordingly, areas with lower than average vertical stress at reference depth L get elevated in order to achieve uniform vertical stress at reference level while those with higher than average vertical stress at depth L are lowered in elevation. Thus, the difference between the compensated topography and observed topography should provide an estimate of the magnitude of dynamic topography. The highest magnitude dynamic topography ($\sim$ 3.5 km) occurs in eastern Africa (Figure 8) (*Lithgow-Bertelloni and Silver*, 1998). Other areas of positive dynamic topography are northern Atlantic near Greenland and parts of western North America. Somewhat lower magnitude positive dynamic topography occurs along the mid-oceanic ridges. These are the possible areas of upwelling, while areas of negative dynamic topography include eastern North America, parts of western Europe, and the deeper oceans. Our results bear considerable similarities to that of *Panasyuk and Hager* (2000) who computed dynamic topography in the above procedure; the only difference is that they used a less fine crustal dataset than we have. There might be possible errors in our estimates of dynamic topography magnitudes due to uncertainties in the upper mantle densities. However, this will not have any consid-

erable effect on the styles of dynamic topography. This result indicates the significance of dynamic topography in understanding the global distribution of deviatoric stresses.

2.9 Deviatoric Stress Magnitudes

We argue that many previous calculations of depth integrals or depth averages of deviatoric stress magnitudes in Tibet as well as in the mid-oceanic ridges, have been overestimated (*Ghosh et al.*, 2006). Maximum difference in depth integrals of deviatoric stress between Tibet and surrounding lowlands ($\bar{\tau}_{xx}|_{Tibet} - \bar{\tau}_{xx}|_{lowlands}$) is around $3.5 - 4 \times 10^{12} N/m$, which is about a factor of two lower than previous estimates of deviatoric stress difference ($\sim 6 - 7 \times 10^{12}$ N/m) there (*Molnar and Lyon-Caen*, 1988; *Molnar et al.*, 1993). Also, the ridge-push force, or the vertically integrated deviatoric stress magnitudes associated with the mid-oceanic ridges in our solution ($\sim 1.5 \times 10^{12}$ N/m), is lower than previous estimates of ridge-push ($\sim 3 \times 10^{12}$ N/m) (*Harper*, 1975; *Lister*, 1975; *Parsons and Richter*, 1980). This difference in deviatoric stress magnitudes from previous estimates can be attributed to two factors: (i) either a two dimensional approximation of the thin sheet applied along a single profile and/or (ii) the form assumed for the hydrostatic state of stress, or both (*Dalmayrac and Molnar*, 1981; *Molnar and Lyon-Caen*, 1988). We use the term hydrostatic stress to refer to the reference pressure, P, subtracted from the total stress to obtain the deviatoric stress: $\tau_{ij} = \sigma_{ij} - P\delta_{ij}$. If P is assumed to be the lithostatic or vertical stress, σ_{zz}, then the deviatoric stress is defined as $\tau_{ij} = \sigma_{ij} - \sigma_{zz}\delta_{ij}$ (which we call 2-D definition of deviatoric stress). Such an assumption implies the vertical component of the deviatoric stress, $\bar{\tau}_{zz}$, to be equal to 0, which is entirely a special case, and is unlikely to be applicable in many areas (*Engelder*, 1994). If P is defined as the mean stress, then deviatoric stress becomes $\tau_{ij} = \sigma_{ij} - \frac{1}{3}\sigma_{kk}\delta_{ij}$ (which we call a 3-D definition of deviatoric stress), with the constraint $\bar{\tau}_{xx} + \bar{\tau}_{yy} + \bar{\tau}_{zz} = 0$ (*Flesch et al.*, 2001). The largest estimates of deviatoric stresses have resulted from solutions to simplified 2-D thin sheet equations, applied along a single profile, along with the assumption that hydrostatic stress P is equal to the vertical stress, and $\tau_{zz} = 0$. In that case, the two horizontal force balance equations reduce to a

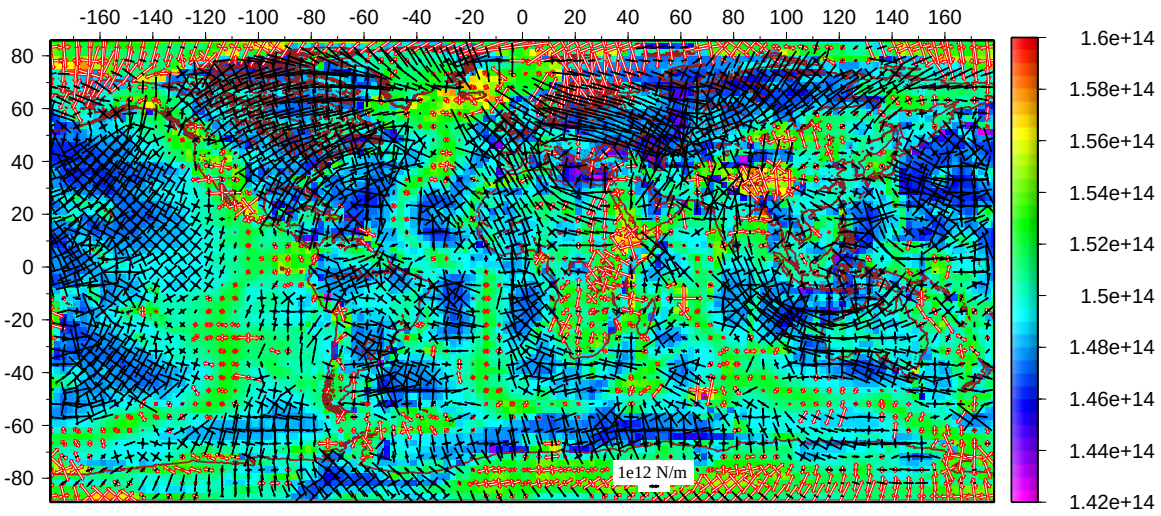

Figure 8: Global distribution of vertically integrated horizontal deviatoric stresses, calculated from an uncompensated Crust 2.0 dataset, based on a 2-D definition of deviatoric stress (equations (24)-(26)). The stress magnitudes are a factor of two higher than all our previous solutions, calculated using a 3-D definition.

single equation:

$$\frac{\partial \sigma_{xx}}{\partial x} = 0, \tag{21}$$

which, after using a 2-D definition of deviatoric stress, gives $\bar{\tau}_{xx} = -\bar{\sigma}_{zz} +$ a constant C as a solution to the depth integrated force balance equation. That is, the depth integrated deviatoric stress magnitude equals GPE. On the other hand, using the same force balance equation, but a definition of hydrostatic stress as the mean stress, yields $\bar{\tau}_{xx} = -\frac{1}{2}\bar{\sigma}_{zz} +$ a constant C, a magnitude of a factor of two lower than the previous case. The reason for lower stresses using the 3-D definition of deviatoric stress is that some of the potential energy differences get absorbed in the vertical term $\bar{\tau}_{zz}$, which is zero in the case with the 2-D definition.

Using the 3-D force balance equations, one of the horizontal deviatoric stresses, say $\bar{\tau}_{xx}$, can be given as:

$$\bar{\tau}_{xx}^{3D} = \sigma_{xx} - \frac{1}{3}(\sigma_{xx} + \sigma_{yy} + \sigma_{zz}) \tag{22}$$

and

$$\bar{\tau}_{xx}^{2D} = \sigma_{xx} - \sigma_{zz}, \tag{23}$$

according to the 3-D and the 2-D definitions of deviatoric stress, respectively. From this,

the relation between the 2-D and the 3-D deviatoric stresses can be written as:

$$\bar{\tau}^{2D}_{xx} = 2\bar{\tau}^{3D}_{xx} + \bar{\tau}^{3D}_{yy}, \tag{24}$$

and similarly,

$$\bar{\tau}^{2D}_{yy} = 2\bar{\tau}^{3D}_{yy} + \bar{\tau}^{3D}_{xx} \tag{25}$$

$$\bar{\tau}^{2D}_{xy} = \bar{\tau}^{3D}_{xy}. \tag{26}$$

The reason for still lower stresses by using the full 3-D equations is the presence of the horizontal terms $\bar{\tau}_{yy}$ and $\bar{\tau}_{xy}$ which are absent in the 2-D case. Solutions using the full 3-D force balance equations, but a 2-D definition of deviatoric stress, yield deviatoric stress magnitudes a factor of two or more higher than our previous 3-D solutions (Figure 9). The Tibetan plateau, for example, exhibits deviatoric tension of $\sim 5 \times 10^{12}$ N/m, while the mid-oceanic ridges show deviatoric tension of $\sim 2 - 2.5 \times 10^{12}$ N/m, similar to the deviatoric stress magnitudes given previously for Tibet by *Molnar and Lyon-Caen* (1988); *Molnar et al.* (1993), and for the mid-oceanic ridges by *Harper* (1975); *Lister* (1975); *Parsons and Richter* (1980).

One importance of evaluating the correct magnitude of deviatoric stresses lies in the fact that the onset of deformation of the Indian ocean lithosphere has been explained by the high deviatoric stress magnitude ($\sim 8 \times 10^{12}$N/m) in that area associated with the large GPE differences between Tibet and the Indian Ocean (*Molnar et al.*, 1993). According to *Molnar et al.* (1993), a sediment laden oceanic lithosphere would be capable of buckling at a deviatoric stress magnitude of $\sim 4.4 \times 10^{12}$N/m. We do not disagree with this. However, the vertically integrated deviatoric stress magnitude in that area, associated with the large GPE differences between Tibet and surrounding Indian Ocean, is not more than $\sim 1.5 \times 10^{12}$N/m. Therefore, deviatoric stresses to produce buckling must arise from additional sources other than GPE differences alone. Moreover, the magnitude of the ridge-push force has been used to constrain the intra-plate stress magnitude of the Indo-Australian plate (*Reynolds et al.*, 2002) and to infer the degree of slab-plate coupling for the Java and Sumatra slabs (*Sandiford et al.*, 2005). However, the ridge-push force magnitude falls

short of balancing the $\sim 3 \times 10^{12}$N/m NNW-SSE oriented deviatoric tension at the Tibetan plateau (*Ghosh et al.*, 2006). Since the total depth integrated deviatoric stress acting on the lithosphere can be attributed to stress related to (1) GPE differences and (2) basal tractions arising from deeper density buoyancies, the insufficiency of the ridge-push force in balancing the deviatoric tension at the Tibetan plateau calls for additional deviatoric stresses of magnitude $\sim 3 \times 10^{12}$N/m associated with driving shear tractions at the base of the lithosphere in the Indian plate region. The density buoyancy distribution giving rise to these driving tractions is likely related to the long history of subduction of the Indian and Australian plates (*Lithgow-Bertelloni and Richards*, 1995; *Wen and Anderson*, 1997b).

2.10 Comparison of Calculated Deviatoric Stresses with the Strain Rate Tensor Field in the Plate Boundary Zones

We introduce a quantitative way of testing our modeled deviatoric stresses with strain rate information from the Global Strain Rate Map (*Kreemer et al.*, 2003; *Holt et al.*, 2005). The Global Strain Rate Map (GSRM) model is a velocity gradient tensor field solution for the entire Earth's surface. It is a high resolution dataset along the Earth's diffuse plate boundary zones. The GSRM model is based on 5170 GPS stations as well as Quarternary fault slip rate data. Our calculated deviatoric stress tensor is scored with the strain rate tensor from GSRM and we seek to match direction of principal axes as well as style of faulting. We define a correlation coefficient (*Flesch et al.*, 2007)

$$-1 \leq \sum_{areas} (\varepsilon \cdot \tau)\Delta S / \left(\sqrt{\sum_{areas} (E^2)\Delta S} * \sqrt{\sum_{areas} (T^2)\Delta S} \right) \leq 1 \tag{27}$$

where $E = \sqrt{\varepsilon_{xx}^2 + \varepsilon_{yy}^2 + \varepsilon_{zz}^2 + \varepsilon_{xy}^2 + \varepsilon_{yx}^2} = \sqrt{2\varepsilon_{xx}^2 + 2\varepsilon_{xx}\varepsilon_{yy} + 2\varepsilon_{yy}^2 + 2\varepsilon_{xy}^2}$,
$T = \sqrt{\tau_{xx}^2 + \tau_{yy}^2 + \tau_{zz}^2 + \tau_{xy}^2 + \tau_{yx}^2} = \sqrt{2\tau_{xx}^2 + 2\tau_{xx}\tau_{yy} + 2\tau_{yy}^2 + 2\tau_{xy}^2}$
and $\varepsilon \cdot \tau = 2\varepsilon_{xx}\tau_{xx} + \varepsilon_{xx}\tau_{yy} + \varepsilon_{yy}\tau_{xx} + 2\varepsilon_{yy}\tau_{yy} + 2\varepsilon_{xy}\tau_{xy}$.
E and T are the second invariants of strain rate and deviatoric stress respectively, ε_{ij} are

Region of interest	Number of areas	$\mu_{ref} \sim \frac{1}{3}$			$\mu_{ref} \sim \frac{1}{30}$			$\mu_{ref} \sim \frac{1}{300}$			$\mu_{ref} \sim \frac{1}{3000}$		
		U	CD	CE	U	CD	CE	U	CD	CE	U	CD	CE
Western N. America	132	0.39	0.66	0.74	0.53	0.72	0.75	0.44	0.68	0.75	0.45	0.70	0.73
Andes	89	0.14	0.60	-0.04	0.25	0.69	0.06	0.15	0.54	-0.04	0.22	0.67	0
Eastern Africa	164	0.40	0.09	0.10	0.31	-0.04	-0.06	0.38	0.16	0.06	0.40	-0.01	0.04
Mediterranean	83	0.52	0.44	0.49	0.55	0.52	0.50	0.55	0.54	0.49	0.50	0.48	0.46
Central Asia	187	0.26	0.33	0.14	0.32	0.41	0.32	0.31	0.42	0.30	0.30	0.38	0.27
Indo-Australian plate boundary	174	0.68	0.71	0.70	0.69	0.77	0.74	0.64	0.61	0.67	0.60	0.70	0.67
Mid-oceanic ridges	292	0.82	0.86	0.87	0.79	0.85	0.87	0.77	0.83	0.84	0.66	0.76	0.76
Western Pacific	109	0.48	0.62	0.56	0.51	0.60	0.53	0.42	0.58	0.42	0.46	0.57	0.52
South East Asia	167	0.48	0.62	0.59	0.61	0.68	0.65	0.54	0.66	0.58	0.55	0.65	0.61
Total	1944	0.51	0.57	0.51	0.54	0.60	0.52	0.50	0.58	0.49	0.50	0.56	0.49

Table 1: Correlation coefficients obtained from a comparison between different deviatoric stress models with the strain rate tensor field from the GSRM model (see equation (27)) with reference level, $L = 100$ km and viscosities varying as a function of strain rates only (Figure 1a). The abbreviations U, CD and CE denote models that are uncompensated, compensated by density adjustment and compensated by elevation adjustment respectively.

strain rates from *Kreemer et al.* (2003), ΔS is the grid area and τ_{ij} are the calculated vertically integrated deviatoric stresses. Normalization of $\varepsilon \cdot \tau$ by E and T in equation (27) ensures that the correlation coefficient has no dependence on stress or strain rate magnitudes. The correlation coefficient only depends on a match of the deviatoric stress tensor to the inferred style of faulting (relative magnitude of extensional and compressional strain rate principal axes) and the match to the directions of principal axes between the stress and the strain rate tensors. A maximum correlation coefficient of +1 indicates perfect fit. That is, the stress tensor and the strain rate tensor are exactly the same in terms of style and direction of principal axes, while a coefficient of -1 indicates anti-correlation. For example, if the observed strain rate shows thrust faulting in an area, while our calculated deviatoric stress predicts normal faulting in the same area, then the correlation coefficient will predict a value of -1. A value of 0 will imply that the stress and the strain are uncorrelated. That is, for example, our modeled stresses predicting strike-slip faulting in an area of thrust or normal faulting, where the compressional and extensional principal axes differ from those in the GSRM by 45°.

Region of interest	Number of areas	$\mu_{ref} \sim \frac{1}{3}$			$\mu_{ref} \sim \frac{1}{30}$			$\mu_{ref} \sim \frac{1}{300}$			$\mu_{ref} \sim \frac{1}{3000}$		
		U	CD	CE	U	CD	CE	U	CD	CE	U	CD	CE
Western N. America	132	0.47	0.65	0.71	0.56	0.69	0.72	0.52	0.69	0.75	0.44	0.66	0.68
Andes	89	0.48	0.83	0.36	0.51	0.86	0.37	0.44	0.84	0.24	0.41	0.83	0.23
Eastern Africa	164	0.20	-0.31	-0.27	0.08	-0.35	-0.32	0.24	-0.17	-0.17	0.30	-0.3	-0.18
Mediterranean	83	0.44	0.40	0.44	0.52	0.48	0.51	0.55	0.52	0.49	0.50	0.43	0.49
Central Asia	187	0.25	0.33	0.20	0.33	0.40	0.36	0.37	0.46	0.39	0.29	0.37	0.33
Indo-Australian plate boundary zone	174	0.65	0.75	0.70	0.60	0.75	0.68	0.61	0.72	0.69	0.56	0.68	0.62
Mid-oceanic ridges	292	0.70	0.81	0.81	0.63	0.78	0.78	0.65	0.76	0.76	0.53	0.64	0.65
Western Pacific	109	0.56	0.63	0.61	0.58	0.60	0.59	0.57	0.61	0.57	0.53	0.58	0.57
South East Asia	167	0.57	0.61	0.61	0.66	0.68	0.68	0.63	0.68	0.66	0.61	0.66	0.64
Total	1944	0.50	0.53	0.49	0.50	0.54	0.50	0.52	0.57	0.51	0.48	0.51	0.47

Table 2: Same as Table 1 but with viscosities varying as a function of both strain rates and lithosphere thickness (Figure 1b).

Region of interest	Number of areas	$\mu_{ref} = 1$
Western N. America	132	0.08
Andes	89	-0.20
Eastern Africa	164	0.63
Mediterranean	83	0.33
Central Asia	187	0.10
Indo-Australian plate boundary zone	174	0.30
Mid-oceanic ridges	292	0.78
Western Pacific	109	0.09
South East Asia	167	0.08
Total	1944	0.31

Table 3: Correlation coefficients obtained from comparison between deviatoric stress field from an uncompensated Crust 2.0 dataset with the strain rate tensor field from the GSRM model with laterally uniform viscosity in the lithosphere.

Region of interest	Number of areas	$\mu_{ref} \sim \frac{1}{3}$	$\mu_{ref} \sim \frac{1}{30}$	$\mu_{ref} \sim \frac{1}{300}$	$\mu_{ref} \sim \frac{1}{3000}$
Western N. America	132	0.44	0.57	0.50	0.50
Andes	89	0.21	0.35	0.22	0.30
Eastern Africa	164	0.45	0.40	0.45	0.43
Mediterranean	83	0.51	0.54	0.53	0.48
Central Asia	187	0.24	0.27	0.26	0.26
Indo-Australian plate boundary zone	174	0.74	0.77	0.72	0.73
Mid-oceanic ridges	292	0.86	0.84	0.82	0.73
Western Pacific	109	0.52	0.53	0.45	0.49
South East Asia	167	0.61	0.66	0.61	0.63
Total	1944	0.55	0.58	0.54	0.54

Table 4: Correlation coefficients obtained from a comparison between different deviatoric stress models with the strain rate tensor field from the GSRM model with reference level, $L = 270$ km and viscosities varying as a function of strain rates only.

Region of interest	Number of areas	$\mu_{ref} \sim \frac{1}{3}$	$\mu_{ref} \sim \frac{1}{30}$	$\mu_{ref} \sim \frac{1}{300}$	$\mu_{ref} \sim \frac{1}{3000}$
Western N. America	132	0.52	0.60	0.56	0.47
Andes	89	0.56	0.60	0.54	0.51
Eastern Africa	164	0.26	0.13	0.27	0.28
Mediterranean	83	0.43	0.50	0.51	0.48
Central Asia	187	0.24	0.29	0.32	0.25
Indo-Australian plate boundary zone	174	0.69	0.67	0.70	0.62
Mid-oceanic ridges	292	0.76	0.69	0.69	0.58
Western Pacific	109	0.57	0.58	0.56	0.54
South East Asia	167	0.61	0.69	0.68	0.65
Total	1944	0.53	0.54	0.55	0.50

Table 5: Same as Table 4, but with viscosities varying as a function of both strain rates and lithosphere thickness.

The different stress models from two different datasets (Crust 2.0 and EGM96 Geoid) are compared with the strain rate tensor field from GSRM. Such a comparison provides a quantitative means of evaluating the contribution that the lithospheric component of buoyancies make to the total stress tensor field within the plate boundary zones. A poor match, for example, highlights regions where additional stress component associated with deeper density buoyancies, and associated tractions, are necessary to explain the deformation indicators, and hence total deviatoric stress field. Higher correlation coefficients indicate a closer match between the stress tensor and strain tensor fields. Amongst the different models that we test, the best fit to the deformation indicators is given by the one calculated from Crust2.0 dataset, compensated by density adjustment at 100 km, and with viscosities dependent only on strain rates (with reference viscosity $\sim 1/30$). The overall correlation for this model is 0.60 (Table 1, Figure 10c). Nevertheless, individual regions react differently to different models. For example, for a 100 km reference level, the uncompensated model provides the best fit in areas like Eastern Africa and the Mediterranean (Tables 1 and 2, Figures 10a and 10b), whereas in regions like Andes, Central Asia and to some extent in Western Pacific, Indo-Australian plate boundary zone and South East Asia, the best fit is given by a model compensated by density adjustment (Tables 1 and 2, Figures 10c and 10d). A model compensated by adjusting the topography, on the other hand, gives the best fit to the strain rate tensor data in western North America, as well as in the mid-oceanic ridges (Tables 1 and 2, Figures 10e and 10f).

Region of interest	Number of areas	$\mu_{ref} \sim \frac{1}{3}$	$\mu_{ref} \sim \frac{1}{30}$	$\mu_{ref} \sim \frac{1}{300}$	$\mu_{ref} \sim \frac{1}{3000}$
Western N. America	132	-0.31	-0.20	-0.20	-0.22
Andes	89	-0.32	-0.31	-0.30	-0.34
Eastern Africa	164	-0.03	-0.06	-0.03	-0.04
Mediterranean	83	0.15	0.32	0.32	0.22
Central Asia	187	0.24	0.34	0.36	0.28
Indo-Australian plate boundary zone	174	0.29	0.46	0.41	0.35
Mid-oceanic ridges	292	0.81	0.81	0.76	0.62
Western Pacific	109	-0.06	-0.07	-0.09	-0.13
South East Asia	167	0.20	0.23	0.19	0.17
Total	1944	0.17	0.22	0.21	0.15

Table 6: Correlation coefficients obtained from a comparison between different deviatoric stress models from the Geoid dataset with the strain rate tensor field from the GSRM model with viscosities varying as a function of strain rates only.

Models with viscosities varying as a function of both strain rates and lithosphere thickness fare worse when the overall fit is considered (Table 2, Figures 10b, 10d and 10f), with a highest correlation coefficient of 0.57 (with reference viscosity $\sim 1/300$). The overall poor fit could potentially arise from errors in the lithosphere thickness model. However, areas, in particular, Andes and to a certain extent Central Asia, Southeast Asia and Western Pacific exhibit improved fit when viscosities along plate boundaries are allowed to vary with lithospheric thickness as well. A lithospheric model with a laterally uniform viscosity structure provides a poor fit to the strain rate tensor data (Table 3) with an overall correlation coefficient of 0.31.

For models inclusive of deeper density buoyancy within the keels, the only region that undergoes a considerable improvement in fitting is Eastern Africa (Tables 4 and 5, Figures 10g and 10h). For all the other areas the fit either degrades or stays unchanged.

The Geoid model displays a poor fit in almost all the areas (Figures 10i and 10j, Tables 6 and 7). The mid-oceanic ridges exhibit a substantially better fit compared to all the other areas for the geoid model. However, the fit to the mid-oceanic ridges is still worse than in the Crust 2.0 case. In fact, the mid-oceanic ridges show high correlation for both the Crust2.0 and the EGM96 models. The failure of the Geoid model to match the observed deformation in the plate boundaries could be associated with the sensitivity of the geoid anomalies, and consequently the GPE values, to the filtering techniques. Calculation of

Region of interest	Number of areas	$\mu_{ref} \sim \frac{1}{3}$	$\mu_{ref} \sim \frac{1}{30}$	$\mu_{ref} \sim \frac{1}{300}$	$\mu_{ref} \sim \frac{1}{3000}$
Western N. America	132	-0.33	-0.20	-0.19	-0.20
Andes	89	-0.27	-0.24	-0.27	-0.32
Eastern Africa	164	-0.11	-0.19	-0.10	-0.09
Mediterranean	83	0.17	0.31	0.27	0.19
Central Asia	187	0.25	0.36	0.38	0.31
Indo-Australian plate boundary zone	174	0.26	0.47	0.45	0.36
Mid-oceanic ridges	292	0.74	0.69	0.68	0.50
Western Pacific	109	-0.01	0	-0.04	-0.10
South East Asia	167	0.27	0.29	0.24	0.19
Total	1944	0.17	0.22	0.21	0.15

Table 7: Same as Table 6, but with viscosities varying as a function of both strain rates and lithosphere thickness.

GPE from geoid anomalies also assumes no dynamic topography, as mentioned earlier in section 2.6. The assumptions embedded in the use of geoid as a proxy for GPE may therefore only be appropriate for regional scale modeling (e.g. *Humphreys and Coblentz* (2007)), but on a global scale are problematic due to the importance of dynamic topography.

The low to moderate values of correlation coefficients in many areas imply the inadequacy of lateral density variations within the lithosphere alone to satisfy the observed deformation. Stresses, arising from density buoyancy-driven basal tractions are required in order to explain the observed deformation along the plate boundaries (*Ghosh et al.*, 2008).

2.11 Conclusions

The two main factors controlling lithospheric stress field are (1) gravitational potential energy differences arising from lateral density variations within the lithosphere and (2) basal tractions arising from mantle convection, which are coupled to the base of the lithosphere. In this study, we quantify only the first of the above two factors. A correct quantification of (1) will enable us to estimate the bounds on the magnitude of the basal tractions associated with lithospheric coupling, associated with deeper mantle circulation. We calculate GPE from the Crust2.0 and the EGM96 geoid dataset using both uniform lithospheric viscosity and varying viscosities for plate boundaries as well as intraplate regions and show that laterally varying lithospheric strength is required to match the observed

stress and strain rate pattern. We take into account deeper density buoyancies associated with cratonic roots. We find that inclusion of deeper lithospheric density buoyancies has little effect on the style and direction of the deviatoric stress field. Moreover, consideration of these deeper density buoyancies in the keels is based on the premise that there is no buoyancy driven mantle convection and no dynamic topography. A simpler model excluding the deeper keels fits the deformation indicators better. We clarify the usage of a correct level of reference (maximum depth of integration) for a thin sheet approach and show that GPE and associated deviatoric stresses calculated from geoid do not fit the observed deformation in the Earth's deforming plate boundary zones. We also demonstrate how a 2-D definition of deviatoric stress, along with 2-D force balance equations, can yield overestimates of the depth integrals of the deviatoric stress magnitudes. We calculate both compensated and uncompensated solutions and estimate dynamic topography by adjusting elevations of lithospheric blocks, based on an average pressure for oceans and continents. Finally, we introduce a quantitative way of testing our stress models with strain rate information from Global Strain Rate Map. The stress models indicate that GPE differences are an important component of the total stress field. However, GPE differences by themselves are, in general, insufficient to explain the total deviatoric stress field, particularly in areas such as Eastern Africa, Andes, and Central Asia; an added contribution from basal tractions is required to explain the observed discrepancies between the models and observations (*Ghosh et al.*, 2008).

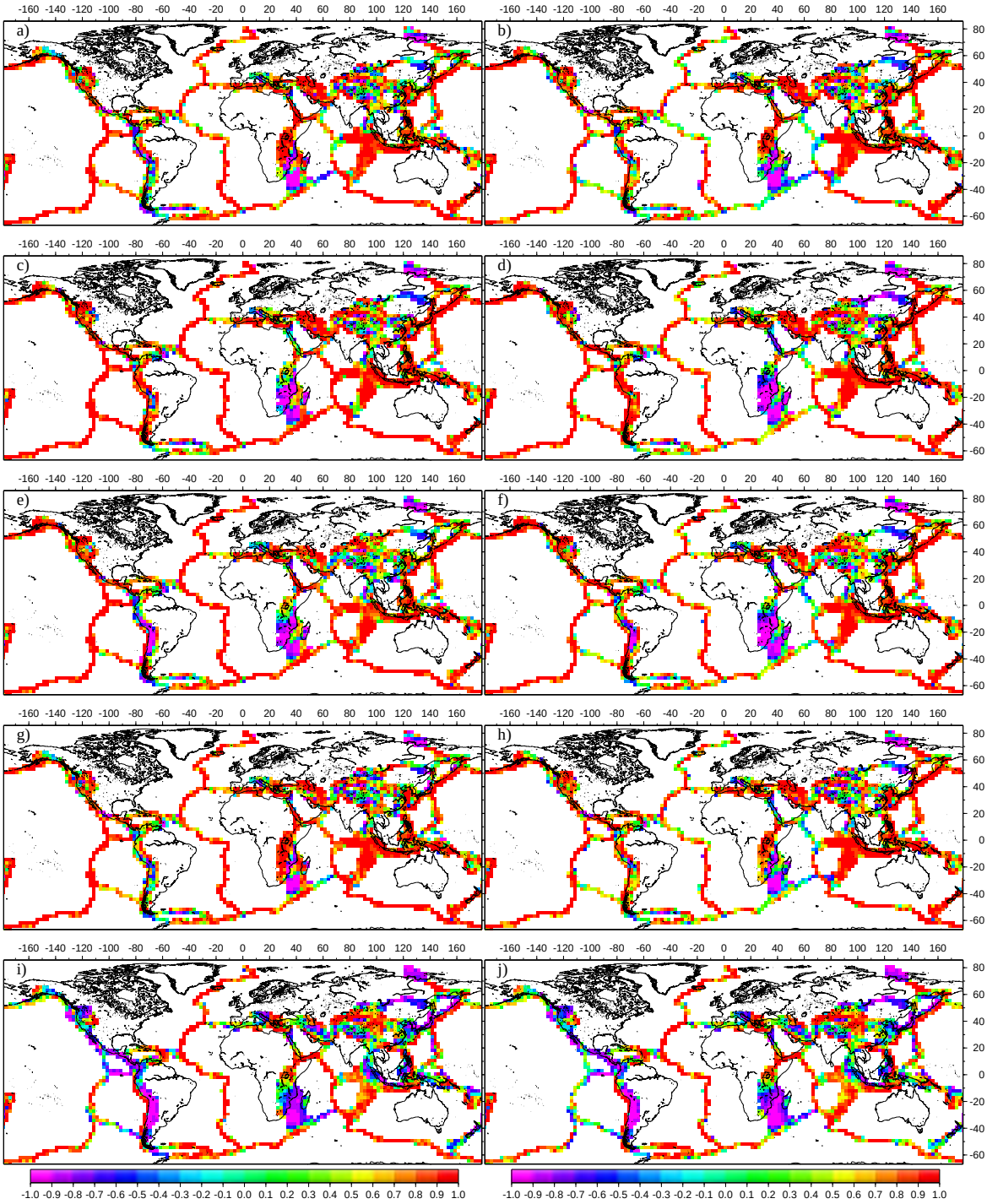

Figure 9: Correlation coefficients between observed strain rate tensors from the Global Strain Rate Map and deviatoric stress tensors, varying as a function of strain rates only, arising from GPE differences from a) an uncompensated Crust 2.0 model (Figure 2), c) a Crust 2.0 model compensated by density adjustment (Figure 3), e) a Crust 2.0 model compensated by elevation adjustment (Figure 4), g) a Crust 2.0 model compensated at a depth of $\sim$ 270 km (Figure 6) and i) an EGM96 Geoid model (Figure 7). b), d), f), h) and j) are the same as a), c), e), g) and i), but with viscosities varying as a function of both strain rates and lithospheric thickness.

Appendix

Spherical Treatment

In spherical coordinates, the x,y and z directions of cartesian coordinates change to the ϕ, θ and r (radial) components, respectively. The deviatoric stress tensor in the radial direction is

$$\tau_{rr} = \sigma_{rr} - \frac{1}{3}\sigma_{kk}, \tag{A1}$$

where σ_{rr} is the total stress tensor in the radial direction and $\frac{1}{3}\sigma_{kk}$ is the mean total stress. The total stress tensor, $\sigma_{ij} = \tau_{ij} + \frac{1}{3}\sigma_{kk}\delta_{ij}$, then becomes

$$\sigma_{ij} = \tau_{ij} + \delta_{ij}(\sigma_{rr} - \tau_{rr}), \tag{A2}$$

where δ_{ij} represents the Kronecker delta. The force balance equation (1) can be written in spherical coordinates as

$$\frac{1}{\cos\theta}\frac{\partial}{\partial\phi}\left(r^2\sigma_{\phi\phi}\right) + \frac{1}{\cos^2\theta}\frac{\partial}{\partial\theta}\left(r^2\sigma_{\phi\theta}\cos^2\theta\right) + \frac{\partial}{\partial r}\left(r^3\sigma_{\phi r}\right) = 0 \tag{A3}$$

$$\frac{1}{\cos\theta}\frac{\partial}{\partial\phi}\left(r^2\sigma_{\phi\theta}\right) + \frac{1}{2}\frac{\partial}{\partial\theta}\left(r^2\left[\sigma_{\theta\theta}+\sigma_{\phi\phi}\right]\right) + \frac{1}{2\cos^2\theta}\frac{\partial}{\partial\theta}\left(r^2\cos^2\theta\left[\sigma_{\theta\theta}-\sigma_{\phi\phi}\right]\right) + \frac{\partial}{\partial r}\left(r^3\sigma_{\theta r}\right) = 0 \tag{A4}$$

$$\frac{1}{r\cos\theta}\frac{\partial\sigma_{\phi r}}{\partial\phi} + \frac{1}{r\cos\theta}\frac{\partial}{\partial\theta}\left(\cos\theta\sigma_{\theta r}\right) + \frac{1}{r}\left(2\sigma_{rr} - \sigma_{\phi\phi} - \sigma_{\theta\theta}\right) + \frac{\partial\sigma_{rr}}{\partial r} - \rho g = 0 \tag{A5}$$

Vertically integrating (A3) and (A4) yields

$$\frac{1}{\cos\theta}\frac{\partial}{\partial\phi}\left(\int_{r_L}^{r_0} r^2\sigma_{\phi\phi}dr\right) + \frac{1}{\cos^2\theta}\frac{\partial}{\partial\theta}\left(\int_{r_L}^{r_0} r^2\sigma_{\phi\theta}dr\cos^2\theta\right) + r_0^3\sigma_{\phi r}(r_0) - r_L^3\sigma_{\phi r}(r_L) = 0 \tag{A6}$$

and

$$\frac{1}{\cos\theta}\frac{\partial}{\partial\phi}\left(\int_{r_L}^{r_0} r^2\sigma_{\phi\theta}\right) + \frac{1}{2}\frac{\partial}{\partial\theta}\left(\int_{r_L}^{r_0} r^2\left[\sigma_{\theta\theta}+\sigma_{\phi\phi}\right]\right) + \frac{1}{2\cos^2\theta}\frac{\partial}{\partial\theta}\left(\int_{r_L}^{r_0} r^2\cos^2\theta\left[\sigma_{\theta\theta}-\sigma_{\phi\phi}\right]\right)$$

$$+ r_0^3\sigma_{\theta r}(r_0) - r_L^3\sigma_{\theta r}(r_L) = 0 \tag{A7}$$

where r_0 is the radius from the center of the Earth to the surface and r_L is the radius from the center to the base of the lithosphere. Substituting (A2) in (A6) and (A7), we arrive at

$$\frac{1}{\cos\theta}\frac{\partial}{\partial\phi}\left(\int_{r_L}^{r_0} r^2\tau_{\phi\phi}dr\right) - \frac{1}{\cos\theta}\frac{\partial}{\partial\phi}\left(\int_{r_L}^{r_0} r^2\tau_{rr}dr\right) + \frac{1}{\cos^2\theta}\frac{\partial}{\partial\theta}\left(\cos^2\theta\int_{r_L}^{r_0} r^2\tau_{\phi\theta}dr\right)$$

$$+\frac{1}{\cos\theta}\frac{\partial}{\partial\phi}\left(\int_{r_L}^{r_0} r^2\sigma_{rr}dr\right) - r_L^3\tau_{\phi r}(r_L) = 0 \tag{A8}$$

and

$$\frac{1}{\cos\theta}\frac{\partial}{\partial\phi}\left(\int_{r_L}^{r_0} r^2\tau_{\phi\theta}dr\right) + \frac{1}{2}\frac{\partial}{\partial\theta}\left(\int_{r_L}^{r_0} r^2\tau_{\theta\theta}dr + \int_{r_L}^{r_0} r^2\tau_{\phi\phi}dr\right) - \frac{\partial}{\partial\theta}\left(\int_{r_L}^{r_0} r^2\tau_{rr}dr\right)$$

$$+\frac{1}{2\cos^2\theta}\frac{\partial}{\partial\theta}\left(\cos^2\theta\left[\int_{r_L}^{r_0} r^2\tau_{\theta\theta}dr - \int_{r_L}^{r_0} r^2\tau_{\phi\phi}dr\right]\right) + \frac{\partial}{\partial\theta}\left(\int_{r_L}^{r_0} r^2\sigma_{rr}dr\right) - r_L^3\tau_{\theta r}(r_L) = 0, \tag{A9}$$

which are equivalent to equations (5) and (6) in text. Note that $\sigma_{\phi r}(r_0)$ and $\sigma_{\theta r}(r_0)$ are zero. For a thin sheet, the gradients of $\sigma_{\phi r}$ and $\sigma_{\theta r}$ are negligibly small (see text) . Moreover, the term $\frac{1}{r}(2\sigma_{rr} - \sigma_{\phi\phi} - \sigma_{\theta\theta})$ is small compared to ρg. Hence, (A5) can be approximated as

$$\frac{\partial\sigma_{rr}}{\partial r} - \rho g = 0 \tag{A10}$$

which implies

$$\sigma_{rr} = -\int_r^{r_0} \rho g dr \tag{A11}$$

so that the GPE equation (7) in spherical coordinates is equivalent to

$$\int_{r_L}^{r_0} r^2\sigma_{rr}dr = -\int_{r_L}^{r_0} r^2\left[\int_r^{r_0}\rho g dr'\right]dr = -\int_{r_L}^{r_0}\rho g\left[\int_{r_L}^{r'} r^2 dr\right]dr' = -\int_{r_L}^{r_0}\frac{1}{3}\rho g\left(r'^3 - r_L^3\right)dr' \tag{A12}$$

Substituting $r' = r_E - z'$, and $r_L = r_E - L$, we have

$$\frac{1}{3}\left(r'^3 - r_L^3\right) = \frac{1}{3}\left((r_E - z')^3 - (r_E - L)^3\right) \quad \text{(A13)}$$

$$= r_E^2(L - z') - r_E(L^2 - z'^2) + \frac{1}{3}(L^3 - z'^3) \quad \text{(A14)}$$

$$= r_E^2(L - z')\left[1 - \frac{1}{r_E}(L + z') + \frac{1}{3r_E^2}(L^2 + Lz' + z'^2)\right] \quad \text{(A15)}$$

where r_E is the constant radius of the Earth and L is the depth to the base of the lithosphere. Equation (A15), therefore, provides the magnitude of error in GPE introduced by the flat-Earth approximation.

Let us denote GPE with the correct level of reference at the base of the lithosphere as $\bar{\sigma}_{zz}^{base}$ (equation (7) in text), and let GPE with the sea-level or geoid as reference level be $\bar{\sigma}_{zz}^{geoid}$ (equation (8) in text). From equations (7) and (8),

$$\bar{\sigma}_{zz}^{geoid} = \bar{\sigma}_{zz}^{base} + L\int_{-h}^{L} \rho(z) g dz, \quad \text{(A16)}$$

which in spherical coordinates can be written as

$$\int_{r_L}^{r_0} r^2 \sigma_{rr} dr + \int_{r_L}^{r_E} r^2 P_L dr = -\int_{r_L}^{r_0} \frac{1}{3}\rho g(r^3 - r_L^3) dr + \int_{r_L}^{r_0} \frac{1}{3}\rho g(r_E^3 - r_L^3) dr \quad \text{(A17)}$$

$$= \int_{r_L}^{r_0} \frac{1}{3}\rho g(r_E^3 - r^3) dr \quad \text{(A18)}$$

$$\frac{1}{3}(r_E^3 - r^3) = \frac{1}{3}\left(r_E^3 - (r_E - z)^3\right) = r_E^2 z - r_E z^2 + \frac{1}{3}z^3 \quad \text{(A19)}$$

where $P_L = \int_{r_L}^{r_0} \rho g dr$, is the pressure at the base of the lithosphere. The first term on the left hand side of (A17) is the GPE term in (A12).

The I functional in equation (9) is given by

$$I = \int\int \frac{1}{\mu}\left[\bar{\tau}_{\phi\phi}^2 + 2\bar{\tau}_{\phi\theta}^2 + \bar{\tau}_{\theta\theta}^2 + (\bar{\tau}_{\phi\phi} + \bar{\tau}_{\theta\theta})^2\right] \cos\theta d\phi d\theta$$

$$+ \int\int \left\{ 2\lambda_\phi \left[\frac{1}{\cos\theta}\frac{\partial \bar{\tau}_{\phi\phi}}{\partial\phi} + \frac{1}{\cos\theta}\frac{\partial}{\partial\phi}(\bar{\tau}_{\phi\phi} + \bar{\tau}_{\theta\theta}) + \frac{1}{\cos^2\theta}\frac{\partial}{\partial\theta}(\cos^2\theta \bar{\tau}_{\phi\theta}) + \frac{1}{\cos\theta}\frac{\partial}{\partial\phi}\bar{\sigma}_{rr}\right]\right.$$

$$+2\lambda_\theta\left[\frac{1}{\cos\theta}\frac{\partial}{\partial\phi}\bar{\tau}_{\phi\theta}+\frac{3}{2}\frac{\partial}{\partial\theta}(\bar{\tau}_{\theta\theta}+\bar{\tau}_{\phi\phi})+\frac{1}{2\cos^2\theta}\frac{\partial}{\partial\theta}(\cos^2\theta[\bar{\tau}_{\theta\theta}-\bar{\tau}_{\phi\phi}])+\frac{\partial\bar{\sigma}_{rr}}{\partial\theta}\right]\Bigg\}\cos\theta d\phi d\theta \tag{A20}$$

where $\bar{\tau}_{ij}$ are the vertically integrated deviatoric stresses, $\bar{\sigma}_{rr}$ is the vertically integrated vertical stress, or GPE, λ_ϕ, λ_θ represent the horizontal components of the Lagrange multipliers, and μ is the relative viscosity.

The J functional in equation (13) can be written in spherical coordinates as

$$J=\int\int\left\{\left[\begin{pmatrix}\bar{\tau}_{\phi\phi}\\ \bar{\tau}_{\theta\theta}\\ \bar{\tau}_{\phi\theta}\end{pmatrix}-\begin{pmatrix}\Phi^{obs}_{\phi\phi}\\ \Phi^{obs}_{\theta\theta}\\ \Phi^{obs}_{\phi\theta}\end{pmatrix}\right]^T\widetilde{V}^{-1}\left[\begin{pmatrix}\bar{\tau}_{\phi\phi}\\ \bar{\tau}_{\theta\theta}\\ \bar{\tau}_{\phi\theta}\end{pmatrix}-\begin{pmatrix}\Phi^{obs}_{\phi\phi}\\ \Phi^{obs}_{\theta\theta}\\ \Phi^{obs}_{\phi\theta}\end{pmatrix}\right]\Bigg\}\cos\theta d\phi d\theta \tag{A21}$$

where

$$\bar{\tau}_{\phi\phi}=\mu\left(\frac{1}{\cos\theta}\frac{\partial\lambda_\phi}{\partial\phi}-\lambda_\theta\tan\theta\right), \tag{A22}$$

$$\bar{\tau}_{\theta\theta}=\mu\frac{\partial\lambda_\theta}{\partial\theta}, \tag{A23}$$

$$\bar{\tau}_{\phi\theta}=\frac{\mu}{2}\left(\frac{\partial\lambda_\phi}{\partial\theta}+\frac{1}{\cos\theta}\frac{\partial\lambda_\theta}{\partial\phi}+\lambda_\phi\tan\theta\right), \tag{A24}$$

$$\widetilde{\mathbf{V}}^{-\mathbf{1}}=\frac{1}{\mu}\begin{pmatrix}2&1&0\\1&2&0\\0&0&2\end{pmatrix} \tag{A25}$$

and

$$(\Phi^{obs}_{\phi\phi},\Phi^{obs}_{\theta\theta},\Phi^{obs}_{\phi\theta})^T=(-\frac{\bar{\sigma}_{rr}}{3},-\frac{\bar{\sigma}_{rr}}{3},0)^T \tag{A26}$$

The relation between 2-D and 3-D stresses (equations (24)-(26) in text) is given by

$$\bar{\tau}^{2D}_{\theta\theta}=2\bar{\tau}^{3D}_{\theta\theta}+\bar{\tau}^{3D}_{\phi\phi} \tag{A27}$$

$$\bar{\tau}^{2D}_{\phi\phi}=\bar{\tau}^{3D}_{\theta\theta}+2\bar{\tau}^{3D}_{\phi\phi} \tag{A28}$$

$$\bar{\tau}^{2D}_{\phi\theta}=\bar{\tau}^{3D}_{\phi\theta} \tag{A29}$$

Chapter 3

Gravitational Potential Energy of the Tibetan Plateau and the Forces Driving the Indian Plate

Gravitational potential energy of the Tibetan Plateau and the forces driving the Indian plate

A. Ghosh, W. E. Holt, A. J. Haines and L. M. Flesch

(Published in *Geology*, 34, 321-324, 2006)

Abstract

We present a study of the vertically integrated deviatoric stress field for the Indian plate and the Tibetan Plateau associated with gravitational potential energy (GPE) differences. Although the driving forces for the Indian plate have been attributed solely to the mid-oceanic ridges that surround the entire southern boundary of the plate, previous estimates of vertically integrated stress magnitudes of $\sim 6-7\times10^{12}$ N/m in Tibet far exceed those of $\sim 3\times10^{12}$ N/m associated with GPE at mid-oceanic ridges, calling for an additional force to satisfy the stress magnitudes in Tibet. We use the Crust 2.0 data set to infer gravitational potential energy differences in the lithosphere. We then apply the thin sheet approach in order to obtain a global solution of vertically integrated deviatoric stresses associated only with GPE differences. Our results show large N-S extensional deviatoric stresses in Tibet that the ridge-push force fails to cancel. Our results calibrate the magnitude of the basal tractions, associated with density buoyancy driven mantle flow, that are applied at the base of the lithosphere in order to drive India into Tibet and cancel the N-S extensional stresses within Tibet. Moreover, our deviatoric stress field solution indicates that both the ridge-push influence ($\sim 1\times10^{12}$ N/m) and the vertically integrated deviatoric stresses associated with GPE differences around the Tibetan Plateau ($\sim 3\times10^{12}$ N/m) have previously been overestimated by a factor of two or more. These overestimates have resulted from either simplified two-dimensional approximations of the thin sheet equations, or from an assumption about the mean stress that is unlikely to be correct.

3.1 Introduction

The driving mechanism for the Indian plate has been a source of controversy since the advent of the plate tectonic theory. The Indian plate's velocity relative to Eurasia slowed from 10 cm yr^{-1} to roughly 5 cm yr^{-1} upon impact with Eurasia roughly 50 million years ago (*Molnar and Tapponnier*, 1975; *Molnar et al.*, 1993). The Indian plate continues its northward movement relative to Eurasia at a present-day rate of ~ 3.5 cm yr^{-1} (*Kreemer et al.*, 2003). The Tibetan plateau, which formed as a result of the collision between India and Eurasia, has the largest gravitational potential energy (GPE) signal on earth. However, there exists no complete dynamic explanation for this large GPE of the Tibetan plateau and the relatively fast movement of the Indian plate. There is no apparent downgoing slab attached to the Indian plate that might assist in driving the plate into Eurasia through the slab pull mechanism (*Gripp and Gordon*, 1990). Because the plate is surrounded along its entire southern margin by mid-oceanic ridges, the motion of the Indian plate has been attributed to the ridge-push force, the deviatoric stress that results from differences in vertically integrated vertical stresses between elevated ridge and older oceanic lithosphere (*Richardson*, 1992; *Cloetingh and Wortel*, 1985, 1986; *Sandiford et al.*, 1995; *Coblentz et al.*, 1998). However, the ridge-push, or vertically integrated deviatoric stress magnitude, which is of order 3×10^{12} N/m (*Richardson*, 1992; *Harper*, 1975; *Lister*, 1975; *Parsons and Richter*, 1980), is not sufficient to satisfy inferred stress magnitudes of $6 - 7 \times 10^{12}$ N/m that result from GPE differences between the Tibetan plateau and the surrounding lowlands (*Molnar and Lyon-Caen*, 1988). An additional force is required to explain the disparity between the excess GPE of Tibet relative to that of the mid-oceanic ridges.

Lithospheric density variations associated with the support of the high topography of the Tibetan plateau give rise to lithospheric body forces and hence stresses. Although the sources of stress that drive plate motions have been ascribed to many parameters (*Forsyth and Uyeda*, 1975), from the point of view of stress continuity and force balance, the stresses that drive lithospheric motion arise from two sources: (1) gravity acting on density variations within the lithospheric shell on the earth and (2) gravity acting on density variations deeper than the lithospheric shell. The latter gives rise to tractions (radial and tangen-

tial) that act on the base of the lithosphere, affecting the stress field of the lithosphere and producing dynamic topography. The former involves density variations associated with support of non-dynamic components of topography. The goal of this paper is to quantify the first of these in order to understand the role of density buoyancy variations within the lithosphere in driving India into Eurasia. This is important because such a calculation of the role of lithospheric sources calibrates the magnitude of a density buoyancy driven flow below the lithosphere. Moreover, if ridge-push is the only driving force for India's motion, then the distribution of stresses associated with the high GPE of Tibet together with the GPE of ridges and surrounding ocean basins should explain the entire lithospheric stress field across Tibet and surrounding collision zone (*Zoback*, 1992).

3.2 Method

Plate tectonics enables us to approximate the upper 100-125 kilometers of the earth as a thin shell. A thin sheet approach has been used by many previous authors (*England and McKenzie*, 1982; *England and Houseman*, 1986; *England and Molnar*, 1997b; *Lithgow-Bertelloni and Guynn*, 2004) to solve for the stresses associated with internal horizontal density variations within this thin shell (e.g., crustal thickness contrasts, elevation differences, cooling of oceanic lithosphere, etc.). We also take the thin sheet approach to solve for the stresses associated with density variations intrinsic to the lithosphere. In order to avoid boundary condition problems we compute stress response for the entire earth's surface using a global grid of $2.5^o \times 2.5^o$ resolution. We incorporate weak plate boundaries by assigning relative viscosities to plate boundary zones. These viscosities are inversely proportional to the rate of strain (*Kreemer et al.*, 2003). We make the plates 2 orders of magnitude higher viscosity than that of a mid-oceanic ridge with a moderate spreading rate (eg., the Indian ocean). A model with 3 orders of magnitude strength contrast between plates and plate boundary zones was also investigated (see supplementary section).

We use a finite element method to solve the three-dimensional force balance equations for vertically integrated deviatoric stress for the spherical case. After *Flesch et al.* (2001), the deviatoric stress field solution is the mathematically unique solution that both balances

the body force distribution (GPE differences) and provides a global minima in the second invariant of stress. For this methodology, the magnitudes of deviatoric stresses depend on the magnitudes of the body force distributions and relative viscosity contrasts; the deviatoric stress magnitudes are independent of absolute magnitudes of viscosity. We calculate the vertically integrated vertical stress ($\bar{\sigma}_{zz}$), which is the negative of GPE per unit area as

$$\bar{\sigma}_{zz} = -\int_{-h}^{L}\left[\int_{-h}^{z}\rho(z')gdz'\right]dz = -\int_{-h}^{L}(L-z)\rho(z)gdz$$

(*Jones et al.*, 1996), where $\rho(z)$ is the density, L is the depth to the base of the thin sheet taken to be 100 km, h is the topographic elevation and g is the acceleration due to gravity. We calculate GPE using the Crust 2.0 dataset (G. Laske et al., Crust 2.0: A new global crustal model at 2 $\times$ 2 degrees, 2002, available at http://mahi.ucsd.edu/Gabi/rem.html). We neglect the basal traction terms in the force balance equations for now in order to quantify only the contributions to deviatoric stresses that are intrinsic to the lithosphere.

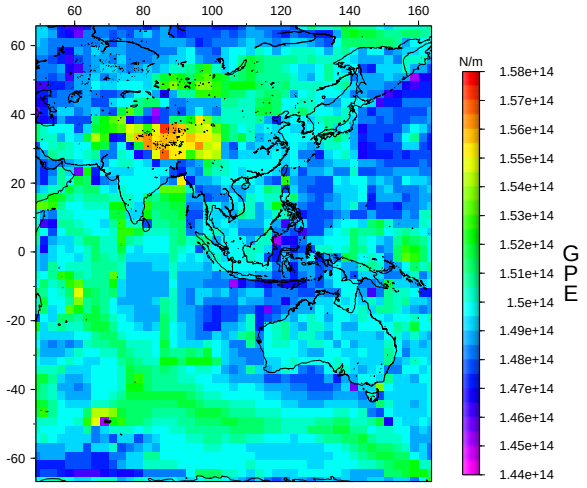

Figure 1: Gravitational potential energy (GPE) distribution for Indian and Eurasian plates. Topographically high areas like Tibet and mid-oceanic ridges have higher GPE than other areas.

Since radial tractions applied to the base of the lithosphere affect topography, they also influence GPE. We have therefore calculated GPE distributions and associated stress field solutions for a compensated model (uniform pressure at the base of lithosphere)(see supplementary materials for details). The conclusions drawn for the Indian plate are the same irrespective of whether the model is compensated or not. However, the uncompensated model provides deviatoric stress magnitudes that are everywhere 10-20% higher than for the compensated model (see supplementary document). Cooling of the oceanic lithosphere is introduced by incorporating the plate model into our calculation, based on ocean floor age data from *Müller et al.* (1997), using the revised parameters given by *Stein and Stein* (1992).

3.3 Results

The force balance associated with the global GPE distribution (Fig. 1) yields deviatoric extension along the mid-oceanic ridges and compressional deviatoric stresses in lower elevation regions of the oceans as well as the continents (Fig. 2). For the compensated model, the vertically integrated stress field in the Indian plate is dominated by NE-SW deviatoric compression of roughly $2.5 - 3 \times 10^{12}$ N/m close to the collisional boundary. However, these compressional stresses decrease in magnitude further to the south.

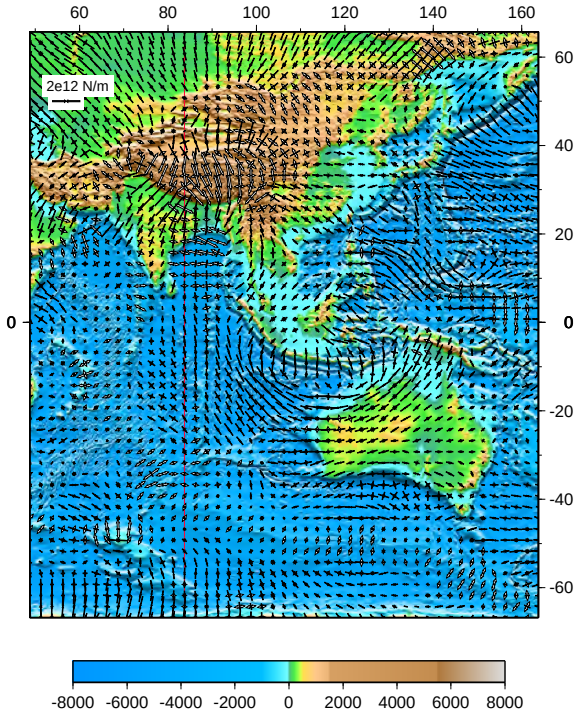

Figure 2: Distribution of vertically integrated horizontal deviatoric stresses for the Indian and Eurasian plates. Extensional stresses are shown by white arrows while compressional stresses are shown by black arrows. Length of the arrows are proportional to the magnitude of deviatoric stresses. Strike-slip regions are indicated by one tensional and one compressional pair of arrows. Areas having high GPE are in deviatoric extension, like Tibet and the mid-oceanic ridges, while those having low GPE are in deviatoric compression like the rest of the oceans. The plate boundaries are assigned variable viscosities depending on their relative strengths, inferred to be inversely proportional to strain rate (Kreemer et al., 2003). A reference viscosity of 0.01 is used for the moderately spreading mid-Indian ridges while the plates have a viscosity of 1. The profile in Fig. 3 is taken along the N-S running red line. Topography is in meters.

The magnitude of stresses associated with GPE differences between Tibet and low-elevation regions in our compensated model is $\sim 2.5 \times 10^{12}$ N/m while the mid-oceanic ridges exert a force of only $\sim 1 \times 10^{12}$ N/m. Moreover, our results show a predominant N-S deviatoric extension at the Tibetan plateau, in addition to a much lower E-W deviatoric extension, in contrast to active faulting patterns that allow only for E-W extension. Our results for the Indo-Australian plate are in agreement with the SH_{max} directions of the World Stress Map (*Zoback*, 1992) and those derived by *Sandiford et al.* (1995).

3.4 Discussion and Conclusion

Our results indicate that the vertically integrated deviatoric stresses associated with elevated ridge and cooling of the lithosphere ($\sim 1 \times 10^{12}$ N/m) are not sufficient to cancel the large N-S extensional deviatoric stresses ($\sim 2.5 \times 10^{12}$ N/m) associated with the large GPE contrasts of Tibet and the surrounding regions. It is clear that something is missing as a driving force that does not have its source within the lithospheric shell. Ideas, like substantial focusing of the ridge-push torque along the northern collisional boundary (*Coblentz et al.*, 1998; *Sandiford et al.*, 1995), have been proposed to support the ridge-push theory as the sole mechanism for driving the Indian plate. However, our results show that such focusing, while important for defining stresses within the Indo-Australian plate, is not enough to cancel out the N-S deviatoric extension in Tibet. *Sandiford et al.* (1995), suggested that the excess potential energy of the Plateau at $\sim$ 4 km elevation (*England and Molnar*, 1997a) provides the right magnitude of the potential energy that can be supported by the ridge-push force, as there occurs a transition from reverse to normal faulting at that elevation. However, the normal faulting observed at an elevation greater than $\sim$ 4 km involves E-W extension (*Molnar et al.*, 1993), whereas our calculations demonstrate that a N-S extension would be expected if GPE is the only source of deviatoric stress operating on the lithosphere. Therefore, an additional long-wavelength N-S compressive stress of order $\sim 2 - 3 \times 10^{12}$ N/m is required in our model to cancel out these north-south extensional deviatoric stresses in Tibet (leaving only E-W extension) (*Flesch et al.*, 2001).

The most compatible driving mechanism that would explain such a long wavelength compressional intraplate stress field distribution is the driving shear tractions associated with coupling of density buoyancy driven flow (eg., *Lithgow-Bertelloni and Guynn* (2004)). These tractions arise due to the 'slab suction' force induced by the surrounding mantle on the base of the surface plate (*Conrad et al.*, 2004). The contribution to lithospheric stresses associated with these shear tractions inferred from self-consistent mantle circulation models can be added to the deviatoric stress field shown in Fig. 2 to obtain the full stress field solution. Therefore, one important result in our study is the absolute magnitudes of deviatoric stresses associated with GPE differences (Fig. 2) because they calibrate the

magnitudes of deviatoric stresses ($\sim 2-3\times10^{12}$ N/m) associated with the driving tractions applied to the base of the lithosphere in the Indian plate region. The density buoyancy distribution responsible for these driving tractions is most likely related to the long history of subduction of the Indian and Australian plates (*Lithgow-Bertelloni and Richards*, 1995; *Wen and Anderson*, 1997b).

Our calculations show vertically integrated deviatoric stress magnitudes a factor of two lower than that proposed by *Molnar and Lyon-Caen* (1988) and *Molnar et al.* (1993) for Tibet as well as for the mid-oceanic ridges (*Richardson*, 1992; *Harper*, 1975; *Lister*, 1975; *Parsons and Richter*, 1980). We argue that deviatoric stress magnitudes resulting from ridge GPE as well as those calculated at the Tibetan plateau have previously been overestimated. Previous overestimates arise from two factors: (1) a two dimensional approximation of the thin sheet equations, applied along a single profile and, or (2) a two dimensional definition of deviatoric stress, as opposed to a three dimensional one (*Dalmayrac and Molnar*, 1981; *Molnar and Lyon-Caen*, 1988). A 2-D definition of deviatoric stress, $\tau_{ij}=\sigma_{ij}-\sigma_{zz}\delta_{ij}$, as opposed to a 3-D one, $\tau_{ij}=\sigma_{ij}-\frac{1}{3}\sigma_{kk}\delta_{ij}$, replaces the "three dimensional" constraint $\bar{\tau}_{xx}+\bar{\tau}_{yy}+\bar{\tau}_{zz}=0$ with the constraint $\bar{\tau}_{zz}=0$ (*Flesch et al.*, 2001). As pointed out by *Engelder* (1994), in the 2-D definition, the lithostatic stress, σ_{zz}, is set equal to the mean stress, $\frac{1}{3}\sigma_{kk}$. This is entirely a special case, unlikely to apply in many regions. The relationship between the 2-D and the 3-D stresses are given by:

$$\bar{\tau}_{xx}^{2D}=2\bar{\tau}_{xx}^{3D}+\bar{\tau}_{yy}^{3D} \tag{1}$$

$$\bar{\tau}_{yy}^{2D}=2\bar{\tau}_{yy}^{3D}+\bar{\tau}_{xx}^{3D} \tag{2}$$

$$\bar{\tau}_{xy}^{2D}=\bar{\tau}_{xy}^{3D} \tag{3}$$

where the bars indicate depth integration over the entire plate thickness. We use horizontal deviatoric stresses projected along a N-S profile ($\bar{\tau}_{yy}$) of 83.75^{o}E to demonstrate how the different ways of solving the force balance equations as well as the usage of different definitions of deviatoric stress have led to different results, and possible misunderstandings, for deviatoric stress magnitudes (Fig. 3). This profile is chosen because it passes through

the Tibetan plateau, the deeper Indian ocean, and the mid-oceanic ridge. The largest estimates of deviatoric stresses arise from solving simplified 2-D thin sheet equations, applied along a single profile, along with the use of the 2-D definition of deviatoric stress. As such, the horizontal force balance equations reduce to $\frac{\partial \sigma_{yy}}{\partial y} = 0$, which gives $\overline{\tau}_{yy} = -\overline{\sigma}_{zz} +$ a constant C, as a solution to the force balance equation. With a 2-D definition of deviatoric stress, vertically integrated deviatoric stress magnitudes are $6 - 7 \times 10^{12}$ N/m for the Tibetan plateau and $3 - 4 \times 10^{12}$ N/m for the mid-oceanic ridge (dotted line in Fig. 3), which were predicted by *Molnar and Lyon-Caen* (1988). Usage of the 3-D definition of deviatoric stress reduces these stress magnitudes in half (dashed line in Fig. 3), as predicted by equation (2). If one solves the full 3-D thin sheet equations for vertically integrated deviatoric stresses, but uses the 2-D definition of deviatoric stress, stress magnitudes (dash-dotted line, Fig. 3) are slightly lower than the solution computed for a single profile (with the two dimensional definition of deviatoric stress) because some of the potential energy differences are absorbed into other non-zero terms, $\overline{\tau}_{xx}, \overline{\tau}_{xy}$. The smallest magnitudes are obtained for solutions to 3-D force balance with three dimensional definition of deviatoric stress (this paper, solid line in Fig. 3) because differences in GPE are absorbed not only into all of the horizontal terms, but $\overline{\tau}_{zz}$ as well.

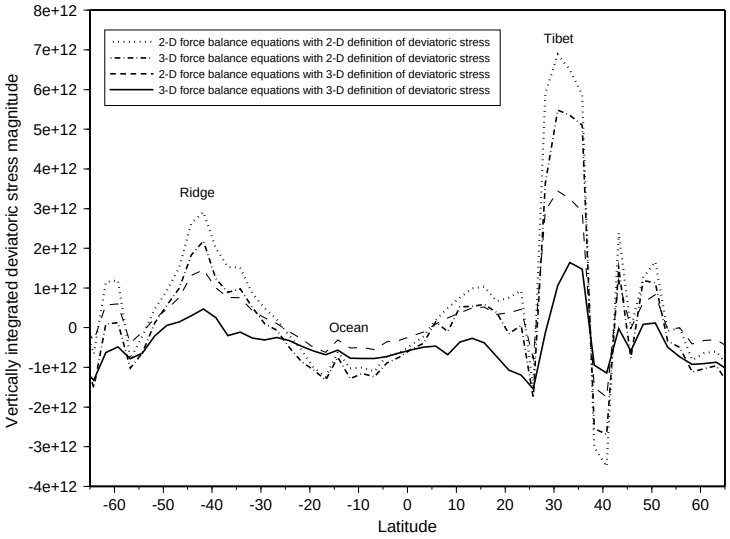

Figure 3: Comparison of different methods of solving the force balance equations along a N-S profile passing through 83.75^{o}E. The x-y axes show vertically integrated deviatoric stress magnitudes projected along the y-axis ($\overline{\tau}_{yy}$) and latitude respectively. The solid line indicates our results. A reference GPE equal to the GPE at sea-level has been subtracted from the actual GPE values.

Our calibration of the vertically integrated deviatoric stress magnitudes and directions associated with GPE variations has other implications as well. (*Molnar et al.*, 1993) argued

that the rapid uplift of Tibet around 10-11 million years ago resulted in an increased GPE of Tibet that produced increased compressional stresses in the Indian Ocean ($\sim 8 \times 10^{12}$ N/m), which was hypothesized to be sufficient to buckle the lithosphere there. These estimates are based on a 2-D approximation of the thin sheet equations, applied along a single profile, with the 2-D definition of deviatoric stress. We show here that deviatoric stresses associated with GPE differences between the elevated ridges, the deeper Indian Ocean, and the elevated Tibetan plateau are much lower than *Molnar et al.* (1993)'s prediction, suggesting that the uplift of Tibet is unlikely to be the single factor for the onset of folding and reverse faulting that is now occurring in the Indian Ocean.

Appendix

Methodology with variable relative viscosities

The functional that is minimized in the method of *Flesch et al.* (2001) is :

$$I = \int_S \frac{1}{\mu}[\bar{\tau}_{\alpha\beta}\bar{\tau}_{\alpha\beta} + \tau_{\gamma\gamma}^2]dS + \int_S 2\lambda_\alpha \Big[\frac{\partial}{\partial x_\beta}(\bar{\tau}_{\alpha\beta} + \delta_{\alpha\beta}\bar{\tau}_{\gamma\gamma}) + \frac{\partial \bar{\sigma}_{zz}}{\partial x_\alpha}\Big] dS \tag{A1}$$

where μ is the relative viscosity, $\tau_{\alpha\beta}$ is the vertically integrated horizontal deviatoric stress, $\bar{\tau}_{\gamma\gamma} = \bar{\tau}_{xx} + \bar{\tau}_{yy}$, λ_α is the horizontal component of the Lagrange multiplier for the force balance differential equation constraint, $\bar{\sigma}_{zz}$ is the vertically integrated vertical stress defined in the main paper and S represents area on the entire Earth's surface. *Flesch et al.* (2001) assumed a constant μ equal to 1. In this paper we use a variable value of μ to approximate weak plate boundary zones and strong plates. We assume an inverse relationship between strain rates and relative viscosities, μ. We obtain the relative viscosities of the deforming plate boundary regions, such as the mid-oceanic ridges and subduction zones, by assigning a reference viscosity to the moderately straining mid-Indian ridge, using the relation:

$$\frac{1}{\mu} = 1 + \Big(\frac{1}{\mu_{ref}} - 1\Big)\sqrt{\frac{E^2}{E_{ref}^2}} \tag{A2}$$

where μ_{ref} is the reference viscosity corresponding to a mid-oceanic ridge with a moderate spreading rate, such as the Indian ocean, $E^2 = 2(\dot{\varepsilon}_{\theta\theta}^2 + \dot{\varepsilon}_{\phi\phi}^2 + \dot{\varepsilon}_{\phi\theta}^2 + \dot{\varepsilon}_{\phi\phi}\dot{\varepsilon}_{\theta\theta})$, where $\dot{\varepsilon}_{\theta\theta}, \dot{\varepsilon}_{\phi\phi}$ and $\dot{\varepsilon}_{\phi\theta}$ are the strain rates from *Kreemer et al.* (2003), and E_{ref}^2 is the reference value for E^2, corresponding to the value for μ_{ref}. A plot of relative viscosities (Fig. A2) shows the lowest viscosities along the mid-oceanic ridges and higher viscosities in the deforming continents, while the blank areas (the plates) have a μ value of 1. We try reference viscosities of 0.01, in which the mid-oceanic ridges are 100 times weaker than the plates (Fig. A3 and the solution in the main paper), and also 0.001, in which the mid-oceanic ridges are 1000 times weaker than the plates. We show the global stress solutions for three cases: the case where $\mu = 1$ everywhere (Fig. A1) and cases in which μ varies according to the inverse of strain rate (Figs. A3 and A4). The solutions with reference viscosities of 0.01 and 0.001

respectively yield a focusing of stresses within the plates and fits well with the observed SH_{max} orientations (*Zoback*, 1992) in most places (Figs. A3 and A4). Moreover, solutions with weak plate boundaries provide agreement of SH_{max} for Indo-Australian plate region (*Sandiford et al.*, 1995). However the N-S deviatoric extension in Tibet remains as a prominent feature in the global solution. We also considered a special case in which the Tibetan Plateau and the Himalayas were assigned viscosities equal to the rigid plate interiors (Fig. A5). Although there occurs a marginal reduction in the N-S deviatoric stresses within the Tibetan Plateau for this case (Fig. A6), such a strong resistant plate boundary is insufficient to focus deviatoric stresses to cancel large N-S deviatoric extension associated with excess GPE of Tibet. Moreover, the assumption of plate-like strength of this plate boundary zone is not reasonable, given the high rates of deformation occurring there (see Fig. A2).

Dynamic topography

Actual topography, in some places, already contains a contribution from dynamically induced radial tractions. We argue here that GPE values from the uncompensated model (Fig. A7) contain the influence of dynamic topography. In the presence of dynamic topography, the weight of the lithospheric column, σ_{rr}^{total}, at reference depth L is $\sigma_{rr}^{total} = \int_{-h}^{L} \rho(r)g(r)dr = \sigma_{rr}^{o} + \tau_{rr}$ (note: this ignores the contribution from flexure), where σ_{rr}^{o} is a reference stress, and τ_{rr} is the radial traction associated with deeper mantle flow that is responsible for dynamic topography. The physical effect of this dynamic topography is therefore taken into account already in the GPE calculations that are uncompensated (Fig. A7), since these involve the vertical integral of $\sigma_{rr}(r)$ down to the depth L. In order to remove the contribution from dynamic topography, an isostatically compensated solution (uniform pressure, σ_{rr}^{o}, at depth L) was calculated by adjusting the densities of the subcrustal part (upper mantle) of each lithospheric column. The GPE and the resulting stresses were then calculated as usual. Compensation can also be achieved by adjusting the elevation of each column instead of adjusting the density. However, since greater uncertainty lies in the values of densities of the upper mantle than in the values of the crustal thickness, compensation obtained by density adjustment seems to be more reasonable than that

obtained by adjusting the elevation. As stated earlier, the uncompensated solution only contributes 20% higher stresses. The Tibetan plateau shows vertically integrated deviatoric extension of the order $\sim 3 \times 10^{12}$ N/m. The ridge-push force magnitude is $\sim 1 - 1.5 \times 10^{12}$ N/m, which, again falls short of providing the right magnitude of vertically integrated deviatoric stress for supporting the Tibetan plateau. The large N-S deviatoric extension in Tibet calls for an additional N-S compressional force of $\sim 3 \times 10^{12}$ N/m that can cancel the deviatoric extension. The stress magnitudes for Tibet as well as the ridge-push force are a factor of two lower that what was proposed in previous studies.

Figure A1: Global distribution of vertically integrated horizontal deviatoric stresses with a uniform viscosity distribution ($\mu = 1$) for both plate boundaries and plate interiors. Topography is in meters. Besides the solution in Fig. A7, all the other solutions are compensated.

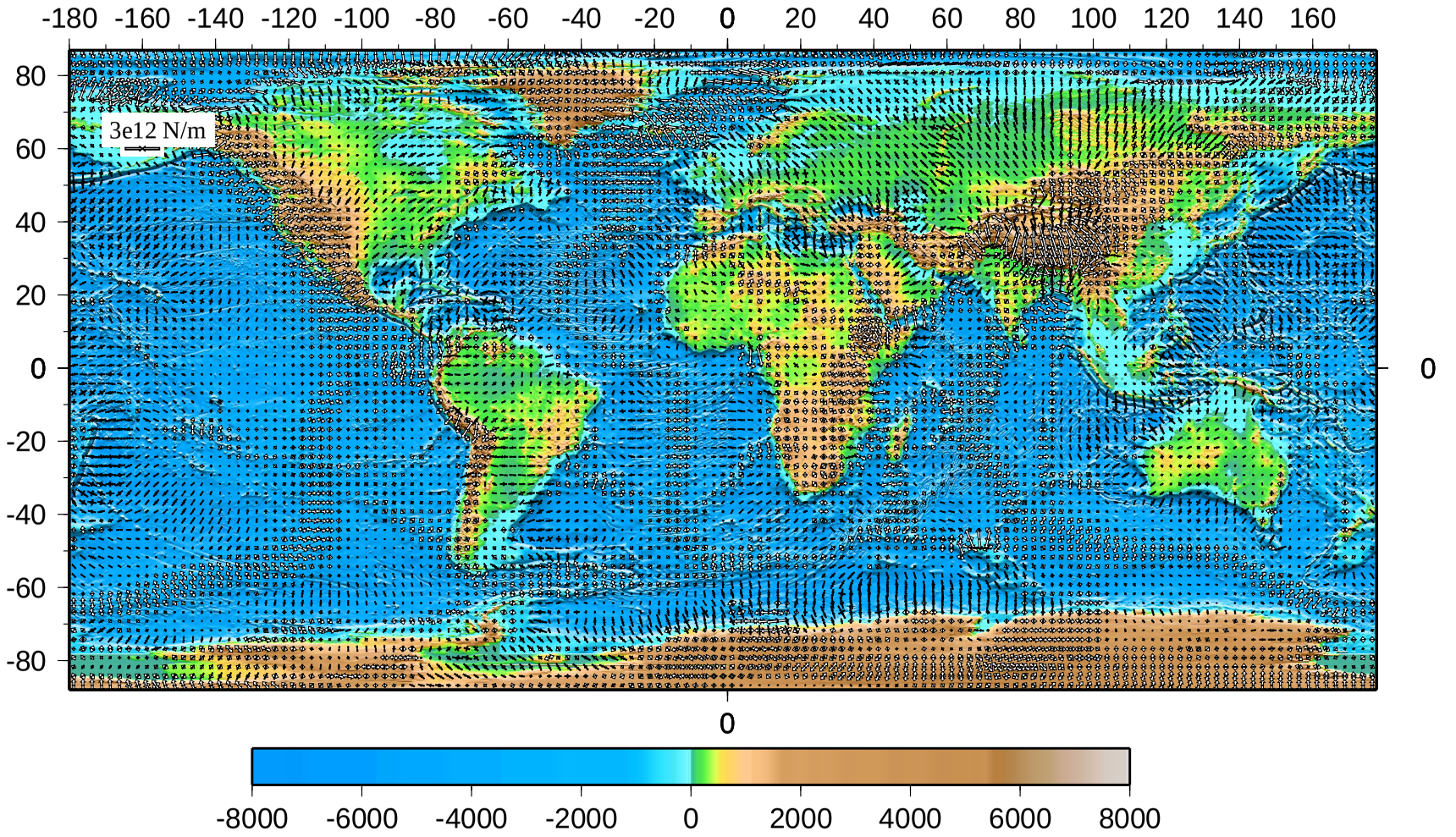
-180 -160 -140 -120 -100 -80 -60 -40 -20 0 20 40 60 80 100 120 140 160
80
60
40
20
0
-20
-40
-60
-80
3e12 N/m
0
0
-8000 -6000 -4000 -2000 0 2000 4000 6000 8000

Figure A2: Relative viscosity distribution for all the plates. The white areas represent intra-plate regions with reference viscosity 1. The deforming areas are assigned viscosities inversely proportional to the strain rate. A reference viscosity of $\mu_{ref} = 0.01$ is chosen at the moderately spreading mid-oceanic ridge in the Indian Ocean. Places with higher viscosities than μ_{ref} are deforming at a slower rate.

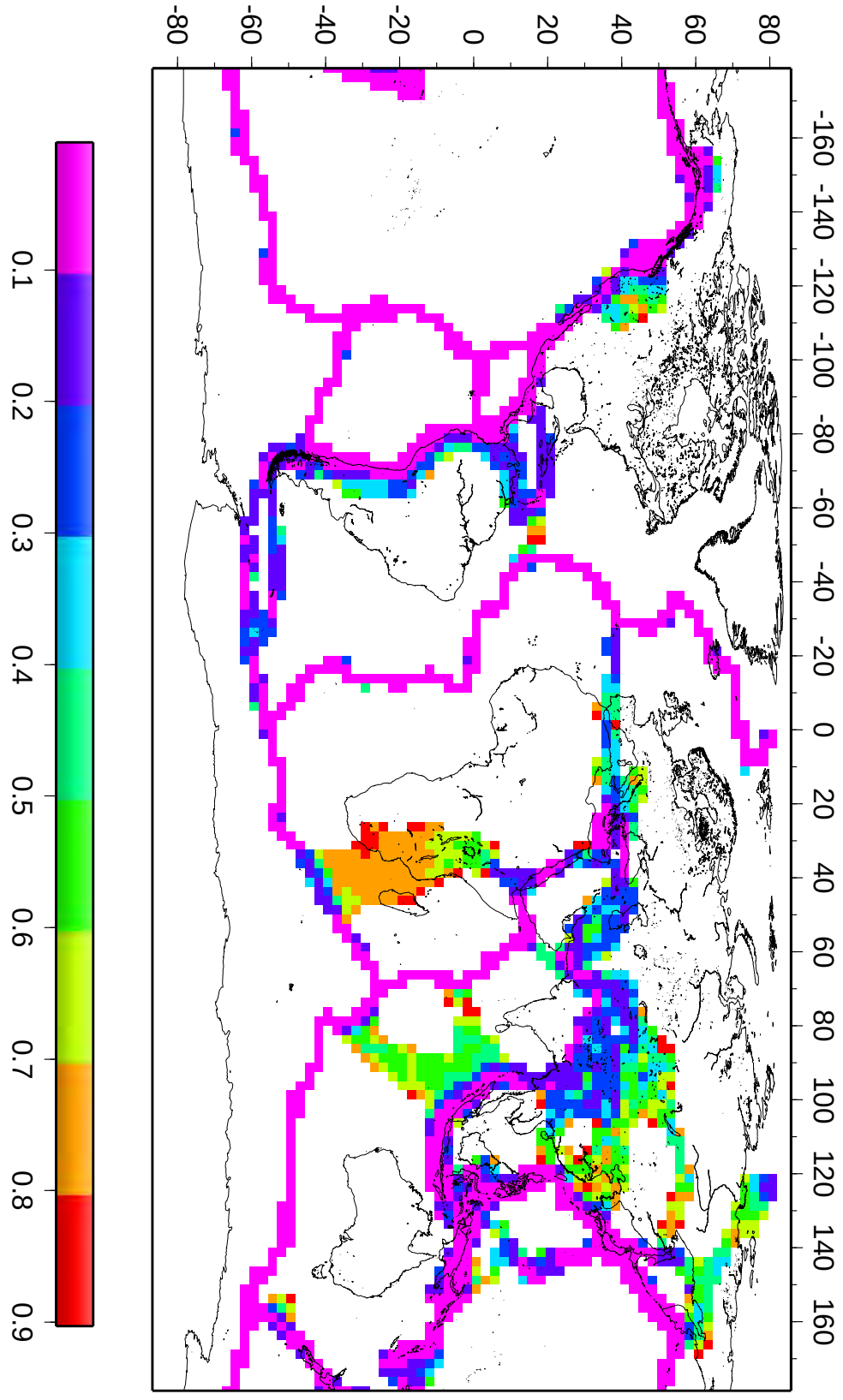
80
60
40
20
0
-20
-40
-60
-80
-160 -140 -120 -100 -80 -60 -40 -20 0 20 40 60 80 100 120 140 160
0.1
0.2
0.3
0.4
0.5
0.6
0.7
0.8
0.9

Figure A3: Global distribution of vertically integrated horizontal deviatoric stresses. The plate boundaries are assigned variable viscosities based on their strain rates. A reference viscosity, μ_{ref} of 0.01 is used for the mid-Indian ridges. This compensated solution corresponds to the uncompensated solution in Fig. A7. Topography is in meters.

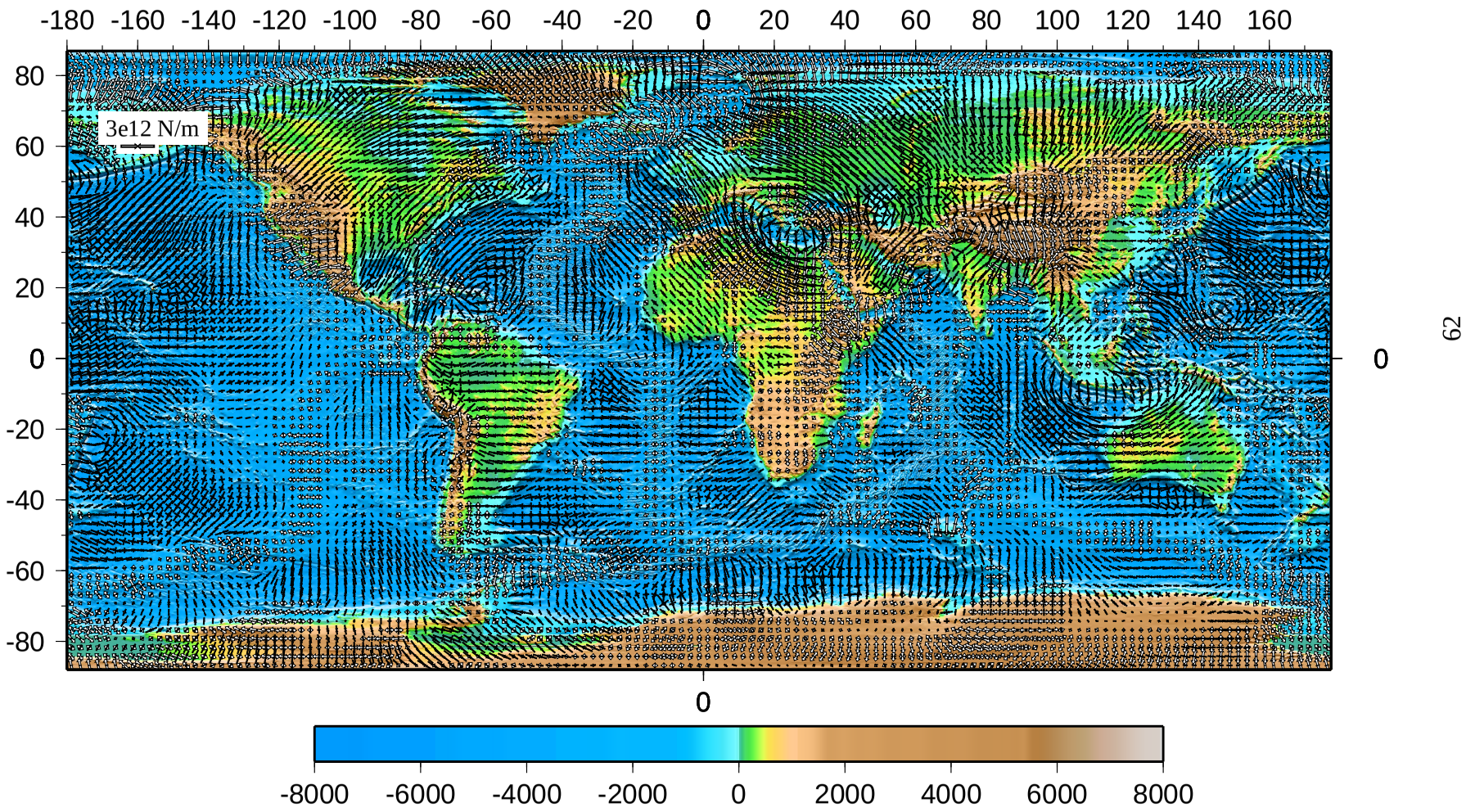
-180 -160 -140 -120 -100 -80 -60 -40 -20 0 20 40 60 80 100 120 140 160
80
60
40
20
0
-20
-40
-60
-80
3e12 N/m
0
0
-8000 -6000 -4000 -2000 0 2000 4000 6000 8000

Figure A4: Global distribution of vertically integrated horizontal deviatoric stresses. The plate boundaries are assigned variable viscosities based on their strain rates. A reference viscosity, μ_{ref} of 0.001 is used for the mid-Indian ridges. Topography is in meters.

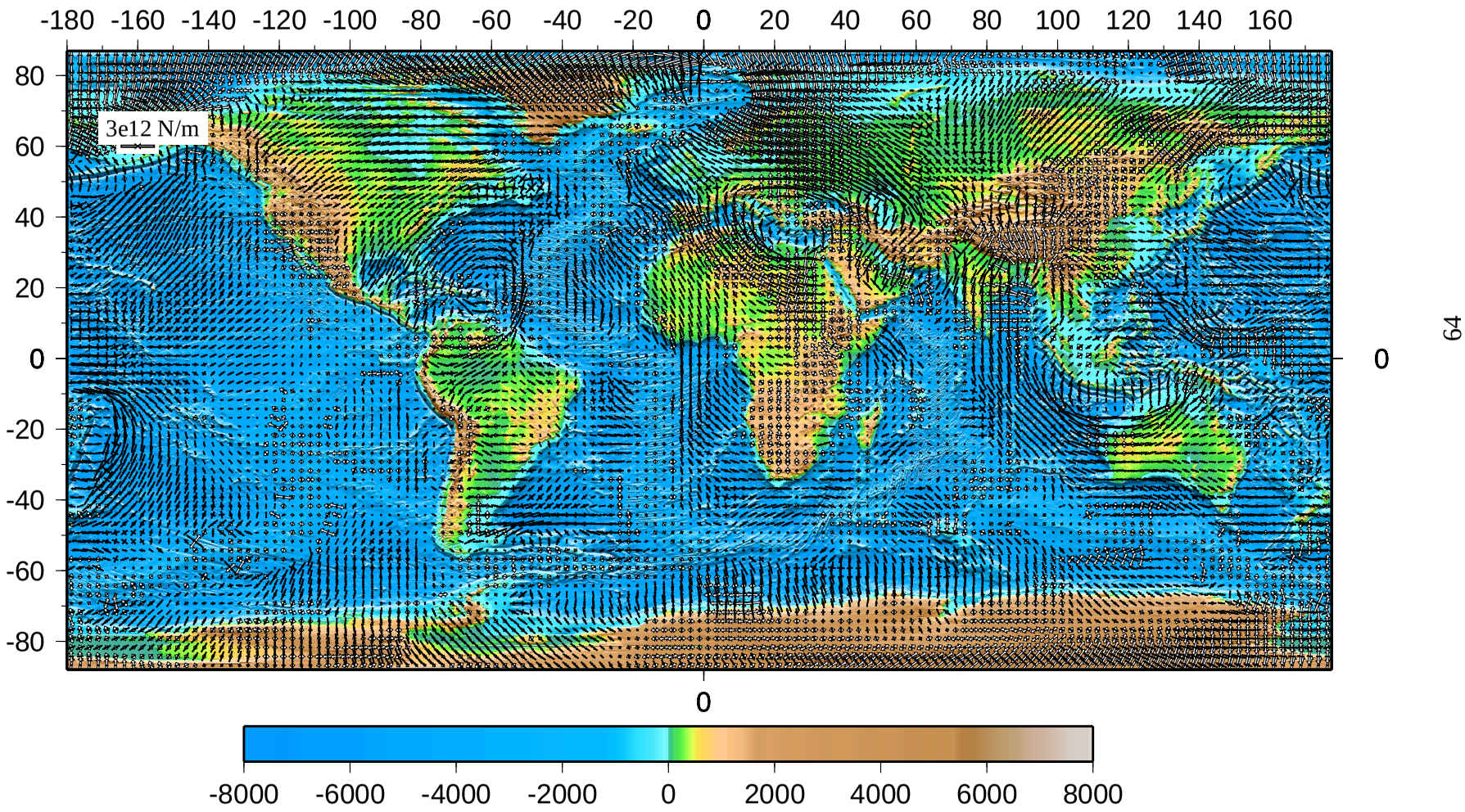
-180 -160 -140 -120 -100 -80 -60 -40 -20 0 20 40 60 80 100 120 140 160
80
60
40
20
0
-20
-40
-60
-80
3e12 N/m
0
0
-8000 -6000 -4000 -2000 0 2000 4000 6000 8000

Figure A5: Relative viscosity distribution for all the plates. The white areas represent high viscosity intra-plate regions. The difference with Fig. A2 is that Tibet and the Himalayas are assigned viscosities equal to the undeforming plate interiors.

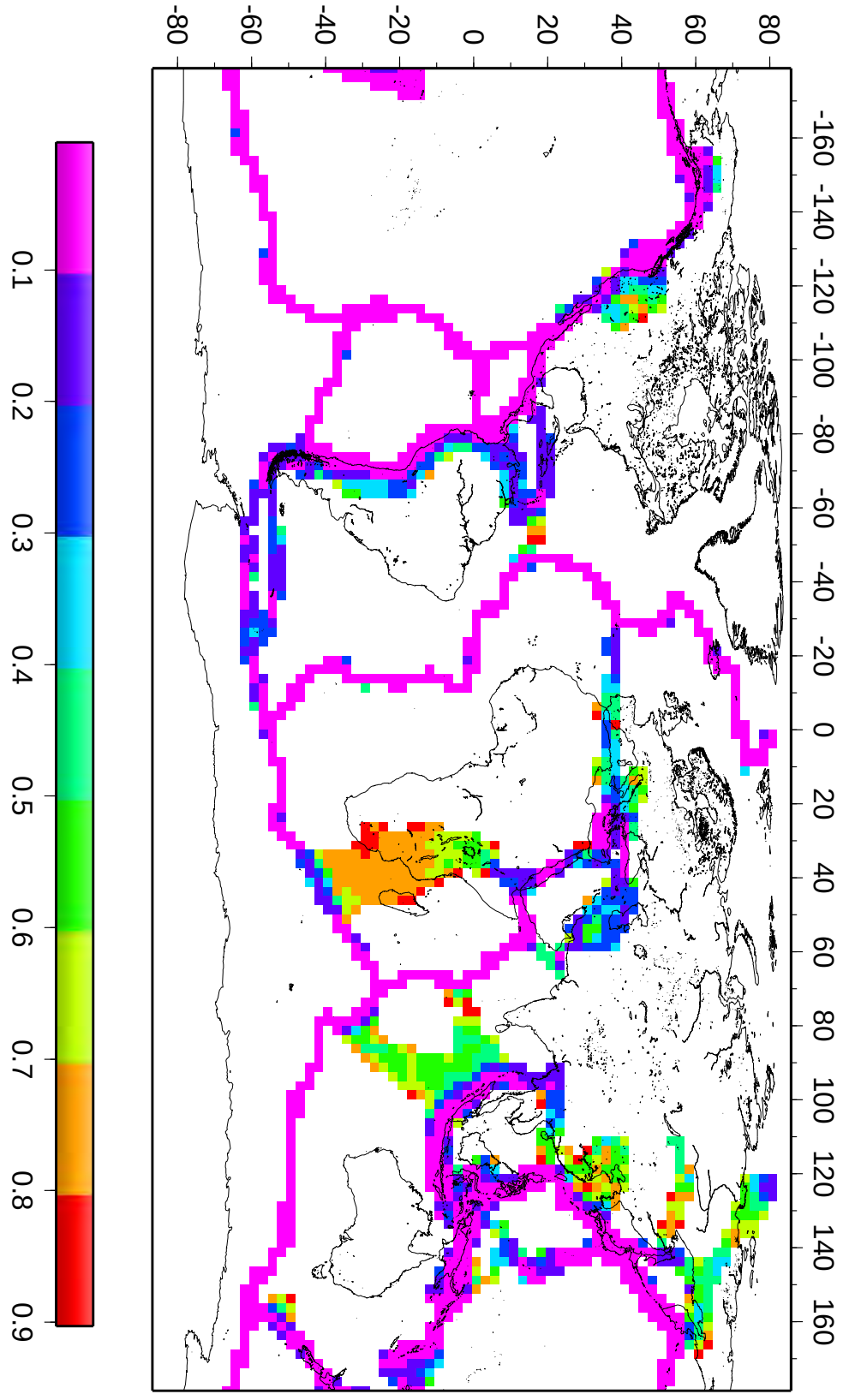
80
60
40
20
0
-20
-40
-60
-80
-160 -140 -120 -100 -80 -60 -40 -20 0 20 40 60 80 100 120 140 160
0.1
0.2
0.3
0.4
0.5
0.6
0.7
0.8
0.9

Figure A6: Global distribution of vertically integrated horizontal deviatoric stresses. The plate boundaries are assigned variable viscosities based on their strain rates, except the Tibetan Plateau and the Himalayas which are assigned a viscosity equal to the undeformed plate interiors. A reference viscosity of 0.01 is used for the mid-Indian ridges.

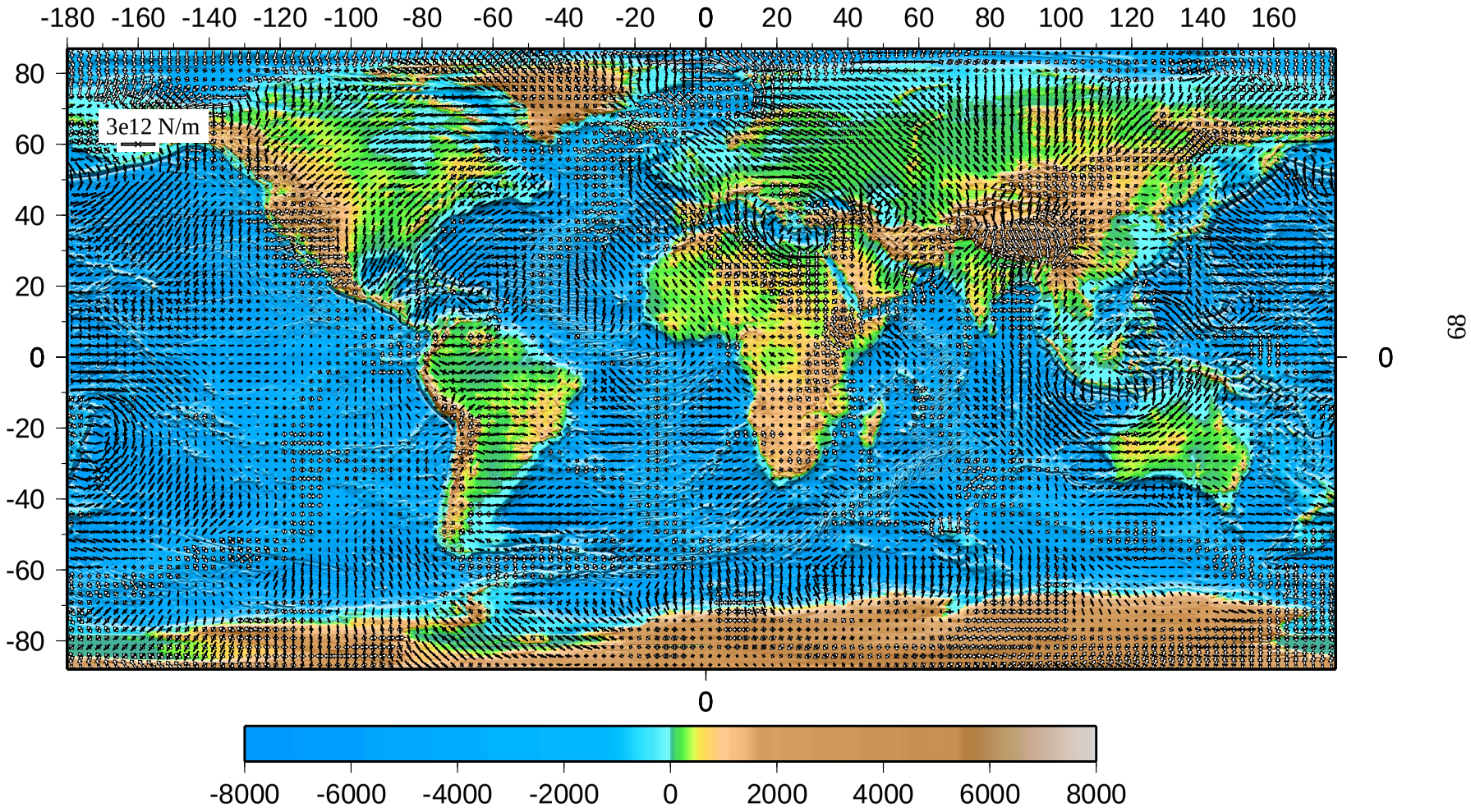
-180 -160 -140 -120 -100 -80 -60 -40 -20 0 20 40 60 80 100 120 140 160
80
60
40
20
0
-20
-40
-60
-80
3e12 N/m
0
0
-8000 -6000 -4000 -2000 0 2000 4000 6000 8000

Figure A7: Global distribution of vertically integrated horizontal deviatoric stresses in the uncompensated case corresponding to the compensated case in Fig. A3. The plate boundaries are assigned variable viscosities based on their strain rates. A reference viscosity, μ_{ref} of 0.01 is used for the mid-Indian ridges.

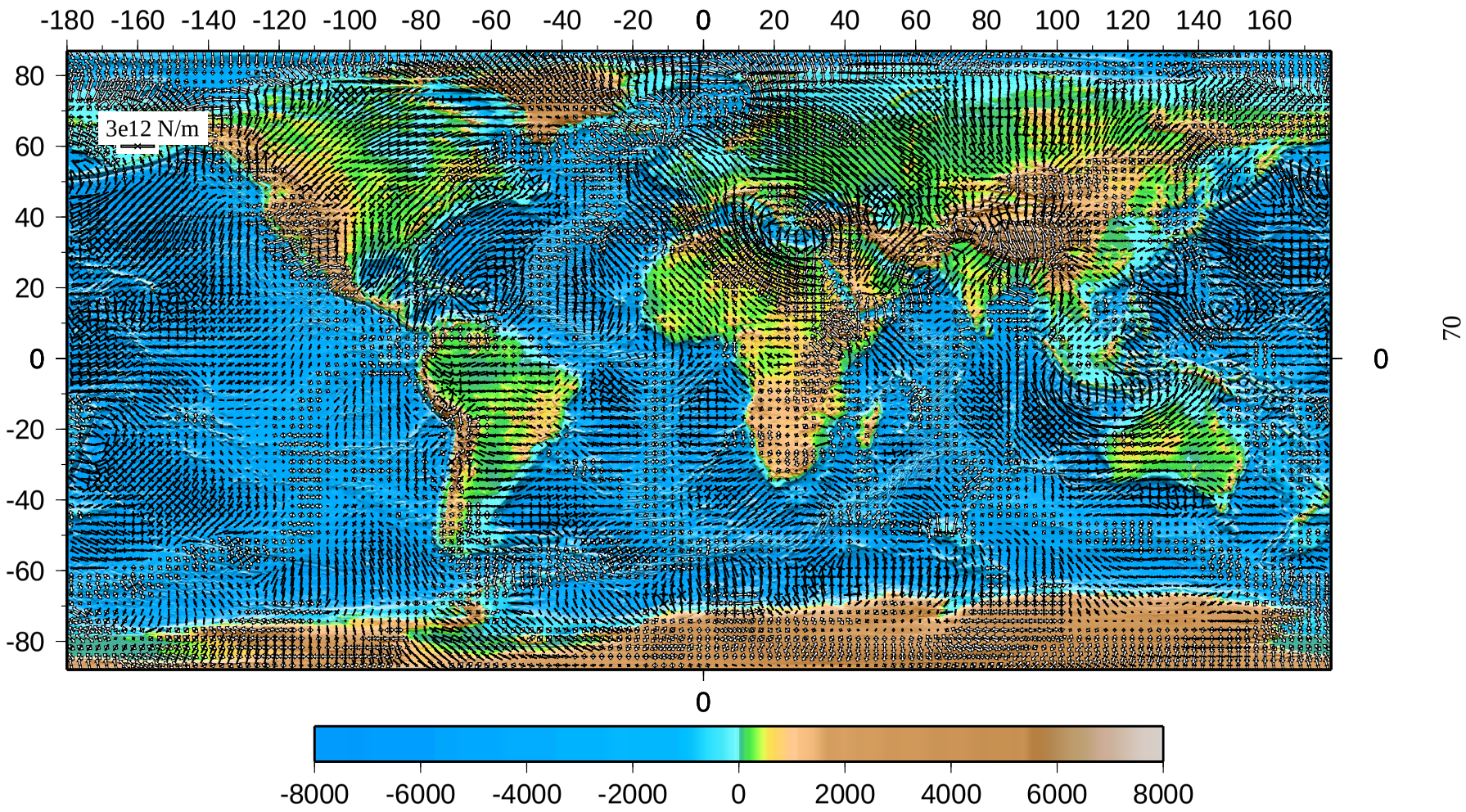
-180 -160 -140 -120 -100 -80 -60 -40 -20 0 20 40 60 80 100 120 140 160
80
60
40
20
0
-20
-40
-60
-80
3e12 N/m
0
0
-8000 -6000 -4000 -2000 0 2000 4000 6000 8000

70

Chapter 4

Joint Modeling of Lithosphere and Mantle Dynamics Elucidating Lithosphere-Mantle Coupling

Joint modeling of lithosphere and mantle dynamics elucidating lithosphere-mantle coupling

A. Ghosh, W. E. Holt, L. Wen, A. J. Haines and L. M. Flesch

(*Geophysical Research Letters*, under revision)

Abstract

We provide new insights into the lithosphere-mantle coupling problem through a joint modeling of lithosphere dynamics and mantle convection and through comparison of model results with the high resolution velocity gradient tensor dataset along the Earth's plate boundary zones. Using a laterally variable effective viscosity lithosphere model, we first compute vertically integrated deviatoric stresses associated with gravitational potential energy (GPE) differences. In many areas, deviatoric stresses from GPE differences alone provide a good fit to the observed strain rate tensors. However, in some areas, mostly in areas of continental deformation, GPE differences fall short of predicting the observed deformation styles and principal axes orientations. When deviatoric stresses from horizontal basal tractions, associated with deeper density buoyancy-driven convective circulation of the mantle, are added to those from GPE differences, the fit to the observed velocity gradient tensors improves dramatically in most areas. We find that the stresses induced by the horizontal tractions arising from deep mantle convection contribute approximately 50% of the magnitude of the Earth's deviatoric lithospheric stress field. We also demonstrate that lithosphere-asthenosphere viscosity contrasts play an important role in generating the right direction and magnitude of tractions that yield an optimal match to the observed stress pattern.

4.1 Introduction

The lithosphere-mantle coupling problem has been a controversial issue in geodynamics for the past few decades. The question that has divided the earth science community

is the degree of coupling between deeper density buoyancy-driven mantle circulation and the lithosphere, and whether such coupling has a role to play in lithosphere dynamics. The methods for tackling this problem consist of either predicting the velocities of the surface plates or modeling the lithospheric stress field. If the initial plate-mantle coupling model is correct, then the predicted velocities will match the observed plate motions and the modeled stress field will match the stress observations. Here, we investigate the problem of lithosphere-mantle coupling by modeling the lithospheric stress field and comparing our results with strain rate tensor observations from the Global Strain Rate Map (GSRM) (*Kreemer et al.,* 2003).

We address two principal sources of stress within the lithosphere : (1) internal buoyancy forces arising from lateral density variations within the lithosphere (lithosphere buoyancy) and (2) basal tractions associated with large-scale mantle convection arising from deeper density buoyancies below the lithosphere (mantle buoyancy). Most of the early attempts to model lithospheric stress field addressed either lithosphere buoyancy alone or lithosphere buoyancy with tractions acting at the base of the lithosphere playing a role in torque balance (*Solomon et al.,* 1975; *Richardson et al.,* 1979). However, in those models, tractions associated with model estimates of mantle density buoyancy-driven flow were not specifically put in. Mantle density buoyancy estimates, on the other hand, have mostly been used to model plate velocities, geoid, and topography (*Hager*, 1984; *Hager et al.*, 1985; *Richards and Hager*, 1984; *Gable et al.*, 1991; *Forte et al.*, 1993; *Wen and Anderson*, 1997b,c; *Becker and O'Connell*, 2001). *Bai et al.* (1992), *Bird* (1998), and more recently *Steinberger et al.* (2001) and *Lithgow-Bertelloni and Guynn* (2004), have modeled the lithospheric stress field by combining the above two sources. In most of these studies the modeled stress field was compared with stress observations from the World Stress Map (WSM) (*Zoback*, 1992; *Reinecker et al.,* 2005). One of the factors that distinguishes our study is a quantitative comparison of the modeled deviatoric stress tensor field with the GSRM's horizontal deformation tensor field within the Earth's plate boundary zones as well as a sensitivity analysis on the role of lithosphere-asthenosphere viscosity contrasts in generating the optimal wavelength and magnitude of tractions applied to the base of the lithosphere. In this paper we use a long-wavelength traction field generated by a simple convection model.

The aim of our study is to investigate the joint contribution of internal lithospheric density buoyancies and these long-wavelength tractions. The tractions are applied to the base of a thin sheet model possessing lateral viscosity variations due to weak plate boundaries and strong plates.

4.2 Method

Internal buoyancy sources within the lithosphere influence the lithospheric stress field (*Artyushkov*, 1973; *Fleitout and Froidevoux*, 1982; *Fleitout*, 1991; *Coblentz et al.*, 1994) by giving rise to gravitational potential energy (GPE) differences, which in turn produce deviatoric stresses. Density buoyancy-driven mantle convection gives rise to basal tractions that act upon the base of the lithosphere to yield a contribution to deviatoric stresses. We use the thin sheet approximation to solve for vertically integrated deviatoric stresses associated with both of these effects. This involves vertically integrating the force-balance equations from a reference level at radius r_L (usually the base of the lithosphere) to the Earth's surface, radius r_S:

$$\frac{2}{\cos\theta}\frac{\partial}{\partial\phi}\left(\int_{r_L}^{r_S} r^2\tau_{\phi\phi}dr\right)+\frac{1}{\cos\theta}\frac{\partial}{\partial\phi}\left(\int_{r_L}^{r_S} r^2\tau_{\theta\theta}dr\right)+\frac{1}{\cos^2\theta}\frac{\partial}{\partial\theta}\left(\cos^2\theta\int_{r_L}^{r_S} r^2\tau_{\phi\theta}dr\right)$$

$$=-\frac{1}{\cos\theta}\frac{\partial}{\partial\phi}\left(\int_{r_L}^{r_S} r^2\sigma_{rr}dr\right)+r_L^3\tau_{\phi r}(r_L) \qquad (1)$$

and

$$\frac{1}{\cos\theta}\frac{\partial}{\partial\phi}\left(\int_{r_L}^{r_S} r^2\tau_{\phi\theta}dr\right)+\frac{3}{2}\frac{\partial}{\partial\theta}\left(\int_{r_L}^{r_S} r^2\tau_{\theta\theta}dr+\int_{r_L}^{r_S} r^2\tau_{\phi\phi}dr\right)$$

$$+\frac{1}{2\cos^2\theta}\frac{\partial}{\partial\theta}\left(\cos^2\theta\left[\int_{r_L}^{r_S} r^2\tau_{\theta\theta}dr-\int_{r_L}^{r_S} r^2\tau_{\phi\phi}dr\right]\right)=-\frac{\partial}{\partial\theta}\left(\int_{r_L}^{r_S} r^2\sigma_{rr}dr\right)+r_L^3\tau_{\theta r}(r_L), \qquad (2)$$

where $\tau_{\phi\phi},\tau_{\theta\theta}$ and $\tau_{\phi\theta}$ are deviatoric stresses, which are vertically integrated, $\tau_{\phi r}(r_L)$ and $\tau_{\theta r}(r_L)$ are tractions applied at the base of the thin sheet at depth r_L, and σ_{rr} is the vertical

stress that is vertically integrated to give:

$$\begin{aligned}\int_{r_L}^{r_S} r^2\sigma_{rr}dr &= -\int_{r_L}^{r_S} r^2\left[\int_r^{r_S}\rho(r')gdr'\right]dr = -\int_{r_L}^{r_S}\rho(r')g\left[\int_{r_L}^{r'} r^2dr\right]dr' \\ &= -\int_{r_L}^{r_S}\frac{1}{3}\rho(r')g\left(r'^3 - r_L^3\right)dr', \end{aligned} \quad (3)$$

which is equal to the negative of GPE. Here, ρ is the density, g is the gravitational acceleration, and r_L is taken to be a constant depth of 100 km below the sea-level. The viscosity variations deeper than the reference level, including possible deeper extension of cratonic roots, are treated in the convection calculations. Note that r_S varies in continents due to variable surface topography, whereas in oceans r_S constitutes the sea level and is thus constant.

Solutions to equations (1) and (2) for the vertical integrals of $\tau_{\phi\phi}, \tau_{\theta\theta}$ and $\tau_{\phi\theta}$ can be obtained given GPE differences of $\frac{\partial}{\partial\phi}(\int_{r_L}^{r_S} r^2\sigma_{rr}dr)$ and $\frac{\partial}{\partial\theta}(\int_{r_L}^{r_S} r^2\sigma_{rr}dr)$ (e.g. *Flesch et al.*, 2001; *Ghosh et al.*, 2006). Density buoyancy-driven mantle convection also produces radial and horizontal tractions that act at the bottom of the lithosphere. The radial tractions yield dynamic topography at the Earth's surface. The influence of this dynamic topography (or radial traction) on lithospheric stress can be dealt with in two ways. First, because the present-day topography already contains the dynamic contribution related to deep mantle convection, one can calculate the depth integrals of vertical stresses (equation (3)) using the present-day topography and density structures in the lithosphere (the crustal and upper mantle structure in the top 100 km of the Earth). The depth integrals of vertical stresses following this procedure should be viewed as the summation of two components, with one contributed by the lithosphere buoyancies and the other by the radial tractions acting at the base of the lithosphere from the deep mantle density buoyancies. Such an approach does not address the consistency problem between the observed and predicted dynamic topography (*Wen and Anderson*, 1997c). In the present case, the densities in the lithosphere are obtained from the seismically inferred crustal structures (e.g., Crust 2.0 [*G. Laske et al.,* Crust 2.0: A new global crustal model at 2 × 2 degrees, 2002, available at http://mahi.ucsd.edu/Gabi/rem.html]). Alternatively, one can directly compute the corresponding deviatoric stresses in the lithosphere from the predicted dynamic topography or

radial tractions from the convection models. These deviatoric stresses are then added to those associated with a compensated lithosphere model. In such a treatment, the surface topography used to calculate the GPE differences in the lithosphere model is the compensated component based on the density buoyancies in the lithosphere. The deviatoric stress field produced by the compensated lithosphere model represent the contributions from the density buoyancies in the lithosphere. If a convection model is self-consistent, that is, it predicts dynamic topography that matches, in both pattern and magnitude, the observed residual topography (total observed topography minus the compensated component), the above two approaches should yield same results. In this study, we adopt the first approach and address the self consistency of predicting dynamic topography in future studies.

In order to obtain the deviatoric stresses associated with the horizontal tractions that are generated by density-buoyancy driven mantle flow, solutions to (1) and (2) can be calculated given distributions of $-\tau_{\phi r}(r_L)$, $-\tau_{\theta r}(r_L)$. The solution from horizontal tractions is then added to the solution from GPE differences described above to obtain the total deviatoric stress field.

In our global model, we solve equations (1) and (2) on a $2.5^o \times 2.5^o$ global grid using a finite element technique (*Flesch et al.*, 2001) such that the deviatoric stress field solution provides a global minimum in the second invariant of deviatoric stress (Appendix B).

We calculate GPE (equation (3)) from the crustal thickness and density dataset, Crust 2.0. The cooling plate model based on ocean floor age data (*Müller et al.*, 1997) with revised parameters from *Stein and Stein* (1992) is used to define densities for oceanic regions. The plate boundary zones are assigned variable viscosities (Appendix B) based on strain rates from the GSRM (*Kreemer et al.*, 2003), where the rapidly straining areas (e.g., subduction zones, narrow mid-ocean ridges for rapidly spreading plates) have lower viscosities compared to more slowly deforming regions, while the plate interiors have the highest constant relative viscosity. A best fit is obtained with plates having an effective viscosity ~ 30 times higher than that of a relatively rapidly deforming region in western North America with a reference strain rate of 1.5×10^{-7}/yr (Figure B1 in Appendix). The Crust 2.0 is an uncompensated model. We calculate GPE and the associated deviatoric stresses from the uncompensated Crust 2.0 model, which incorporates the contribution from radial tractions

(dynamic topography) in addition to the contribution from lithosphere buoyancy sources.

The terms $\tau_{\phi r}(r_L)$ and $\tau_{\theta r}(r_L)$ in equations (1) and (2) are derived from a convection model by *Wen and Anderson* (1997b) on solving the conservation equations of mass and momentum, using the constitutive equation between stress and strain rate with free slip boundary conditions, by a standard propagator matrix technique. Our mantle convection model is a whole mantle (WM) model with radially variable viscosities, the lower mantle being 10 times more viscous than the upper mantle. Unlike *Wen and Anderson* (1997b), we do not consider lateral viscosity variations within the lithosphere in our simple convection models. The density anomalies in the upper mantle are inferred by adjusting the relative weights of density anomalies related to subducting slabs (*Wen and Anderson*, 1995) and residual tomography (*Wen and Anderson*, 1997a), on the basis of fitting the geoid. The density structure in the lower mantle was derived from a seismic tomographic model (*Su et al.*, 1994). The detailed information for the density model and the velocity density scalings were presented in *Wen and Anderson* (1997b). The contributions that the horizontal tractions make on the lithospheric deviatoric stress field are computed using the thin sheet model with laterally variable viscosity. These horizontal tractions, or body force equivalents, are applied at the base of the thin sheet as a boundary condition (see Appendix A). The contribution from the basal tractions is then added to the contribution from GPE differences to determine a total deviatoric stress field.

4.3 A Quantitative Comparison with Deformation Indicators at Plate Boundary Zones

We test our modeled deviatoric stresses quantitatively with stress tensor indicators from the GSRM (*Kreemer et al.*, 2003). GSRM is a high resolution model based on 5170 GPS stations and Quarternary fault slip data, confined along the deforming plate boundary zones. The modeled deviatoric stress tensors are scored with the strain rate tensors in GSRM, and we seek to match direction of principal axes as well as style of faulting inferred from the

strain rate tensors. We define a correlation coefficient (*Flesch et al.*, 2007):

$$-1 \leq \sum_{areas} (\varepsilon \cdot \tau)\Delta S \Big/ \left(\sqrt{\sum_{areas} (E^2)\Delta S} * \sqrt{\sum_{areas} (T^2)\Delta S} \right) \leq 1 \tag{4}$$

where $E = \sqrt{\varepsilon_{\phi\phi}^2 + \varepsilon_{\theta\theta}^2 + \varepsilon_{rr}^2 + \varepsilon_{\phi\theta}^2 + \varepsilon_{\theta\phi}^2} = \sqrt{2\varepsilon_{\phi\phi}^2 + 2\varepsilon_{\phi\phi}\varepsilon_{\theta\theta} + 2\varepsilon_{\theta\theta}^2 + 2\varepsilon_{\phi\theta}^2}$,
$T = \sqrt{\tau_{\phi\phi}^2 + \tau_{\theta\theta}^2 + \tau_{rr}^2 + \tau_{\phi\theta}^2 + \tau_{\theta\phi}^2} = \sqrt{2\tau_{\phi\phi}^2 + 2\tau_{\phi\phi}\tau_{\theta\theta} + 2\tau_{\theta\theta}^2 + 2\tau_{\phi\theta}^2}$
and $\varepsilon \cdot \tau = 2\varepsilon_{\phi\phi}\tau_{\phi\phi} + \varepsilon_{\phi\phi}\tau_{\theta\theta} + \varepsilon_{\theta\theta}\tau_{\phi\phi} + 2\varepsilon_{\theta\theta}\tau_{\theta\theta} + 2\varepsilon_{\phi\theta}\tau_{\phi\theta}$.

E and T are the second invariants of strain and stress, ε_{ij} are strain rates from *Kreemer et al.* (2003), ΔS is the grid area, and τ_{ij} are the calculated deviatoric stresses. Normalization by E and T ensures that the correlation coefficient depends only on the inferred style of faulting embedded in the deviatoric stress and strain rate tensors as well as the direction of principal axes of strain rate and stress tensors; there is no dependence on magnitude of stress or strain rate. The maximum correlation coefficient of +1 indicates a perfect fit between the directions of principal axes of deviatoric stress and directions of principal axes of strain rate as well as a perfect fit between expected styles of faulting associated with the deviatoric stress and strain rate tensors. The minimum coefficient of -1 indicates anti-correlation. A value of 0 implies no fit, including, for example, predicted strike-slip style of deviatoric stress, where the compressional and tensional principal axes differ from those in the GSRM by 45^o.

4.4 Results

4.4.1 Deviatoric Stress from GPE Differences

There occurs a positive correlation between higher elevation areas and areas of high GPE, such as Andes, western North America, and the Tibetan Plateau. These high GPE areas are also in deviatoric tension. Topographically low areas and older oceans exhibit low GPE and consequently are in deviatoric compression (Figure 1). The Tibetan Plateau, with a very large crustal thickness and high elevation, shows large N-S deviatoric tension ($\sim 3 \times 10^{12}$ N/m), associated with large GPE contrasts with the surrounding regions, which

the ridge-push force fails to cancel (*Ghosh et al.*, 2006). It is clear that an additional N-S compressive driving force that does not have its origin within the lithospheric shell needs to be accounted for in order to cancel out the N-S deviatoric tension in Tibet. As we will see next, this additional force is provided by basal tractions associated with density buoyancy-driven mantle convection.

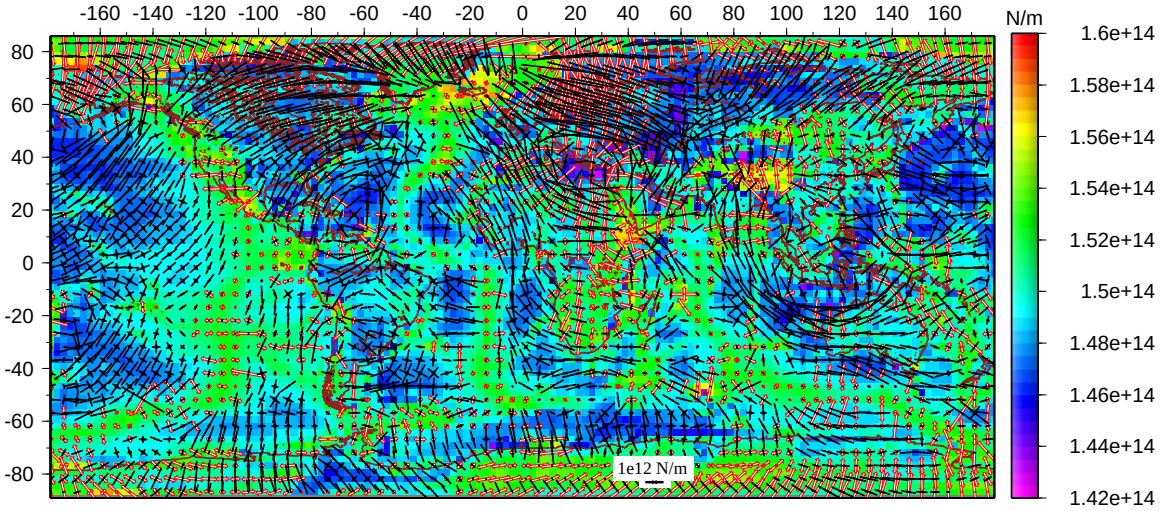

Figure 1: Global distribution of vertically integrated horizontal deviatoric stresses and GPE (on scale bar) calculated from the Crust 2.0 data with viscosities varying as a function of strain rates (Figure B1 in Appendix) where a reference viscosity, μ_{ref} is chosen such that a moderately straining region in western North America (with a strain rate of 1.5×10^{-7}/yr) has an effective viscosity ~ 30 times lower than the plates. Tensional deviatoric stresses are shown by red arrows while compressional deviatoric stresses are shown by black arrows. Length of the arrows are proportional to the magnitude of stresses. Strike-slip regions are indicated by one tensional and one compressional pair of arrows. Areas having high GPE are in deviatoric tension while those having low GPE are in deviatoric compression.

Comparison of modeled stresses from GPE differences to the deformation indicators in GSRM indicates an excellent fit along the mid-oceanic ridges and the Indo-Australian boundary zone. Areas of continental deformation, such as western North America, Andes and central Asia, exhibit a poor fit (Figure 4a, Table 1), clearly indicating that at least in those areas, lateral variations in GPE are not sufficient to explain the observed deformation.

4.4.2 Total Deviatoric Stress Field from Combined GPE Differences and Mantle Buoyancies

In the mantle convection models used to generate basal traction estimates, we test a range of lithosphere viscosities from slightly strong (5×10^{21} Pa-s) to very strong (100×10^{21} Pa-s) (Figure 2). The asthenosphere viscosity is also varied by 4 orders of magnitude, from 10^{18} to 10^{21} Pa-s. Amongst the various models of radially symmetric viscosity structures that we test, the ones marked within the ellipse generate deviatoric stresses, which when added to the deviatoric stresses from GPE differences (Figure 1), yield global correlation coefficients with GSRM of 0.65 and above. One aspect common to all these models is the need for a strong viscosity contrast between the lithosphere and the asthenosphere (100-10,000 times stronger lithosphere). All successful models (1-9) yield a consistent long-wavelength pattern of body force equivalents ($-\tau_{\phi r}$ and $-\tau_{\theta r}$) (see Appendix, Figure C1). These optimal models involve mantle flow velocities that are generally greater at depth than at the base of the plates in regions such as the Indo-Australian plates, Nazca and South American plates, and Eastern North America (Figure C1 in Appendix). The downwelling flow in these areas is generated by deeper density anomalies of ancient subducted lithosphere. The deviatoric stress result, associated with these horizontal tractions, yields compression over these downwelling zones, whereas tension occurs in areas of upwelling or divergent flow, such as eastern Africa and the Pacific. Viscosity models 2-5, which have strong asthenosphere (10^{20} Pa-s), along with model 1, which has no asthenosphere, yield tractions that are of magnitude 3-6 MPa (Figure C2 in Appendix). The resultant stresses from models

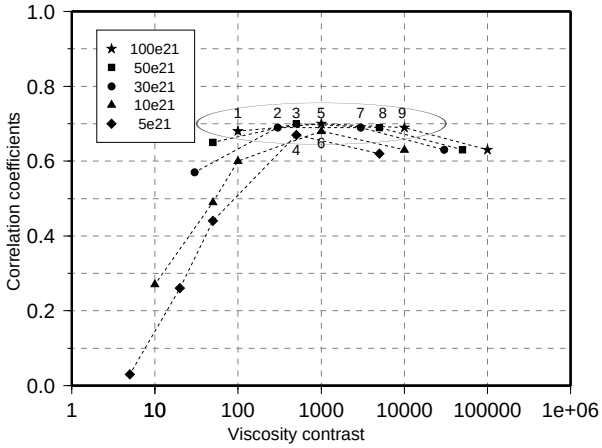

Figure 2: Viscosity contrast between lithosphere and asthenosphere vs. correlation coefficients. The different symbols indicate lithosphere of different strengths. The models within the ellipse yield correlation coefficients greater that 0.65. Viscosities are given in Pa-s.

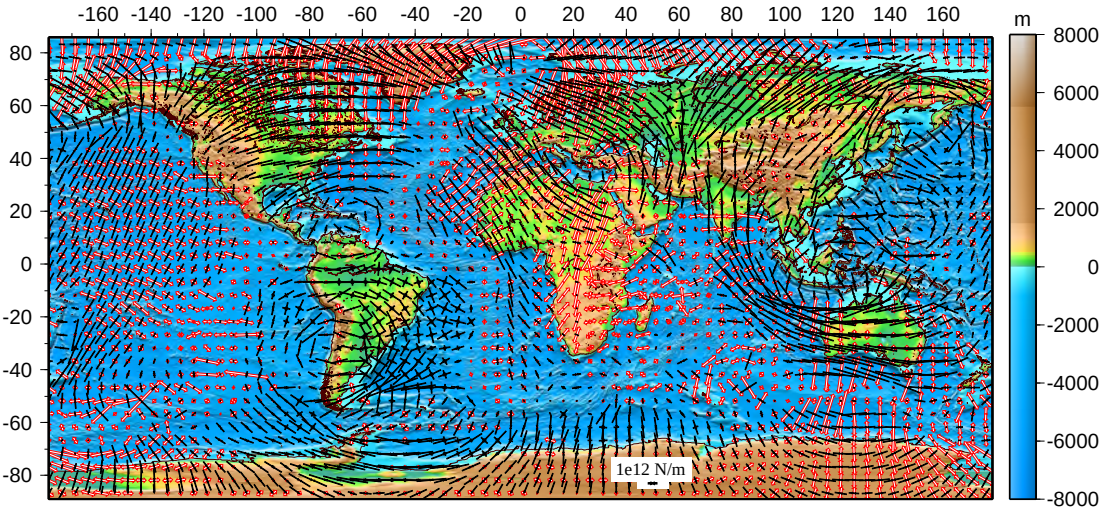

Figure 3: Global distribution of vertically integrated horizontal deviatoric stresses from GPE differences (Figure 1) and horizontal tractions combined, plotted on topography. The mantle convection model is a radially variable viscosity model with a strong lithosphere (50×10^{21} Pa-s) and a weak asthenosphere (10^{19} Pa-s) (model 8).

1-5 dominate the deviatoric stresses from GPE differences (Figure C3a in Appendix). Although not obvious from examination of global average correlation coefficients, models 1-5 produce tractions that are apparently too large. For example, Tibet shows more dominant thrust faulting than strike-slip in models 1-5. Parts of the Lake Baikal region become more dominantly thrust in these models with larger traction magnitudes. Furthermore, models 1-5 yield no tension in Basin and Range and much less tension in parts of the Aegean region compared to models 6-9.

Viscosity models 6-9, on the other hand, with a weak asthenosphere (10^{19} Pa-s), yield deviatoric stress magnitudes closer to stress magnitudes from GPE differences (Figure C3b in Appendix) and provide a more favorable match to deformation indicators in the above mentioned regions. Models 6-9 are our preferred models. The traction magnitudes for 6-9 range between 1-2.5 MPa (Figure C1 in Appendix). We show the combined deviatoric stress response from GPE differences and horizontal tractions (Figure 3) and also the score with the strain rate information (Figure 4b) for model 8 (Figure 2). Deviatoric stresses from the combined sources of GPE differences and horizontal tractions from mantle buoyancies show improvement of fitting in all areas, particularly in regions of continental deformation (Figure 4b, Table 1). A major change takes place in the Tibetan Plateau, where the

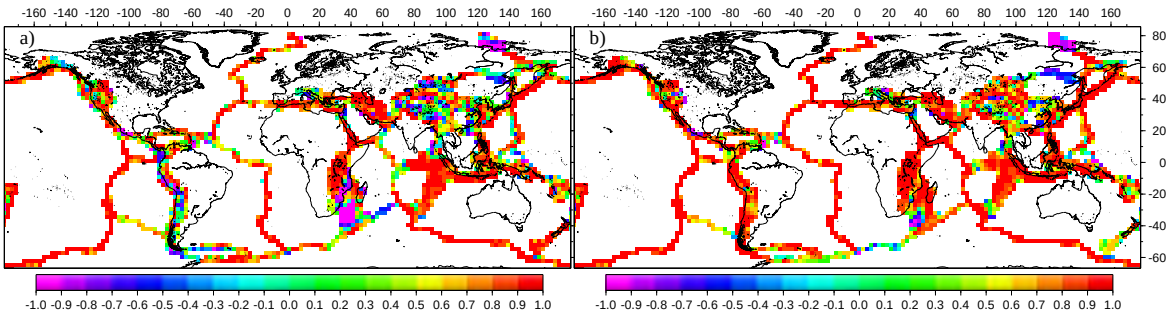

Figure 4: Correlation coefficients between observed strain rate tensors from the Global Strain Rate Map and deviatoric stress tensors arising from a) GPE differences from the Crust 2.0 model (Figure 1), and b) combined deviatoric stresses from GPE differences and mantle buoyancies (Figure 3).

dominantly N-S deviatoric tension from GPE differences is replaced by a mixed strike-slip style of deviatoric stress, in accord with a larger percentage of the deformation style there. This improvement can again be explained by addition of the influence of deeper subduction-related density buoyancies within the mantle. However, in some areas, such as New Zealand and parts of Asia, the fit degrades. Considering all the areas simultaneously, stresses from GPE differences yield an overall correlation coefficient of 0.54, whereas those from combined GPE differences and horizontal tractions produced by the mantle buoyancies yield an overall coefficient of 0.69 (Table 1).

A qualitative comparison of our deviatoric stresses with the style and direction of principal axes of stresses in the WSM reveals a good match, particularly in areas like the Indo-Australian plate, most of central Asia, and North America.

It is also necessary to have lateral viscosity variations in the lithosphere in the thin sheet model for the stresses to match deformation indicators. A test with no lateral variations in the lithosphere in the thin sheet model still improves the fit to the strain rate tensor information when the mantle contribution is added to the lithospheric contribution. However, the overall fit is much lower than when lateral variations are present (Table 1).

Viscosity models with too small a contrast between the lithosphere and asthenosphere (models outside the ellipse) yield a poor fit to the deformation indicators (Figure 2). The effective body force distribution (negative of the tractions) for these models (Figure C4 in Appendix) are different to those from models of large viscosity contrasts (within the

Region of interest	Number of areas	GPE differences with rheological variations	GPE differences plus basal tractions	GPE differences with constant viscosity	GPE differences plus basal tractions
W. North America	132	0.53	0.64	0.08	0.11
Andes	89	0.24	0.84	-0.20	0.78
Eastern Africa	164	0.32	0.76	0.63	0.81
Mediterranean	83	0.55	0.57	0.33	0.39
Central Asia	187	0.33	0.57	0.10	0.29
Indo-Australian plate boundary zone	174	0.69	0.76	0.30	0.31
Mid-oceanic ridges	292	0.80	0.85	0.78	0.76
Western Pacific	109	0.51	0.63	0.08	0.61
South East Asia	167	0.61	0.66	0.08	0.34
Total	1944	0.54	0.69	0.31	0.48

Table 1: Correlation coefficients obtained from a comparison between different deviatoric stress models with the strain rate tensor field from the GSRM model (see equation (4)). The mantle viscosity model considered is model 8. The viscosities in the lithosphere of the thin sheet model vary as function of strain rates (Figure B1 in Appendix) for columns 3 and 4, whereas for the last two columns, the lithosphere in the thin sheet model has uniform viscosity.

ellipse). For instance, these forces vary over much smaller wavelengths than for optimal models 6-9.

4.5 Discussion and Conclusion

Our results show that deviatoric stresses from GPE differences alone are not able to match the direction of principal axes and style of faulting in many of the deformation zones of the Earth's surface, particularly within the continental zones of deformation; horizontal basal tractions arising from mantle convection are also required to match the deformation indicators. These horizontal basal tractions that are coupled to the base of the lithospheric plates arise from mantle flow induced by current and past subducted lithosphere in the areas (e.g., the Indian plate, Andes, Figure C1 in Appendix). An aspect that is of prime importance is the viscosity contrast between the lithosphere and the asthenosphere, where a sufficiently large contrast (100-10,000 times) is required for the effective body forces associated with horizontal tractions to have the right directions and magnitudes. Although a wide range of models involving viscosity contrasts between lithosphere and asthenosphere appear to adequately match the global GSRM data (models 1-9), our preferred models are

those in which horizontal tractions and GPE differences (produced by the lithosphere buoyancies and the radial tractions) contribute approximately equally to the deviatoric stress field. These models (6-9) involve a weak asthenosphere of 10^{19} Pa-s, horizontal traction magnitudes of 1-2.5 MPa, and vertically integrated compressional deviatoric stress magnitudes ranging between $1 - 4 \times 10^{12}$ N/m, consistent with deviatoric stress magnitudes obtained by *Richardson* (1992).

Acknowledgement

This work benefited considerably from reviews provided by Peter Bird, Bernhard Steinberger and an anonymous reviewer. Maps were prepared using GMT version 3.4.4 by P. Wessel and W. F. Smith and the work was supported by NSF grant EAR-0310193 and a NASA grant NNG04GQ17G.

Appendix

Appendix A: Spherical Treatment

In spherical coordinates, the x,y and z directions of Cartesian coordinates change to the ϕ, θ and r (radial) components, respectively. The deviatoric stress tensor in the radial direction is

$$\tau_{rr} = \sigma_{rr} - \frac{1}{3}\sigma_{kk}, \tag{A1}$$

where σ_{rr} is the total stress tensor in the radial direction and $\frac{1}{3}\sigma_{kk}$ is the mean total stress. This is the 3-D definition of deviatoric stress, discussed by *Flesch et al.* (2001); *Ghosh et al.* (2006). The total stress tensor, $\sigma_{ij} = \tau_{ij} + \frac{1}{3}\sigma_{kk}\delta_{ij}$, then becomes

$$\sigma_{ij} = \tau_{ij} + \delta_{ij}(\sigma_{rr} - \tau_{rr}). \tag{A2}$$

where δ_{ij} represents the Kronecker delta. The force balance equation is:

$$\nabla \cdot \sigma + \rho \mathbf{g} = 0, \tag{A3}$$

where **g** is a vector in the negative radial direction. (A3) can be written in spherical coordinates as

$$\frac{1}{\cos\theta}\frac{\partial}{\partial\phi}\left(r^2\sigma_{\phi\phi}\right) + \frac{1}{\cos^2\theta}\frac{\partial}{\partial\theta}\left(r^2\sigma_{\phi\theta}\cos^2\theta\right) + \frac{\partial}{\partial r}\left(r^3\sigma_{\phi r}\right) = 0 \tag{A4}$$

$$\frac{1}{\cos\theta}\frac{\partial}{\partial\phi}\left(r^2\sigma_{\phi\theta}\right) + \frac{1}{2}\frac{\partial}{\partial\theta}\left(r^2\left[\sigma_{\theta\theta}+\sigma_{\phi\phi}\right]\right) + \frac{1}{2\cos^2\theta}\frac{\partial}{\partial\theta}\left(r^2\cos^2\theta\left[\sigma_{\theta\theta}-\sigma_{\phi\phi}\right]\right) + \frac{\partial}{\partial r}\left(r^3\sigma_{\theta r}\right) = 0 \tag{A5}$$

$$\frac{1}{r\cos\theta}\frac{\partial\sigma_{\phi r}}{\partial\phi} + \frac{1}{r\cos\theta}\frac{\partial}{\partial\theta}\left(\cos\theta\sigma_{\theta r}\right) + \frac{1}{r}\left(2\sigma_{rr} - \sigma_{\phi\phi} - \sigma_{\theta\theta}\right) + \frac{\partial\sigma_{rr}}{\partial r} - \rho g = 0 \tag{A6}$$

Vertically integrating (A4) and (A5) yields

$$\frac{1}{\cos\theta}\frac{\partial}{\partial\phi}\left(\int_{r_L}^{r_S} r^2\sigma_{\phi\phi}dr\right) + \frac{1}{\cos^2\theta}\frac{\partial}{\partial\theta}\left(\int_{r_L}^{r_S} r^2\sigma_{\phi\theta}dr\cos^2\theta\right) - r_L^3\sigma_{\phi r}r_L = 0 \tag{A7}$$

and

$$\frac{1}{\cos\theta}\frac{\partial}{\partial\phi}\left(\int_{r_L}^{r_S} r^2\sigma_{\phi\theta}dr\right) + \frac{1}{2}\frac{\partial}{\partial\theta}\left(\int_{r_L}^{r_S} r^2\left[\sigma_{\theta\theta}+\sigma_{\phi\phi}\right]dr\right) + \frac{1}{2\cos^2\theta}\frac{\partial}{\partial\theta}\left(\int_{r_L}^{r_S} r^2\cos^2\theta\left[\sigma_{\theta\theta}-\sigma_{\phi\phi}\right]dr\right)$$
$$-r_L^3\sigma_{\theta r}r_L = 0 \tag{A8}$$

where r_S is the radius from the center of the Earth to the surface of variable topography and r_L is the radius from the center to the base of the lithosphere. Substituting (A2) in (A7) and (A8), we arrive at equations (1) and (2) in the text. For a thin sheet, the gradients of $\sigma_{\phi r}$ and $\sigma_{\theta r}$ are negligibly small. Moreover, the term $\frac{1}{r}(2\sigma_{rr} - \sigma_{\phi\phi} - \sigma_{\theta\theta})$ is small compared to ρg. Hence, (A6) can be approximated as

$$\frac{\partial \sigma_{rr}}{\partial r} - \rho g = 0 \tag{A9}$$

which implies

$$\sigma_{rr} = -\int_r^{r_S} \rho g dr' \tag{A10}$$

which is used to provide the GPE equation (3) in text. Substituting $r' = r_E - z'$, and $r_L = r_E - L$, we have

$$\begin{aligned}
\frac{1}{3}\left(r'^3 - r_L^3\right) &= \frac{1}{3}\left((r_E - z')^3 - (r_E - L)^3\right) && \text{(A11)} \\
&= r_E^2(L - z') - r_E(L^2 - z'^2) + \frac{1}{3}(L^3 - z'^3) && \text{(A12)} \\
&= r_E^2(L - z')\left[1 - \frac{1}{r_E}(L + z') + \frac{1}{3r_E^2}(L^2 + Lz' + z'^2)\right] && \text{(A13)}
\end{aligned}$$

where L is the depth to the constant reference level, or base of the lithosphere. Equation (A13), therefore, provides the magnitude of error in GPE introduced by the flat-Earth approximation in comparison with the exact spherical case.

In order to compute deviatoric stresses from mantle buoyancy sources, the horizontal tractions are first calculated from the mantle convection model. With θ as positive north latitude, the equivalent expressions for $\tau_{\phi r}$ and $\tau_{\theta r}$ in *Wen and Anderson* (1997b) can be written as:

$$r_L \tau_{\phi r}/\eta_0 = Z_4^{lm} \frac{1}{\cos\theta} \frac{\partial}{\partial \phi} Y_{lm}(\theta, \phi) + Z_6^{lm} \frac{\partial}{\partial \theta} Y_{lm}(\theta, \phi) \tag{A14}$$

$$r_L \tau_{\theta r}/\eta_0 = Z_4^{lm} \frac{\partial}{\partial \theta} Y_{lm}(\theta, \phi) - Z_6^{lm} \frac{1}{\cos\theta} \frac{\partial}{\partial \phi} Y_{lm}(\theta, \phi) \tag{A15}$$

where η_0 is the reference viscosity, Z_4^{lm} and Z_6^{lm} are the spherical harmonic coefficients for the poloidal and toroidal components of stress, $Y_{lm}(\theta, \phi)$ is the surface normalized spherical harmonic of degree l, whose maximum value is 12 in this study, and order m. For a radially symmetric viscosity structure, the Z_6^{lm} terms are zero.

Appendix B: Variable Viscosities

The functional that is minimized in the method of *Flesch et al.* (2001) is :

$$I = \int\int \frac{1}{\mu}\left[\bar{\tau}_{\phi\phi}^2 + 2\bar{\tau}_{\phi\theta}^2 + \bar{\tau}_{\theta\theta}^2 + (\bar{\tau}_{\phi\phi}+\bar{\tau}_{\theta\theta})^2\right]\cos\theta d\phi d\theta$$

$$+\int\int\left\{2\lambda_\phi\left[\frac{1}{\cos\theta}\frac{\partial\bar{\tau}_{\phi\phi}}{\partial\phi}+\frac{1}{\cos\theta}\frac{\partial}{\partial\phi}(\bar{\tau}_{\phi\phi}+\bar{\tau}_{\theta\theta})+\frac{1}{\cos^2\theta}\frac{\partial}{\partial\theta}(\cos^2\theta\bar{\tau}_{\phi\theta})+\frac{1}{\cos\theta}\frac{\partial\bar{\sigma}_{rr}}{\partial\phi}-r_L^3\sigma_{\phi r}(r_L)\right]\right.$$

$$\left.+2\lambda_\theta\left[\frac{1}{\cos\theta}\frac{\partial\bar{\tau}_{\phi\theta}}{\partial\phi}+\frac{3}{2}\frac{\partial}{\partial\theta}(\bar{\tau}_{\theta\theta}+\bar{\tau}_{\phi\phi})+\frac{1}{2\cos^2\theta}\frac{\partial}{\partial\theta}(\cos^2\theta[\bar{\tau}_{\theta\theta}-\bar{\tau}_{\phi\phi}])+\frac{\partial\bar{\sigma}_{rr}}{\partial\theta}-r_L^3\sigma_{\theta r}(r_L)\right]\right\}\cos\theta d\phi d\theta \quad \text{(B1)}$$

where $\bar{\tau}_{\phi\phi}$, $\bar{\tau}_{\theta\theta}$ and $\bar{\tau}_{\phi\theta}$ are the vertically integrated deviatoric stresses, $\bar{\sigma}_{rr}$ is the vertically integrated vertical stress, λ_ϕ, λ_θ represent the horizontal components of the Lagrange multipliers, and μ is the relative viscosity, which in this case varies laterally. *Flesch et al.* (2001) assumed a constant μ equal to 1. In this paper, we use a variable value of μ to approximate weak plate boundary zones and strong plates. We assume an inverse relationship between strain rates and relative viscosities, μ. We obtain the relative viscosities of the deforming plate boundary regions, such as the mid-oceanic ridges and subduction zones, by assigning a reference viscosity to a moderately deforming region in western North America with a strain rate of 1.5×10^{-7}/yr , using the relation:

$$\frac{1}{\mu} = 1 + \left(\frac{1}{\mu_{ref}} - 1\right)\sqrt{\frac{E^2}{E_{ref}^2}} \quad \text{(B2)}$$

where μ_{ref} is the reference viscosity corresponding to the above mentioned area in western North America, $E^2 = 2(\dot{\varepsilon}_{\theta\theta}^2 + \dot{\varepsilon}_{\phi\phi}^2 + \dot{\varepsilon}_{\phi\theta}^2 + \dot{\varepsilon}_{\phi\phi}\dot{\varepsilon}_{\theta\theta})$, where $\dot{\varepsilon}_{\theta\theta}, \dot{\varepsilon}_{\phi\phi}$ and $\dot{\varepsilon}_{\phi\theta}$ are the strain rates from *Kreemer et al.* (2003), and E_{ref}^2 is the reference value for E^2, corresponding to the value for μ_{ref}. A plot of relative viscosities (Figure B1) shows the lowest viscosities along the mid-oceanic ridges, relatively higher viscosities in the deforming continents, while the blank areas (the plates) have the highest viscosities with a μ value of 1. We try reference viscosities of 1/3, in which our reference area in western North America is 3 times weaker than the plates, 1/30 (Figure B1 and the solution in the main paper), 1/300 and also 1/3000; the viscosity structure yielding deviatoric stress field that matches the deformation indicators best is chosen.

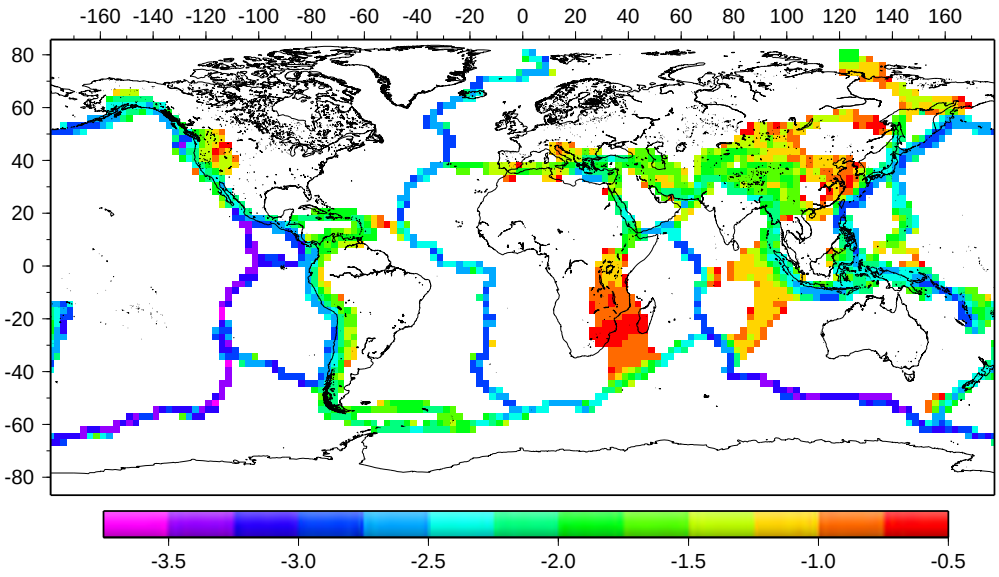

Figure B1: Logarithm (log 10) of relative viscosity distribution for all the plates in the lithosphere model. The white areas represent intra-plate regions with reference viscosity 1. The deforming areas are assigned viscosities inversely proportional to the strain rates from GSRM (equation B2). A reference viscosity of $\mu_{ref} \sim \frac{1}{30}$ is chosen at the moderately straining western North America (1.5×10^{-7}/yr). Places with viscosities higher than μ_{ref} are deforming at a slower rate.

We minimize a second functional J with respect to λ_ϕ and λ_θ that when minimized satisfies the force-balance equations (*Flesch et al.*, 2001),

$$J = \int\int \left\{ \left[\begin{pmatrix} \bar{\tau}_{\phi\phi} \\ \bar{\tau}_{\theta\theta} \\ \bar{\tau}_{\phi\theta} \end{pmatrix} - \begin{pmatrix} \Phi^{obs}_{\phi\phi} \\ \Phi^{obs}_{\theta\theta} \\ \Phi^{obs}_{\phi\theta} \end{pmatrix} \right]^T \widetilde{V}^{-1} \left[\begin{pmatrix} \bar{\tau}_{\phi\phi} \\ \bar{\tau}_{\theta\theta} \\ \bar{\tau}_{\phi\theta} \end{pmatrix} - \begin{pmatrix} \Phi^{obs}_{\phi\phi} \\ \Phi^{obs}_{\theta\theta} \\ \Phi^{obs}_{\phi\theta} \end{pmatrix} \right] \right\} \cos\theta d\phi d\theta \tag{B3}$$

where

$$\bar{\tau}_{\phi\phi} = \mu\left(\frac{1}{\cos\theta}\frac{\partial\lambda_\phi}{\partial\phi} - \lambda_\theta \tan\theta \right), \tag{B4}$$

$$\bar{\tau}_{\theta\theta} = \mu\frac{\partial\lambda_\theta}{\partial\theta}, \tag{B5}$$

$$\bar{\tau}_{\phi\theta} = \frac{\mu}{2}\left(\frac{\partial\lambda_\phi}{\partial\theta} + \frac{1}{\cos\theta}\frac{\partial\lambda_\theta}{\partial\phi} + \lambda_\phi \tan\theta \right), \tag{B6}$$

$$\widetilde{\mathbf{V}}^{-\mathbf{1}} = \frac{1}{\mu}\begin{pmatrix} 2 & 1 & 0 \\ 1 & 2 & 0 \\ 0 & 0 & 2 \end{pmatrix}, \tag{B7}$$

$$(\Phi_{\phi\phi}^{obs}, \Phi_{\theta\theta}^{obs}, \Phi_{\phi\theta}^{obs})^T = \left(-\frac{\bar{\sigma}_{rr}}{3}, -\frac{\bar{\sigma}_{rr}}{3}, 0\right)^T \tag{B8}$$

for the GPE case, and

$$(\Phi_{\phi\phi}^{obs}, \Phi_{\theta\theta}^{obs}, \Phi_{\phi\theta}^{obs})^T = \left(\frac{Z_4^{lm} Y_{lm}}{3}, \frac{Z_4^{lm} Y_{lm}}{3}, 0\right)^T \tag{B9}$$

for the traction case. Minimizing J is equivalent to minimizing I in (B1) (see proof in *Flesch et al.* (2001)) and provides a vertically integrated deviatoric stress field that balances the body force inputs and is also a global minimum in the second invariant of deviatoric stress (for given distribution of relative effective viscosities).

Appendix C

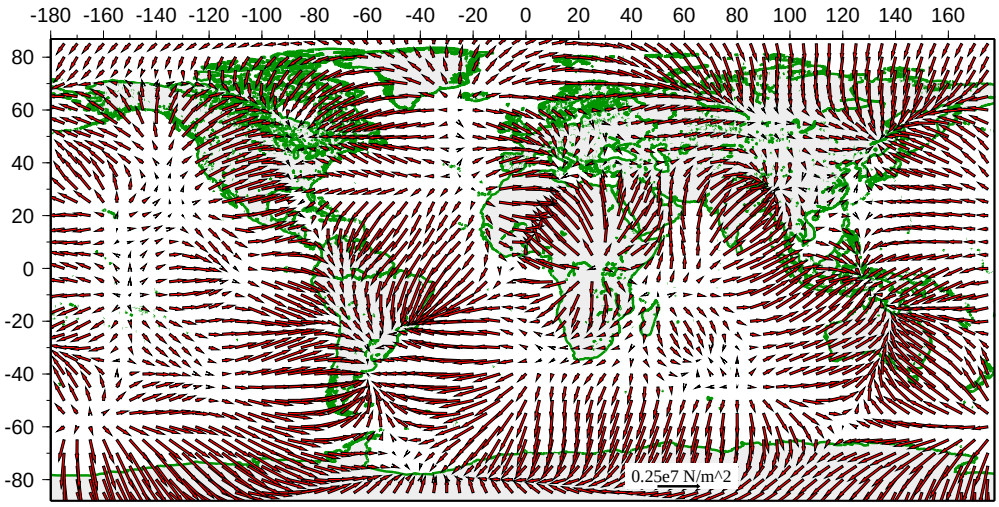

Figure C1: Global distribution of effective horizontal body forces, which are the negative of the tractions, $\tau_{r\phi}, \tau_{r\theta}$ (equations (A14) and (A15)), applied at the base of the lithosphere (100 km depth). The tractions are generated by a convection model (model 8) with radially variable viscosity structure, a weak asthenosphere (with viscosity of 10^{19} Pa-s) and a stronger lithosphere (with viscosity of 50×10^{21} Pa-s). A site of upwelling or divergence is beneath Eastern Africa, as well as beneath parts of Pacific and beneath mid-oceanic ridges, whereas areas of convergence or downwelling are middle North America, South America, Central and eastern Asia and the Southeast Asian subduction zones.

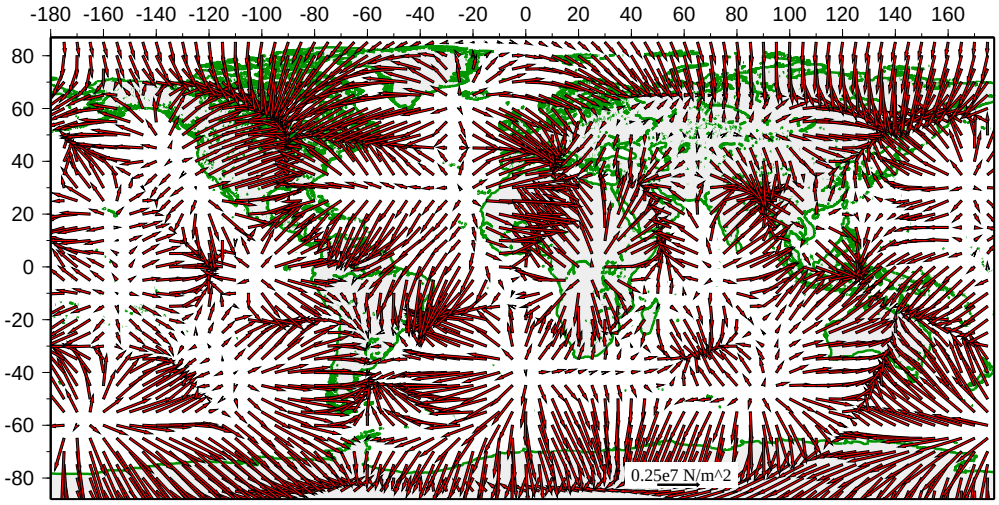

Figure C2: Same as Figure C1, but for viscosity model 2, with stronger asthenosphere (10^{20} Pa-s). Note the large traction magnitudes, which are about a factor of 2 larger than for optimal models 6-9.

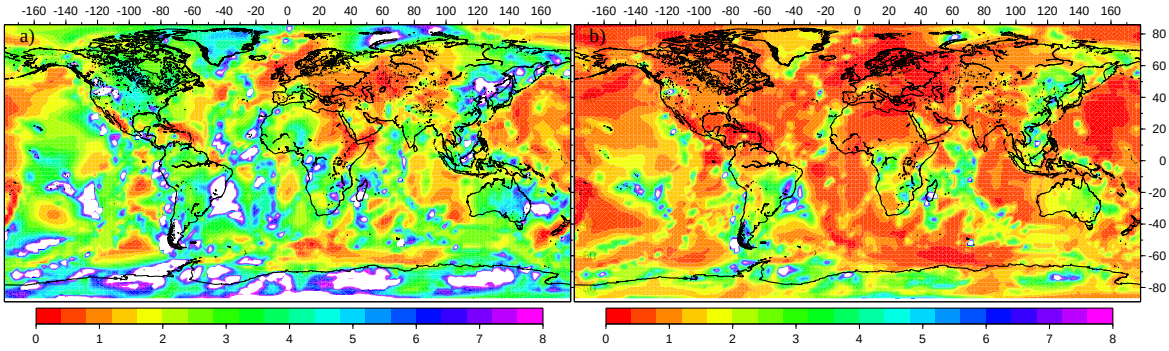

Figure C3: Contour maps of ratio, T_1/T_2, where T is the second invariant of the deviatoric stress field. T_1 is predicted by mantle buoyancies and T_2 is predicted by lithospheric GPE differences (Figure 1). a) is for model 1, with strong lithosphere and no asthenosphere. Note that ratios here indicate that tractions from this model generate deviatoric stresses that are on average 3-5 times larger than the deviatoric stresses associated with GPE differences. b) is for model 8, with a weak asthenosphere of 10^{19} Pa-s. Note that the ratios in b) generally show that the contribution of deviatoric stresses from tractions are the same magnitude as stresses from GPE differences. Areas of strong upwelling and downwelling in (b), however, have larger stresses from tractions. White areas are where the ratio is out of range (greater than 8).

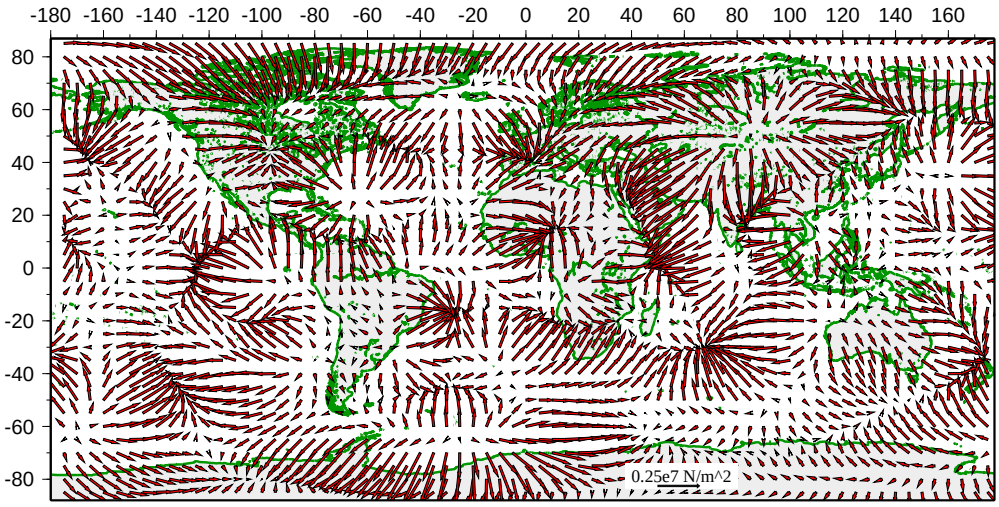

Figure C4: Same as Figure C1, but for a viscosity model with lithosphere viscosity 5×10^{21} Pa-s and asthenosphere viscosity of 25×10^{19} Pa-s, which yields a viscosity contrast of 20. Note that the effective force distribution is very different from Figures C1 and C2, and of much smaller wavelength. This traction field provides a very poor fit to the GSRM stress tensor indicators.

Appendix D: Benchmarking

We discuss the suitability of the thin sheet approximation in its ability to recover the depth integrals of deviatoric stress in the presence of large-scale three dimensional flow. That is, we intend to test whether the vertically integrated horizontal deviatoric stresses from the thin sheet model can recover the horizontal deviatoric stress field from the 3-D convection model (*Wen and Anderson*, 1997b). For this test we use two models of radially variable viscosity structures: 1) one with no lithosphere (an isoviscous model) and 2) one with a strong lithosphere (a lid model). The lithosphere in the thin sheet model is assumed to be with no lateral viscosity variations. The density buoyancy distributions for the convection models used here to generate 3-D flow and 3-D stress are the same as for models described in the text.

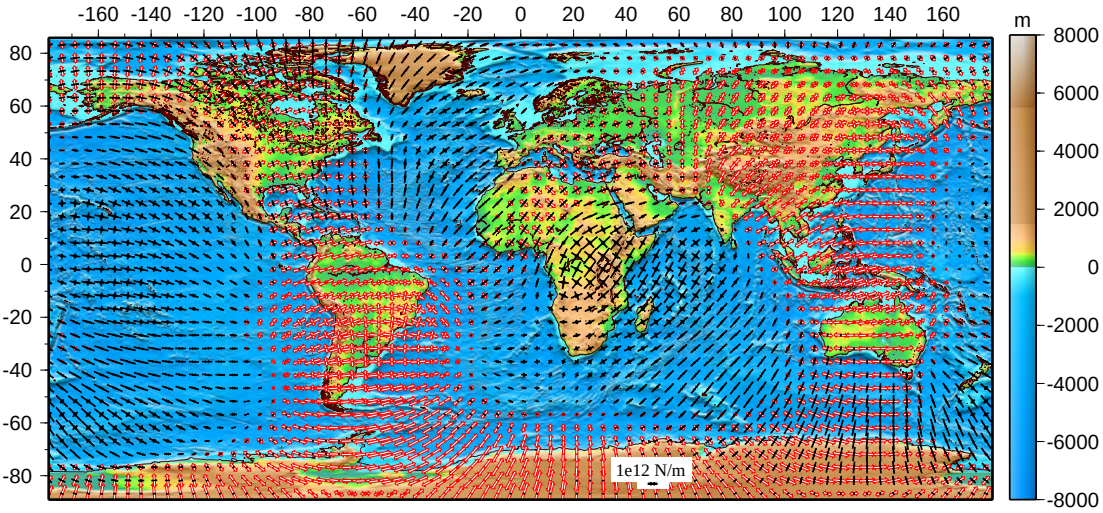

Figure D1: Deviatoric stress field, computed via the thin sheet method for an isoviscous case. The stresses are produced by horizontal tractions, which are generated by a 3-D convection model, output at 100 km depth, and applied to the base of the thin sheet.

The vertical and horizontal components of the three-dimensional convective flow in the mantle generate radial and horizontal tractions. The radial tractions are responsible for producing dynamic topography. In this section, we will show that the combined deviatoric stress field, from radial and horizontal tractions, computed via the thin sheet method, is able to match the deviatoric stress field predicted by the full 3-D convection model. The radial and horizontal tractions are generated by a 3-D convection model. We first consider

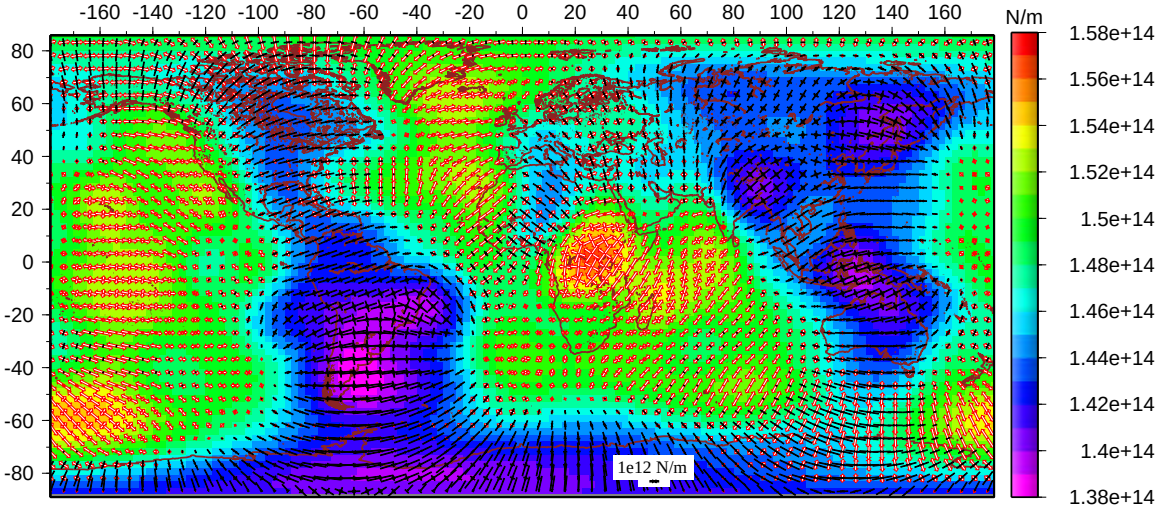

Figure D2: GPE , or depth integral of σ_{rr} (on scalebar), and deviatoric stress field, computed via the thin sheet method, for an isoviscous case. The GPE is calculated from dynamic topography predicted by the 3-D convection model. The radial component of the 3-D mantle flow gives rise to the dynamic topography.

an isoviscous case.

The horizontal tractions generated by the 3-D convection model, output at 100 km depth, are applied to the base of the thin sheet, and the deviatoric stresses are then computed using the thin sheet method (Figure D1). These stresses associated with horizontal tractions produce deviatoric tension in areas of convergence (central Asia, southeast Asian subduction zone, south America) and deviatoric compression in areas of divergence (eastern Africa). Next, the dynamic topography, predicted by the isoviscous convection model, is used to calculate depth integrals of σ_{rr}, assuming PREM as the background density model. The resultant GPE differences are only due to the presence of dynamic topography. From these GPE differences, the deviatoric stress field (Figure D2) is computed via the thin sheet method. The resultant deviatoric stresses show convergence over areas of negative dynamic topography, and divergence over areas of positive dynamic topography, such as eastern Africa and the Pacific. In other words, the deviatoric stresses from radial tractions are opposite in sign to the deviatoric stresses from horizontal tractions for the isoviscous case (Figure D1). These stresses from radial tractions are then added to the stresses from horizontal tractions in order to produce an estimate of the depth integral of the total deviatoric stress field (Figure D3). The two stress fields nearly cancel each other, but the

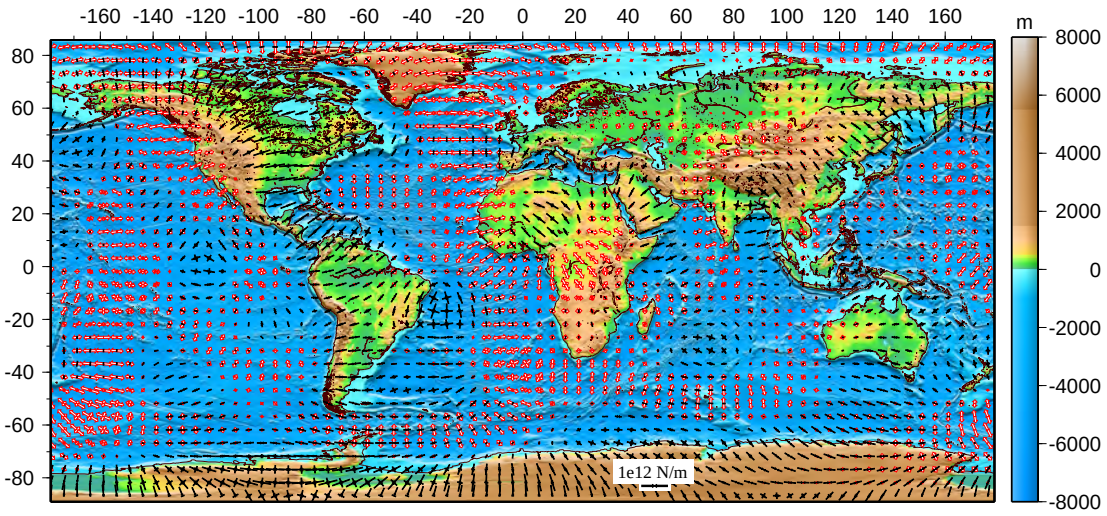

Figure D3: Total depth integral estimate of the deviatoric stress field, obtained from combining both the contributions to deviatoric stresses associated with horizontal (Figure D1) and radial tractions (Figure D2), via the thin sheet method, for an isoviscous case.

resultant deviatoric stresses show that the influence of radial tractions is dominant in most areas, such that there is deviatoric compression over most areas of mantle downwelling and tension above regions of mantle upwelling (Figure D3).

When the combined stress field obtained above is compared to the deviatoric stress field computed directly from the full 3-D convection model (Figure D4), we see a significant match for almost all regions. We compute the ratio of the second invariant of stress tensors for the respective stress fields, T_1/T_2 (Figure D5a), where T is given by $T = \sqrt{\tau_{\phi\phi}^2 + \tau_{\theta\theta}^2 + \tau_{rr}^2 + \tau_{\phi\theta}^2 + \tau_{\theta\phi}^2} = \sqrt{2\tau_{\phi\phi}^2 + 2\tau_{\phi\phi}\tau_{\theta\theta} + 2\tau_{\theta\theta}^2 + 2\tau_{\phi\theta}^2}$, τ_{ij} being the deviatoric stresses. We also calculate correlation coefficients between the two deviatoric stress fields (Figure D5b), given by equation (6) in text. Here, the strain rate tensor is replaced by the second deviatoric stress tensor. The ratio, T_1/T_2, yields a measure of the match in magnitude for the two deviatoric stress fields, whereas the correlation coefficient measures the match in direction and style of the two stress fields. Hence, a value of 1 for both would indicate that the two stress fields are of exactly the same magnitude and style. For the isoviscous case, in most regions the magnitudes are close to exact agreement (Figure D5a) and the styles and directions (Figure D5b) are also close to exact agreement. Most of the differences occur in the crossover areas, where a transition takes place from deviatoric

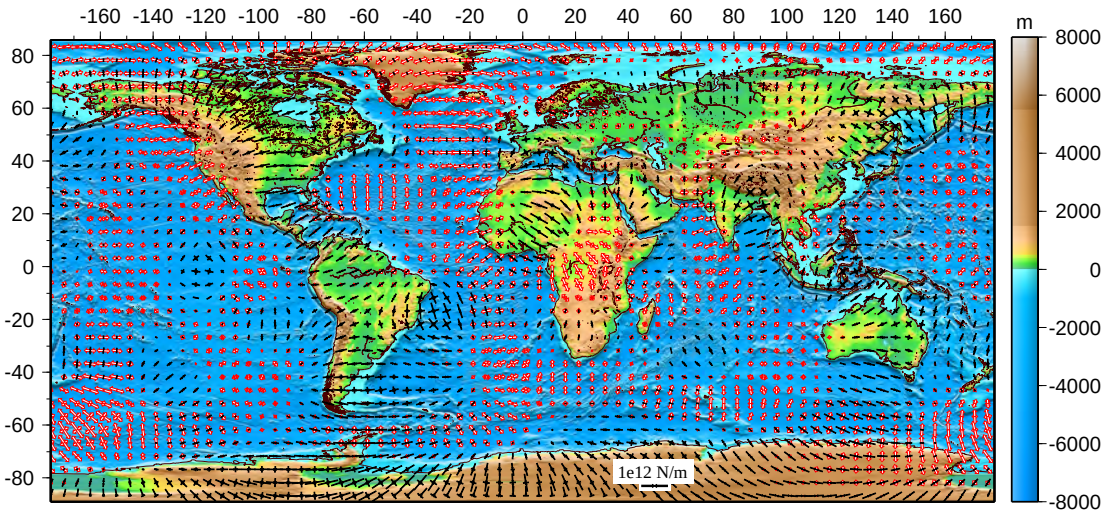

Figure D4: Deviatoric stress field obtained from the full 3-D convection model for an isoviscous case. Note the similarity with Figure D3, which is obtained using the thin sheet approximation .

tension to compression, or vice-versa. The reason is most likely due to the fact that two large stress fields - one from radial tractions (Figure D2), and the other from horizontal tractions (Figure D1) - nearly cancel each other, yielding a much smaller total deviatoric stress field (Figure D3). In the crossover areas, where the stresses are even smaller, this cancellation has to be exact. The tractions generated from the convection model are averaged and mapped onto the 2.5×2.5 degree grid of the thin sheet model in order to calculate the deviatoric stresses via the thin sheet method. A slight error in averaging could cause misfits between the two stress fields (Figure D5a,b), particularly in the crossover regions. Moreover, the deviatoric stress field computed via the thin sheet method is the vertically integrated horizontal stress field, whereas for the 3-D convection model we have only output the horizontal deviatoric stress field close to the surface of the lithosphere. This could account for additional differences. In summary, we have shown that the thin sheet approximation method that we use has done a remarkably good job of recovering the stress field from a full 3-D, degree 12 convection model with an isoviscous structure.

We next test a lid model for the compatibility between the thin sheet and convection methods. The deviatoric stress field calculated via the thin sheet method (Figure D6) from horizontal tractions shows expected style of stresses: compression over areas of convergence and tension over areas of divergence. Deviatoric stresses computed from radial trac-

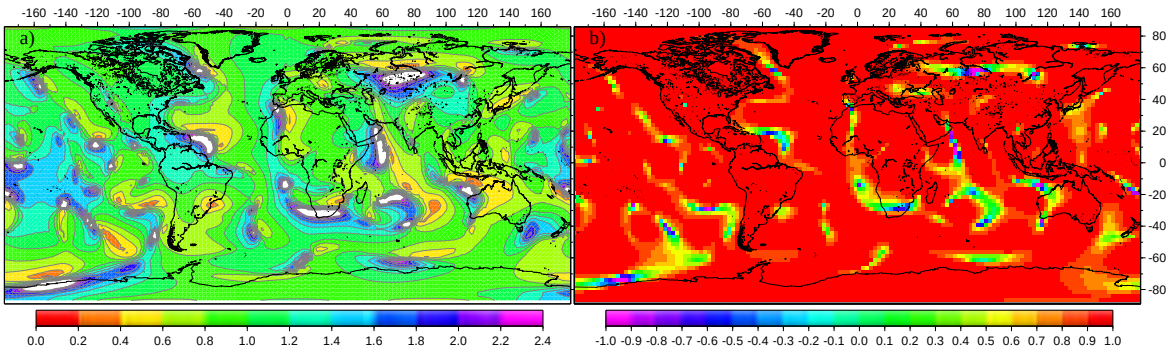

Figure D5: a) Contour map of ratio, T_1/T_2, between the two deviatoric stress fields for the isoviscous model. T_1 is the second invariant of deviatoric stress field predicted by the thin sheet model (Figure D3), whereas T_2 is the second invariant of deviatoric stress field output by the 3-D convection model (Figure D4). White areas indicate that values are out of range (greater than 2.4). These areas normally correspond to the crossover areas, mentioned in text, where the deviatoric stresses are switching from tension to compression, and vice-versa. b) Correlation coefficients between the two deviatoric stress fields for the isoviscous model.

tions (Figure D7) act in the same direction as stresses from horizontal tractions. The combined stress field (Figure D8) from the two components, when compared to the deviatoric stress field from a full 3-D convection model (Figure D9), shows a nearly exact match. The quantitative comparison between the two stress fields (Figure D10a,b) shows only minor differences in magnitude and style in a few regions.

What we demonstrate in this section is the ability of the thin sheet model to reproduce the same stresses as predicted by a full 3-D convection model. This has important implications regarding the validity of the thin sheet method that we use.

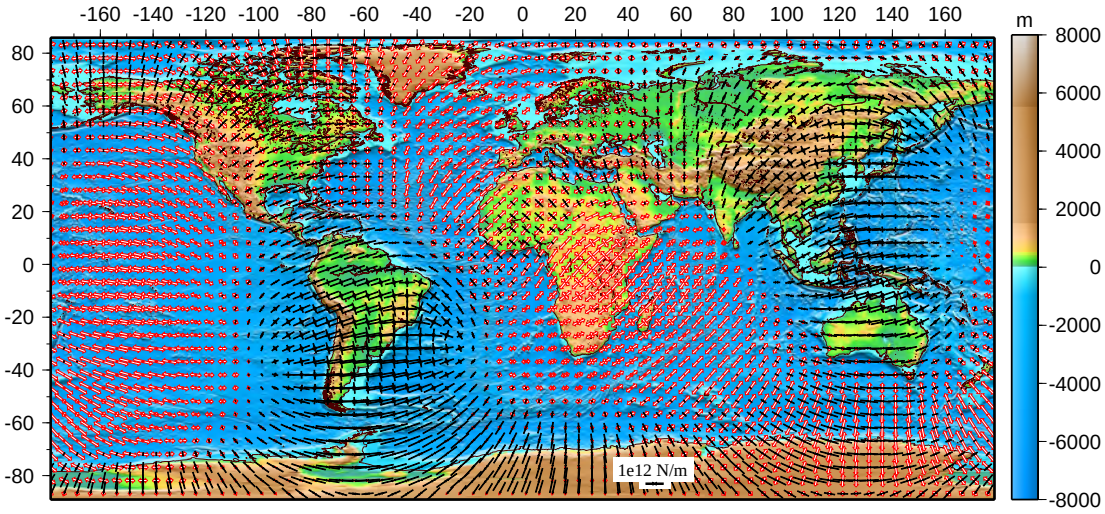

Figure D6: Vertically integrated deviatoric stresses, calculated using the thin sheet method, associated with basal tractions. The basal tractions are generated by a 3-D convection model with a higher viscosity lid. Note that in contrast to the isoviscous case (Figure D1) the tractions from the lid model yield a pattern opposite to the isoviscous case - compression over downwellings and extension over upwellings.

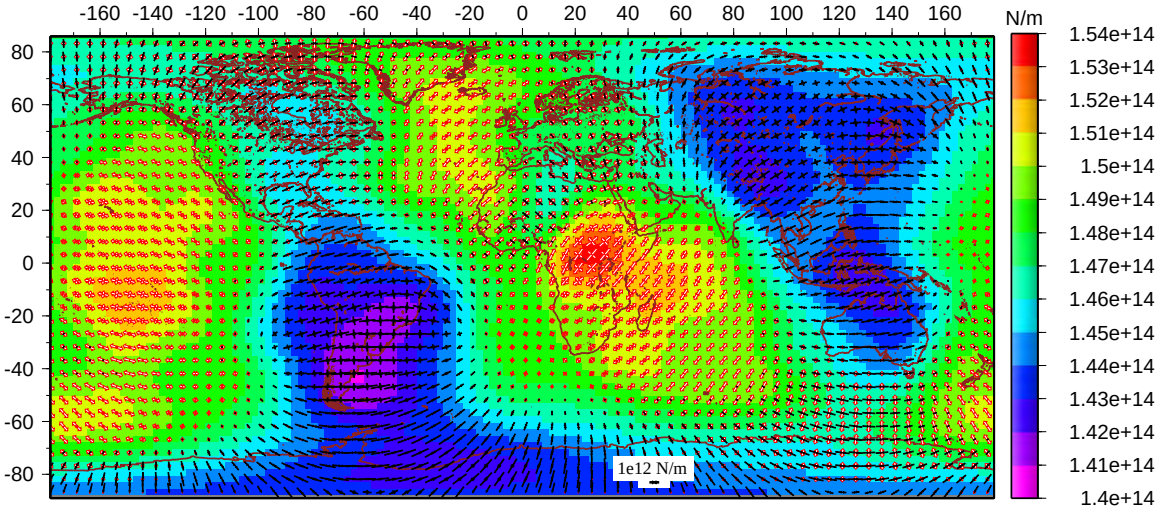

Figure D7: Vertically integrated deviatoric stresses, calculated via the thin sheet method associated with lateral variations in the depth integral of radial stress, σ_{rr} (or GPE). The lateral variations in GPE are associated with dynamic topography produced by radial tractions in a full 3-D mantle circulation model with a high viscosity lid (same as Figure D6). Note the similarity with isoviscous case (Figure D2).

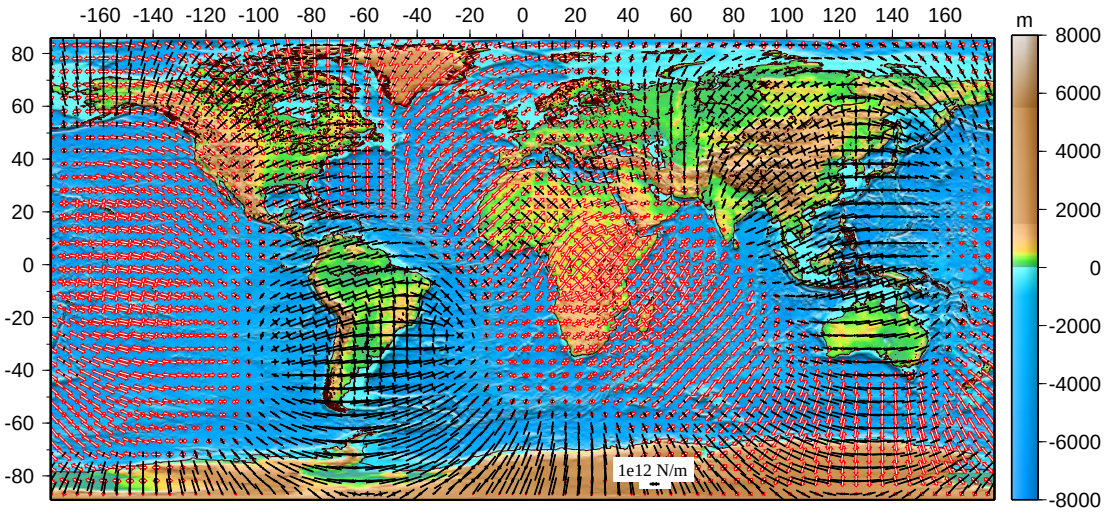

Figure D8: Total depth integral of horizontal deviatoric stresses produced by adding solutions in Figures D6 and D7.

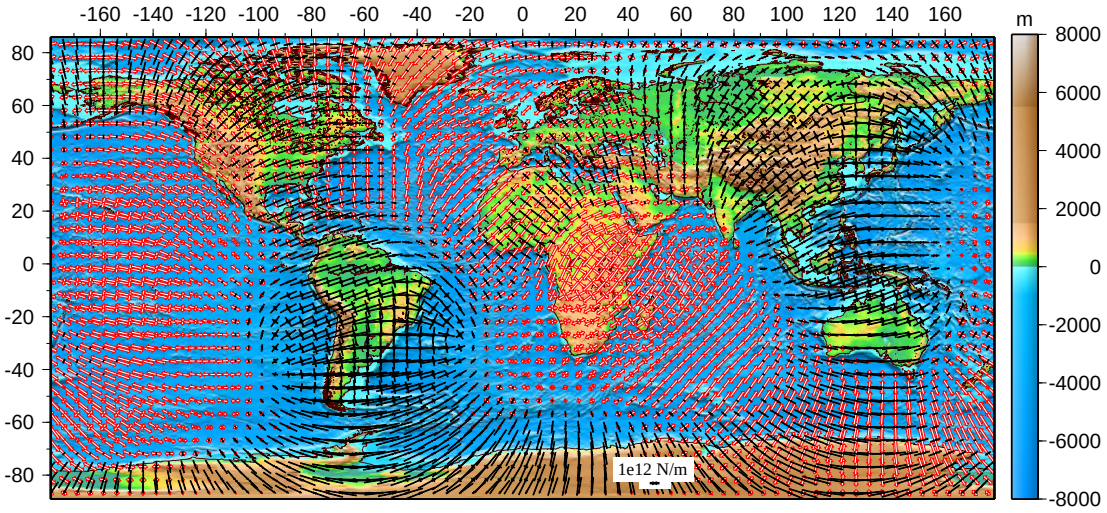

Figure D9: Horizontal deviatoric stress field obtained from the full 3-D convection model for the lid case. Note the similarity with calculations in Figure D8, obtained using the thin sheet approximation.

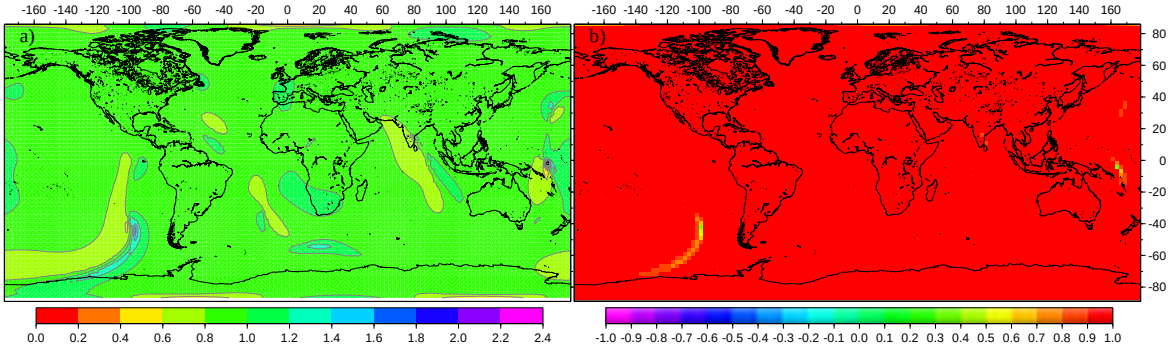

Figure D10: a) Contour map of ratio, T_1/T_2, between the two deviatoric stress fields for the lid model. T_1 is the second invariant of deviatoric stress field predicted by the thin sheet model (Figure D8), whereas T_2 is the second invariant of deviatoric stress field output by the 3-D convection model (Figure D9). b) Correlation coefficients between the two deviatoric stress fields for the lid model.

Chapter 5

Predicting the Lithospheric Stress Field and Plate Motions by Joint Modeling of Lithosphere and Mantle Dynamics

Predicting the lithospheric stress field and plate motions by joint modeling of lithosphere and mantle dynamics

Abstract

The way in which basal tractions, associated with density buoyancy-driven mantle convection, affect lithospheric deformation is a fundamental problem in geodynamics. The goal of the present study is to achieve a best-fit lithosphere-mantle coupling model for the Earth. That is, we seek to estimate a model with appropriate radial and lateral viscosity variations that would successfully predict not only plate motions, but also deformation indicators along the Earth's plate boundaries. The convection model used is a whole mantle model driven by density buoyancies within the mantle with free slip boundary conditions at the surface and at the core-mantle boundary. We test viscosity structures by incorporating lateral viscosity variations in the lithosphere, as well as by varying the thickness and viscosity of the asthenosphere layer. We introduce lateral viscosity variations generated by major geological features of the Earth, such as the continent-ocean divide, the presence of cratonic roots, and age differences in the oceanic lithosphere. For each structure, we predict the deviatoric stress field, the pattern of poloidal and toroidal flow, and the toroidal/poloidal partitioning ratio. The deviatoric stresses are computed for the entire lithosphere using the thinsheet method, with laterally variable effective viscosity. The tractions from the 3-D convection model are output at 100 km depth and applied to the base of the thinsheet as a boundary condition. The predicted deviatoric stress field, associated with these tractions, is added to the deviatoric stresses generated by lateral variations in the depth integral of radial stress (lateral variations in gravitational potential energy per unit area or GPE), calculated based on the Crust 2.0 dataset. The combined, depth integrated deviatoric stress field is compared with velocity gradient tensor field along the Earth's deforming plate boundary zones from the Global Strain Rate Map (GSRM), as well as with earthquake moment tensor data. The best-fit model has to satisfy both the constraints of matching the plate motions and the deviatoric stress field simultaneously. We find that models, dominated by strong viscosity contrasts between the oceanic and continental lithosphere, and a weak (low vis-

cosity) asthenosphere, are able to match plate motions, the observed toroidal/poloidal ratio, and the strain rate tensor data from GSRM.

5.1 Introduction

The plate-mantle coupling problem has been one of the central problems in present-day geodynamics. It refers to the way deeper, density buoyancy-driven basal tractions affect lithospheric deformation. This coupling problem has implications on the age-old questions of what drives the Earth's tectonic plates; what role does mantle convection play and what is the nature of coupling between plates and deep mantle flow? Many studies have attempted to model plate tectonics (through the torque balance method or through calculating the lithospheric stress field) as a mere lithospheric process, independent of active deeper density buoyancy-driven convective flow in the mantle (*Solomon et al.*, 1975; *Richardson et al.*, 1979; *Sandiford and Coblentz*, 1994). On the other hand, various other studies have considered mantle convection and plate tectonics as a single system in order to explain the plate tectonic phenomenon (*Zhong and Gurnis*, 1996; *Bercovici*, 1995, 1998; *Tackley*, 1998, 2000; *Trompert and Hansen*, 1998) or to explain observables such as the geoid, dynamic topography, and plate motions (*Hager*, 1984; *Hager et al.*, 1985; *Richards and Hager*, 1984; *Gable et al.*, 1991; *Forte et al.*, 1993; *Wen and Anderson*, 1997b; *Becker and O'Connell*, 2001). However, the problem with directly relating mantle convection with plate tectonics is that the latter is not strictly a fluid dynamical process, as evident from the existence of nearly rigid plates. In this paper, we seek to address the role and nature of lithosphere-mantle coupling by performing a joint modeling of lithosphere dynamics and mantle convection. The two most important observations that are sensitive to the nature of plate-mantle coupling are the lithospheric deviatoric stress field and plate motions. If the initial coupling model is correct, the predicted deviatoric stress tensor field will match deformation indicators, and the predicted plate motions will also match the observed plate motions. However, use of either one of these constraints, by itself, leads to non-unique inferences about the plate-mantle coupling system. That is, a particular coupling model may satisfy one constraint but not the other. Hence, both of these constraints are necessary

to delineate a coupling model for the Earth.

The prediction of the Earth's lithospheric stress field, as well as its plate motions, is largely influenced by the distribution of density buoyancies as well as radial and lateral variation of viscosities in the lithosphere and the mantle. In the past, there have been studies that investigated this lithosphere-mantle coupling problem (*Bai et al.*, 1992; *Bird*, 1998; *Steinberger et al.*, 2001; *Lithgow-Bertelloni and Guynn*, 2004; *Ghosh et al.*, 2008) by jointly modeling lithosphere and mantle dynamics and predicting the lithospheric stress field. *Bai et al.* (1992) were the first to perform such a joint modeling. They used the intraplate stress field to evaluate their models. However, they failed to achieve a good correlation between their predicted stresses and observed stress directions. *Bird* (1998) utilized a thin sheet method with faults at plate boundaries and temperature dependent viscous rheology in his approach to model the lithospheric stress field. He concluded that basal driving tractions were necessary to match the observed stress field. *Steinberger et al.* (2001) computed the global stress field from mantle convection based on global seismic tomography and added it to the contribution from intra-lithospheric sources. They, on the other hand, found that predicted stress directions with or without mantle flow matched stress observations equally well. They also predicted plate motions in addition to predicting the intraplate stress field. *Lithgow-Bertelloni and Guynn* (2004) performed a joint modeling of lithospheric and mantle sources of stress and explored the effects of radial changes in viscosity in the mantle. Like *Bird* (1998), they too argued for importance of basal tractions and concluded that the stress field is significantly affected by lateral viscosity variations that leads to varying degrees of coupling between the lithosphere and the mantle. *Ghosh et al.* (2008) performed similar joint modeling using a thin sheet approach to model the stress field from lithosphere and mantle buoyancies. They found that stresses from basal tractions, arising due to density buoyancy-driven mantle convection, when added to stresses from intra-lithospheric sources, yield a better fit to deformation indicators along the Earth's plate boundary zones. They also tested the sensitivity of different radially variable viscosity structures and argued for strong lithosphere-asthenosphere viscosity contrasts. Excluding the first and last-mentioned study, all the other studies used the World Stress Map (WSM) (*Zoback*, 1992; *Reinecker et al.*, 2005) to constrain their modeled lithospheric stress field.

Ghosh et al. (2008), on the other hand, used the velocity gradient tensor field along the deforming plate boundary zones from the Global Strain Rate Map (GSRM) (*Kreemer et al.*, 2003) to constrain their predicted stresses. None of the above studies, however, looked at the specific nature of coupling between the lithosphere and the mantle. That is, whether lateral variation in lithosphere and asthenosphere viscosity is important in influencing the lithospheric stress field. In order to investigate this problem, lateral viscosity variations in the lithosphere and/or asthenosphere are required to be incorporated in models of mantle convection. The addition of lateral variation of viscosity also enables one to adequately predict plate motions. Lateral variation in lithosphere and asthenosphere viscosity will also profoundly influence the mantle flow, plate coupling, and the lithospheric stress field. It is thus important to satisfy both the deformation constraint and the plate motion constraint in order to delineate the best plate-mantle coupling model.

In this study we compute the lithospheric stress field from sources within the lithosphere and from a full 3-D mantle flow field, driven by density buoyancies within the mantle, that includes both poloidal and toroidal components. The poloidal component is associated with upwelling (divergence) in mid-oceanic ridges and downwelling (convergence) in subduction zones, whereas the toroidal component is related to strike-slip faulting along transform fault boundaries. We generate plate motions self-consistently from our convection models, instead of placing them as a priori boundary conditions. The combination of predicting lithospheric stress field and plate motions enables us to investigate the nature of plate-mantle coupling. Another important contribution of the present study is the matching of the relative toroidal and poloidal flow magnitudes. Matching the toroidal/poloidal velocity ratio has proved to be a difficult problem in studies of mantle convection (discussed in section 4.2). In this study, we not only match the direction of plate velocities, but also their relative magnitudes via the computation of the toroidal/poloidal velocity ratio. A very important consequence of using all the three constraints of lithospheric stress field, plate motions and the toroidal/poloidal velocity ratio is the elimination of a wide range of viscosity models that fail to satisfy these constraints simultaneously. As mentioned before, these constraints, individually, are non-unique. However, when considered simultaneously, these constraints are able to narrow down a range of viscosity models that can explain observa-

tions. Another aspect of our study is the usage of velocity gradient tensor field from GSRM as well as earthquake moment tensor data for observations to be fitted by our depth integrals of deviatoric stress. A qualitative matching of our predicted stresses with the stresses from the WSM provides a further constraint, in addition to the quantitative matching with the strain rate tensor information in GSRM and the moment tensor data.

5.2 Method

On a longer timescale, plates behave as viscous bodies and flow horizontally under their own weight. *Frank* (1972) drew the analogy of the Earth's lithospheric motion to the flow in glaciers. Lateral density variations within the lithosphere, along with varying crustal thickness and topography, give rise to gravitational potential energy per unit area (GPE) differences. A higher elevation column of lithosphere stores more GPE than a lower elevation column of the same density. The horizontal gradients in GPE produce deviatoric stresses that give rise to horizontal flow from points of high GPE to points of low GPE. Effects of these density variations within the lithosphere have been studied by *Artyushkov* (1973); *Fleitout and Froidevoux* (1982, 1983); *Fleitout* (1991); *Richardson* (1992); *Coblentz et al.* (1994). On the other hand, mantle convection can be envisaged as a fluid dynamical process whereby the flow is driven by sources of buoyancy deep into the mantle (mostly subducting slabs). These buoyancy sources stir the mantle and set up convective flow that gives rise to basal tractions, which, acting at the base of the lithosphere, contribute to the lithospheric stress field.

5.2.1 Thin Sheet Approximation for Estimating Depth Integrals of Deviatoric Stress

We use the thin sheet approximation to solve for the stresses associated with density heterogeneities both within and below the lithosphere. The force balance equations, in spherical coordinates, are given as:

$$\frac{1}{\cos\theta}\frac{\partial}{\partial\phi}\left(r^2\sigma_{\phi\phi}\right)+\frac{1}{\cos^2\theta}\frac{\partial}{\partial\theta}\left(r^2\sigma_{\phi\theta}\cos^2\theta\right)+\frac{\partial}{\partial r}\left(r^3\sigma_{\phi r}\right)=0 \qquad (1)$$

$$\frac{1}{\cos\theta}\frac{\partial}{\partial\phi}\left(r^2\sigma_{\phi\theta}\right)+\frac{1}{2}\frac{\partial}{\partial\theta}\left(r^2\left[\sigma_{\theta\theta}+\sigma_{\phi\phi}\right]\right)+\frac{1}{2\cos^2\theta}\frac{\partial}{\partial\theta}\left(r^2\cos^2\theta\left[\sigma_{\theta\theta}-\sigma_{\phi\phi}\right]\right)+\frac{\partial}{\partial r}\left(r^3\sigma_{\theta r}\right)=0 \quad (2)$$

$$\frac{1}{r\cos\theta}\frac{\partial\sigma_{\phi r}}{\partial\phi}+\frac{1}{r\cos\theta}\frac{\partial}{\partial\theta}\left(\cos\theta\sigma_{\theta r}\right)+\frac{1}{r}\left(2\sigma_{rr}-\sigma_{\phi\phi}-\sigma_{\theta\theta}\right)+\frac{\partial\sigma_{rr}}{\partial r}-\rho g=0 \quad (3)$$

(*Ghosh et al.*, 2008), where r is the radius of the Earth, ρ is the density, g is the gravitational acceleration, σ_{ij} are the total stresses, θ is the latitude and ϕ, the longitude. Vertically integrating (1) and (2) and substituting the total stress tensor, σ_{ij}, by the deviatoric stress tensor, τ_{ij}, via $\sigma_{ij}=\tau_{ij}+\frac{1}{3}\sigma_{kk}\delta_{ij}$, we arrive at

$$\frac{1}{\cos\theta}\frac{\partial}{\partial\phi}\left(\int_{r_L}^{r_0}r^2\tau_{\phi\phi}dr\right)-\frac{1}{\cos\theta}\frac{\partial}{\partial\phi}\left(\int_{r_L}^{r_0}r^2\tau_{rr}dr\right)+\frac{1}{\cos^2\theta}\frac{\partial}{\partial\theta}\left(\cos^2\theta\int_{r_L}^{r_0}r^2\tau_{\phi\theta}dr\right)$$

$$=-\frac{1}{\cos\theta}\frac{\partial}{\partial\phi}\left(\int_{r_L}^{r_0}r^2\sigma_{rr}dr\right)-r_0^3\tau_{\phi r}(r_0)+r_L^3\tau_{\phi r}(r_L) \quad (4)$$

and

$$\frac{1}{\cos\theta}\frac{\partial}{\partial\phi}\left(\int_{r_L}^{r_0}r^2\tau_{\phi\theta}dr\right)+\frac{1}{2}\frac{\partial}{\partial\theta}\left(\int_{r_L}^{r_0}r^2\tau_{\theta\theta}dr+\int_{r_L}^{r_0}r^2\tau_{\phi\phi}dr\right)+\frac{\partial}{\partial\theta}\left(\int_{r_L}^{r_0}r^2\tau_{rr}dr\right)$$

$$+\frac{1}{2\cos^2\theta}\frac{\partial}{\partial\theta}\left(\cos^2\theta\left[\int_{r_L}^{r_0}r^2\tau_{\theta\theta}dr-\int_{r_L}^{r_0}r^2\tau_{\phi\phi}dr\right]\right)=-\frac{\partial}{\partial\theta}\left(\int_{r_L}^{r_0}r^2\sigma_{rr}dr\right)-r_0^3\tau_{\theta r}(r_0)+r_L^3\tau_{\theta r}(r_L) \quad (5)$$

Here, r_0 is the radius from the centre of the Earth to the surface, r_L is the radius from the centre to a constant reference level, and δ_{ij} is the Kronecker delta. Because horizontal tractions at the surface are zero, the last integral yields the horizontal tractions acting at the reference level, r_L, $r_L^3\tau_{\phi r}(r_L)$ and $r_L^3\tau_{\theta r}(r_L)$. Density buoyancy driven mantle convection plays a fundamental role in generating these tractions. As long as the depth integral of horizontal tractions is small in comparison with the depth integrals of horizontal deviatoric stress, it is appropriate to use the thin sheet approach. The first two terms on the right hand side of equations (4) and (5) represent horizontal gradients in the depth integrals of vertical stress, or GPE, while the second two terms are depth integrals of horizontal tractions acting within the lithosphere. As such, the positive gradients in GPE and the negative of the tractions constitute body-force-like terms, and are constrained by observations: GPE by gravity and seismically defined crustal thickness dataset (Crust 2.0), and tractions by a self-consistent circulation model (*Wen and Anderson*, 1997a; *Ghosh et al.*, 2008) that match

plate motions and geoid.

For a thin sheet, the gradients of $\sigma_{\phi r}$ and $\sigma_{\theta r}$ are negligibly small as is the term $\frac{1}{r}(2\sigma_{rr} - \sigma_{\phi\phi} - \sigma_{\theta\theta})$ compared to ρg. Hence, (3) can be approximated as

$$\sigma_{rr} = -\int_r^{r_0} \rho g dr, \tag{6}$$

so that the GPE equation is given by

$$\int_{r_L}^{r_0} r^2 \sigma_{rr} dr = -\int_{r_L}^{r_0} r^2 \left[\int_r^{r_0} \rho g dr'\right] dr = -\int_{r_L}^{r_0} \rho g \left[\int_{r_L}^{r'} r^2 dr\right] dr' = -\int_{r_L}^{r_0} \frac{1}{3}\rho g\left(r'^3 - r_L^3\right) dr' \tag{7}$$

based on a reference level at depth r_L. We take r_L to be 100 km below sea-level, coinciding with a generalized base of lithosphere. In the estimation of lithosphere GPE we do not take into account deeper lithospheric buoyancies arising from cratonic roots; instead, they are considered part of the convection problem. In order to consider these deeper lithospheric buoyancies in the lithospheric calculation of GPE, a variable base lithosphere needs to be accounted for, which involves sophisticated methods that are beyond the scope of this paper. In oceans, r_0 constitutes sea-level and hence is constant, whereas it varies in continents in accordance with varying topography. Given the GPE differences, solutions to (4) and (5) can be obtained with $\tau_{\phi r}$ and $\tau_{\theta r}$ set to zero. Alternatively, given the basal tractions, gradients in GPE (equation (7)) can be set to zero in order to compute the stress response from basal tractions. The two contributions from each set of forcings can simply be added to obtain the total lithospheric stress field. We use a finite element technique (*Flesch et al.*, 2001) on a global grid of $2.5^o \times 2.5^o$ such that the deviatoric stress field solution provides a global minimum in the second invariant of deviatoric stress, taking into account rheological variations due to strong plates and weak plate boundaries. Based on the strain rates from GSRM, the plate boundaries are assigned variable viscosities using the method of *Ghosh et al.* (2008),

$$\frac{1}{\mu} = 1 + \left(\frac{1}{\mu_{ref}} - 1\right)\sqrt{\frac{E^2}{E_{ref}^2}}, \tag{8}$$

where $E^2 = 2(\dot{\varepsilon}_{\theta\theta}^2 + \dot{\varepsilon}_{\phi\phi}^2 + \dot{\varepsilon}_{\phi\theta}^2 + \dot{\varepsilon}_{\phi\phi}\dot{\varepsilon}_{\theta\theta})$, and $\dot{\varepsilon}_{\theta\theta}, \dot{\varepsilon}_{\phi\phi}$ and $\dot{\varepsilon}_{\phi\theta}$ are the strain rates from *Kreemer et al.* (2003). A reference viscosity is assigned to a moderately straining region in

western North America (straining at a rate of 1.5×10^{-7}/yr) having an effective viscosity ~ 30 times lower than the non-deforming intraplate regions. E^2_{ref} is the reference value for E^2 corresponding to the value for μ_{ref}.

The GPE in equation (7) is calculated from the crustal thickness and density dataset in Crust 2.0 [*G. Laske et al.*, Crust 2.0: A new global crustal model at 2 $\times$ 2 degrees, 2002, available at http://mahi.ucsd.edu/Gabi/rem.html]; the densities in the oceanic lithosphere are defined by the cooling plate model based on ocean floor age data (*Müller et al.*, 1997) with revised parameters from *Stein and Stein* (1992).

5.2.2 Mantle Convection Treatment

The basal tractions are obtained from a convection model using the methodology of *Wen and Anderson* (1997b), assuming an incompressible Newtonian viscous fluid with zero Reynold's number. The governing equations are the equation of continuity,

$$\nabla \cdot U = 0, \tag{9}$$

U being the surface velocity, the equation of motion,

$$\nabla \cdot \tau + \delta\rho g = 0, \tag{10}$$

and the constitutive equation between stress and strain rate,

$$\tau = -p + 2\eta\varepsilon. \tag{11}$$

Here τ is the stress tensor, $\delta\rho$ the density anomaly, g the acceleration due to gravity, p the pressure, η the viscosity and ε the strain rate tensor. The variables are expanded in terms of spherical harmonics. For a radially symmetric viscosity structure, poloidal-poloidal, poloidal-toroidal, and toroidal-toroidal equations are decoupled at every spherical harmonic degree and order (*Kaula*, 1975; *Hager and O'Connell*, 1981). For a laterally variable viscosity structure, poloidal and toroidal equations are coupled at each degree and order. If the coefficients are truncated at a certain spherical harmonic degree, the above equations can be reduced to a set of linear equations and can be solved in 3 dimensions

using a semi-spectral iterative method (*Karpychev and Fleitout*, 1996). The boundary conditions are free-slip at the surface and at CMB. Our mantle convection models include both radial and lateral variations of viscosity, with the lower mantle being 10 times more viscous than the upper mantle. The density anomalies in the upper mantle are inferred by adjusting the relative weights of density anomalies related to subducting slabs and residual tomography (*Wen and Anderson*, 1997a) on the basis of fitting the geoid. The density structure in the lower mantle was derived from a seismic tomographic model (*Su et al.*, 1994). With latitude θ as positive north latitude, the basal tractions can be given as:

$$r_L(\tau_{\phi r})/\eta_0 = Z_4^{lm}\frac{1}{\cos\theta}\frac{\partial}{\partial\phi}Y_{lm}(\theta,\phi) + Z_6^{lm}\frac{\partial}{\partial\theta}Y_{lm}(\theta,\phi) \tag{12}$$

$$r_L(\tau_{\theta r})/\eta_0 = Z_4^{lm}\frac{\partial}{\partial\theta}Y_{lm}(\theta,\phi) - Z_6^{lm}\frac{1}{\cos\theta}\frac{\partial}{\partial\phi}Y_{lm}(\theta,\phi) \tag{13}$$

(*Ghosh et al.*, 2008) where η_0 is the reference viscosity, Z_4^{lm} and Z_6^{lm} are the spherical harmonic coefficients for the poloidal and toroidal components of stress, $Y_{lm}(\theta,\phi)$ is the surface normalized spherical harmonic of degree l and order m, whose maximum value is 12 in this study. The horizontal velocities are given by:

$$U_\phi = Z_2^{lm}\frac{1}{cos\theta}\frac{\partial Y_{lm}(\theta,\phi)}{\partial\phi} + Z_5^{lm}\frac{\partial Y_{lm}(\theta,\phi)}{\partial\theta} \tag{14}$$

$$U_\theta = Z_2^{lm}\frac{\partial Y_{lm}(\theta,\phi)}{\partial\theta} - Z_5^{lm}\frac{1}{cos\theta}\frac{\partial Y_{lm}(\theta,\phi)}{\partial\phi} \tag{15}$$

where Z_2 and Z_5 are the poloidal and toroidal components of velocity, expressed as divergence ($\nabla\cdot U$) and vorticity ($\nabla\times U$, U being the velocity). It should be noted that the calculation of the tractions and the deviatoric stresses are derived from two separate models. The convection model, from which the tractions are derived using the methodology of *Wen and Anderson* (1997b), is a degree 12 model that also predicts plate motions and the toroidal and poloidal velocities. Using a solution method described below, the tractions are applied to a constant reference level r_L below a laterally variable lithosphere of much higher resolution (2.5×2.5 degree) to yield estimates of the depth integral of deviatoric stress associated with the tractions.

We experiment with various radially symmetric, as well as laterally variable viscosity

structures (Table 1). Note that the truncation degree is quite low in our study ($l = 12$) and hence, small scale features are missing in our convection model. We are therefore investigating the contribution of long-wavelength components of density buoyancy-driven mantle flow, which generates basal tractions at the reference level r_L, as well as the prediction of long wavelength components of lithosphere motion. The lateral viscosity variations in the lithosphere model, in which the depth integral predictions of deviatoric stress are performed, is of much higher resolution (2.5×2.5 degree). The main goal of the study is to explain the first order features of generating plate motion and lithosphere deviatoric stress by a simple model, and not to match all the detailed features of these, which would require much higher resolution and sophisticated models for both the mantle flow and lithosphere stress predictions.

5.2.3 Solving the Thin Sheet Equations

Our solution provides depth integrals of deviatoric stress that both balance the body force distributions and simultaneously constitute a global minimum of the second invariant of deviatoric stress. This is accomplished through minimization of the following functional (*Flesch et al.*, 2001):

$$I = \int\int \frac{1}{\mu}\left[\bar{\tau}_{\phi\phi}^2 + 2\bar{\tau}_{\phi\theta}^2 + \bar{\tau}_{\theta\theta}^2 + (\bar{\tau}_{\phi\phi} + \bar{\tau}_{\theta\theta})^2\right]\cos\theta d\phi d\theta$$

$$+\int\int\left\{2\lambda_\phi\left[\frac{1}{\cos\theta}\frac{\partial\bar{\tau}_{\phi\phi}}{\partial\phi} + \frac{1}{\cos\theta}\frac{\partial}{\partial\phi}(\bar{\tau}_{\phi\phi}+\bar{\tau}_{\theta\theta}) + \frac{1}{\cos^2\theta}\frac{\partial}{\partial\theta}(\cos^2\theta\bar{\tau}_{\phi\theta}) + \frac{1}{\cos\theta}\frac{\partial\bar{\sigma}_{rr}}{\partial\phi} - r_L^3\sigma_{\phi r}(r_L)\right]\right.$$

$$\left.+2\lambda_\theta\left[\frac{1}{\cos\theta}\frac{\partial\bar{\tau}_{\phi\theta}}{\partial\phi} + \frac{3}{2}\frac{\partial}{\partial\theta}(\bar{\tau}_{\theta\theta}+\bar{\tau}_{\phi\phi}) + \frac{1}{2\cos^2\theta}\frac{\partial}{\partial\theta}(\cos^2\theta[\bar{\tau}_{\theta\theta}-\bar{\tau}_{\phi\phi}]) + \frac{\partial\bar{\sigma}_{rr}}{\partial\theta} - r_L^3\sigma_{\theta r}(r_L)\right]\right\}\cos\theta d\phi d\theta \quad (16)$$

(*Flesch et al.*, 2001; *Ghosh et al.*, 2006, 2008) where $\bar{\tau}_{\phi\phi}$, $\bar{\tau}_{\theta\theta}$ and $\bar{\tau}_{\phi\theta}$ are the vertically integrated deviatoric stresses, $\bar{\sigma}_{rr}$ is the vertically integrated total vertical stress, λ_ϕ, λ_θ represent the horizontal components of the Lagrange multipliers for the force balance equation constraint, and μ is the relative viscosity, which varies laterally in order to take into account weak plate boundaries and strong plates in the lithosphere model (*Ghosh et al.*, 2008). The body force equivalents that go into making up the potentials are distributions of GPE and distributions of the negative of the tractions. Optimizing equation 16 yields a relation be-

tween the deviatoric stresses, $\tau_{\alpha\beta}$, and the Lagrange multipliers, λ_ϕ and λ_θ (*Flesch et al.*, 2001):

$$\bar{\tau}_{\phi\phi} = \mu\left(\frac{1}{\cos\theta}\frac{\partial\lambda_\phi}{\partial\phi} - \lambda_\theta\tan\theta\right), \tag{17}$$

$$\bar{\tau}_{\theta\theta} = \mu\frac{\partial\lambda_\theta}{\partial\theta}, \tag{18}$$

$$\bar{\tau}_{\phi\theta} = \frac{\mu}{2}\left(\frac{\partial\lambda_\phi}{\partial\theta} + \frac{1}{\cos\theta}\frac{\partial\lambda_\theta}{\partial\phi} + \lambda_\phi\tan\theta\right), \tag{19}$$

Note that the relation between τ and the Lagrange multipliers, $\lambda_\phi, \lambda_\theta$, is identical to the relation between strain rate and velocities. Substitution of 17-19 into $\bar{\tau}_{\phi\phi}, \bar{\tau}_{\theta\theta}$ and $\bar{\tau}_{\phi\theta}$ in the following J functional, and then minimization of J with respect to λ_ϕ and λ_θ provides a solution to the force balance equations in (4) and (5), where J is:

$$J = \int\int \left\{ \left[\begin{pmatrix} \bar{\tau}_{\phi\phi} \\ \bar{\tau}_{\theta\theta} \\ \bar{\tau}_{\phi\theta} \end{pmatrix} - \begin{pmatrix} \Phi^{obs}_{\phi\phi} \\ \Phi^{obs}_{\theta\theta} \\ \Phi^{obs}_{\phi\theta} \end{pmatrix} \right]^T \widetilde{V}^{-1} \left[\begin{pmatrix} \bar{\tau}_{\phi\phi} \\ \bar{\tau}_{\theta\theta} \\ \bar{\tau}_{\phi\theta} \end{pmatrix} - \begin{pmatrix} \Phi^{obs}_{\phi\phi} \\ \Phi^{obs}_{\theta\theta} \\ \Phi^{obs}_{\phi\theta} \end{pmatrix} \right] \right\} \cos\theta d\phi d\theta. \tag{20}$$

Here, $\bar{\tau}_{\phi\phi}, \bar{\tau}_{\theta\theta}$ and $\bar{\tau}_{\phi\theta}$ are the depth integrated deviatoric stresses we are solving for, $\Phi^{obs}_{\phi\phi}, \Phi^{obs}_{\theta\theta}$ and $\Phi^{obs}_{\phi\theta}$ are the potentials consisting of horizontal integrals of the body force equivalents and $\widetilde{V}$ is the variance-covariance matrix (see Appendix B in *Ghosh et al.* (2008)). For calculation of the depth integrals of deviatoric stress, we solve equations (4) and (5) , given distributions of GPE, $\frac{1}{\cos\theta}\frac{\partial\bar{\sigma}_{rr}}{\partial\phi}$ and $\frac{\partial\bar{\sigma}_{rr}}{\partial\theta}$, and given distributions of the negative of the tractions, $-r_L^3\sigma_{\phi r}(r_L)$ and $-r_L^3\sigma_{\theta r}(r_L)$, obtained from mantle convection models.

5.2.4 Treatment of the Radial Tractions

The tangential tractions, $\tau_{\phi r}$ and $\tau_{\theta r}$ in equations (12) and (13), arise from the horizontal component of the 3-D convective flow. The vertical component, τ_{rr}, that gives rise to dynamic topography, could potentially play an important role in affecting the total deviatoric stress field. In this section, we will discuss ways of incorporating these radial tractions in our calculation.

There are two ways of dealing with the radial tractions (*Ghosh et al.*, 2008). One way is to calculate them as part of the lithospheric contribution. The other way is to predict

them from the mantle convection models. We will first discuss the method that treats radial tractions as part of the lithospheric contribution. The observed topography is a combination of both static and dynamic parts. The former is generated by shallow density buoyancies within the lithosphere, whereas the latter is produced by deeper density buoyancies within the mantle. Hence, the depth integrals of σ_{rr} for the observed topography, down to a constant reference level (approximated base of the lithosphere), already contain contributions from both static and dynamic parts. In this case, the density variations are obtained from a seismically constrained crust and upper mantle structure that is uncompensated. Although the contribution from dynamic topography is not explicitly known, it is implicitly included in the calculation of the depth integral of σ_{rr}.

The second way is to treat the radial tractions as part of the convection problem. From the dynamic topography predicted by the respective convection models, the GPE differences and the associated deviatoric stress field can be calculated. This stress field is the response of the radial tractions. These stresses can then be added to the stresses obtained from tangential tractions, $\tau_{\phi r}$ and $\tau_{\theta r}$, in order to obtain the total stress field produced by the convection model. This combined stress field is then added to the deviatoric stresses from a compensated (equal pressure at the reference level, r_L) lithosphere model in order to obtain a total lithospheric deviatoric stress field. The lithosphere model must be compensated via elevation adjustment of the crustal columns (removal of dynamic topography) such that after the adjustment, the pressure at the reference level, r_L, is constant. Hence, this method deals with the additional step of compensating the Crust 2.0 model.

Although the second method is a more self-consistent way of treating the radial component of the mantle flow field, there are other problems involved in this methodology. First, the compensation of the crustal model is likely to introduce errors. For complete self-consistency, the dynamic topography predicted by the convection model should be identical to the dynamic topography computed through compensation of the Crust 2.0 model via elevation adjustment. This is difficult to achieve, mainly because of differences in resolution between the convection and the Crust 2.0 models. Moreover, the radial tractions are found to be insensitive to the changes in convection models. That is, while the tangential tractions and the associated deviatoric stresses are very sensitive to the different viscosity structures,

the radial tractions do not vary much, irrespective of the viscosity model used. Hence, in the investigation of a best-fitting viscosity model, incorporation of the radial tractions via the second method does not add a significant constraint. Although we have tried both methods, we prefer the first method, in which the contribution of radial tractions is assumed to be embedded in the total depth integral of σ_{rr}, from surface topography to reference level, r_L. In this paper, therefore, we will only present results that are obtained by using the first method.

5.3 GPE Differences

We calculate the depth integral of σ_{rr} down to a constant reference level, r_L, in order to calculate GPE. Based on these GPE differences, the deviatoric stress field is calculated through optimization of equation (20) (Figure 1). We compare the style and direction of our modeled stresses with strain rate tensor information from GSRM along the Earth's deforming plate boundary zones. A correlation coefficient is defined, whose value lies between -1 and +1. A higher value indicates a better match between our modeled deviatoric stresses and the deformation indicators. The method of this quantitative comparison is explained in detail in *Flesch et al.* (2007) and *Ghosh et al.* (2008). The moment tensor data from Harvard CMT catalogue (1976-2007) is also used as an additional constraint. This dataset is based on more than 13,000 events occurring between 0-30 km depth, and we perform a Kostrov (**?**) moment tensor summation so that comparisons between the seismic strain tensors and the deviatoric strain tensors can be made.

We use the Crust 2.0 dataset to calculate GPE. We take the reference level, r_L, in equation (7) as 100 km below the sea level. A fixed mantle density of $3300 kg/m^3$ is assumed from the crustal base to the depth r_L. We do not take into account density variations due to continental roots below old cratons as part of the lithosphere model; they are instead included as part of the convection model. The cooling plate model based on ocean floor age data (*Müller et al.*, 1997) with revised parameters from *Stein and Stein* (1992) is used to define densities for oceanic regions. The Crust 2.0 model is not compensated (unequal pressure at the reference level r_L), and we assume the depth integrals of of σ_{rr} down to

Figure 1: Global distribution of vertically integrated horizontal deviatoric stresses and GPE (on scalebar) calculated from the uncompensated Crust 2.0 data. Tensional deviatoric stresses are shown by red arrows while compressional deviatoric stresses are shown by black arrows. Length of the arrows are proportional to the magnitude of vertically integrated stresses. Strike-slip regions are indicated by one tensional and one compressional pair of arrows. High GPE areas are in deviatoric tension while low GPE ares are in deviatoric compression.

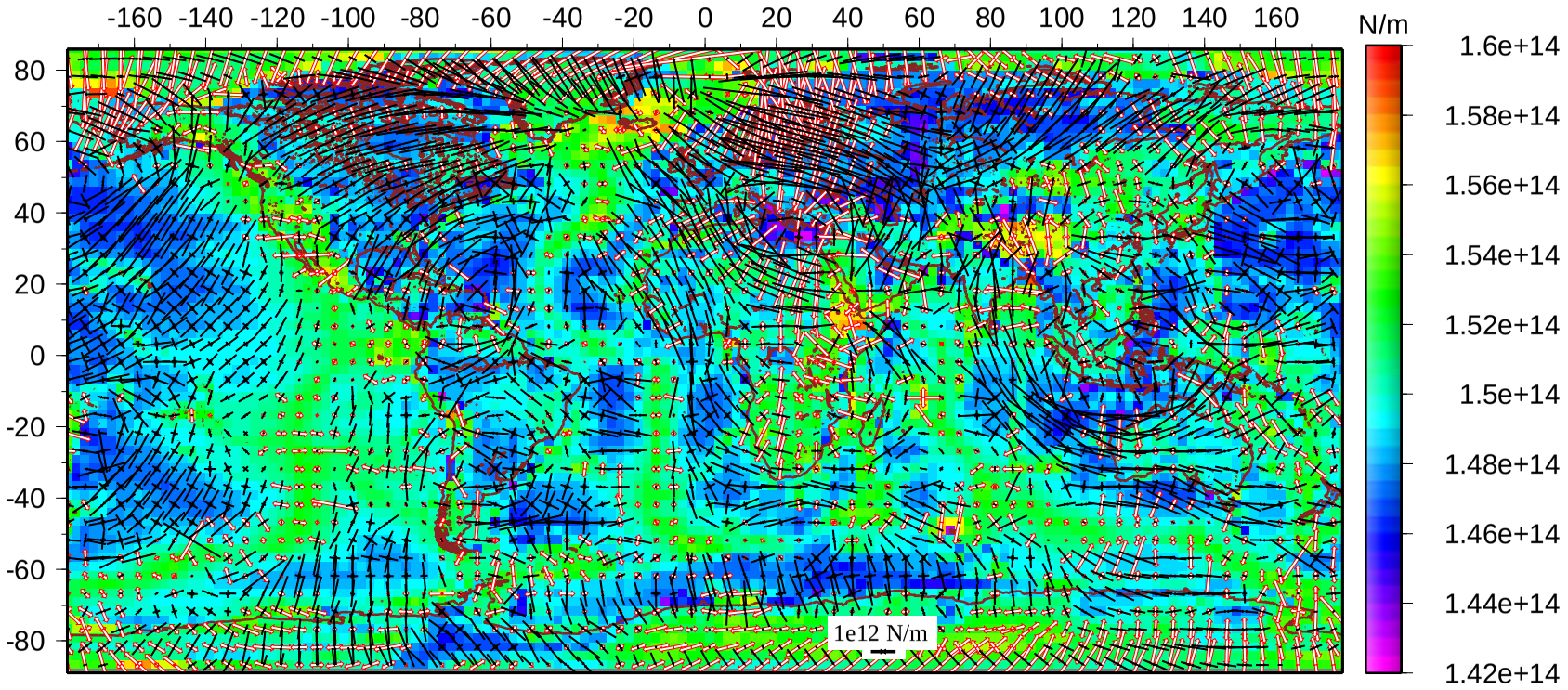
-160 -140 -120 -100 -80 -60 -40 -20 0 20 40 60 80 100 120 140 160
80 60 40 20 0 -20 -40 -60 -80
1e12 N/m
N/m
1.6e+14
1.58e+14
1.56e+14
1.54e+14
1.52e+14
1.5e+14
1.48e+14
1.46e+14
1.44e+14
1.42e+14

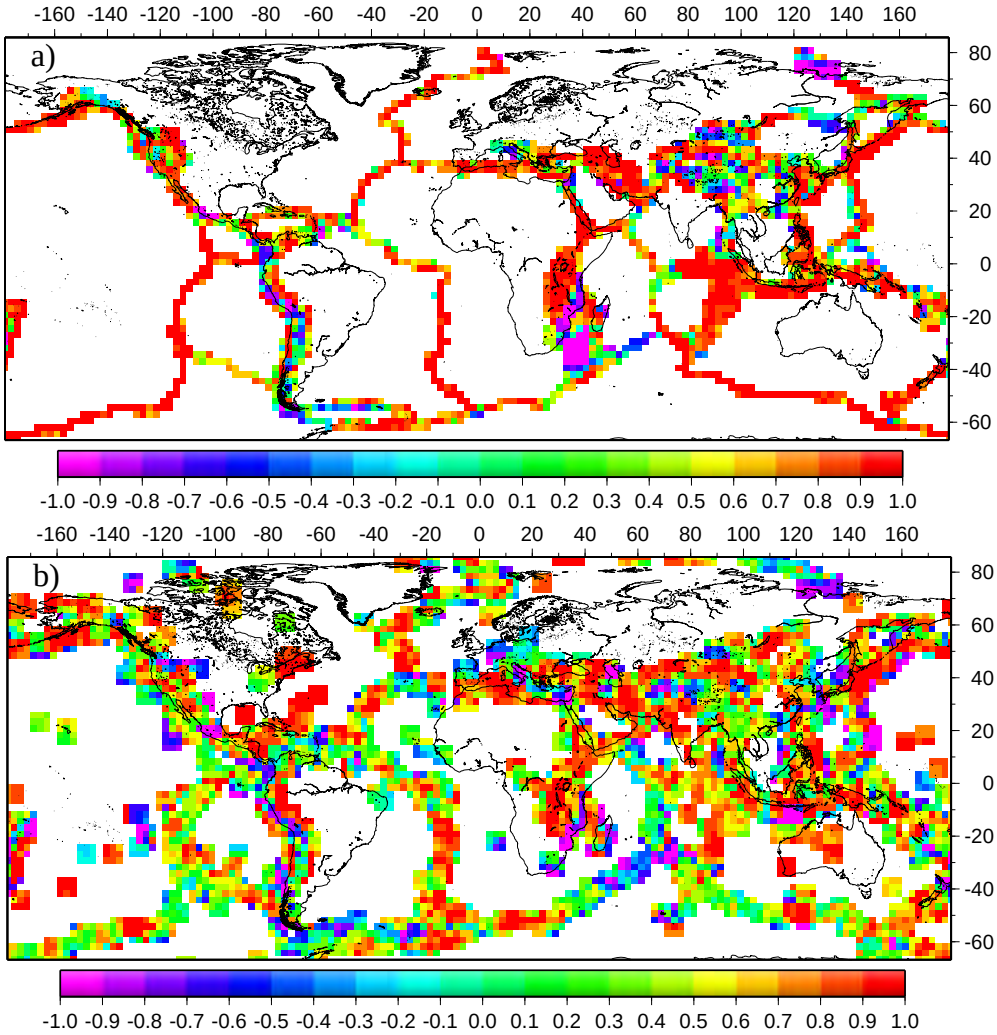

Figure 2: Correlation coefficients between deviatoric stress tensors arising from GPE differences from the Crust 2.0 model and a) observed strain rate tensors from the Global Strain Rate Map and b) moment tensor data from Harvard CMT catalogue.

reference level r_L already contain the contribution from the radial tractions responsible for dynamic topography. The deviatoric stress field from GPE differences shows deviatoric tension in areas such as Andes, western North America, eastern Africa, Tibetan plateau, and the mid-oceanic ridges, whereas older oceanic areas and majority of the continents show low GPE and deviatoric compression (Figure 1). The Tibetan plateau shows large N-S deviatoric tension ($\sim 3 \times 10^{12}$ N/m), associated with large GPE contrasts with the surrounding regions. We will later show that this N-S component of deviatoric tension is cancelled out by a compressive stress associated with basal tractions, generated by large

scale density buoyancy-driven mantle circulation.

The comparison of the deviatoric stress field associated with GPE differences with strain rate tensor data in GSRM shows good fitting in mid-oceanic ridges and a moderate fit in Indo-Australian plate boundary zone and Southeast Asia (Figure 2a, Table 2). However, areas of continental deformation exhibit a poor fit with the deformation indicators. Considering all the areas together, the overall correlation coefficient for the GPE distribution is 0.54. For the moment tensor data, a smoothing kernel is applied to the strain rates, in which smoothing over one grid radius is applied. For this data set, parts of Asia, Australia, as well as Africa show a high correlation (Figure 2b). Comparison with Figure 2a shows that in some areas, the correlation is high for the strain rate data, but poor for the moment tensor data. This is particularly true for some areas of the mid-oceanic ridges. This arises mainly because of the dominance of some big strike-slip type earthquakes at the transform fault boundaries connecting ridge segments, and a relative paucity of moment release in normal fault earthquakes along the ridges themselves. The GSRM tensor field, on the other hand, possesses a dominant signal associated with the spreading process at the mid-oceanic ridges, in agreement with the dominant tension at the mid-oceanic ridges associated with GPE differences (Figure 2a).

5.4 Mantle Buoyancies

5.4.1 Lateral Viscosity Variations

The convection model is based on the model by *Wen and Anderson* (1997b). In a previous paper, we have discussed the sensitivity of different radially symmetric viscosity models in influencing the lithospheric stress field (*Ghosh et al.*, 2008). Since one of the goals of the present paper is to predict plate motions as well, and since lateral viscosity variations are necessary to generate plate motions, we restrict our discussion to models of laterally variable viscosity structures only.

We introduce lateral viscosity variations in our convection model on the basis of the major geological features (Figures 3-6). The continent-ocean divide has already been argued to be a major cause of viscosity differences within the lithosphere by *Wen and Anderson*

(1997b). The cold roots of continental cratons are also thought to be one of the principal causes of lateral viscosity variations in the shallow mantle. These high seismic velocity areas, seen in seismic tomography images, have been attributed to a chemically different composition, having a much higher viscosity than the surrounding mantle at the same depth (*Jordan*, 1978, 1988; *Rudnick and Nyblade*, 1999). Age differences in the oceanic lithosphere can also be a major factor in giving rise to lateral viscosity differences. As the thickness of the oceanic lithosphere varies with age, the mantle close to the ridges can be expected to be weaker than that under old oceans. We consider these first order features to introduce lateral viscosity variations in both the lithosphere and the asthenosphere of the convection models.

The lower mantle is assigned a viscosity 10 times higher than the upper mantle and the lateral changes in viscosity are confined within the top 400 km. The viscosity changes due to the ocean-continent divide, as well as due to strength differences between old and young oceans, are confined within the lithosphere (top 100 km), whereas the viscosity changes arising due to cratonic keels are extended to depths below 100 km. Within each category, we test different lateral viscosity contrasts (from 1 to 100). Finally, these three categories are combined in order to yield mixed viscosity structures.

For each viscosity structure, we generate plate motions and compare them with present-day plate motions. The toroidal/poloidal velocity ratio is also computed and based on the match with the deformation indicators and plate motions, we delineate a range of viscosity models that satisfy both these constraints.

In order to obtain the deviatoric stress field associated with mantle convection, we calculate the tangential tractions for each viscosity model, which are used as a boundary condition at the reference level r_L beneath a lithosphere model of much higher resolution. This deviatoric stress field from tangential tractions is then added to the deviatoric stresses from lateral variations in depth integrals of σ_{rr} in the uncompensated crustal model to obtain the total lithospheric deviatoric stress field. This total deviatoric stress field is then compared with the velocity gradient tensor field from GSRM. Viscosity models yielding a correlation coefficient of 0.65 and above are considered as yielding a good fit to the strain rate tensors. The moment tensor data set is used as an additional constraint.

5.4.2 Generation of Toroidal Flow

As mentioned earlier, the convective flow of the Earth has a toroidal component in addition to a poloidal one, which is responsible for the strike-slip motion along transform fault boundaries. The generation of this toroidal motion is, however, somewhat enigmatic. An incompressible Boussinesq fluid can only give rise to a toroidal flow field in presence of lateral viscosity variations. Moreover, it has been shown by *Hager and O'Connell* (1979) that there occurs an equipartitioning of the Earth's poloidal and toroidal energy at each degree of spherical harmonic expansion. Toroidal flow cannot arise in 2-D models of mantle convection and hence only 3-D models of mantle convection can attempt to generate toroidal flow.

In the past, a number of studies have attempted to generate toroidal motions in 3-D models of mantle convection. *Ricard and Vigny* (1989) created toroidal flow in their cartesian model by imposing plate geometries as well as by determining plate motions through a torque balance method. *Gable et al.* (1991) also generated toroidal motion by imposing a hybrid stress and velocity boundary conditions in their models of spherical geometry. Both the above studies ignored lateral viscosity variations. The first study to generate toroidal flow in a dynamically self-consistent way was by *Christensen and Harder* (1991). However, because of small lateral viscosity variations in their model, they were able to generate only a very small percentage of the observed toroidal velocity. *Ribe* (1992) included lateral viscosity variations in the lithosphere of his thin viscous shell and was able to give rise to a substantial toroidal flow field. *Bercovici* (1995), on the other hand, employed special rheology in order to generate sufficient toroidal flow. *Zhang and Christensen* (1993) used a temperature dependent Newtonian viscosity model, as well as strain-rate dependent non-Newtonian model, to generate toroidal motion in a dynamically self-consistent way. However, they failed to achieve the required toroidal/poloidal partitioning ratio. *Wen and Anderson* (1997b) generated toroidal motion self-consistently in their convection model by taking into account lateral viscosity variations in the lithosphere between continents and oceans. They found that a relative lateral viscosity difference of a factor of 30, along with a weak asthenosphere, were able to generate a flow field that matched the observed

toroidal/poloidal ratio as well as the observed plate motions. They concluded that it was the viscosity difference between oceans and continents, and not that between weak plate boundaries and plates, that controls plate motions. In the following section, we discuss the various types of viscosity structures and we explore which models yield a good match to both the plate motion and deformation indicator data.

5.5 The Viscosity Models

5.5.1 Old oceans

The ocean floor age data of *Müller et al.* (1997) is used to introduce lateral viscosity variations in the lithosphere (Figure 3); oceans older than 70 my are assigned higher viscosities than younger oceans. The thickness and viscosity of the asthenosphere is varied from 100 km to 300 km and from 10^{19} Pa-s to 10^{21} Pa-s. The old oceanic lithosphere is assigned viscosities between 10×10^{21} Pa-s and 25×10^{21} Pa-s (green areas in Figure 3). The white regions in Figure 3 are assigned a constant viscosity of 10^{21} Pa-s. For this category of models, all the viscosity structures tested yield a very poor match to the plate motions, especially because of their inability to generate sufficient toroidal motion. The predicted deviatoric stresses also fail to match the deformation indicators. That is, the global correlation coefficient between the predicted combined deviatoric stress tensors and the strain rate tensors from GSRM is much lower than 0.65 for all models tested.

5.5.2 Continental Keels

We use the keel model of *Wen and Anderson* (1997a) (henceforth called as keel model A, Figure 4a) and a modified lithosphere thickness model from *Conrad and Lithgow-Bertelloni* (2006) (henceforth called as keel model B, Figure 4b) to introduce strong keels within the continents. The lithosphere thickness model of *Conrad and Lithgow-Bertelloni* (2006) shows very thick lithosphere below the Tibetan plateau, which is likely to be an artifact of the seismic model used (*Gung et al.*, 2003) to calculate the lithosphere thickness and is absent in local tomographic studies of the area (*Huang and Zhao*, 2006). We have, therefore, removed the cratonic root beneath Tibet and have assigned a normal thickness

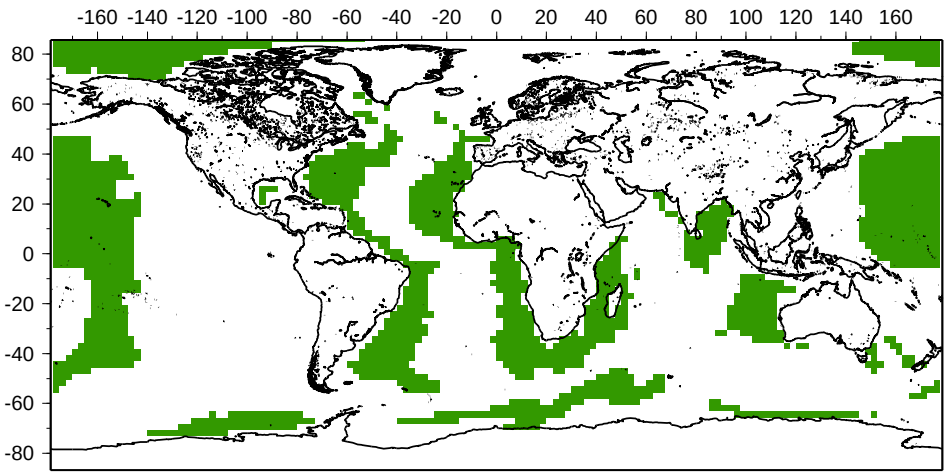

Figure 3: Distribution of old ocean floors. The green areas are more than 70 my old (*Müller et al.*, 1997) and are assigned higher viscosities. The white regions are assigned a constant viscosity of 10^{21} Pa-s.

(100 km) to the lithosphere there (Figure 4b). We vary the viscosity of the keels from 10^{21} Pa-s to 10^{23} Pa-s. Hence, in Figure 4a, the cratonic areas (blue) are assigned higher viscosities compared to the rest of the Earth (white areas in map), which are given a constant viscosity of 10^{21} Pa-s. In Figure 4b, the areas with thickness greater than 150 km are assigned higher viscosities compared to the rest of the areas. We test models where the keels are just confined to the top 100 km of the lithosphere, as well as models in which the keels extend to deeper depths (between 200-400 km depth). That is, we introduce lateral viscosity variations in both the lithosphere and within asthenosphere equivalent depths. The asthenosphere viscosity is varied from 10^{19} Pa-s to 10^{21} Pa-s and its thickness from 100 km to 300 km.

When the keels are confined to the lithosphere, they fail to match both the deformation indicators and the plate motion data. Some of the viscosity structures where the keels extend below 100 km do a moderate job of of fitting plate motions. However, when the deviatoric stresses from these models are compared to the deformation indicators, they fail, yielding correlations with GSRM of far less than 0.65. Therefore, none of the keel models described are able to match the constraints of lithospheric stress field and plate motions simultaneously. The results for both the keel models A and B are found to be very similar.

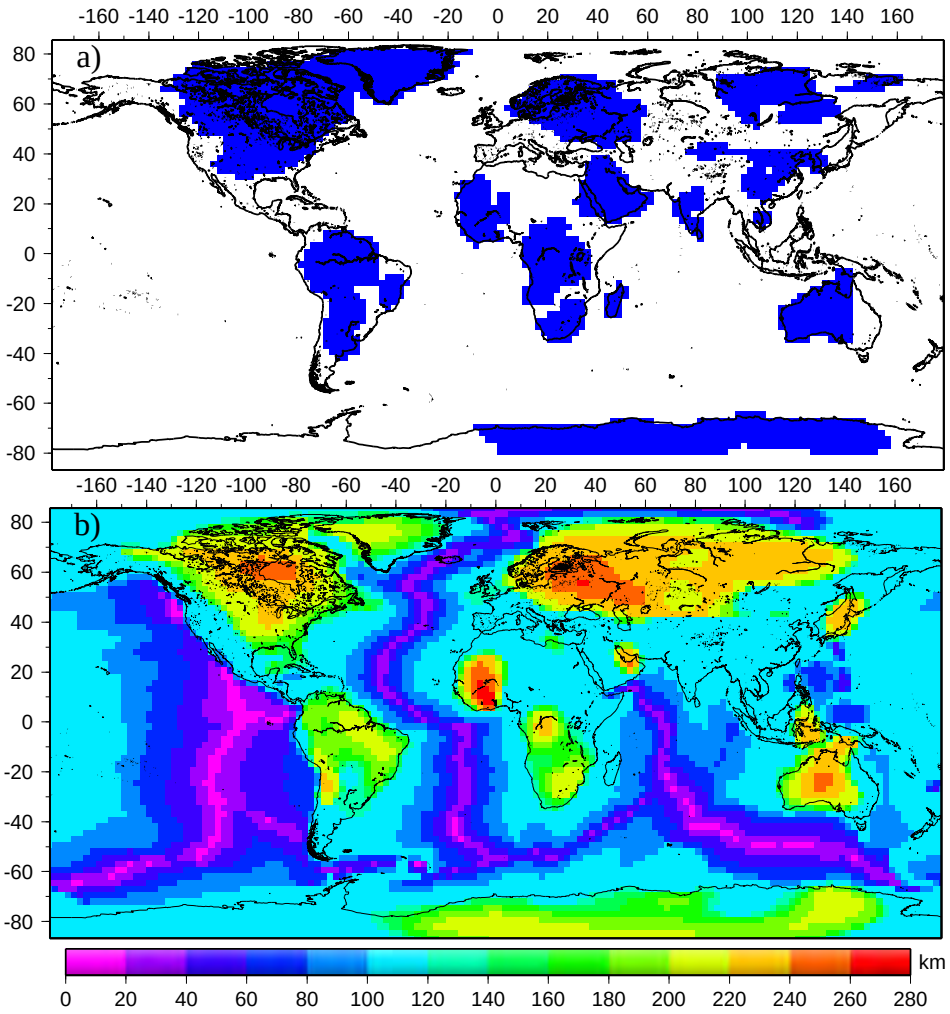

Figure 4: a) Distribution of cratonic areas based on keel model A. The blue regions are assigned higher viscosities than the surrounding white regions, which are given a constant viscosity value of 10^{21} Pa-s. b) Lithosphere thickness model modified from *Conrad and Lithgow-Bertelloni* (2006). Areas greater than 150 km thickness are assigned higher viscosities.

5.5.3 High viscosity continents

We then consider the influence of the higher viscosity continents with respect to the oceans on the lithospheric stress field and plate motions. The continents are assigned different viscosity contrasts, from 10 to 100 ($10 - 100 \times 10^{21}$ Pa-s) while the entire oceanic lithosphere is assigned a uniform viscosity value of $1 - 30 \times 10^{21}$ Pa-s. The asthenosphere viscosity is also varied from 10^{19} to 10^{21} Pa-s and its thickness varied from 100-300 km.

A strong asthenosphere (of viscosity 10^{20} Pa-s) or no asthenosphere (of viscosity 10^{21} Pa-s) viscosity model fails to yield stresses that can match the deformation indicators.

These models are also unable to match plate motions. The same is true for an asthenosphere with smaller thickness ($<$ 300 km). Amongst those models with a sufficiently thick asthenosphere ($\sim$ 300 km) with viscosity 10^{19} Pa-s, models with moderate to high lateral viscosity variations ($10 - 100 \times 10^{21}$ Pa-s) in the lithosphere, due to higher viscosity continents, are able to generate deviatoric stresses, which when combined with the deviatoric stress field from GPE differences, match deformation indicators (models 1-5 in Table 1). These viscosity models are also able to match plate motions, achieving an almost equipartitioning of the toroidal/poloidal velocity ratio. However, as the viscosity difference between the continents and the oceans is increased, the fit to the deformation indicators improves slightly (from 0.66 to 0.68), but the toroidal/poloidal velocity ratio (T/P) for degrees 4 and 5 are over-predicted (models 2-5), indicating that the models are predicting too much toroidal motion.

5.5.4 Combined models

Various paired combinations of the above viscosity structures are tested against the constraints of strain rate tensor information, plate motions and toroidal/poloidal velocity ratio. We first test models with lateral variations due to continent-ocean divide combined with lateral variations due to old oceans (Figure 5a). The continents (red) and the old oceans (green) are made stronger ($10 - 100 \times 10^{21}$ Pa-s) compared to the rest of the Earth (white). The asthenospheric viscosity and thickness are varied as before, from $10^{19} - 10^{21}$ Pa-s, and from 100-300 km respectively.

For the above case, models with sufficient viscosity contrasts (models 6-9 in Table 1) yield a good match to the observed plate motions, as well as to the strain rate tensor information. However, the match to the toroidal velocity pattern is not as good as those with only strong continents (models 1-5). Amongst models 6-9, model 7, with very strong continental lithosphere and moderately strong old oceanic lithosphere, gives the closest match to the toroidal velocity pattern. It also yields a good fit to the strain rate tensor information (0.68).

Next, models with lateral strength variations due to continental regions and cratonic keels (Figure 5b) are considered. In this case, again, the colored regions (red and blue) are

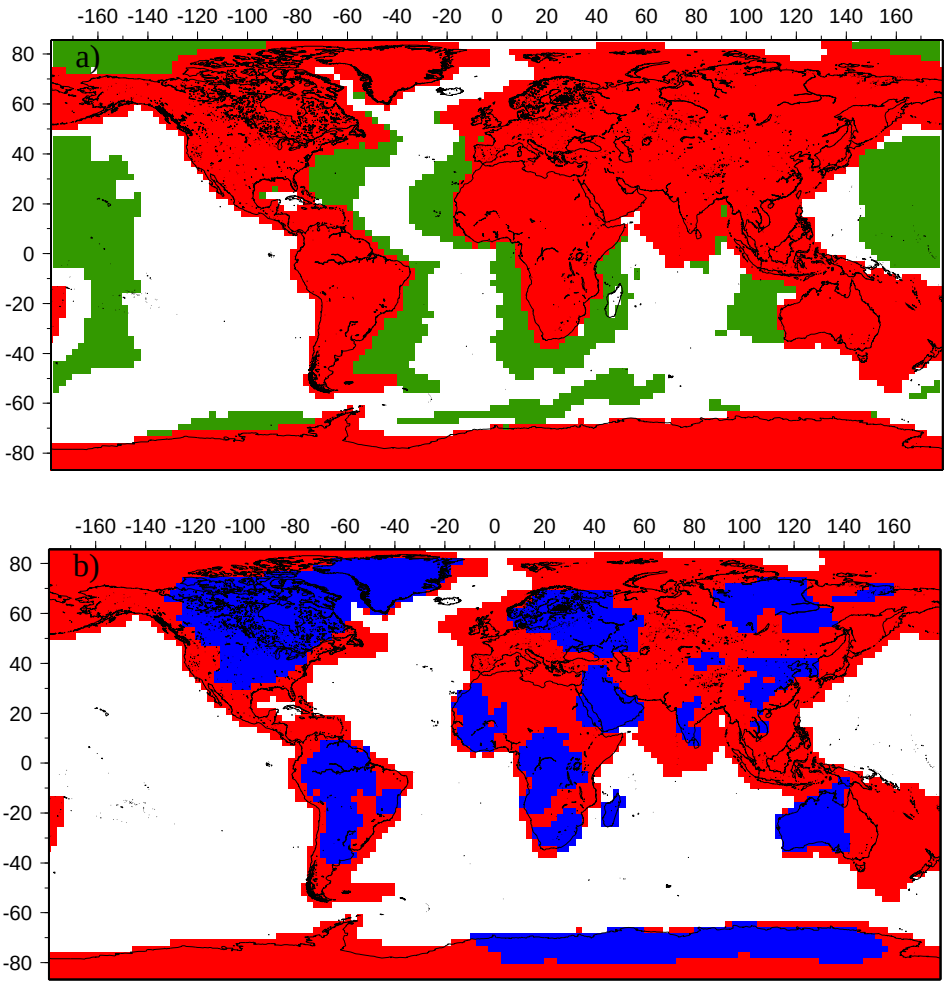

Figure 5: Distribution of a) old ocean floors (green), and continents (red), b) cratonic areas (blue) and continents (red). Higher viscosities are assigned to the blue, green and red areas, whereas the white areas are given a constant viscosity of 10^{21} Pa-s.

assigned higher viscosities ($10 - 100 \times 10^{21}$ Pa-s) compared to the white regions. These white areas are given a constant viscosity value of 10^{21} Pa-s. The continental keels are also allowed to go deeper, which means that there are lateral viscosity variations in the depth range of 200-400 km. The viscosity of the remaining non-keel parts of the asthenosphere is allowed to vary between $10^{19} - 10^{21}$ Pa-s. The asthenosphere thickness is also varied between 100 and 300 km.

Viscosity structures caused by a combination of higher viscosity continental lithosphere and high viscosity continental keels yield a good match with the divergence and vorticity patterns and also generate sufficient toroidal velocity, as long as the lateral variations are

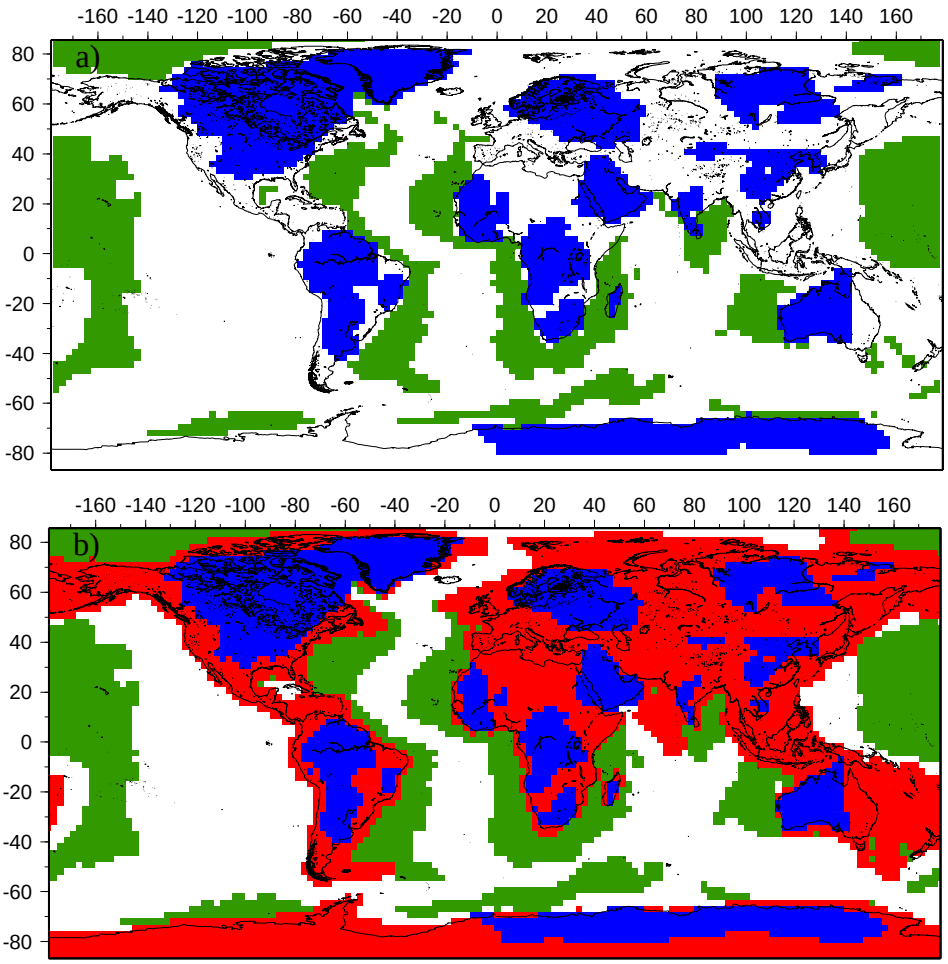

Figure 6: a) Distribution of old ocean floors (green) and cratonic areas having a very thick lithosphere (blue). b) Viscosity structures combining all three factors of lateral strength variations. Red areas are the continental regions, blue are cratons, whereas green indicate old oceanic lithosphere.

confined to the top 100 km and there exist strong lateral variations in the top 100 km of the lithosphere (models 10-14 in Table 1). The most favorable model in this group is model 11, in which the lateral variations are caused by high viscosity continents and higher viscosity cratonic keels (keel model B). This viscosity structure yields a good match with the deformation indicators (0.67) in addition to matching the poloidal and toroidal pattern, as well as generating sufficient toroidal velocity. Note, however, that models with high viscosities for the keels (12-14) predict too much toroidal motion for degrees 4 and 5.

Next, the keel models are combined with old oceanic lithosphere (Figure 6a). Cratonic areas (blue) and old oceans (green) are given higher viscosity values compared to the white

regions in the map, which are assigned a constant value of 10^{21} Pa-s. We test models with both uniform asthenosphere (when cratons are confined to the top 100 km) and laterally variable asthenosphere (when cratonic roots are allowed to go deeper, between 200 and 400 km depths). The viscosity and the thickness of the asthenosphere are varied as before.

Keel model A, combined with old ocean model, is able to match both plate motions and stress indicators only when there exists a very strong lateral variation in the top 100 km of the lithosphere on top of a weak and thick asthenosphere (model 17 in Table 1). Keel model B, on the other hand, does not require such strong lateral variations in order to yield a good fit to the strain rate tensor information and plate motions (models 15 and 16 in Table 1). The asthenosphere needs to be weak (10^{19} Pa-s) and thick ($\sim$ 300 km) in both keel cases. Within this particular group, model 16 does the best job in matching the constraints, although its degree 4 toroidal/poloidal ratio (T/P) is somewhat low.

Finally, all the three features including ocean-continent divide, young-old oceans, and cratonic keels are considered simultaneously (Figure 6b). The colored areas are assigned higher viscosities as compared to the white regions in the map. Red areas are the continental regions, whereas blue areas are cratonic regions. The old oceanic floor is indicated by green. Once again, the viscosities in each of these regions are varied from $10 - 100 \times 10^{21}$ Pa-s, with the cratonic areas being assigned the highest strength. White regions in the map have a constant viscosity of 10^{21} Pa-s. Both uniform asthenosphere ($10^{19} - 10^{21}$ Pa-s) and laterally variable asthenosphere are considered, with its thickness varying from 100-300 km.

Structures 18-20 in Table 1 are able to satisfy the observational constraints. These models incorporate lateral strength variations only in the top 100 km of the lithosphere due to these major geological features. The asthenosphere for these successful models, once more, is uniformly weak (10^{19} Pa-s) and thick ($\sim$ 300 km). Amongst all these models, model 19 is the most favorable, with a fit of 0.68 to the stress indicators and an almost equipartitioning of the toroidal/poloidal velocity ratio for degree 3 and above. The match to the divergence and vorticity pattern is also good for model 19. Structures with lateral viscosity variations below 100 km depth fail to match the constraints; the fit of the deviatoric stress tensor field to the strain rate tensor field fails when a laterally variable asthenosphere

Table 1: Results from our successful viscosity models (1-20) and two unsuccessful models (21 and 22). The three columns under Viscosity denote the depth of occurrence of lateral viscosity variations (between 0-400 km). k, o, c and lith stand for continental keels (k), old oceanic lithosphere (o), normal continental lithosphere (c) and normal oceanic lithosphere (lith). The reference viscosity is 10^{21} Pa-s. Hence, a value of 10 would mean an absolute viscosity of 10×10^{21} Pa-s. A value of 0 would mean no viscosity variation due to that particular feature. The letter B following some of the viscosity values under keels indicate that the keel model B is used. The two columns next to Viscosity indicate correlation coefficients between strain rate tensor field from GSRM and predicted deviatoric stress fields from tractions and combined GPE plus tractions. The P/P and T/P under Plate motions denote the correlation coefficients between the predicted and observed patterns of divergence and vorticity, respectively. T/P denotes the ratio of the magnitudes of the toroidal and poloidal velocities. The numbers 2-6 indicate spherical harmonic degrees. For example, the first row denotes that the lateral viscosity variations in the top 100 km is only due to the presence of higher viscosity continents. From below 100 km up to 400 km, there is no lateral variation in viscosity, but a weak asthenosphere of strength 10^{19} Pa-s.

Model	Viscosity								Corr. (trac-	Corr. (GPE +	Plate motions														
	0-100				100-200		200-400				P/P					T/T					T/P				
	k	o	c	lith	k	asth	k	asth	(ions)	tractions)	2	3	4	5	6	2	3	4	5	6	2	3	4	5	6
1	0	0	10	1	0	0.01	0	0.01	0.60	0.66	0.78	0.44	0.41	0.31	-0.10	0.56	0.21	0.26	0.28	0.50	0.21	0.42	0.82	1.2	0.69
2	0	0	30	1	0	0.01	0	0.01	0.58	0.66	0.80	0.43	0.11	0.09	-0.09	0.69	0.49	0.37	0.36	0.55	0.31	0.70	1.37	1.80	0.80
3	0	0	70	1	0	0.01	0	0.01	0.58	0.67	0.81	0.40	-0.14	-0.06	-0.09	0.72	0.63	0.42	0.40	0.58	0.40	0.92	1.64	1.89	0.88
4	0	0	100	1	0	0.01	0	0.01	0.59	0.68	0.80	0.38	-0.23	-0.12	-0.09	0.71	0.67	0.44	0.41	0.58	0.44	1.0	1.7	1.9	0.90
5	0	0	100	10	0	0.01	0	0.01	0.61	0.68	0.80	0.46	0.11	0.12	-0.10	0.62	0.34	0.35	0.29	0.48	0.32	0.52	1.13	1.63	0.76
6	0	10	30	1	0	0.01	0	0.01	0.61	0.68	0.82	0.51	0.43	0.45	-0.22	0.57	0.04	0.42	0.57	0.71	0.36	0.45	0.96	1.07	0.68
7	0	10	100	1	0	0.01	0	0.01	0.60	0.68	0.82	0.47	0.22	0.25	-0.25	0.59	0.33	0.42	0.55	0.80	0.44	0.67	1.22	1.18	0.74
8	0	30	30	1	0	0.01	0	0.01	0.61	0.68	0.83	0.55	0.47	0.54	-0.20	0.50	-0.11	0.45	0.62	0.73	0.40	0.48	0.84	0.85	0.67
9	0	100	10	1	0	0.01	0	0.01	0.61	0.66	0.84	0.61	0.60	0.67	-0.13	0.53	0.11	0.53	0.69	0.72	0.30	0.56	0.70	0.55	0.76
10	30	0	10	1	0	0.01	0	0.01	0.60	0.67	0.79	0.47	0.39	0.23	0.02	0.61	0.30	0.28	0.26	0.51	0.25	0.56	1.03	1.29	0.72
11	30B	0	10	1	0	0.01	0	0.01	0.60	0.67	0.80	0.45	0.28	0.20	0	0.60	0.46	0.42	0.33	0.54	0.21	0.70	1.08	1.67	0.78
12	70	0	30	1	0	0.01	0	0.01	0.58	0.66	0.80	0.46	0.08	0.04	0	0.72	0.53	0.34	0.38	0.57	0.33	0.78	1.53	1.68	0.78
13	100	0	30	1	0	0.01	0	0.01	0.58	0.66	0.80	0.46	0.06	0.04	0.01	0.73	0.53	0.34	0.37	0.60	0.34	0.82	1.6	1.68	0.80
14	100B	0	30	1	0	0.01	0	0.01	0.60	0.66	0.82	0.45	0.01	0.02	-0.04	0.72	0.62	0.49	0.42	0.62	0.28	1.02	1.53	1.96	0.91
15	30B	10	0	1	0	0.01	0	0.01	0.62	0.66	0.79	0.39	0.40	0.39	0.25	0.67	0.43	0.20	0.35	0.03	0.13	0.73	0.46	0.84	1.04
16	30B	30	0	1	0	0.01	0	0.01	0.62	0.68	0.81	0.44	0.40	0.51	0.21	0.75	0.33	0.22	0.57	0.14	0.16	0.95	0.45	0.81	1.05
17	100	100	0	1	0	0.01	0	0.01	0.56	0.67	0.86	0.66	0.61	0.66	0.08	0.27	0.50	0.31	0.52	0.52	0.42	0.51	0.61	0.55	1.0
18	30	10	10	1	0	0.01	0	0.01	0.60	0.67	0.82	0.54	0.55	0.57	-0.10	0.57	0.05	0.41	0.55	0.61	0.29	0.38	0.73	0.79	0.66
19	100	10	30	1	0	0.01	0	0.01	0.60	0.68	0.83	0.53	0.40	0.40	-0.15	0.59	0.15	0.40	0.56	0.74	0.38	0.57	1.06	1.11	0.71
20	100	30	30	1	0	0.01	0	0.01	0.60	0.68	0.83	0.56	0.44	0.51	-0.16	0.50	0	0.42	0.61	0.74	0.44	0.56	0.91	0.89	0.71
21	100	30	30	1	10	0.01	0	0.01	0.09	0.54	0.82	0.53	0.37	0.35	-0.17	0.64	0.18	0.39	0.54	0.71	0.39	0.58	1.08	1.11	0.74
22	1	1	30	1	10	0.01	10	0.01	-0.46	0.26	0.82	0.45	0.03	0.07	-0.14	0.74	0.52	0.26	0.32	0.46	0.35	0.78	1.30	1.68	0.92

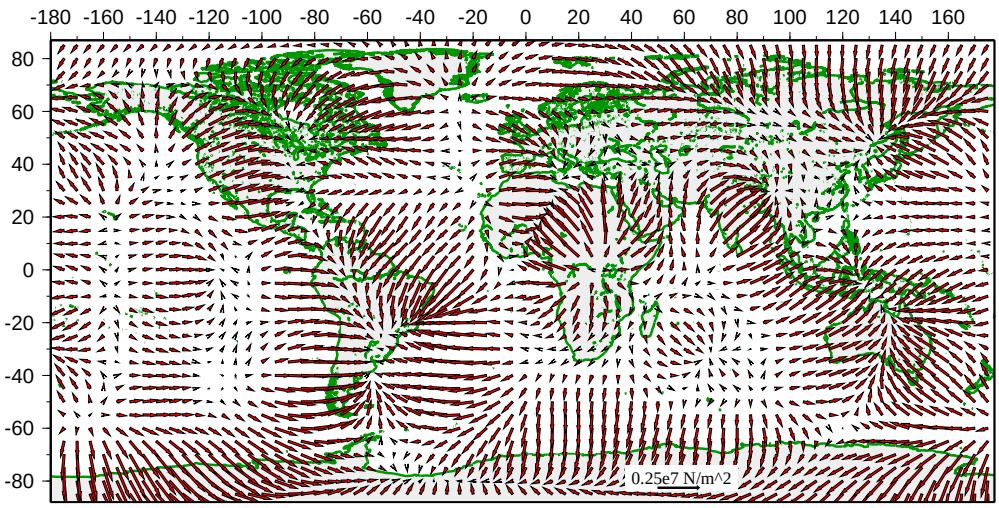

Figure 7: Global distribution of horizontal body forces at the reference level r_L (100 km depth) based on a convection model with laterally variable viscosity structure in the lithosphere and a weak asthenosphere (with viscosity of 10^{19} Pa-s) (model 19 in Table 1). These effective body forces are exerted on the lithosphere from below and are equivalent to the negative of tractions, $\tau_{r\phi}, \tau_{r\theta}$ (equations (12) and (13)), as defined in our coordinate system.

is considered, yielding correlation coefficients close to 0, or sometimes even negative.

5.6 Deviatoric Stress Field and Plate Motions from the Successful Models

All the models that yield a good fit to both the constraints of plate motions and deformation indicators display a similarity in the long-wavelength pattern of body force equivalents, which are the negative of the tractions ($-\tau_{\phi r}, -\tau_{\theta r}$, equations (12) and (13)) (Figure 7), and are applied to the base of the thin sheet at 100 km. The tractions are associated with the density buoyancy-driven mantle convection. These models show greater flow velocities at depth compared to the reference level r_L in areas of downwelling flow, such as central Asia, southeast Asian subduction zone, South America, and eastern North America. The same depth dependence of flow velocity magnitudes applies to upwelling regions, such as East Africa and the Pacific. The flow velocity directions at greater depth will be in the direction of the effective body forces ($-\tau_{\phi r}, -\tau_{\theta r}$) shown in Figure 7. The traction magnitudes range from $1-2.5$ MPa. The downwelling flow is caused by deeper density buoyancies of old subducted lithosphere. Similarity in the magnitude and distribution of the body force

Figure 8: Global distribution of vertically integrated horizontal deviatoric stresses from mantle buoyancies based on body forces in Figure 7 from model 19 (Table 1). Note the compressive deviatoric stresses in areas of convergence and the tensional deviatoric stresses in areas of divergence.

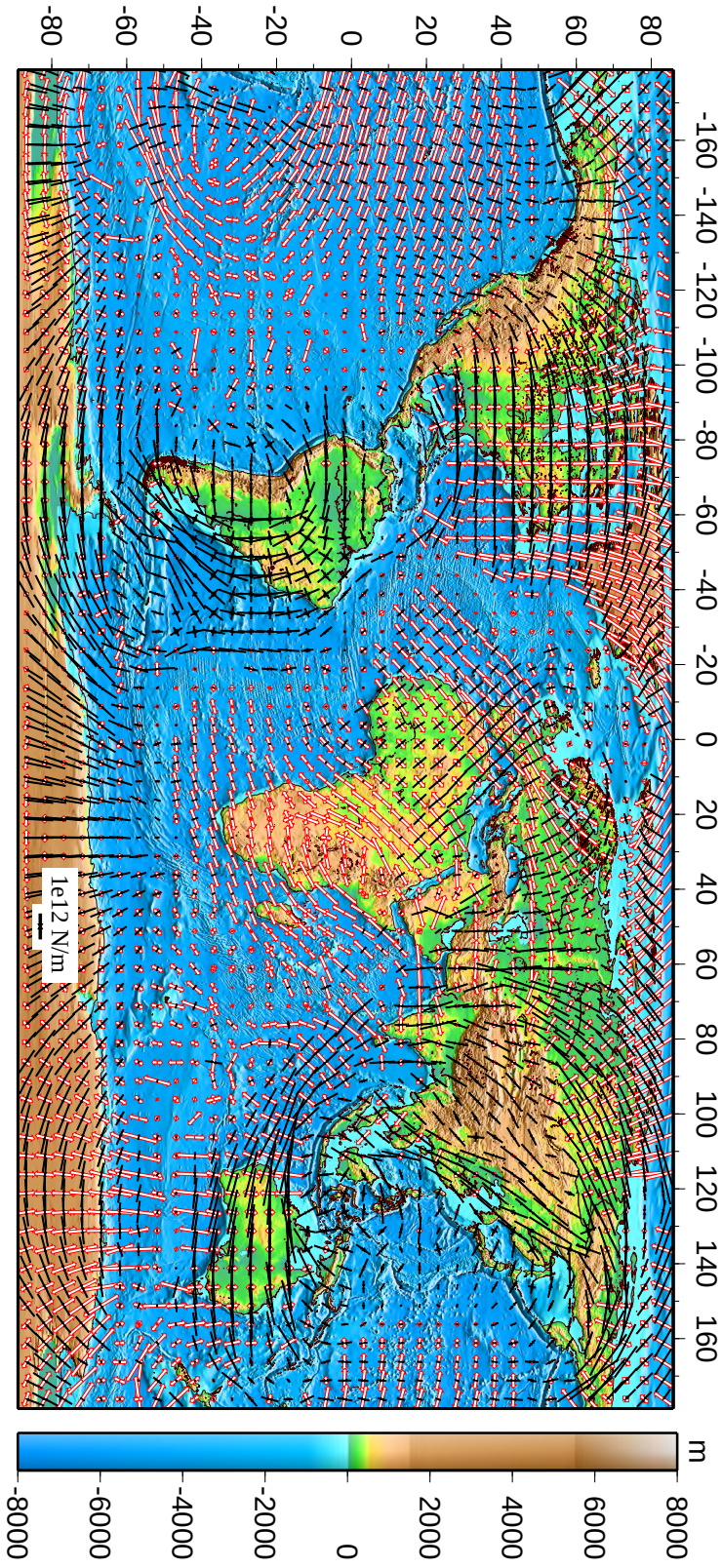
-80
-60
-40
-20
0
20
40
60
80
-160 -140 -120 -100 -80 -60 -40 -20 0 20 40 60 80 100 120 140 160
1e12 N/m
-8000
-6000
-4000
-2000
0
2000
4000
6000
8000
m

Figure 9: Global distribution of vertically integrated horizontal deviatoric stresses from both GPE differences (Figure 1) and basal tractions (Figure 8).

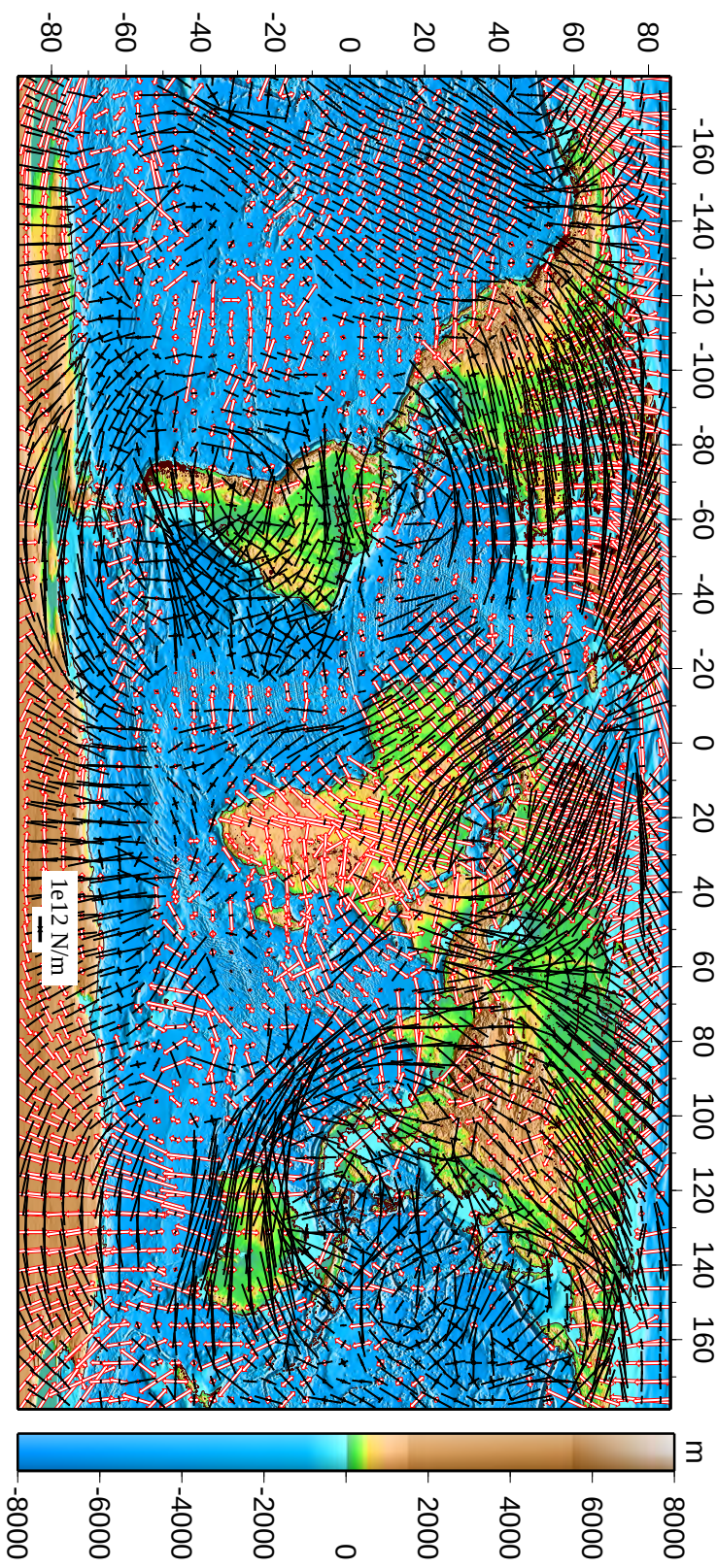
-80
-60
-40
-20
0
20
40
60
80
-160 -140 -120 -100 -80 -60 -40 -20 0 20 40 60 80 100 120 140 160
1e12 N/m
-8000
-6000
-4000
-2000
0
2000
4000
6000
8000
m

equivalents for all successful models also means similarity in the resultant deviatoric stress pattern (Figure 8). The poloidal and toroidal velocities for the successful models also bear much similarity with each other. Hence, here we present the results of one of our successful models (model 19 in Table 1). The combined stress field (from GPE differences and basal tractions) (Figure 9), as well as the correlation coefficients with the strain rate tensor information (Figure 10a, Table 2), are also shown for this particular model. The viscosity model that generates the tangential tractions and plate motion predictions combines all the three features of continent-ocean divide, continental cratons, and old vs. young oceanic lithosphere (model 19 in Table 1, Figure 6b).

Figure 7 shows strong convective downwelling (convergence) occurring in areas such as central Asia, southeast Asian subduction zone, Andes, and eastern North America. Strong upwelling (divergence) is seen in eastern Africa and mild upwelling in the Pacific, in accordance with the low seismic velocity zones in those areas. The mid-oceanic ridges also show mild upwelling beneath them. The deviatoric stress field from these tangential tractions exhibit deviatoric compression in areas of convergence and deviatoric tension in areas of divergence (Figure 8). The stress magnitudes from tractions, which range from $1-4\times10^{12}$ N/m (Figure 8), are comparable to those from lithospheric GPE differences (Figure 1). The total depth integrated deviatoric stress field (Figure 9), which is the combined deviatoric stress field from lithospheric GPE differences (Figure 1) and mantle convection (Figure 8), shows significant changes from both Figures 1 and 8. The magnitudes of total depth integrated deviatoric stresses range from $2-6\times10^{12}$ N/m (Figure 9) for most areas, which are consistent with deviatoric stress magnitudes obtained by *Richardson* (1992). Also, it should be mentioned that the deviatoric stress magnitudes do not depend on absolute viscosity values, but are only dependent on relative viscosity variations. This is true for both the lithosphere model and for the convection model. The deviatoric stresses from basal tractions are dependent on the magnitudes of the tractions (Figure 7), which in addition to being dependent on the density model, are a function of the relative viscosity distribution. Likewise, the magnitudes of deviatoric stress from lithospheric GPE differences (Figure 1) is dependent on present-day topography, crustal structure, crustal and mantle densities used for those structures, and the relative viscosity variations for lithosphere, not the absolute

values of viscosity for the lithosphere.

There occurs large deviatoric tension in Eastern Africa, while the tension in the vicinity of the Andes largely vanishes for the total field. Deviatoric compression in the northern part of the North American continent is replaced by strike-slip style of deformation, whereas in the southern part of North America the style is deviatoric compression. The boundary zone between the Indian and Australian plates shows more deviatoric tension on the western side of the plate boundary zone, with dominant compression mixed with strike-slip on the east. A major change takes place in the Tibetan plateau, where the dominantly N-S deviatoric tension from GPE differences is replaced by strike-slip type of deformation, as per observations.

Comparison of the deviatoric stress tensor from the combined influence of lithospheric GPE and mantle circulation (Figure 9) with the strain rate tensors in the plate boundary zones (GSRM) shows an improvement in fitting in most of the areas, especially in areas of continental deformation (Table 2, Figure 10a). Andes and Africa show a dramatic improvement in fitting. Some areas, such as the mid-oceanic ridges and the Mediterranean undergo moderate to slight improvement. Comparison with the moment tensor data also show significant improvement in Andes, eastern Africa, central Asia, and the Indo-Australian plate boundary region (Figure 10b). The fit, however, degrades in areas such as Baikal in Asia, New Zealand, Hawaii (for the moment tensor data) and also in a few areas of the mid-oceanic ridges (south of Africa). The overall fit for the combined case is 0.68 for model 19 (Tables 1 and 2) as opposed to a much lower 0.54 from GPE differences only (Table 2).

The above results show the importance of density buoyancy-driven basal tractions in explaining the deformation in the Earth's plate boundary zones. Addition of basal tractions marks a substantial improvement in fitting, especially in areas of continental deformation. Tractions, coupled to the base of the plates are generated by mantle flow induced by current and past subducted lithosphere in the areas such as the Indian plate, North America, and Andes.

We do a qualitative comparison between the most compressive principal axes direction of our predicted deviatoric stresses from our best fitting combined model and the orientation of the horizontal most compressive principal axes from the stresses in the World Stress

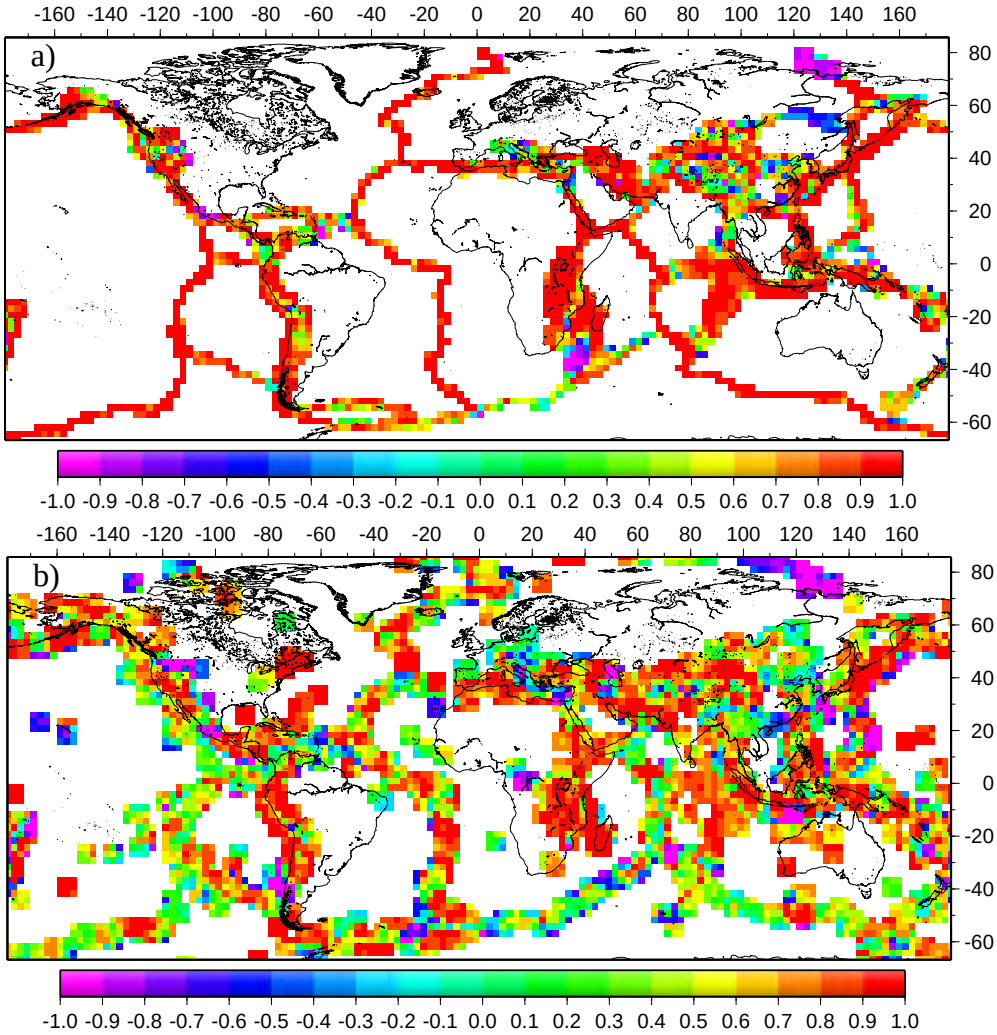

Figure 10: Correlation coefficients between deviatoric stress tensors arising from combined GPE differences and basal tractions (Figure 9) and a) observed strain rate tensors from the Global Strain Rate Map and b) moment tensor data from Harvard CMT catalogue.

Map (WSM) (*Zoback*, 1992; *Reinecker et al.*, 2005). WSM is a compilation of measured principal stress directions based on earthquake focal mechanisms, borehole breakout data and Quarternary fault slip directions. We use the WSM data interpolated on a grid used by *Lithgow-Bertelloni and Guynn* (2004) (Figure 11a). This interpolated dataset is compared with the most compressive principal axes of deviatoric stress from GPE differences (Figure 11b) and from GPE differences and tractions (from model 19) combined (Figure 11c). A qualitative comparison shows large swathes of regions which demonstrate an excellent match. That is, in those areas, the difference in most compressive principal axes directions

Figure 11: Most compressive principal axes orientation of the deviatoric stresses from a) the World Stress Map interpolated by *Lithgow-Bertelloni and Guynn* (2004), b) GPE differences and c) combined GPE differences and tractions from model 19. Red indicates normal faulting, blue indicates thrust faulting and green indicates strike-slip regime.

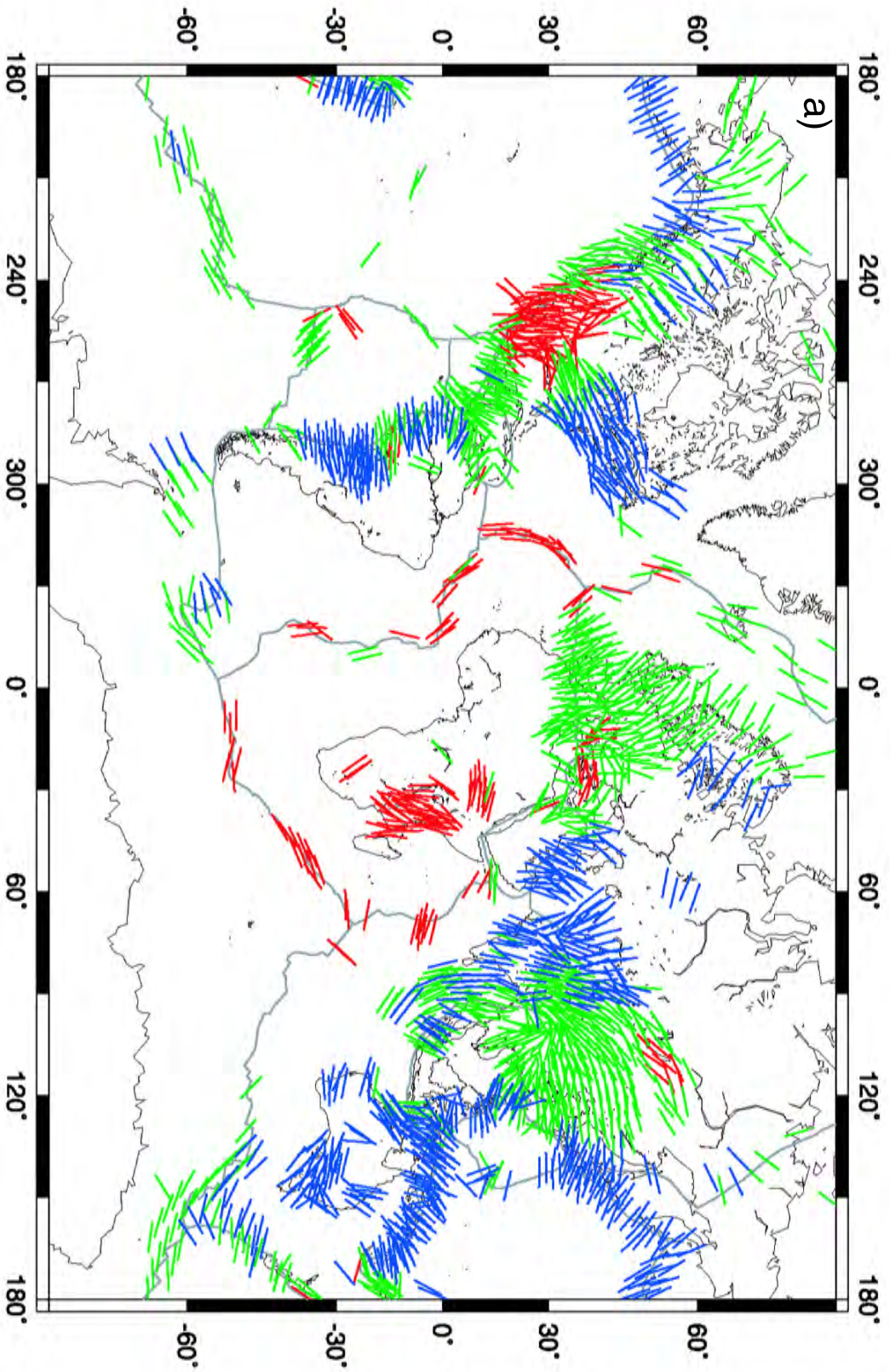
a)
-60°
-30°
0°
30°
60°
180°
240°
300°
0°
60°
120°
180°

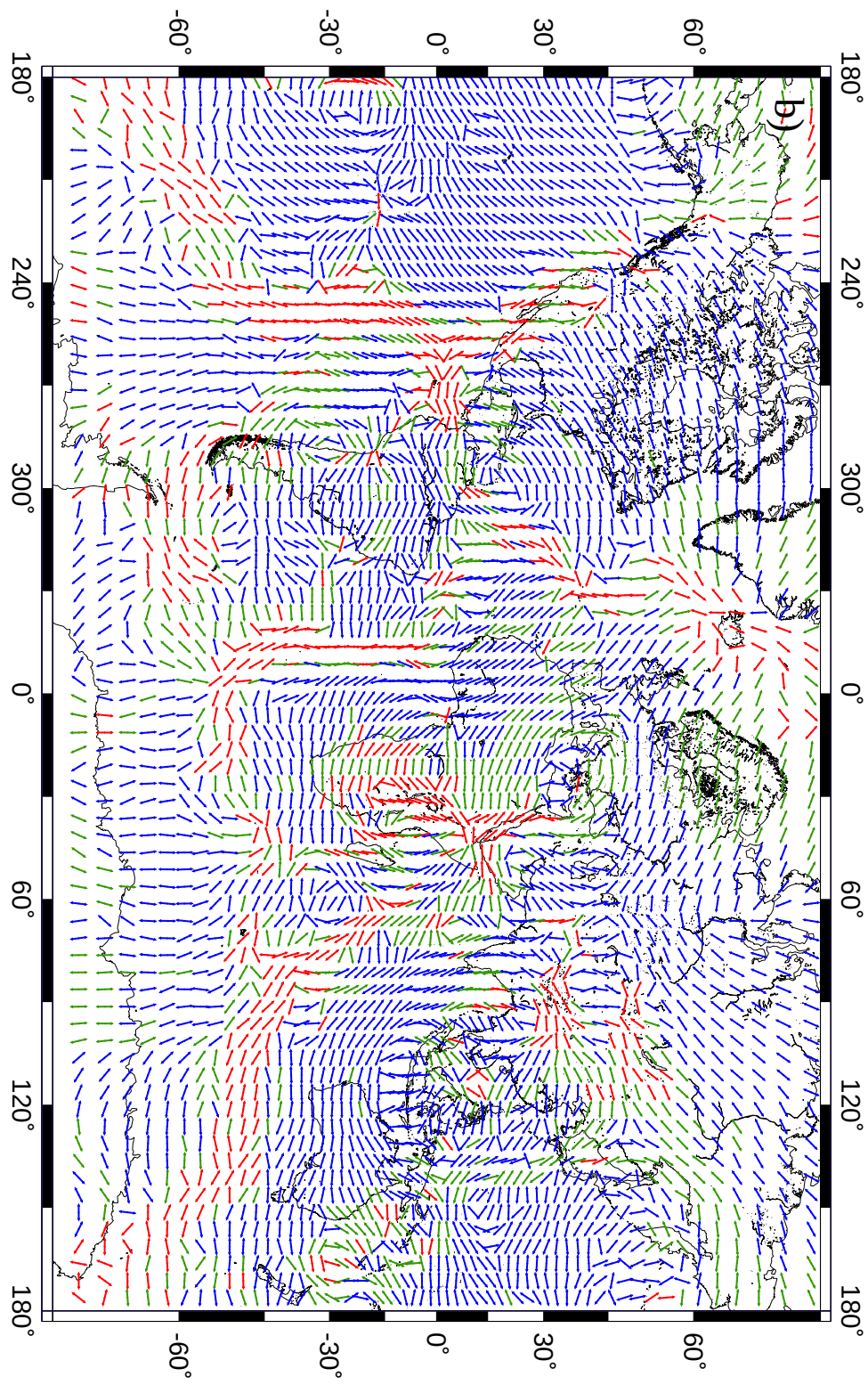
b)
-60°
-30°
0°
30°
60°
180°
240°
300°
0°
60°
120°
180°

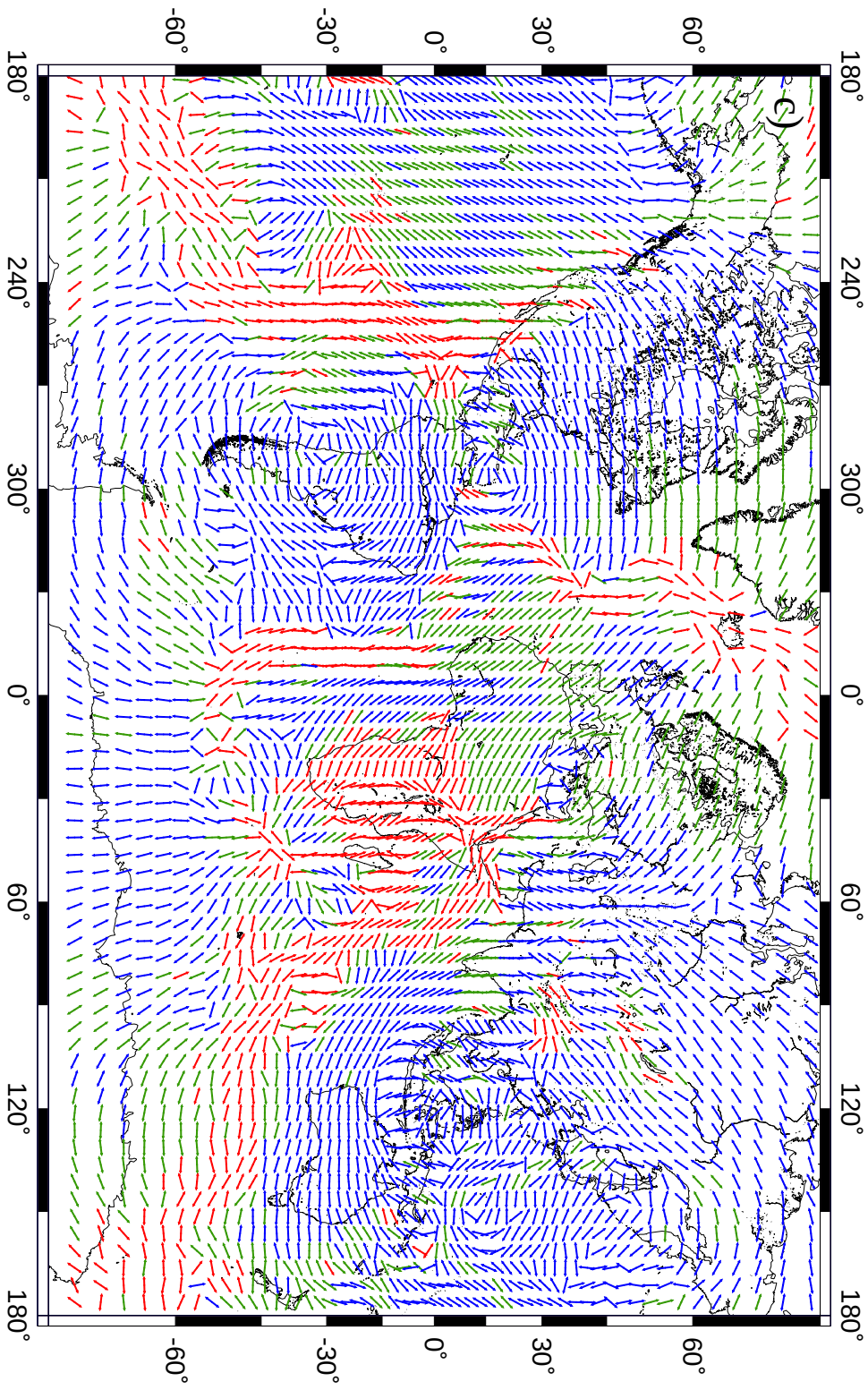
c)
-60°
-30°
0°
30°
60°
180°
240°
300°
0°
60°
120°
180°

between our predicted stresses and those from WSM is less than 15^o. These areas are the entire North and Central America, mid-Atlantic ridge, parts of central Africa, westernmost part of Europe, Mediterranean, Caspian Sea region, eastern Asia, India, as well as the Indo-Australian boundary zone and the southeast Indian ridge. The above fit is true for both the combined case (Figure 11c) and the case with GPE differences only (Figure 11b). Areas that yield a moderate fit (most compressive principal axes directions varying between $20^o - 30^o$) are the southwest and central Indian ridges and southeast Asia. Central Australia yields a poor fit (most compressive principal axes directions varying between $50^o - 70^o$) for both cases. In some of the regions, the fit improves for the combined case compared to the GPE case, such as Andes, central America, parts of eastern and southern Africa, and the southern part of the East Pacific Rise. A few areas such as central Pacific, part of southwest Indian ridge below Africa, central Europe, however, fare better for the GPE case as compared to the combined case. The above comparison is based only on the principal axes directions and not on their styles. In general, the misfit between our predicted most compressive principal axes and those in WSM do not vary largely between the two cases (deviatoric stresses from GPE differences and combined deviatoric stresses). This is where the GSRM can yield valuable information, since, while comparing to GSRM, we consider the full stress and strain rate tensors instead of only the most compressive principal axes.

The surface plate velocities from model 19 are presented here in terms of divergence (Figure 12c) and vorticity (Figure 12d). When compared with the observed divergence and vorticity on Earth (Figure 12a,b), they appear similar on a large scale. The main differences occur in the positions of the most prominent highs and lows, especially for the poloidal case. The zone of high divergence to the southwest of North America is displaced towards the west, instead of occurring exactly over the mid-oceanic ridges. The low divergence zone observed along the Southeast Asian subduction region is centered slightly to the north of the main subduction area. In the case of vorticity, as well, there occurs some differences between the observed and the predicted velocities. We are over-predicting the left-lateral shear to the south of India and under-predicting the right lateral shear in western North America. Moreover, there are some extra centers of left-lateral shear occurring at the far south, which are absent in the observed vorticity map.

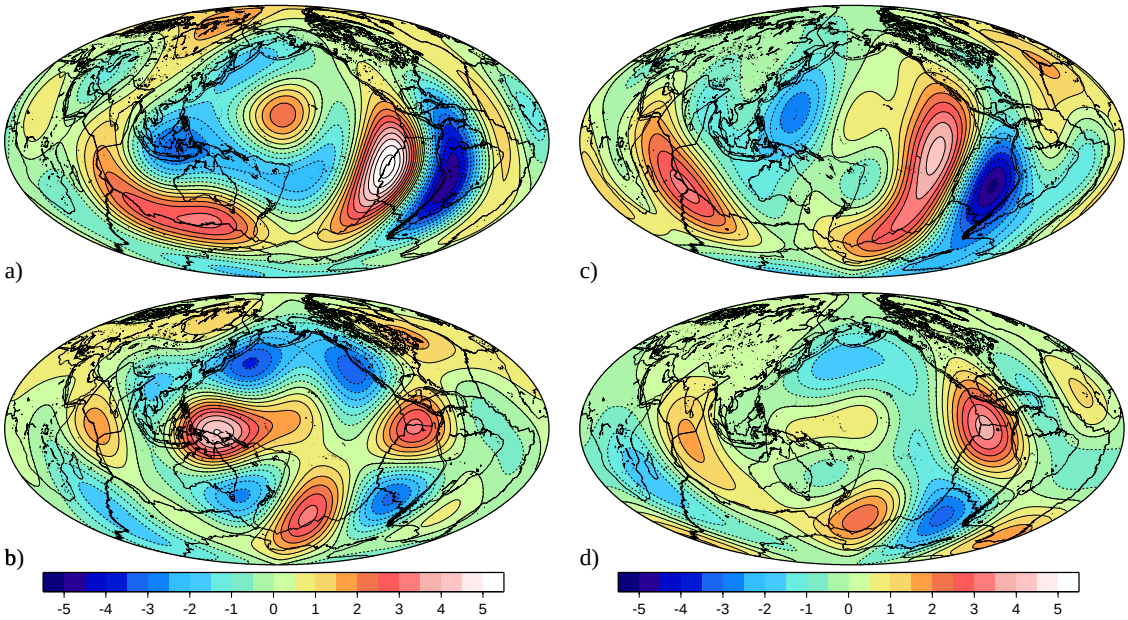

Figure 12: Observed (a and b) and predicted (c and d) divergence (top) and vorticity (bottom). The predicted result is from one of our successful models (model 19 in Table 1) that also produces deviatoric stresses, which yield a high correlation with the GSRM model (Table 2, Figure 10). Contour interval is 5×10^{-9} rad/yr.

Region of interest	Number of areas	GPE Differences	Combined GPE Differences plus Basal Tractions
Western North America	132	0.53	0.63
Andes	89	0.24	0.79
Eastern Africa	164	0.32	0.70
Mediterranean	83	0.55	0.57
Central Asia	187	0.33	0.52
Indo-Australian plate boundary zone	174	0.69	0.75
Mid-oceanic ridges	292	0.80	0.86
Western Pacific	109	0.51	0.62
South East Asia	167	0.61	0.65
Total	1944	0.54	0.68

Table 2: Correlation coefficients obtained from a comparison between the deviatoric stress tensors from one of our successful models (model 19 in Table 1) and strain rate tensors from the GSRM model.

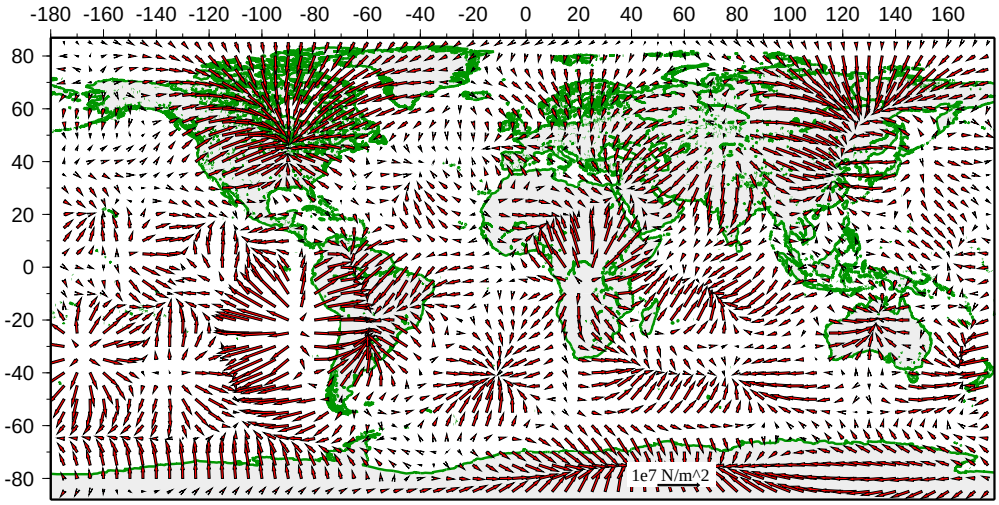

Figure 13: Same as Figure 7, but for model 21.

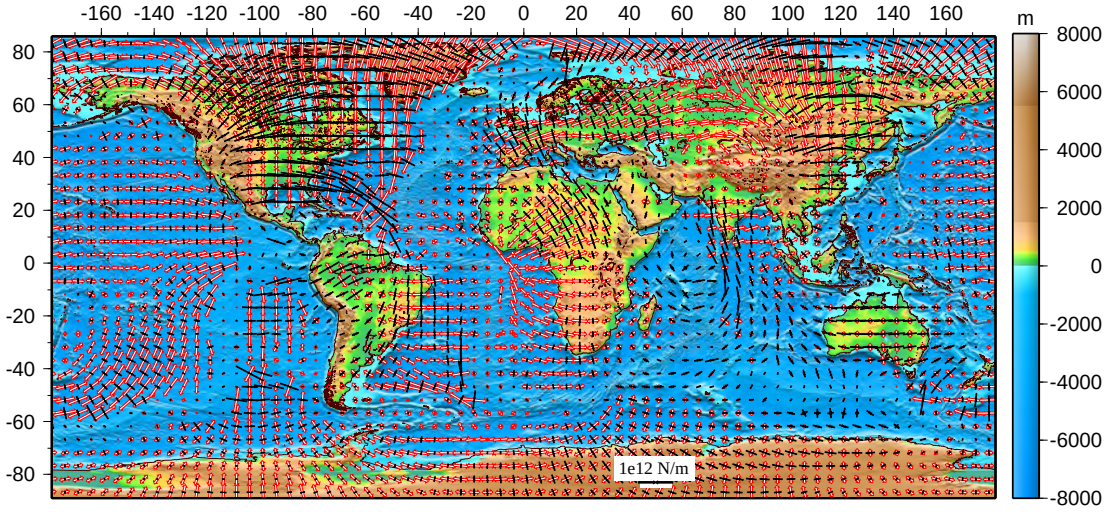

Figure 14: Same as Figure 8, but for model 21.

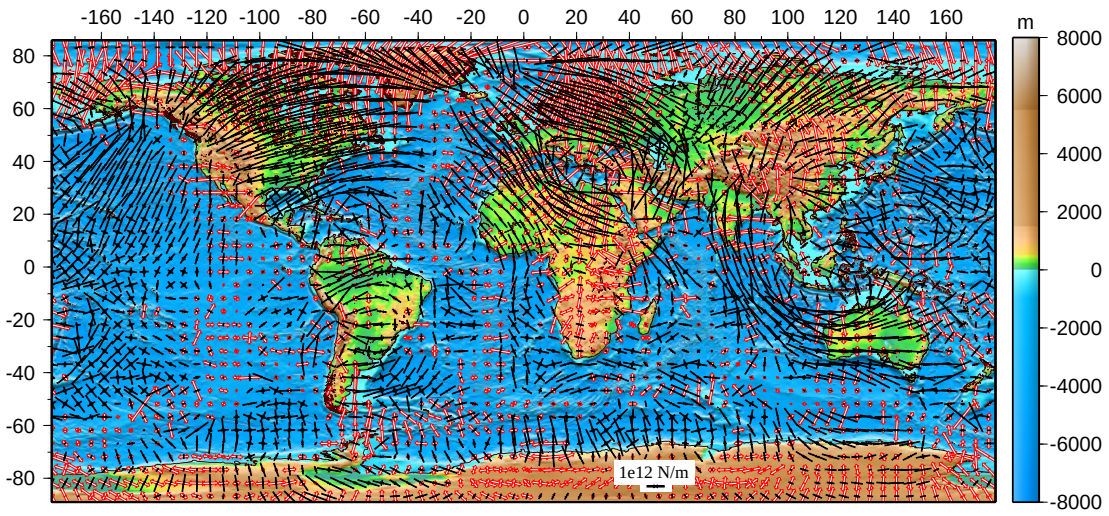

Figure 15: Same as Figure 9, but for model 21.

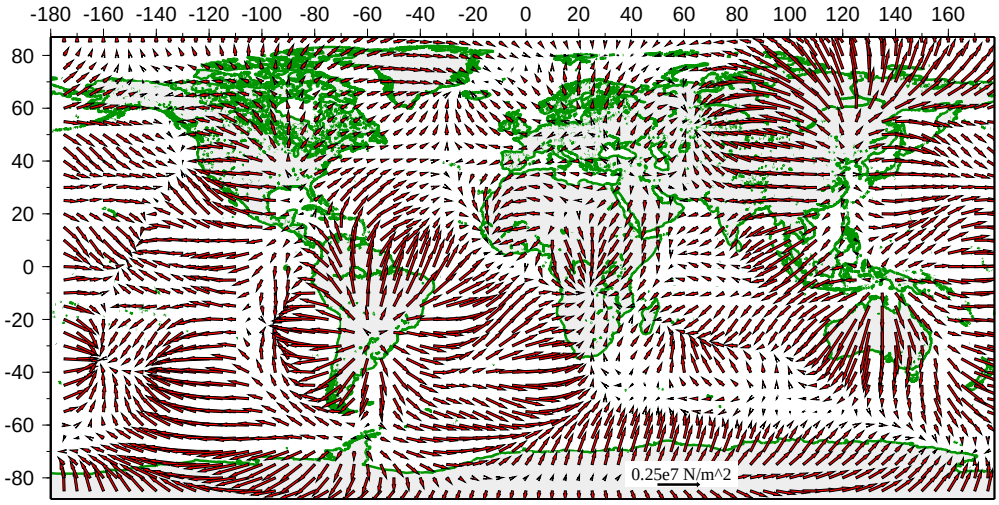

Figure 16: Same as Figure 7, but for model 22.

We would also like to discuss the combined lateral viscosity models where only the keels are allowed to reach depths of 200 km with a 200 km thick asthenosphere below them. The areas outside the cratonic regions are underlain by an asthenosphere that is 300 km thick. The effective body forces (Figure 13) from one such case (model 21) shows a very different pattern compared to the successful models. The magnitudes of these effective body forces are also smaller. The resultant deviatoric stresses from this model (Figure 14) also exhibits a completely different style and reduced magnitudes. This arises due to the fact that lateral viscosity variations below 100 km induces a flow pattern in which

the lithosphere in some regions leads the mantle, as opposed to the mantle leading the lithosphere for the successful models. These stresses combined with the deviatoric stresses from GPE differences only show the dominant effect of the latter (Figure 15). The fit to the strain rates from GSRM is poor (Table 1, model 21).

We also test a viscosity structure in which we consider only the ocean-continent divide in the top 100 km with the keels reaching a depth of 400 km (model 22 in Table 1). In areas where there are no keels, the asthenosphere is 300 km thick and is assigned a viscosity of 10^{19} Pa-s. We only show the traction field (Figure 16) for that model. The pattern is exactly opposite to that from our successful models with the lithosphere leading the flow in areas of high density anomalies. The fit to the GSRM is even worse than model 21. The results for this model are shown in Table 1 (model 22). Clearly an asthenosphere is needed beneath the keels, and the best match to stress occurs where the keels have no presence below 100 km (uniform asthenopshere).

5.7 Alternative Method: Radial Tractions from Mantle Convection

As discussed in section 2.4, there are two ways of dealing with the radial tractions. Our preferred way is to treat them as part of the lithospheric contribution, the results of which we have presented so far. In this section, we demonstrate the results of calculating radial tractions from mantle convection models.

We choose a viscosity model that yields a good fit to plate motions but fits the strain rate data poorly (Table 3). This viscosity structure takes into account the ocean-continent divide in the top 100 km with continents 30 times stronger than the oceans. It also contains high viscosity keels (10^{22} Pa-s) reaching to a depth of 200 km with a weak asthenosphere (10^{19} Pa-s) elsewhere. The asthenosphere between 200-400 km is slightly stronger (10^{20} Pa-s). From the dynamic topography predicted by the particular convection model (Figure 17a), the GPE differences and the associated deviatoric stress field (Figure 17b) is calculated. Areas of positive dynamic topography have higher GPE and are in deviatoric tension, whereas those of negative dynamic topography have low GPE and are in deviatoric com-

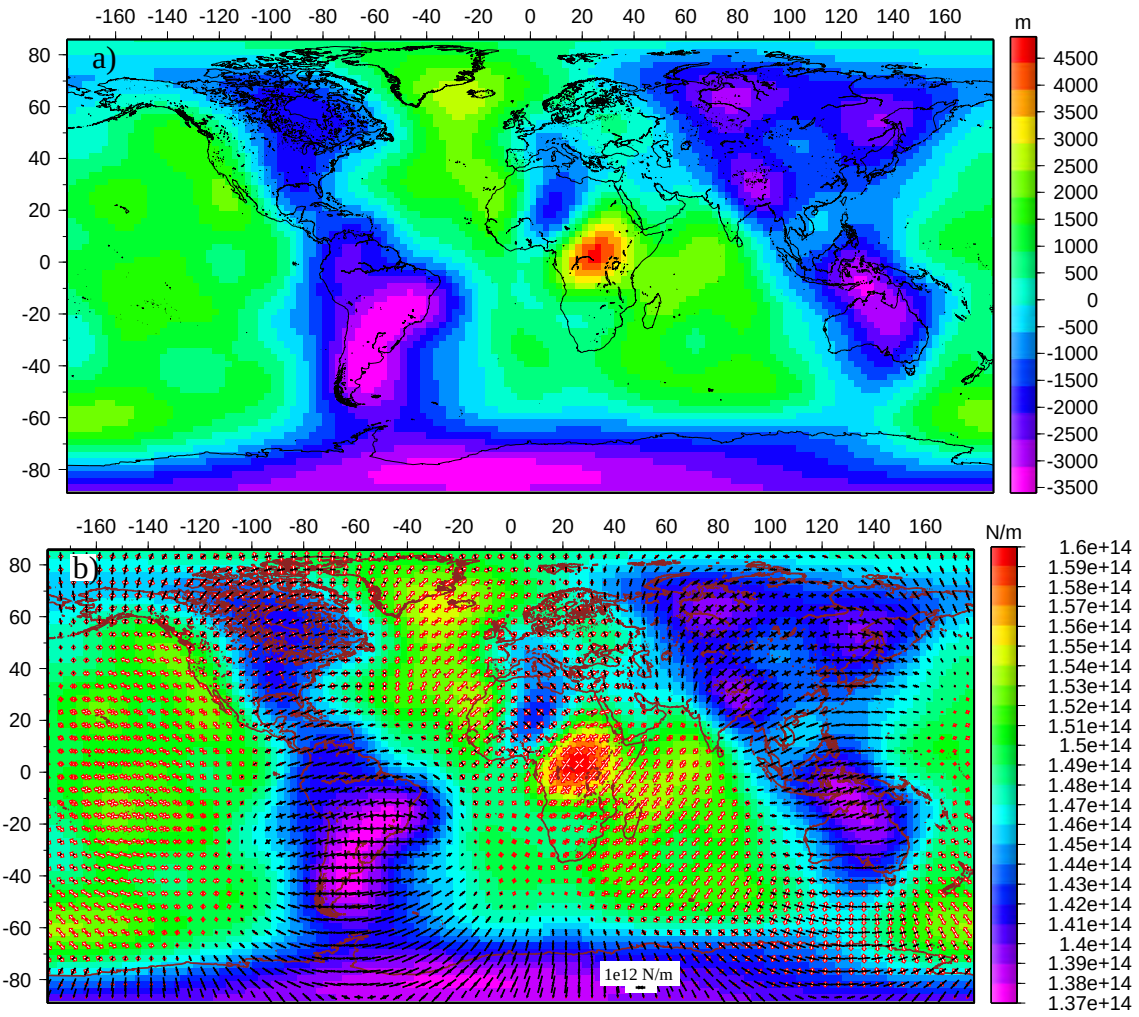

Figure 17: Prediction from radial tractions of the convection model described in section 5.7. a) Dynamic topography predicted by the radial tractions. b) GPE differences and associated deviatoric stresses computed from the dynamic topography in a). Areas of negative dynamic topography are in deviatoric compression, whereas those of positive dynamic topography are in deviatoric tension.

pression. This deviatoric stress field is the response of the radial tractions. The deviatoric stresses from tangential tractions (Figure 18b) for the same model shows opposite sense to the deviatoric stresses from radial tractions. The two stress fields are then added together to generate a combined deviatoric stress field, which is the total deviatoric stress response from the convection model (Figure 19a). The fit to the strain rate data from GSRM for each of the above cases (Figures 18, 19) is also calculated (Table 3). Finally, these deviatoric stresses from convection model are added to those from a compensated lithosphere model in order to yield a total lithospheric deviatoric stress field (Figure 19b). Table 3 lists

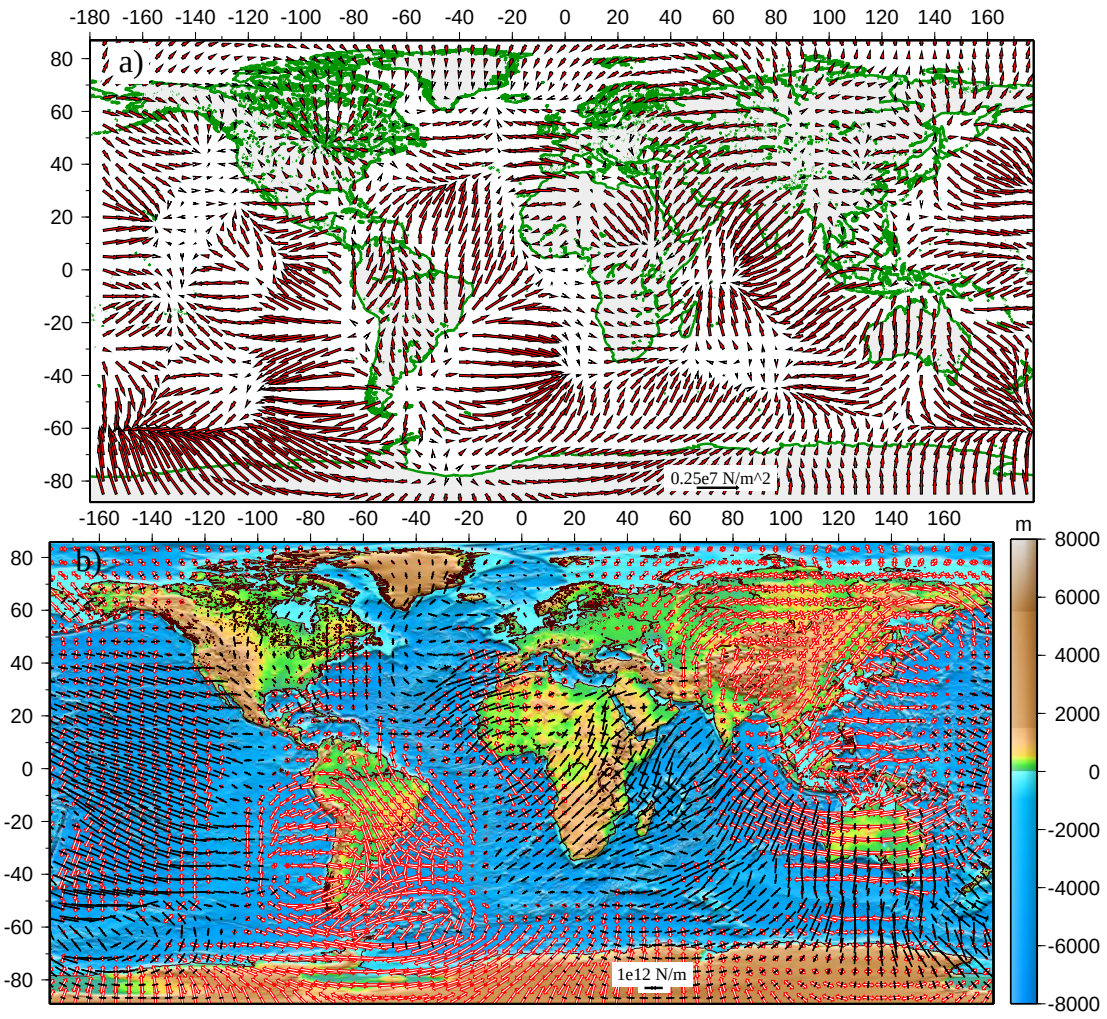

Figure 18: a) Global distribution of horizontal body forces at the reference level r_L (100 km depth) from the convection model described in section 5.7. b) Deviatoric stress field associated with horizontal tractions in a). Note that the deviatoric stresses in most areas are opposite in sense to the deviatoric stresses in Figure 17b.

the global correlation coefficients between the strain rates from GSRM and the deviatoric stresses from different components of the same model. When the radial tractions are dealt with as part of the lithosphere model, the fit to the strain rates is very poor (-0.02 in Table 3). When the radial tractions are dealt with as part of the convection model, the overall fit improves dramatically (0.66 in Table 3). Hence, if using the former method, we would reject this model on the grounds that it fails to fit the deformation indicators. On the other hand, if we use the alternative method, we would accept this model as a successful one as it yields a good fit to both deformation indicators and plate motions. The deviatoric stresses

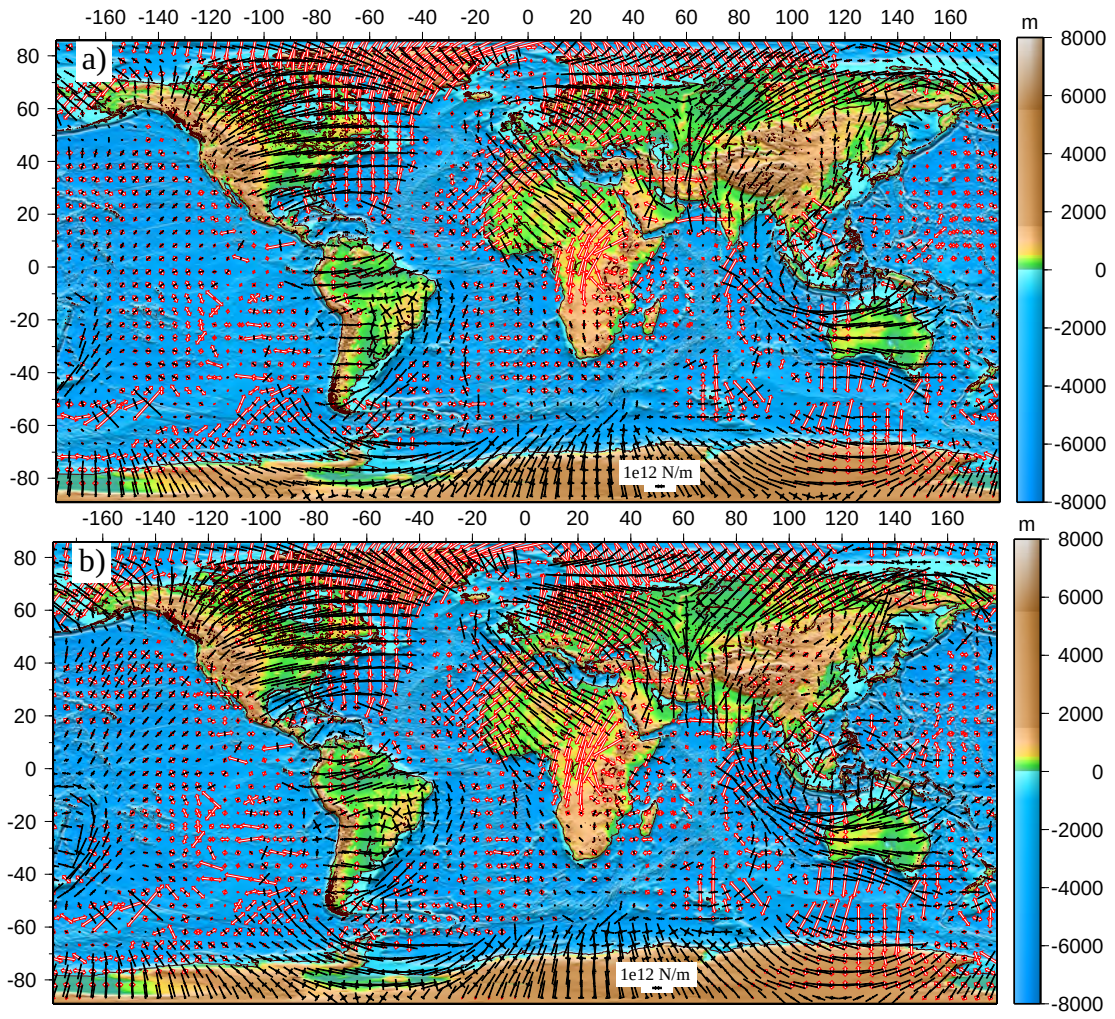

Figure 19: a) Total deviatoric stress field from the convection model in section 5.7 by adding stresses due to radial (Figure 17b) and horizontal (Figure 18b) tractions. b) Total lithospheric deviatoric stress field obtained by combining stresses from convection model (Figure 19a) and those from GPE differences from a compensated lithosphere model.

associated with dynamic topography thus dominate the solution and compensate for the inadequacy of the horizontal tractions. The dominance of the radial traction solution may indicate that we are not adequately removing the influence of dynamic topography from the Crust 2.0 model. The uncertainty in how the Crust2.0 model is compensated in order to remove the dynamic topography signal from it, leads us to prefer the use of the uncompensated model for GPE calculations. For such cases, we assume that the depth integrals of vertical stress already contain the signal from dynamic topography.

Models	Correlation coefficients
Horizontal tractions (from Figure 18b)	-0.53
Combined horizontal tractions plus GPE differences from uncompensated Crust 2.0	-0.02
Horizontal plus radial tractions (from Figure 19a)	0.53
Combined tractions plus GPE differences from compensated Crust 2.0 (from Figure 19b)	0.66

Table 3: Comparison of global correlation coefficients between strain rate tensors from the GSRM model and deviatoric stress tensors from the viscosity model described in section 5.7 that yields a good fit to the plate motion data. Note, that the addition of radial tractions improves the fit dramatically.

5.8 Discussion and Conclusion

The principal aim of this study is to delineate the nature of lithosphere-mantle coupling and to test whether major geological features such as the continent-ocean divide, presence of cratonic roots, and age differences in the oceans, are capable of generating stresses that match the present-day deformation in the Earth's plate boundary zones and are also able to predict the observed plate motions. The results show that these first order features can indeed satisfy these two constraints. All these three factors are found to play important roles in matching the constraints. However, the lateral variation due to continent-ocean divide is the only model that is capable of satisfying the constraints by itself (models 1-5), as long as sufficient strength contrast exists between the oceans and continents. The common feature for all the successful models, besides models 15-17, is the presence of this continent-ocean divide. Hence, this feature is likely playing the dominant role in generating the optimum pattern and magnitude of stresses and plate motions.

From Table 1, it is clear that a weak asthenosphere of viscosity 10^{19} Pa-s with a thick-

ness of $\sim$ 300 km is required for a model to be successful. The low viscosity of the asthenosphere is necessary to generate sufficient toroidal motion so that the T/P ratio approaches unity. Such asthenospheric properties are also required for the convection model to generate the right kind of traction field, which would produce deviatoric stress field that matches deformation indicators. Many studies have argued for the existence of a low viscosity channel below the lithosphere. In fact, the plate motions predicted by *Wen and Anderson* (1997b) with a uniform low viscosity asthenosphere in their convection model, matched the observed plate motions quite well. This study has shown that such a viscosity model also does a very good job of matching the strain rate tensor information along the deforming plate boundary zones. Hence, it is of primary importance to take into account both these constraints when drawing inferences about the Earth's viscosity structure.

We also see from our results that models where the keels reach depths below 100 km, are unable to match the observational constraints, especially the fit to the deformation indicators. In these types of models, the flow velocities near the surface in many regions are larger than those at depths (*Ghosh et al.*, 2008), indicating that, for these particular models, the lithosphere leads the mantle. Hence, the body-force distribution, and the resultant deviatoric stress pattern, are opposite to those of the successful models. The implications of this are potentially enormous, and may indicate that seismic velocity variations at depths below 100 km may not be associated with lithospheric "keels", but may instead reflect variations in seismic properties in the upper mantle that is still rheologically equivalent to asthenosphere in behavior.

Another significance of this study is the generation of toroidal velocity. As mentioned earlier, it has been extremely difficult to incorporate high orders of lateral viscosity variations, and hence generate sufficient toroidal motion in models of mantle convection. Here, with sufficient strength contrasts in the lithosphere of the convection models, we are able to generate a high enough toroidal velocity that satisfies the observed equipartitioning of toroidal-poloidal motion. We believe that we have constrained the relative viscosities of the lithosphere and asthenosphere in order to delineate a best-fit coupling model. We have shown that contribution of density buoyancy-driven basal tractions are extremely important, not only to match the present-day deformation of the lithosphere, but also to fit the

pattern and magnitude of the plate velocities. We have also demonstrated the importance of the ocean-continent difference in controlling the plate motions and the toroidal/poloidal velocity ratio.

An important aspect of our study is constraining the deviatoric stress magnitudes. The magnitudes of depth integrals of compressive deviatoric stress from the combined GPE differences and convection models are $2-8\times10^{12}$ N/m, the largest stresses occurring within the Indo-Australian plate and southeast of South America in the Atlantic. The stress magnitudes in most parts are consistent with stress magnitudes of earlier studies (*Richardson*, 1992). In other parts, our stress magnitudes are larger by a factor of 2. These areas of large stress magnitudes are outside the deforming plate boundary zones in the GSRM. Our stresses in the Indo-Australian plate are about 4-5 times smaller than those of *Cloetingh and Wortel* (1986), who calculated stresses of several kilobars in the Indo-Australian plate. However, *Coblentz et al.* (1998) predicted stress magnitudes about a factor of 2 smaller than ours in the Indo-Australian plate. Deviatoric stresses at the Tibetan Plateau are between $2-3\times10^{12}$ N/m. The stress magnitudes in continental Europe are large, $\sim 6\times10^{12}$ N/m, whereas those in North America are between $3-5\times10^{12}$ N/m. It should be mentioned that these stress magnitudes are mostly dependent on the density models and to some extent on the relative viscosity distributions. They are independent of absolute viscosities.

We also calculate the vertical averages of rheology of the deforming lithosphere by computing the vertically integrated differential stress ($\int_{-h}^{L}(\sigma_1-\sigma_3)dz$). The differential stress is calculated according to the fault styles (*Klein et al.*, 2008). The vertically integrated differential stress will provide an idea about the maximum strength in a deforming region. The deforming areas along the plate boundary zones are chosen from GSRM. The computed differential stress shows strength of $2-8\times10^{12}$N/m or 20-80 MPa in most of the continental regions (Figure 20). We compare these differential stresses with those of *Sonder and England* (1986). Assuming a fixed strain rate and Moho temperature, they calculated the vertically integrated differential stress. Our calculated differential stress in Tibet is $4-7\times10^{12}$ N/m compared to 7×10^{12} N/m of *Sonder and England* (1986). Our strength in San Andreas ranges from $1-5\times10^{12}$ N/m, which is consistent with the 4×10^{12} N/m magnitude determined by *Sonder and England* (1986). Our values in Zagros

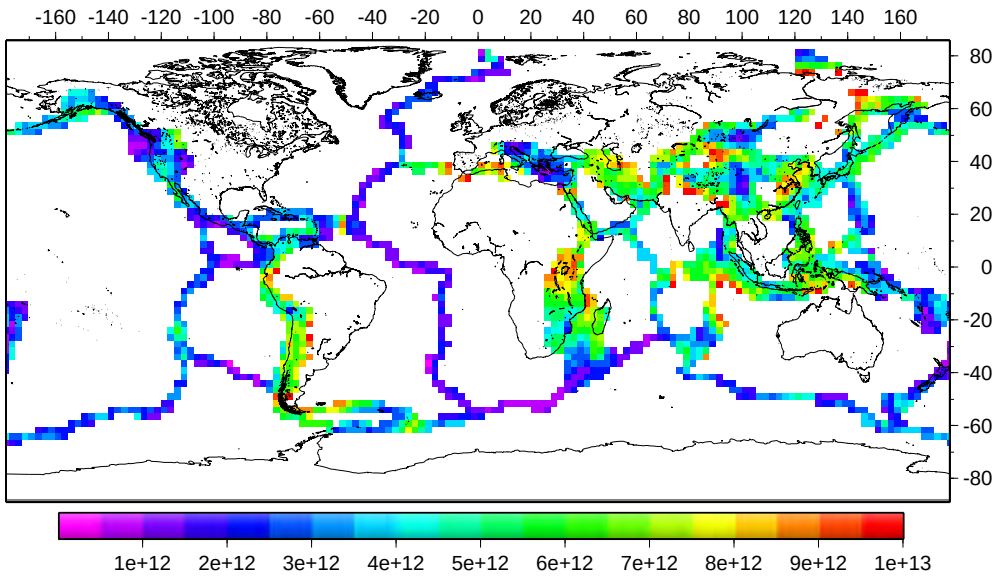

Figure 20: Distribution of vertically integrated strength of the lithosphere, $\int_{-h}^{L}(\sigma_1 - \sigma_3)dz$, in the deforming areas. The scalebar is in N/m.

are larger ($5-7\times10^{12}$ N/m) compared to the 2×10^{12} N/m computed by them, whereas in the Aegean our values are the same as theirs (2×10^{12} N/m).

We achieve the highest correlation coefficient of 0.68 between our predicted deviatoric stresses and the deformation indicators (Tables 1 and 2). There still exists some misfit between our predictions and the observed plate motions and deformation indicators. The remaining misfit for the deviatoric stress field and the plate motions might arise from a number of different factors. For example, although our lithosphere model is a high resolution one (2.5×2.5 degree), the convection model is of much lower resolution (degree 12). The misfit could be due to the lower resolution of the convection model. Increasing the degree of the model could substantially improve the fit to the observations. There occurs substantial viscosity differences between the weak plate boundaries and the more rigid plate interiors. These variations might play an important role. Although, our thin sheet lithosphere model takes into account these viscosity variations, they are not incorporated in our convection model. However, in order to consider these weak, narrow plate boundaries, it is necessary to use a much higher resolution convection model.

In the present study, we have used the lithospheric stress field and plate motions to constrain possible viscosity structures for the Earth. We have demonstrated that both these

constraints are crucial in delineating a best-fit viscosity model. We have successfully narrowed down a set of viscosity structures that satisfy both stresses and plate motions. In order to fine-tune our models, additional constraints such as geoid and dynamic topography could be used. An accepted model would be one that is capable of matching all the four constraints of deviatoric stress field, plate motions, geoid, and topography.

Chapter 6

Mathematical Treatment for Obtaining Deviatoric Stress Field for the Thin sheet Approach

Mathematical treatment for obtaining deviatoric stress field for the thin sheet approach

This chapter describes the methods used to calculate the depth integrated deviatoric stresses within the lithosphere using the thin sheet method, given a distribution of forcing terms. The mathematical treatment of the methods are described and tested.

The vertically integrated force-balance equations in spherical coordinates are:

$$\frac{1}{\cos\theta}\frac{\partial}{\partial\phi}\left(\int_{r_L}^{r_0} r^2\sigma_{\phi\phi}dr\right)+\frac{1}{\cos^2\theta}\frac{\partial}{\partial\theta}\left(\int_{r_L}^{r_0} r^2\sigma_{\phi\theta}\cos^2\theta dr\right)+\frac{\partial}{\partial r}\left(\int_{r_L}^{r_0} r^3\sigma_{\phi r}dr\right)=0 \quad (1)$$

$$\frac{1}{\cos\theta}\frac{\partial}{\partial\phi}\left(\int_{r_L}^{r_0} r^2\sigma_{\phi\theta}dr\right)+\frac{1}{2}\frac{\partial}{\partial\theta}\left(\int_{r_L}^{r_0} r^2\left[\sigma_{\theta\theta}+\sigma_{\phi\phi}\right]dr\right)$$
$$+\frac{1}{2\cos^2\theta}\frac{\partial}{\partial\theta}\left(\int_{r_L}^{r_0} r^2\cos^2\theta\left[\sigma_{\theta\theta}-\sigma_{\phi\phi}\right]dr\right)+\frac{\partial}{\partial r}\left(\int_{r_L}^{r_0} r^3\sigma_{\theta r}dr\right)=0 \quad (2)$$

$$\frac{1}{r\cos\theta}\int_{r_L}^{r_0}\frac{\partial\sigma_{\phi r}}{\partial\phi}dr+\frac{1}{r\cos\theta}\frac{\partial}{\partial\theta}\left(\cos\theta\int_{r_L}^{r_0}\sigma_{\theta r}dr\right)+\frac{1}{r}\int_{r_L}^{r_0}\left(2\sigma_{rr}-\sigma_{\phi\phi}-\sigma_{\theta\theta}\right)dr$$
$$+\int_{r_L}^{r_0}\frac{\partial\sigma_{rr}}{\partial r}dr-\int_{r_L}^{r_0}\rho g dr=0 \quad (3)$$

Let us assume that

$$r_0^2\bar{\sigma}_{rr}=\int_{r_L}^{r_0} r^2\sigma_{rr}dr \quad (4)$$

$$r_0^2\bar{\sigma}_{\phi\phi}=\int_{r_L}^{r_0} r^2\sigma_{\phi\phi}dr \quad (5)$$

$$r_0^2\bar{\sigma}_{\phi\theta}=\int_{r_L}^{r_0} r^2\sigma_{\phi\theta}dr \quad (6)$$

$$r_0^2\bar{\sigma}_{\theta\theta}=\int_{r_L}^{r_0} r^2\sigma_{\theta\theta}dr \quad (7)$$

$$r_0^2\bar{f_\theta}=-(r_L)^3\sigma_{\theta r} \quad (8)$$

$$r_0^2\bar{f_\phi}=-(r_L)^3\sigma_{\phi r}. \quad (9)$$

Then the depth integrals, from r_L to r_0, of the force-balance equations ((1) and (2)) can be written as:

$$\frac{1}{\cos\theta}\frac{\partial\bar{\sigma}_{\phi\phi}}{\partial\phi}+\frac{1}{\cos^2\theta}\frac{\partial}{\partial\theta}(\bar{\sigma}_{\phi\theta}\cos^2\theta)+\bar{f_\phi}=0 \quad (10)$$

and

$$\frac{1}{\cos\theta}\frac{\partial\bar{\sigma}_{\phi\theta}}{\partial\phi}+\frac{1}{2}\frac{\partial}{\partial\theta}[\bar{\sigma}_{\theta\theta}+\bar{\sigma}_{\phi\phi}]+\frac{1}{2\cos^2\theta}\frac{\partial}{\partial\theta}([\bar{\sigma}_{\theta\theta}-\bar{\sigma}_{\phi\phi}]\cos^2\theta)+\bar{f_\theta}=0 \quad (11)$$

where

$$\bar{f_\theta} = -\frac{(r_L)^3}{r_0^2}\sigma_{\theta r}|_{r_L} \tag{12}$$

and

$$\bar{f_\phi} = -\frac{(r_L)^3}{r_0^2}\sigma_{\phi r}|_{r_L} \tag{13}$$

where $\sigma_{\phi r}|_{r_L}$ and $\sigma_{\theta r}|_{r_L}$ are the tractions applied at a constant reference level, r_L. Let

$$\sigma_0 = \frac{1}{2}[\bar{\sigma}_{\phi\phi} + \bar{\sigma}_{\theta\theta}], \tag{14}$$

$$\tilde{\sigma}_{\alpha\beta} = \bar{\sigma}_{\alpha\beta} - \delta_{\alpha\beta}\sigma_0 \tag{15}$$

σ_0 are the dilational terms and $\tilde{\sigma}_{\alpha\beta}$ are the shear terms and $\tilde{\sigma}_{\theta\theta} = -\tilde{\sigma}_{\phi\phi}$. Substituting the above into equations (10) and (11) yields

$$\frac{1}{\cos\theta}\frac{\partial\tilde{\sigma}_{\phi\phi}}{\partial\phi} + \frac{1}{\cos^2\theta}\frac{\partial}{\partial\theta}(\tilde{\sigma}_{\phi\theta}\cos^2\theta) + \frac{1}{\cos\theta}\frac{\partial\sigma_0}{\partial\phi} + \bar{f_\phi} = 0 \tag{16}$$

and

$$\frac{1}{\cos\theta}\frac{\partial\tilde{\sigma}_{\phi\theta}}{\partial\phi} - \frac{1}{\cos^2\theta}\frac{\partial}{\partial\theta}(\tilde{\sigma}_{\phi\phi}\cos^2\theta) + \frac{\partial\sigma_0}{\partial\theta} + \bar{f_\theta} = 0 \tag{17}$$

Only the dilational term is affected by the conversion from total to deviatoric stresses. Substituting $\tau_0 = \sigma_0 - \bar{\sigma}_{rr}$, equations (16) and (17) become

$$\frac{1}{\cos\theta}\frac{\partial\tilde{\sigma}_{\phi\phi}}{\partial\phi} + \frac{1}{\cos^2\theta}\frac{\partial}{\partial\theta}(\tilde{\sigma}_{\phi\theta}\cos^2\theta) + \frac{1}{\cos\theta}\frac{\partial\tau_0}{\partial\phi} + F_\phi = 0 \tag{18}$$

and

$$\frac{1}{\cos\theta}\frac{\partial\tilde{\sigma}_{\phi\theta}}{\partial\phi} - \frac{1}{\cos^2\theta}\frac{\partial}{\partial\theta}(\tilde{\sigma}_{\phi\phi}\cos^2\theta) + \frac{\partial\tau_0}{\partial\theta} + F_\theta = 0 \tag{19}$$

where

$$F_\phi = \bar{f_\phi} + \frac{1}{\cos\theta}\frac{\partial\bar{\sigma}_{rr}}{\partial\phi} \tag{20}$$

$$F_\theta = \bar{f_\theta} + \frac{\partial\bar{\sigma}_{rr}}{\partial\theta}. \tag{21}$$

The second terms of the effective body forces, F_ϕ and F_θ in (20) and (21) are the horizontal gradients of GPE, or the horizontal gradients of the depth integral of total radial stress, $\bar{\sigma}_{rr}$. We solve the force-balance equations in response to the negative of the tractions in $\bar{f_\phi}$ and $\bar{f_\theta}$ (see (12) and (13)) separately from the response to the GPE differences. Although this

chapter deals primarily with solution methods to the force-balance equations associated with the response to mantle flow-related tractions (f_ϕ, f_θ), we point out that the solution form for the response to GPE differences is the same as the solution form for the response to poloidal flow. Equations (18) and (19) can be rewritten as

$$F_\phi = -\frac{1}{\cos\theta}\frac{\partial\tilde{\sigma}_{\phi\phi}}{\partial\phi} - \frac{1}{\cos^2\theta}\frac{\partial}{\partial\theta}(\tilde{\sigma}_{\phi\theta}\cos^2\theta) - \frac{1}{\cos\theta}\frac{\partial\tau_0}{\partial\phi} \tag{22}$$

and

$$F_\theta = -\frac{1}{\cos\theta}\frac{\partial\tilde{\sigma}_{\phi\theta}}{\partial\phi} + \frac{1}{\cos^2\theta}\frac{\partial}{\partial\theta}(\tilde{\sigma}_{\phi\phi}\cos^2\theta) - \frac{\partial\tau_0}{\partial\theta} \tag{23}$$

Recall that we minimize the I functional below in order to solve the above equations, given estimates of F_ϕ and F_θ, where that solution provides a minimum of the second invariant of deviatoric stress:

$$\begin{aligned} I = {} & \frac{1}{2}\int\int\frac{1}{\mu}\left[\frac{2}{3}\tau_0^2 + 2\tilde{\sigma}_{\phi\phi}^2 + 2\tilde{\sigma}_{\phi\theta}^2\right]\cos\theta d\phi d\theta \\ & + \int\int\left\{\lambda_\phi\left[\frac{1}{\cos\theta}\frac{\partial\tilde{\sigma}_{\phi\phi}}{\partial\phi} + \frac{1}{\cos^2\theta}\frac{\partial}{\partial\theta}\left(\tilde{\sigma}_{\phi\theta}\cos^2\theta\right) + \frac{1}{\cos\theta}\frac{\partial\tau_0}{\partial\phi} + F_\phi\right]\right. \\ & \left. + \lambda_\theta\left[\frac{1}{\cos\theta}\frac{\partial\tilde{\sigma}_{\phi\theta}}{\partial\phi} - \frac{1}{\cos_\theta^2}\frac{\partial}{\partial\theta}(\tilde{\sigma}_{\phi\phi}\cos_\theta^2) + \frac{\partial\tau_0}{\partial\theta} + F_\theta\right]\cos\theta d\phi d\theta. \end{aligned} \tag{24}$$

Optimizing this I functional with respect to $\tau_0, \tilde{\sigma}_{\phi\phi}, \tilde{\sigma}_{\phi\theta}$ respectively yields

$$\frac{2}{3\mu}\tau_0\cos\theta - \frac{\partial\lambda_\phi}{\partial\phi} - \frac{\partial}{\partial\theta}\left(\lambda_\theta\cos\theta\right) = 0, \tag{25}$$

$$\frac{2}{\mu}\tilde{\sigma}_{\phi\phi}\cos\theta - \frac{\partial\lambda_\phi}{\partial\phi} + \cos^2\theta\frac{\partial}{\partial\theta}\left(\frac{\lambda_\theta}{\cos\theta}\right) = 0, \tag{26}$$

$$\frac{2}{\mu}\tilde{\sigma}_{\phi\theta}\cos\theta - \cos^2\theta\frac{\partial}{\partial\theta}\left(\frac{\lambda_\phi}{\cos\theta}\right) - \frac{\partial\lambda_\theta}{\partial\phi} = 0. \tag{27}$$

Hence,

$$\tau_0 = \frac{\mu}{2}\left[\frac{1}{\cos\theta}\frac{\partial\lambda_\phi}{\partial\phi} + \frac{1}{\cos\theta}\frac{\partial}{\partial\theta}\left(\lambda_\theta\cos\theta\right)\right] \tag{28}$$

$$\tilde{\sigma}_{\phi\phi} = \frac{\mu}{2}\left[\frac{1}{\cos\theta}\frac{\partial\lambda_\phi}{\partial\phi} - \cos\theta\frac{\partial}{\partial\theta}\left(\frac{\lambda_\theta}{\cos\theta}\right)\right] \tag{29}$$

$$\tilde{\sigma}_{\phi\theta} = \frac{\mu}{2}\left[\cos\theta\frac{\partial}{\partial\theta}\left(\frac{\lambda_\phi}{\cos\theta}\right) + \frac{1}{\cos\theta}\frac{\partial\lambda_\phi}{\partial\phi}\right], \tag{30}$$

which leads to

$$\bar{\tau}_{\phi\phi} = \mu(\tau_0 + \tilde{\sigma}_{\phi\phi}) = \mu\left(\frac{1}{\cos\theta}\frac{\partial\lambda_\phi}{\partial\phi} - \lambda_\theta \tan\theta\right) \tag{31}$$

$$\bar{\tau}_{\theta\theta} = \mu(\tau_0 - \tilde{\sigma}_{\phi\phi}) = \mu\frac{\partial\lambda_\theta}{\partial\theta} \tag{32}$$

$$\bar{\tau}_{\phi\theta} = \mu(\tilde{\sigma}_{\phi\theta}) = \frac{\mu}{2}\left(\frac{\partial\lambda_\phi}{\partial\theta} + \frac{1}{\cos\theta}\frac{\partial\lambda_\theta}{\partial\phi} + \lambda_\phi \tan\theta\right). \tag{33}$$

Note that (31), (32) and (33) have the same form as deviatoric stress on a sphere, where the Lagrange multipliers, λ_ϕ and λ_θ hold the same position as the horizontal velocities, u_ϕ, u_θ, respectively. The one exception is that there is no term equivalent to u_r/r in (31) and (32), as this term is expected to be small and is therefore not dealt with here. Recall that we actually minimize the *J* functional in order to solve the force-balance equations, and doing so is equivalent to minimizing the *I* functional and satisfying the conditions within the *I* functional (*Flesch et al.*, 2001). If we substitute (31)-(33) into the *J* functional,

$$J = \int\int \left\{ \left[\begin{pmatrix} \bar{\tau}_{\phi\phi} \\ \bar{\tau}_{\theta\theta} \\ \bar{\tau}_{\phi\theta} \end{pmatrix} - \begin{pmatrix} \Phi^{obs}_{\phi\phi} \\ \Phi^{obs}_{\theta\theta} \\ \Phi^{obs}_{\phi\theta} \end{pmatrix} \right]^T \widetilde{V}^{-1} \left[\begin{pmatrix} \bar{\tau}_{\phi\phi} \\ \bar{\tau}_{\theta\theta} \\ \bar{\tau}_{\phi\theta} \end{pmatrix} - \begin{pmatrix} \Phi^{obs}_{\phi\phi} \\ \Phi^{obs}_{\theta\theta} \\ \Phi^{obs}_{\phi\theta} \end{pmatrix} \right] \right\} \cos\theta d\phi d\theta \tag{34}$$

(see *Flesch et al.* (2001) and Appendix B in *Ghosh et al.* (2008)) and minimize *J* with respect to $\lambda_\phi, \lambda_\theta$, we have the following:

$$\frac{1}{\cos\theta}\frac{\partial}{\partial\phi}\left[\tilde{\sigma}_{\phi\phi} - \tilde{\sigma}^{obs}_{\phi\phi}\right] + \frac{1}{\cos^2\theta}\frac{\partial}{\partial\theta}\left(\left[\tilde{\sigma}_{\phi\theta} - \tilde{\sigma}^{obs}_{\phi\theta}\right]\cos^2\theta\right) + \frac{1}{\cos\theta}\frac{\partial}{\partial\phi}[\tau_0 - \tau^{obs}_0] = 0 \tag{35}$$

and

$$\frac{1}{\cos\theta}\frac{\partial}{\partial\phi}\left[\tilde{\sigma}_{\phi\theta} - \tilde{\sigma}^{obs}_{\phi\theta}\right] - \frac{1}{\cos^2\theta}\frac{\partial}{\partial\theta}\left(\left[\tilde{\sigma}_{\phi\phi} - \tilde{\sigma}^{obs}_{\phi\phi}\right]\cos^2\theta\right) + \frac{\partial}{\partial\phi}[\tau_0 - \tau^{obs}_0] = 0 \tag{36}$$

where

$$\tau^{obs}_0 = \frac{1}{2}\left(\tau^{obs}_{\phi\phi} + \tau^{obs}_{\theta\theta}\right) \tag{37}$$

$$\tilde{\sigma}^{obs}_{\alpha\beta} = \tau^{obs}_{\alpha\beta} - \delta_{\alpha\beta}\tau^{obs}_0. \tag{38}$$

The potentials $\Phi^{obs}_{\phi\phi}, \Phi^{obs}_{\theta\theta}$, and $\Phi^{obs}_{\phi\theta}$ in the J functional are:

$$\begin{pmatrix} \Phi^{obs}_{\phi\phi} \\ \Phi^{obs}_{\theta\theta} \\ \Phi^{obs}_{\phi\theta} \end{pmatrix} = \widetilde{V} \begin{pmatrix} \tau^{obs}_{\phi\phi} \\ \tau^{obs}_{\theta\theta} \\ 2\tau^{obs}_{\phi\theta} \end{pmatrix} \tag{39}$$

where

$$\widetilde{V} = \begin{pmatrix} \frac{2}{3} & -\frac{1}{3} & 0 \\ -\frac{1}{3} & \frac{2}{3} & 0 \\ 0 & 0 & \frac{1}{2} \end{pmatrix}. \tag{40}$$

Equating terms in (35) and (36) to terms in the force balance equations, (22) and (23), we see that:

$$F_\phi = -\frac{1}{\cos\theta}\frac{\partial \tilde{\sigma}^{obs}_{\phi\phi}}{\partial\phi} - \frac{1}{\cos^2\theta}\frac{\partial}{\partial\theta}(\tilde{\sigma}^{obs}_{\phi\theta}\cos^2\theta) - \frac{1}{\cos\theta}\frac{\partial \tau^{obs}_0}{\partial\phi}, \tag{41}$$

$$F_\theta = -\frac{1}{\cos\theta}\frac{\partial \tilde{\sigma}^{obs}_{\phi\theta}}{\partial\phi} + \frac{1}{\cos^2\theta}\frac{\partial}{\partial\theta}(\tilde{\sigma}^{obs}_{\phi\phi}\cos^2\theta) - \frac{\partial \tau^{obs}_0}{\partial\theta} \tag{42}$$

Note that $\tilde{\sigma}^{obs}_{\phi\phi}, \tilde{\sigma}^{obs}_{\phi\theta}$, and τ^{obs}_0 are potentials, which through (37), (38), (39) and (40) define $\Phi^{obs}_{\phi\phi}, \Phi^{obs}_{\theta\theta}, \Phi^{obs}_{\phi\theta}$ in the J functional . Our procedure consists of the following. We first find solutions to the potentials that satisfy (41) and (42). Once the potentials are obtained, equations (37)-(40) are used to calculate the Φ^{obs}_{ij} potentials. These potentials are substituted into the J functional and the J functional is optimized over a 2.5×2.5 degree grid to define one self-consistent deviatoric stress field that satisfies the force-balance equations. The resultant deviatoric stress field constitutes a global minimum of the second invariant of stress that balances the body force inputs. The potentials that satisfy equations (41) and (42) are non-unique, whereas the resultant deviatoric stress field, obtained from the minimization of the J functional, is unique. Below we will show two different ways of obtaining solutions to (41) and (42) to define the potentials, and we will demonstrate that as long as these potentials are well-behaved at the poles, the deviatoric stress solutions are unique.

The above equations are solved in either of two ways:

(1) taking $\tau_0 = 0$ while $\tilde{\sigma}_{\phi\phi}$ and $\tilde{\sigma}_{\phi\theta}$ are non-zero (Case I), or

(2) taking τ_0 to be non-zero while $\tilde{\sigma}_{\phi\phi} = \tilde{\sigma}_{\phi\theta} = 0$ (Case II).

Although the forms of the potentials are very different, we obtain identical stress fields

from them when appropriate conditions are used.

For Case I, let

$$\sigma_{\phi\phi} = \tilde{\sigma}^{obs}_{\phi\phi}\cos^2\theta; \qquad\qquad \sigma_{\phi\theta} = \tilde{\sigma}^{obs}_{\phi\theta}\cos^2\theta$$

so that

$$F_\phi = -\frac{1}{\cos\theta}\frac{\partial\sigma_{\phi\phi}}{\partial\phi}\frac{1}{\cos^2\theta} - \frac{1}{\cos^2\theta}\frac{\partial\sigma_{\phi\theta}}{\partial\theta}, \tag{43}$$

$$F_\theta = \frac{1}{\cos^2\theta}\frac{\partial\sigma_{\phi\phi}}{\partial\theta} - \frac{1}{\cos^2\theta}\frac{1}{\cos\theta}\frac{\partial\sigma_{\phi\theta}}{\partial\phi}. \tag{44}$$

This implies that

$$\cos^2\theta F_\phi = -\frac{1}{\cos\theta}\frac{\partial\sigma_{\phi\phi}}{\partial\phi} - \frac{\partial\sigma_{\phi\theta}}{\partial\theta} \tag{45}$$

and

$$\cos^2\theta F_\theta = \frac{\partial\sigma_{\phi\phi}}{\partial\theta} - \frac{1}{\cos\theta}\frac{\partial\sigma_{\phi\theta}}{\partial\phi} \tag{46}$$

If we switch from latitude, θ, to colatitude, $\bar{\theta}$, then $\cos\theta$ becomes $\sin\bar{\theta}$, F_θ becomes -$F_{\bar{\theta}}$ and $\frac{\partial}{\partial\theta}$ becomes -$\frac{\partial}{\partial\bar{\theta}}$. Hence, (45) and (46) can be rewritten as:

$$\sin^2\bar{\theta}F_\phi = -\frac{1}{\sin\theta}\frac{\partial\sigma_{\phi\phi}}{\partial\phi} + \frac{\partial\sigma_{\phi\theta}}{\partial\theta} \tag{47}$$

$$\sin^2\bar{\theta}F_{\bar{\theta}} = \frac{\partial\sigma_{\phi\phi}}{\partial\theta} + \frac{1}{\sin\theta}\frac{\partial\sigma_{\phi\theta}}{\partial\phi} \tag{48}$$

Let

$$\sigma_{\phi\phi} = \sum_{l=0,m=0}^{\infty} Z^{lm}_{11}Y_{lm} = Z^{lm}_{11}Y_{lm} \tag{49}$$

and

$$\sigma_{\phi\theta} = \sum_{l=0,m=0}^{\infty} Z^{lm}_{12}Y_{lm} = Z^{lm}_{12}Y_{lm}, \tag{50}$$

where Y_{lm} is the surface normalized spherical harmonic of degree l and order m, and Z^{lm}_{11} and Z^{lm}_{12} are coefficients. Hence,

$$\sin^2\bar{\theta}F_\phi = -Z^{lm}_{11}Y^{01}_{lm} + Z^{lm}_{12}Y^{10}_{lm} \tag{51}$$

$$\sin^2\bar{\theta}F_\theta = Z^{lm}_{11}Y^{10}_{lm} + Z^{lm}_{12}Y^{01}_{lm}, \tag{52}$$

where

$$Y_{lm}^{10} = \frac{\partial Y_{lm}}{\partial \theta}$$

and

$$Y_{lm}^{01} = \frac{1}{\sin\theta}\frac{\partial Y_{lm}}{\partial \phi}.$$

Therefore,

$$Z_{11}^{lm} = \int \left[\sin^2\bar{\theta} F_{\bar{\theta}} Y_{lm}^{10} - \sin^2\bar{\theta} F_{\phi} Y_{lm}^{01}\right] dS \tag{53}$$

$$Z_{12}^{lm} = \int \left[\sin^2\bar{\theta} F_{\bar{\theta}} Y_{lm}^{01} + \sin^2\bar{\theta} F_{\phi} Y_{lm}^{10}\right] dS \tag{54}$$

where from (12) and (13), F_ϕ and $F_{\bar{\theta}}$ are given as:

$$F_\phi = -\frac{{r_L}^3}{{r_0}^2}\tau_{\phi r}|_{r_L} = -\frac{{r_L}^3}{{r_0}^2}\left[Z_4^{lm} Y_{lm}^{01}(\phi,\bar{\theta}) - Z_6^{lm} Y_{lm}^{10}(\phi,\bar{\theta})\right], \tag{55}$$

$$F_{\bar{\theta}} = -F_\theta = \frac{{r_L}^3}{{r_0}^2}\tau_{\bar{\theta} r}|_{r_L} = \frac{{r_L}^3}{{r_0}^2}\left[Z_4^{lm} Y_{lm}^{10}(\phi,\bar{\theta}) + Z_6^{lm} Y_{lm}^{01}(\phi,\bar{\theta})\right], \tag{56}$$

where Z_4^{lm} and Z_6^{lm} are the poloidal and toroidal coefficients from the mantle convection model and Y_{lm}^{10} and Y_{lm}^{01} are defined as above (*Wen and Anderson*, 1997b). Therefore, given distributions of the effective body forces, F_ϕ, F_θ, defined in the circulation model, the coefficients can be obtained from (53) and (54) and then used in (49) and (50) to yield the potentials. In this case, the potentials in (39) are given as:

$$(\Phi_{\phi\phi}^{obs}, \Phi_{\theta\theta}^{obs}, \Phi_{\phi\theta}^{obs})^T = \left(\tilde{\sigma}_{\phi\phi}^{obs}, -\tilde{\sigma}_{\phi\phi}^{obs}, \tilde{\sigma}_{\phi\theta}^{obs}\right)^T. \tag{57}$$

The potentials have a singularity problem at the poles only for $m = 0$ and $m = 1$; there is no singularity at the poles for $m \geq 2$.

Case II is only possible if there are no toroidal components in the flow model. If toroidal flow exists, then, this method for Case II will only yield the poloidal part of the total solution associated with mantle flow. The toroidal part of the solution can be calculated using a methodology that we discuss later. This method of Case II avoids singularity problems at the poles. For Case II, the poloidal components of F_ϕ and F_θ (from (41) and (42)) are:

$$F_\phi = -\frac{1}{\cos\theta}\frac{\partial \tau_0^{obs}}{\partial \phi} = -\frac{{r_L}^3}{{r_0}^2}\tau_{\phi r}|_{r_L} = -\frac{{r_L}^3}{{r_0}^2}\left[\frac{1}{\cos\theta} Z_4^{lm}\frac{\partial Y_{lm}}{\partial \phi}\right], \tag{58}$$

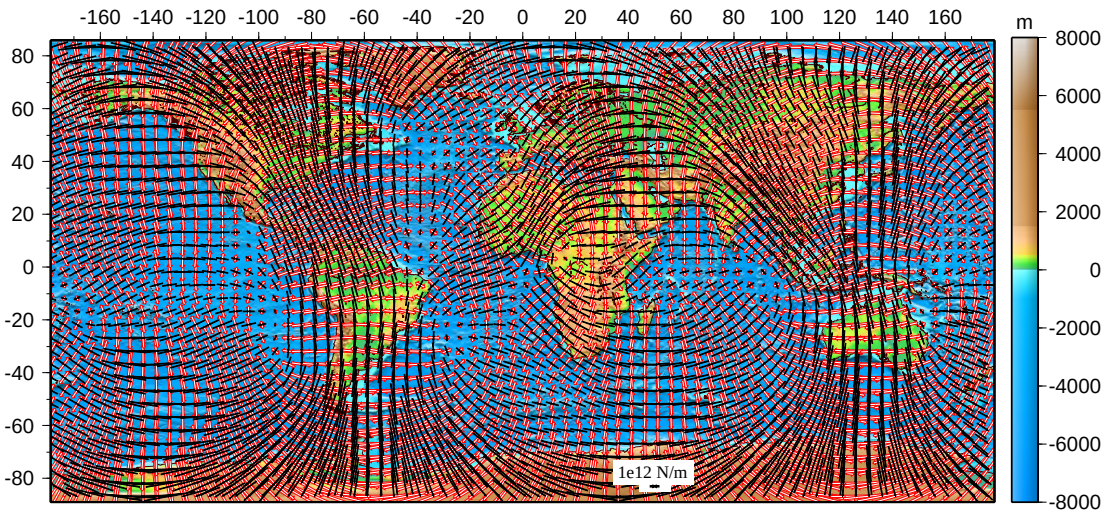

Figure 1: Global distribution of the observed potentials, $\tilde{\sigma}^{obs}_{\phi\phi}, \tilde{\sigma}^{obs}_{\phi\theta}$, from tractions calculated by Case I for $m \geq 2$, for an isoviscous case.

$$F_\theta = -\frac{\partial \tau_0^{obs}}{\partial \theta} = -\frac{{r_L}^3}{{r_0}^2}\tau_{\theta r}|_{r_L} = -\frac{{r_L}^3}{{r_0}^2}\left[Z_4^{lm}\frac{\partial Y_{lm}}{\partial \theta}\right]. \tag{59}$$

A solution that works is

$$\tau_0 = \frac{{r_L}^3}{{r_0}^2} Z_4^{lm} Y_{lm}(\theta, \phi) \tag{60}$$

Hence, the potentials in (39) are

$$(\Phi^{obs}_{\phi\phi}, \Phi^{obs}_{\theta\theta}, \Phi^{obs}_{\phi\theta})^T = \left(\frac{\tau_0}{3}, \frac{\tau_0}{3}, 0\right)^T. \tag{61}$$

Note that for dealing with GPE differences (see equations (18)-(21)) the potentials in (61) will also work, where $\tau_0 = -\bar{\sigma}_{rr}$, the negative of the depth integrated total radial stress, or GPE (see equations (20) and (21)).

In absence of toroidal flow, Cases I and II should yield the same answer. However, the first method fails to yield proper results since at orders $m = 0$ and $m = 1$, $\tilde{\sigma}^{obs}_{\phi\phi}$ and $\tilde{\sigma}^{obs}_{\phi\theta}$ become infinitely large at the poles (discussed later). Hence, only the second approach (Case II, $\tau_0^{obs} \neq 0, \tilde{\sigma}^{obs}_{\phi\phi} = \tilde{\sigma}^{obs}_{\phi\theta} = 0$) is the valid approach for the poloidal only case, irrespective of values of m. For $m \geq 2$, both methods yield identical results.

We demonstrate that the two methods yield identical results for values of $m \geq 2$ in absence of toroidal flow and we use two examples in order to demonstrate that. The first example is that of an isoviscous case, the second is that of one of our best-fitting poloidal

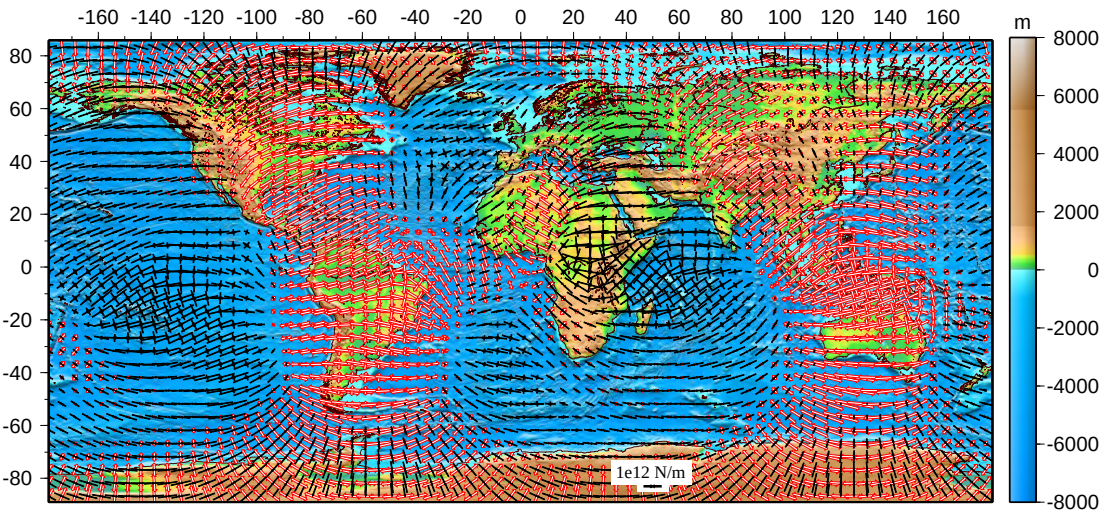

Figure 2: Global distribution of vertically integrated horizontal deviatoric stresses from tractions calculated by Case I, based on potentials in Figure 1.

cases, with strong lithosphere and weak asthenosphere. We first calculate the deviatoric stress response (Figures 2 and 14) from potentials (Figures 1 and 13) calculated using Case I ($\tau_0 = 0$) for $m \geq 2$ for an isoviscous case and our best-fitting poloidal case, respectively. We compare these stress results with deviatoric stresses from potentials (Figures 3 and 15) computed by Case II ($\tau_0 \neq 0$) for $m \geq 2$ values (Figures 4 and 16). The deviatoric stress fields for the two cases are identical, as expected. The potentials (Figures 5 and 17) and the resultant deviatoric stresses (Figures 6 and 18), for Case I, for $m = 0, 1$, demonstrate the singularity phenomenon at the poles, which is absent in Case II (Figures 7, 8 and 19, 20). The deviatoric stresses calculated by Case I and Case II, for all m, show substantial differences between the two stress results in a number of areas (Figures 10, 12 and 22, 24), especially at the poles where the deviatoric stresses for the former case are much larger. Differences also exist in eastern and northern North America, east Pacific as well as large parts of Asia. These differences arise because of differences in deviatoric stresses for orders $m = 0, 1$ for the two approaches. For Case I, the potentials blow up at the poles, whereas for Case II, the potentials are well-behaved at the poles. The potentials for all m for the two cases are shown in Figures 9, 11 and 21, 23. In summary, for poloidal flow only, Case I can only be used for $m \geq 2$. Case II can supply the remaining potentials for $m = 0$, $m = 1$. Alternatively, Case II can be used for all m for the poloidal case only.

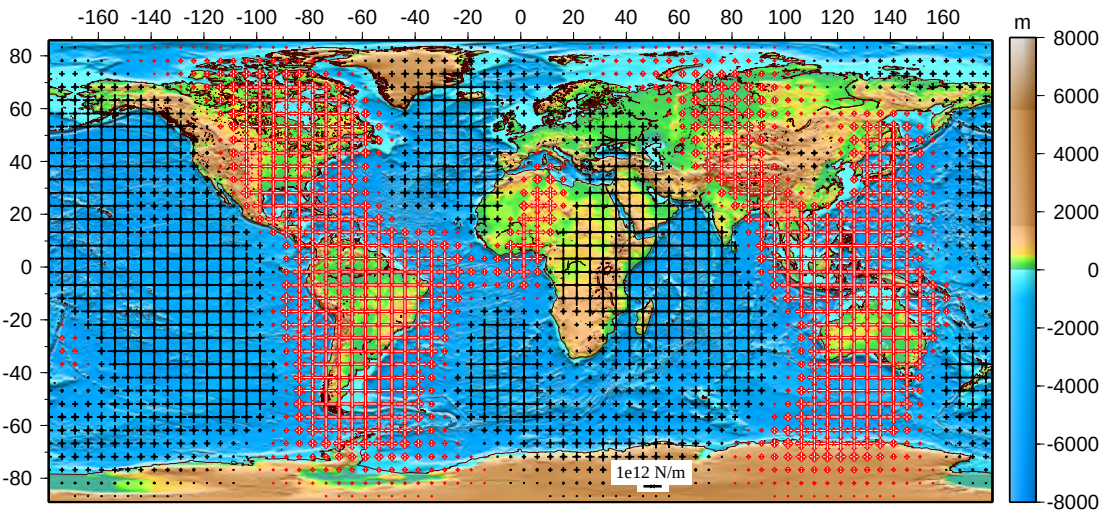

Figure 3: Global distribution of the observed potentials, $\frac{1}{3}\tau_0^{obs}$ (61), from tractions calculated by Case II for $m \geq 2$, for an isoviscous case.

When toroidal flow is present, potentials from Case I will yield the total (both poloidal and toroidal) deviatoric stress field. However, as discussed earlier, Case I yields infinitely large potentials at the poles for $m = 0, 1$ and hence, cannot be used to compute the deviatoric stresses from the total flow field (for all m). It is necessary, therefore, to find a method to supply potentials for $m = 0$, $m = 1$, for the toroidal case. The following section discusses the method (denoted as Case III) in dealing with the toroidal terms of the deviatoric stress field.

Presuming that the terms $\tilde{\sigma}_{\phi\phi}, \tilde{\sigma}_{\phi\theta}$ and $\bar{\tau}_0$ have been Fourier transformed so that they have a ϕ dependence of the form $e^{im\phi}$, (41) and (42) can be rewritten as

$$F_\phi = -\frac{im}{\cos\theta}\tilde{\sigma}_{\phi\phi}^{obs} - \frac{1}{\cos^2\theta}\frac{\partial}{\partial\theta}(\tilde{\sigma}_{\phi\theta}^{obs}\cos^2\theta) - \frac{im}{\cos\theta}\tau_0^{obs} \tag{62}$$

$$F_\theta = -\frac{im}{\cos\theta}\tilde{\sigma}_{\phi\theta}^{obs} + \frac{1}{\cos^2\theta}\frac{\partial}{\partial\theta}(\tilde{\sigma}_{\phi\phi}^{obs}\cos^2\theta) - \frac{\partial\tau_0^{obs}}{\partial\theta} \tag{63}$$

Defining the following:

$$\sigma_{\phi\phi}^{obs} = \tau_0^{obs} + \tilde{\sigma}_{\phi\phi}^{obs} \qquad \tau_0^{obs} = \frac{1}{2}(\sigma_{\phi\phi}^{obs} + \sigma_{\theta\theta}^{obs})$$

$$\sigma_{\phi\theta}^{obs} = \tilde{\sigma}_{\phi\theta}^{obs} \qquad \tilde{\sigma}_{\phi\phi}^{obs} = \frac{1}{2}(\sigma_{\phi\phi}^{obs} - \sigma_{\theta\theta}^{obs})$$

$$\sigma_{\theta\theta}^{obs} = \tau_0^{obs} - \tilde{\sigma}_{\phi\phi}^{obs} \qquad \tilde{\sigma}_{\phi\theta}^{obs} = \sigma_{\phi\theta}^{obs},$$

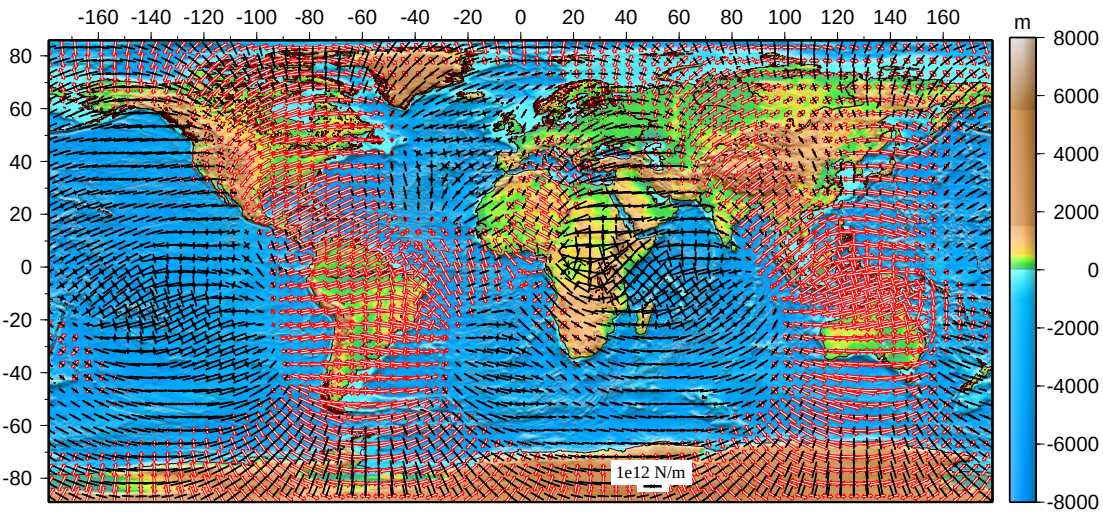

Figure 4: Global distribution of vertically integrated horizontal deviatoric stresses from tractions calculated by Case II, based on potentials in Figure 3. Note that this stress field is identical with the stress field in Figure 2, generated using Case I.

(62) and (63) yield

$$F_\phi = -\frac{im}{\cos\theta}\sigma_{\phi\phi}^{obs} - \frac{1}{\cos^2\theta}\frac{\partial}{\partial\theta}(\sigma_{\phi\theta}^{obs}\cos^2\theta) \tag{64}$$

$$F_\theta = -\frac{\sin\theta}{\cos\theta}\sigma_{\phi\phi}^{obs} - \frac{im}{\cos\theta}\tilde{\sigma}_{\phi\theta}^{obs} - \frac{1}{\cos\theta}\frac{\partial}{\partial\theta}(\sigma_{\theta\theta}^{obs}\cos\theta). \tag{65}$$

A solution that satisfies (64) and (65) is

$$\sigma_{\phi\theta}^{obs} = -\frac{1}{\cos^2\theta}\int_{-\pi/2}^{\theta}\left[F_\phi\cos^2\theta + im\sigma_{\phi\phi}^{obs}\cos\theta\right]d\theta \tag{66}$$

$$\sigma_{\theta\theta}^{obs} = -\frac{1}{\cos\theta}\int_{-\pi/2}^{\theta}\left[F_\theta\cos\theta + imF_\phi\cos\theta\sin\theta + (1-m^2)\sigma_{\phi\phi}^{obs}\sin\theta\right]d\theta - im\sigma_{\phi\theta}^{obs}\sin\theta \tag{67}$$

Once again, presuming that the terms have a ϕ dependence of the form $e^{im\phi}$, the poloidal components of F_ϕ and F_θ can be written as

$$F_\phi = \frac{im}{\cos\theta}\alpha, \qquad\qquad F_\theta = \frac{\partial\alpha}{\partial\theta},$$

where $\alpha = -Z_4^{lm}Y_{lm}(\theta,\phi)$ (*Ghosh et al.*, 2008), so that equations (62) and (63) become

$$\sigma_{\phi\theta}^{obs} = -\frac{im}{\cos^2\theta}\int_{-\pi/2}^{\theta}\left[\alpha\cos\theta + \sigma_{\phi\phi}^{obs}\cos\theta\right]d\theta \tag{68}$$

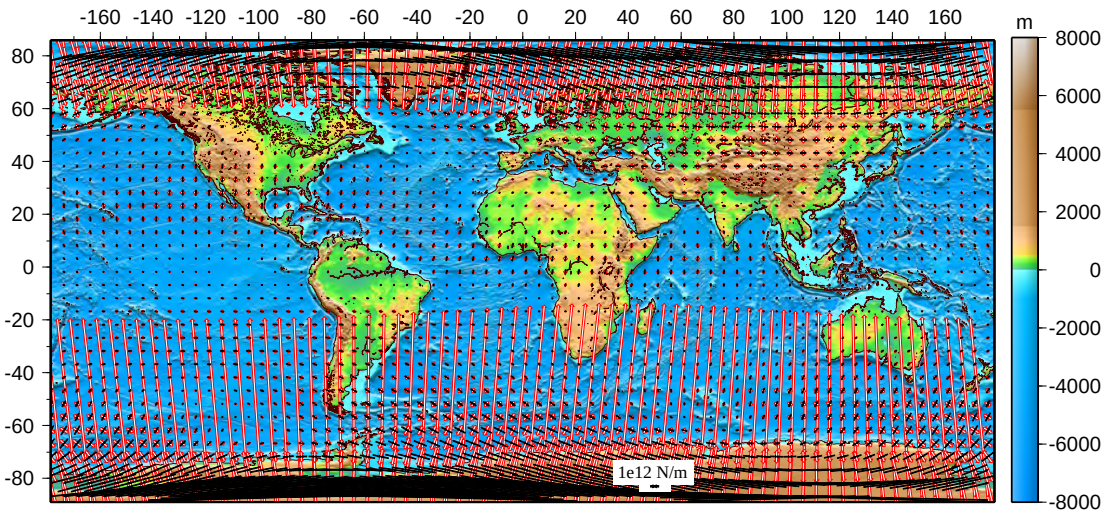

Figure 5: Global distribution of the observed potentials, $\tilde{\sigma}^{obs}_{\phi\phi}, \tilde{\sigma}^{obs}_{\phi\theta}$, from tractions calculated by Case I for $m = 0, 1$ for an isoviscous case. Note the large potentials at the poles.

$$\sigma^{obs}_{\theta\theta} = -\frac{1}{\cos\theta}\int_{-\pi/2}^{\theta}\left[\frac{\partial\alpha}{\partial\theta}\cos\theta - m^2\alpha\sin\theta + (1-m^2)\sigma^{obs}_{\phi\phi}\sin\theta\right]d\theta - im\sigma^{obs}_{\phi\theta}\sin\theta \quad (69)$$

$$= -\alpha - \frac{1}{\cos\theta}\int_{-\pi/2}^{\theta}\left[(1-m^2)\alpha\sin\theta + (1-m^2)\sigma^{obs}_{\phi\phi}\sin\theta\right]d\theta - im\sigma^{obs}_{\phi\theta}\sin\theta \quad (70)$$

A solution that always works is $\sigma^{obs}_{\phi\phi} = -\alpha$, in which case $\sigma^{obs}_{\phi\theta} = 0, \sigma^{obs}_{\theta\theta} = -\alpha$. This is the "$\tau_0$ solution" (equation (60), Case II). Note that the ${r_L}^3/{r_0}^2$ term for F_ϕ, F_θ (equations (58) and (59)) has been dropped here in this notation, but this factor is included in the calculations.

Similarly, the toroidal tractions can be written as

$$F_\phi = \frac{\partial\beta}{\partial\theta}, \qquad F_\theta = -\frac{im}{\cos\theta}\beta,$$

where $\beta = -Z^{lm}_6 Y_{lm}(\theta,\phi)$, such that (66) and (67) become

$$\begin{aligned}\sigma^{obs}_{\phi\theta} &= -\frac{1}{\cos^2\theta}\int_{-\pi/2}^{\theta}\left[\frac{\partial\beta}{\partial\theta}\cos^2\theta + im\sigma^{obs}_{\phi\phi}\cos\theta\right]d\theta \\ &= -\beta - \frac{1}{\cos^2\theta}\int_{-\pi/2}^{\theta}\left[\beta\sin 2\theta + im\sigma^{obs}_{\phi\phi}\cos\theta\right]d\theta \end{aligned} \quad (71)$$

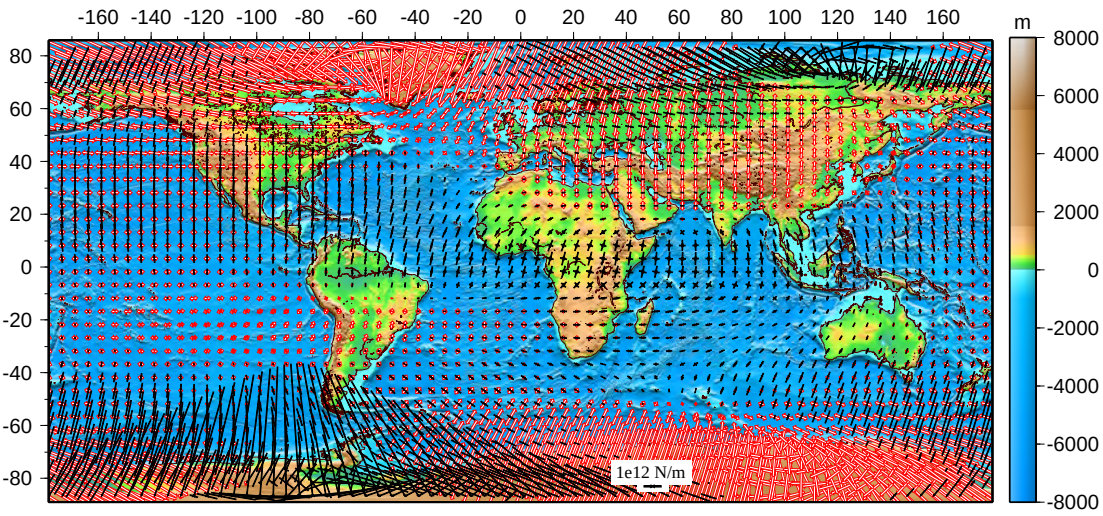

Figure 6: Global distribution of vertically integrated horizontal deviatoric stresses from tractions calculated by Case I, based on potentials in Figure 5. Note the large stresses at the poles.

$$
\begin{aligned}
\sigma^{obs}_{\theta\theta} &= -\frac{1}{\cos\theta}\int_{-\pi/2}^{\theta}\left[-im\beta + im\frac{\partial\beta}{\partial\theta}\cos\theta\sin\theta + (1-m^2)\sigma^{obs}_{\phi\phi}\sin\theta\right]d\theta - im\sigma^{obs}_{\phi\theta}\sin\theta \\
&= -im\beta\sin\theta - \frac{1}{\cos\theta}\int_{-\pi/2}^{\theta}\left[-im\beta(1+\cos 2\theta) + (1-m^2)\sigma^{obs}_{\phi\phi}\sin\theta\right]d\theta - im\sigma^{obs}_{\phi\theta}\sin\theta \\
&= -\frac{1}{\cos\theta}\int_{-\pi/2}^{\theta}\left[-im\beta(1+\cos 2\theta) + (1-m^2)\sigma^{obs}_{\phi\phi}\sin\theta\right]d\theta \\
&\quad + im\frac{\sin\theta}{\cos^2\theta}\int_{-\pi/2}^{\theta}\left[\beta\sin 2\theta + im\sigma^{obs}_{\phi\phi}\cos\theta\right]d\theta \qquad (72)
\end{aligned}
$$

Note that for (71) and (72) the values for $\sigma^{obs}_{\phi\phi}, \sigma^{obs}_{\theta\theta}$, and $\sigma^{obs}_{\phi\theta}$ are found for all l and m.

An infinite number of possible solutions exist for the potentials, $\sigma_{\phi\phi}, \sigma_{\theta\theta}$ and $\sigma_{\phi\theta}$. However, it can be shown that the potentials, $\sigma_{\phi\phi}, \sigma_{\theta\theta}$ and $\sigma_{\phi\theta}$ satisfy (62) and (63) and provide a unique solution to the deviatoric stresses when substituted into the J functional (equation 34). Care must be taken so that these integrals do not become infinitely large at the poles. This situation arises when $\sigma_{\phi\theta}$ or $\sigma_{\theta\theta}$ are odd functions. When these are odd, the integrals become significantly non-zero for latitudes near the poles ($\theta \sim \pi/2$). Division by $\cos\theta$ ($\theta \sim \pi/2$), then makes the values of $\sigma_{\phi\theta}$ and $\sigma_{\theta\theta}$ infinitely large at the poles. Hence, for these cases, the functions within the integrals should be chosen carefully so that the integrals are well behaved at and near the poles (that is, $\int_{-\pi/2}^{\pi/2} = 0$).

We need to consider 2 cases for solutions involving F_ϕ and F_θ:

1) F_ϕ is even and F_θ is odd ($l + m =$ odd). In this case, the problem lies in the integral

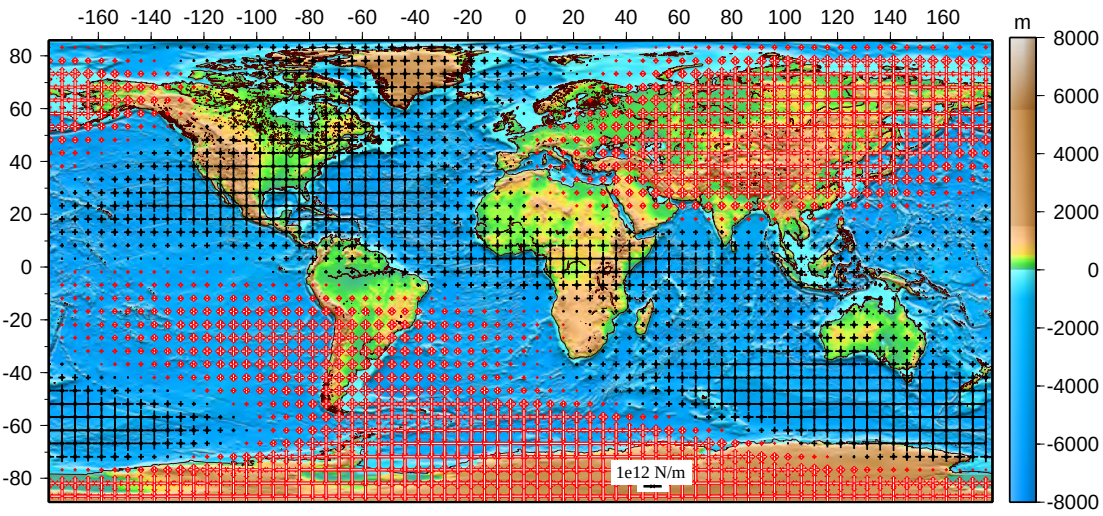

Figure 7: Global distribution of the observed potentials, $\frac{1}{3}\tau_0^{obs}$, from tractions calculated by Case II for $m = 0, 1$ for an isoviscous case. Note that the potentials are well-behaved at the poles.

for $\sigma_{\phi\theta}^{obs}$, which is an odd function, and therefore, $\sigma_{\phi\phi}^{obs}$ within the integral in (71) must be carefully chosen so that the integral from pole to pole goes to zero.

2) F_ϕ is odd and F_θ is even ($l+m =$ even). In this case, the problem lies in the integral for $\sigma_{\theta\theta}^{obs}$ and again $\sigma_{\phi\phi}^{obs}$ in the integral in (72) and must be chosen with caution such that $\int_{-\pi/2}^{\pi/2} = 0$.

Case 1: F_ϕ is even and F_θ is odd ($l+m =$ odd, $\sigma_{\phi\phi}^{obs} =$ even, $\sigma_{\phi\theta}^{obs} =$ odd, $\sigma_{\theta\theta}^{obs} =$ even)

For $m \neq 0$, the constraint on the even function, $\sigma_{\phi\phi}^{obs}$, in addition to being bounded, can take either of the following forms.

(A) Form involving $F_\phi = \frac{\partial\beta}{\partial\theta}$ in equation (71) we want:

$$\int_0^{\pi/2} \Big[\frac{\partial\beta}{\partial\theta}\cos^2\theta + im\sigma_{\phi\phi}^{obs}\cos\theta\Big]d\theta = \int_{-\pi/2}^{0} \Big[\frac{\partial\beta}{\partial\theta}\cos^2\theta + im\sigma_{\phi\phi}^{obs}\cos\theta\Big]d\theta = 0, \qquad (73)$$

Choosing $im\sigma_{\phi\phi}^{obs} = -\frac{\partial\beta}{\partial\theta}\cos\theta$ satisfies (73) and gives $\sigma_{\phi\theta}^{obs} = 0$.

(B) Form involving β in (71) we want:

$$\int_0^{\pi/2} \big[\beta\sin 2\theta + im\sigma_{\phi\phi}^{obs}\cos\theta\big]d\theta = \int_{-\pi/2}^{0} \big[\beta\sin 2\theta + im\sigma_{\phi\phi}^{obs}\cos\theta\big]d\theta = 0 \qquad (74)$$

Choosing

$$\sigma_{\phi\phi}^{obs} = -\frac{2\beta}{im}\sin\theta = \frac{2i\beta}{m}\sin\theta \qquad (75)$$

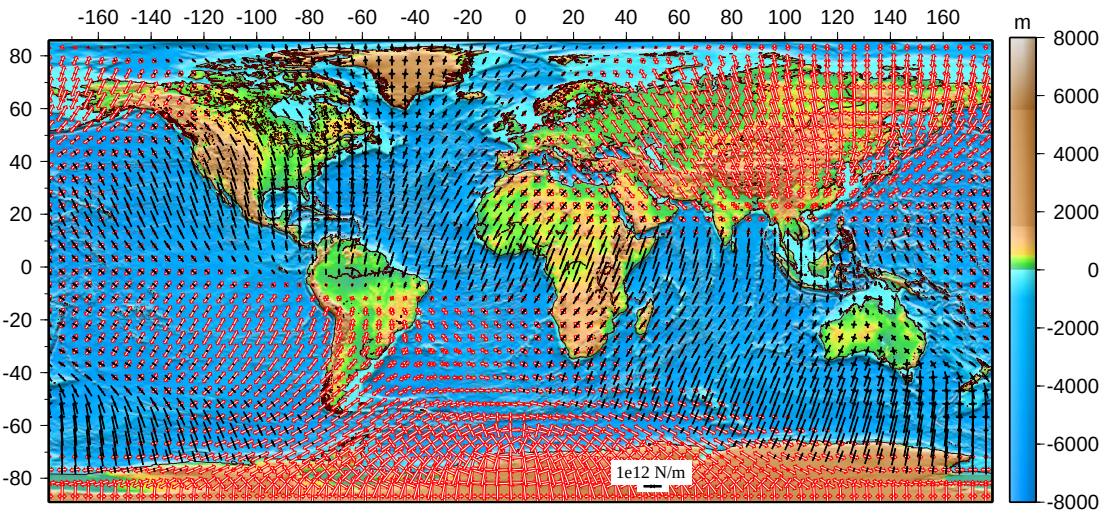

Figure 8: Global distribution of vertically integrated horizontal deviatoric stresses from tractions calculated by Case II, based on potentials in Figure 7 (Case II, $m = 0, 1$).

satisfies (74) and gives

$$\sigma^{obs}_{\phi\theta} = -\beta \tag{76}$$

and

$$\sigma^{obs}_{\theta\theta} = -\frac{1}{\cos\theta}\int_{-\pi/2}^{\theta}\left[-2im\beta + \frac{2i}{m}\beta\sin^2\theta\right]d\theta \tag{77}$$

Case 2: F_ϕ is odd, F_θ is even ($l+m$ = even, $\sigma^{obs}_{\phi\phi}$ = odd, $\sigma^{obs}_{\phi\theta}$ = even, $\sigma^{obs}_{\theta\theta}$ = odd)

The constraint on the odd function $\sigma^{obs}_{\phi\phi}$, in addition to being bounded, can take either of the following forms:

(A) Form involving $\frac{\partial\beta}{\partial\theta}$ and β in (72) we want:

$$\int_0^{\pi/2}\left[-im\beta + im\frac{\partial\beta}{\partial\theta}\cos\theta\sin\theta + (1-m^2)\sigma^{obs}_{\phi\phi}\sin\theta\right]d\theta$$
$$= \int_{-\pi/2}^{0}\left[-im\beta + im\frac{\partial\beta}{\partial\theta}\cos\theta\sin\theta + (1-m^2)\sigma^{obs}_{\phi\phi}\sin\theta\right]d\theta = 0$$

so that

$$(1-m^2)\sigma^{obs}_{\phi\phi}\sin\theta = im\sin\theta\beta - im\frac{\partial\beta}{\partial\theta}\cos\theta\sin\theta \tag{78}$$

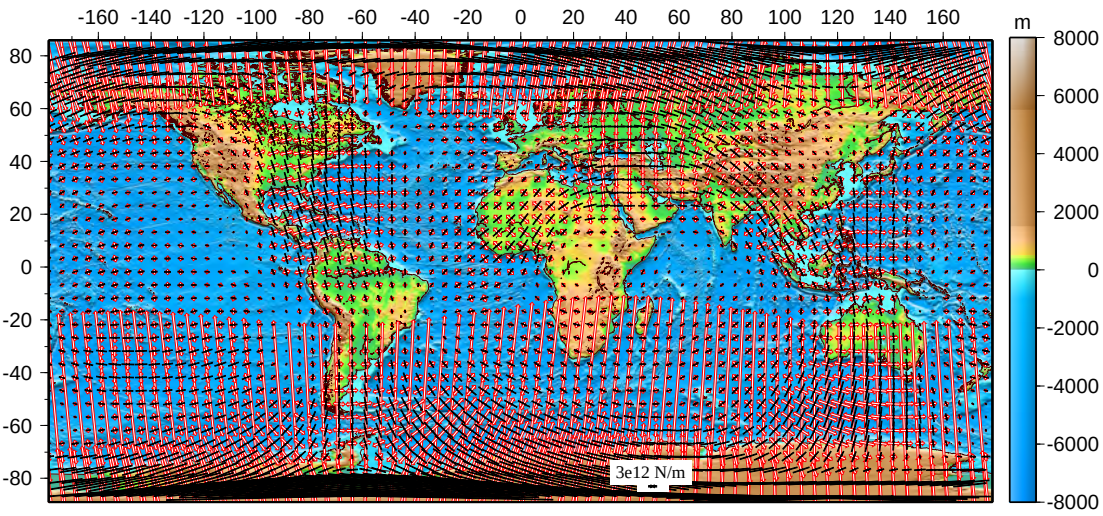

Figure 9: Global distribution of the observed potentials, $\tilde{\sigma}^{obs}_{\phi\phi}, \tilde{\sigma}^{obs}_{\phi\theta}$, from tractions calculated by Case I for all m for an isoviscous case. Note the influence of large potentials at and near the poles from $m = 0$, $m = 1$ terms.

(B) Form involving only β in (72) we want:

$$\int_0^{\pi/2} \left[-im\beta(1+\cos 2\theta) + (1-m^2)\sigma^{obs}_{\phi\phi} \sin\theta \right] d\theta$$
$$= \int_{-\pi/2}^{0} \left[-im\beta(1+\cos 2\theta) + (1-m^2)\sigma^{obs}_{\phi\phi} \sin\theta \right] d\theta = 0$$

so that

$$(1-m^2)\sigma^{obs}_{\phi\phi} \sin\theta = im\beta(1+\cos 2\theta) \tag{79}$$

Multiplying (78) by 2 and subtracting (79) yields

$$(1-m^2)\sigma^{obs}_{\phi\phi} = \frac{im}{\sin\theta}\beta(1-\cos 2\theta) - 2im\frac{\partial\beta}{\partial\theta}\cos\theta. \tag{80}$$

Hence,

$$\sigma^{obs}_{\phi\phi} = \frac{1}{(1-m^2)}\left[2im\beta\sin\theta - 2im\frac{\partial\beta}{\partial\theta}\cos\theta \right], \tag{81}$$

$$\sigma^{obs}_{\theta\theta} = im(\beta - \sigma_{\phi\theta})\sin\theta \tag{82}$$

and

$$\sigma^{obs}_{\phi\theta} = -\left(\frac{1+m^2}{1-m^2}\right)\beta - \frac{1}{(1-m^2)\cos^2\theta}\int_{-\pi/2}^{\theta} \left[\beta\sin 2\theta\right] d\theta \tag{83}$$

The above potentials are calculated for each value of m and for each value of $l \geq 2$.

The solutions of $\sigma^{obs}_{\phi\phi}, \sigma^{obs}_{\theta\theta}$ and $\sigma^{obs}_{\phi\theta}$ for a given value of l and m are either completely

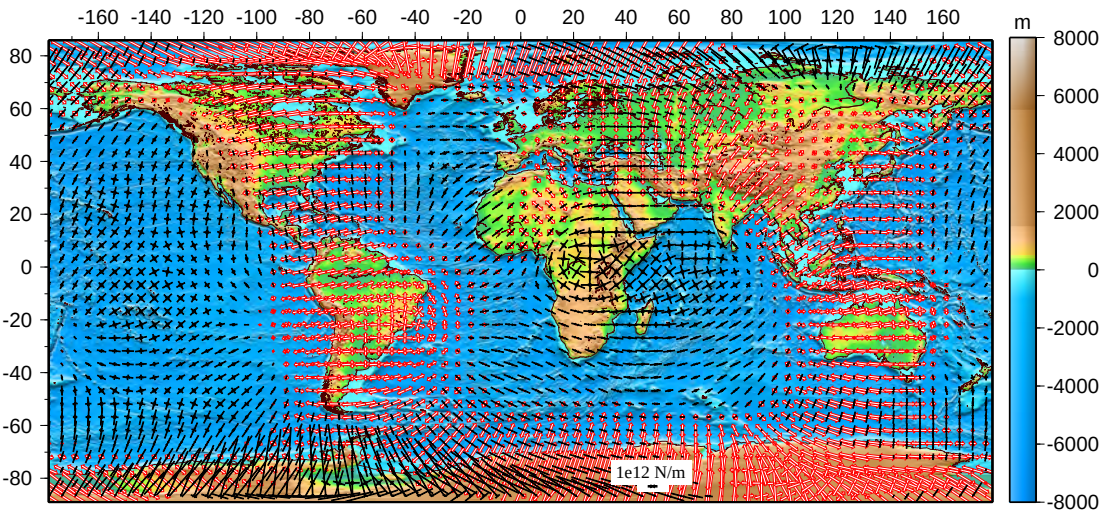

Figure 10: Global distribution of vertically integrated horizontal deviatoric stresses from tractions calculated by Case I, based on potentials in Figure 9. Note the large deviatoric stresses near the poles.

real ((76) and (83)) or completely imaginary ((75), (77), (81) and (82)) and do not combine real and imaginary parts. Let us denote the potentials for a given l, m, $\sigma_{\phi\phi}^{obs}, \sigma_{\theta\theta}^{obs}$ and $\sigma_{\phi\theta}^{obs}$ as

$$\sigma_{ij}^{obs} = A^{l,m} + 0 \tag{84}$$

for those with only real parts, and

$$\sigma_{ij}^{obs} = 0 + iB^{l,m} \tag{85}$$

for those with only imaginary parts. In that case, the complete potential for the forms in (84) can be written, after taking only the real part of the Fourier sum, as

$$\sigma_{ij}^{obs} = \sum_{m=0}^{N} \sum_{l=|m|}^{N} A^{l,m} (Z_6^{l,m,\cos} \cos m\phi + Z_6^{l,m,\sin} \sin m\phi) \tag{86}$$

and those for the forms in (85) can be written as

$$\sigma_{ij}^{obs} = \sum_{m=0}^{N} \sum_{l=|m|}^{N} B^{l,m} (Z_6^{l,m,\sin} \cos m\phi - Z_6^{l,m,\cos} \sin m\phi) \tag{87}$$

where $Z_6^{l,m,\sin}$ and $Z_6^{l,m,\cos}$ are the sine and cosine components of the toroidal coefficient for the tractions in the equivalent body forces, Z_6, that we obtain from the convection model.

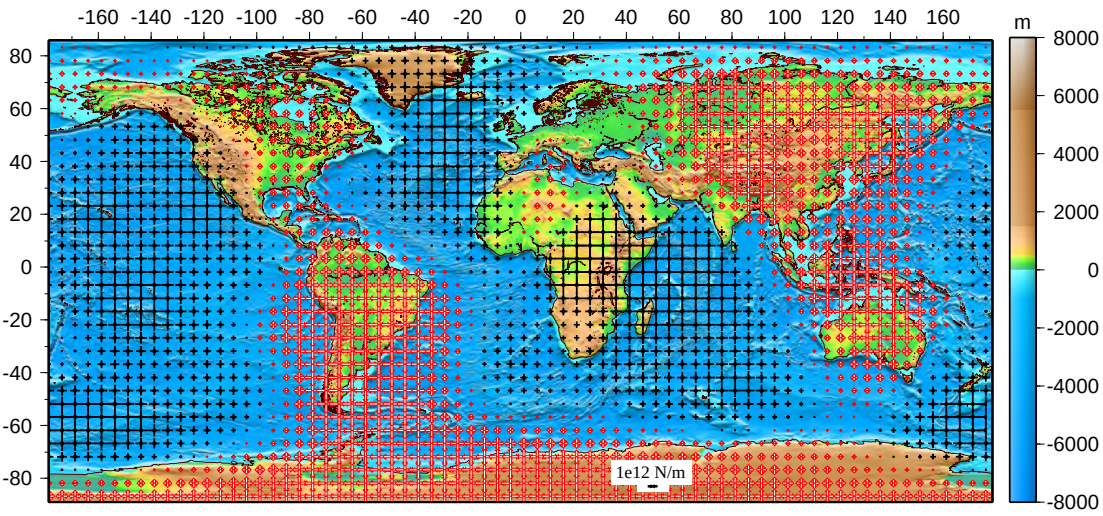

Figure 11: Global distribution of the observed potentials, $\frac{1}{3}\tau_0^{obs}$, from tractions calculated by Case II for all m for an isoviscous case.

Like the poloidal case, we once more demonstrate that this treatment of the toroidal terms (Case III) yield deviatoric stress solutions that are the same as those obtained by Case I for $m \geq 2$ (Figures 26 and 28). We compute the deviatoric stress results for $m = 0, 1$ for the two toroidal cases (Cases I and III) and show how the potentials for Case I (Figure 29) blow up at the poles, whereas for Case III, the potentials are well-behaved at the poles (Figure 31). This singularity problem at the poles therefore disappears for the new treatment, Case III. Likewise, the deviatoric stresses for Case I for $m = 0, 1$ are large at the poles (Figure 30), whereas they are well-behaved for Case III at the poles (Figure 32). A comparison of results for $m \geq 2$ for both Cases I and III for the toroidal case yields identical results (Figures 26 and 28).

In summary, it is possible to use Case I for both poloidal and toroidal fields for $m \geq 2$. For $m = 0, 1$, Case II can be used when there is poloidal flow and Case III can be used when toroidal flow is present. On the other hand, Case II can be used for all m for poloidal flow and Case III for all m for toroidal flow. We have chosen this condition of using both Case II and Case III for all m for poloidal and toroidal flows, respectively.

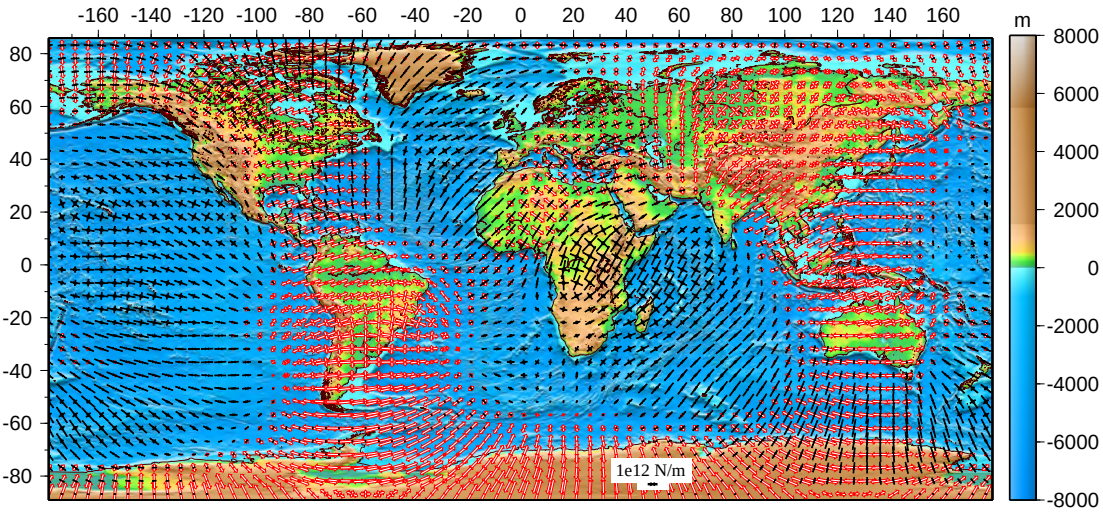

Figure 12: Global distribution of vertically integrated horizontal deviatoric stresses from tractions calculated by Case II, based on potentials in Figure 11. Differences from Figure 10 are due to large potentials for $m = 0$, $m = 1$ in Case I.

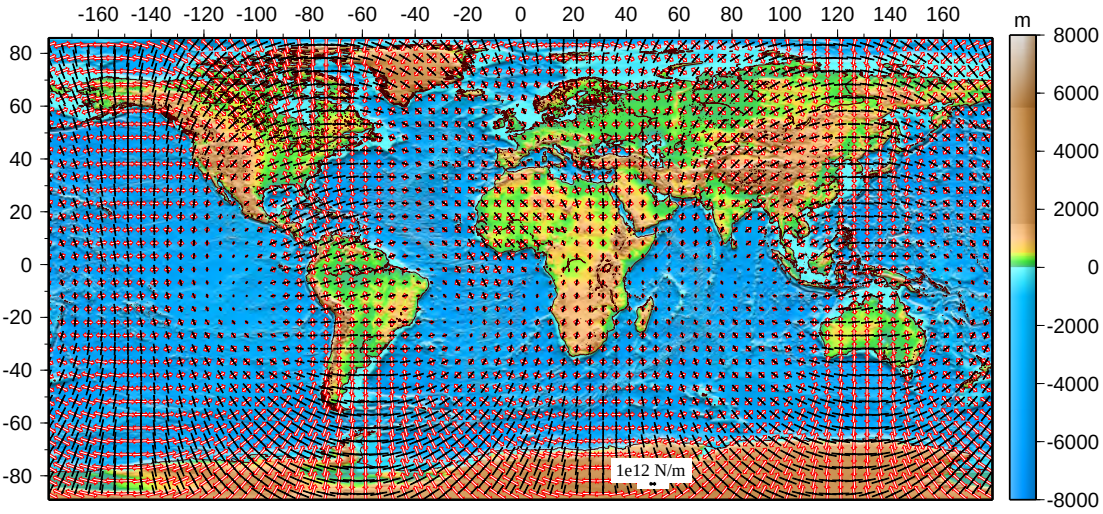

Figure 13: Global distribution of the observed potentials, $\tilde{\sigma}^{obs}_{\phi\phi}, \tilde{\sigma}^{obs}_{\phi\theta}$, from tractions calculated by Case I for $m \geq 2$, for our best-fitting poloidal model.

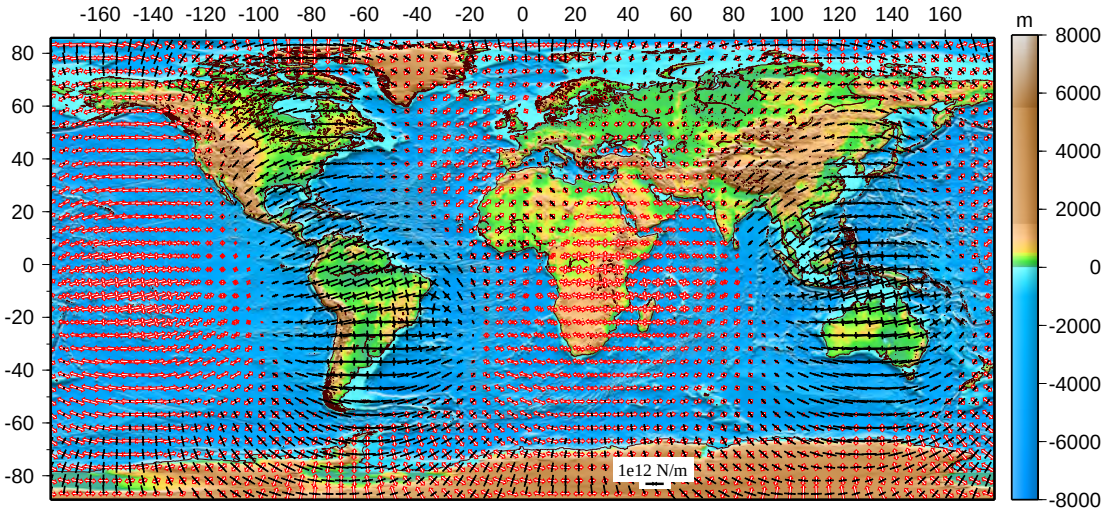

Figure 14: Global distribution of vertically integrated horizontal deviatoric stresses from tractions calculated by Case I, based on potentials in Figure 13.

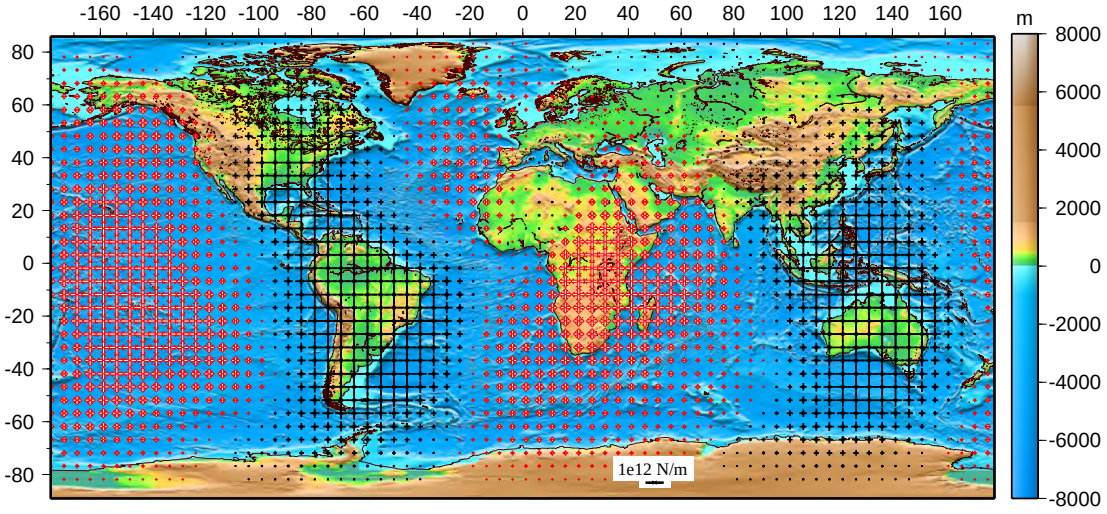

Figure 15: Global distribution of the observed potentials, $\frac{1}{3}\tau_0^{obs}$, from tractions calculated by Case II for $m \geq 2$, for our best-fitting poloidal model.

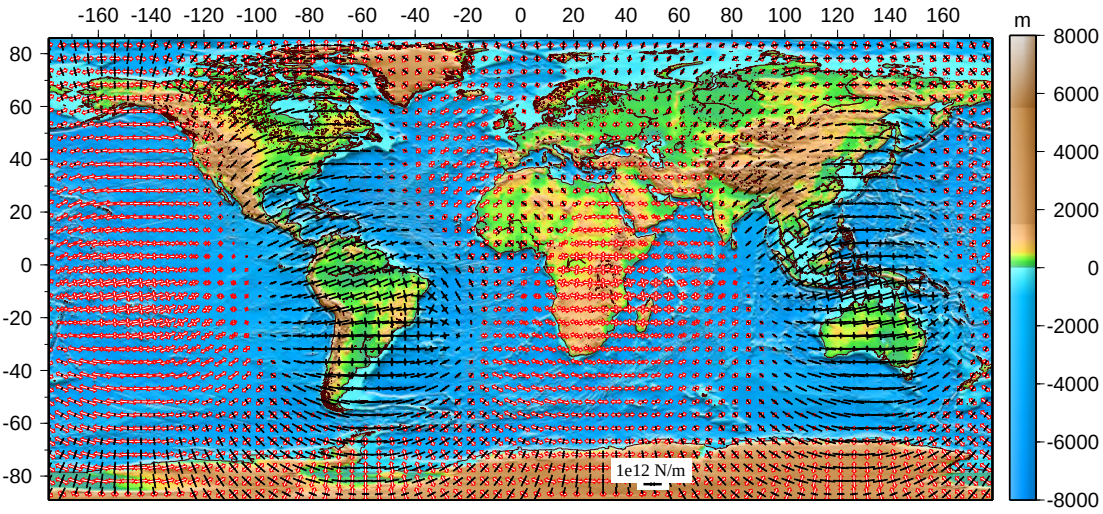

Figure 16: Global distribution of vertically integrated horizontal deviatoric stresses from tractions calculated by Case II, based on potentials in Figure 15. Note the similarity with Figure 14, calculated by Case I.

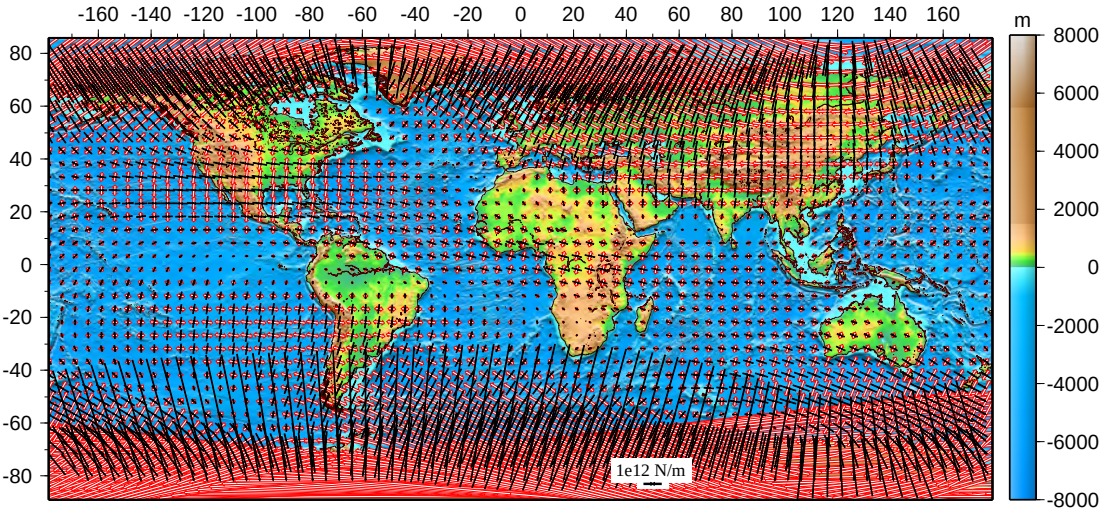

Figure 17: Global distribution of the observed potentials, $\tilde{\sigma}^{obs}_{\phi\phi}, \tilde{\sigma}^{obs}_{\phi\theta}$, from tractions calculated by Case I for $m = 0, 1$ for our best-fitting poloidal model. Note the large potentials near the poles.

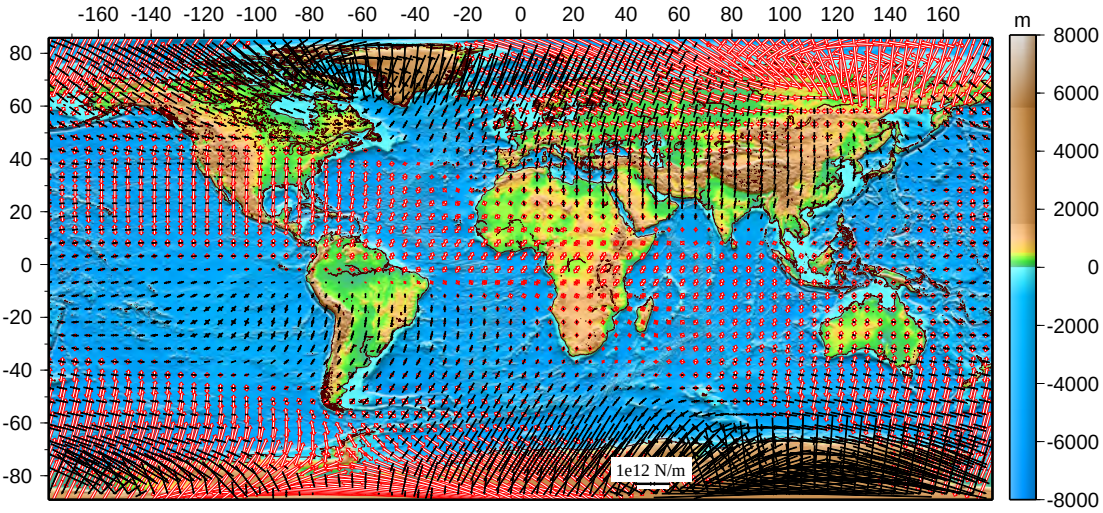

Figure 18: Global distribution of vertically integrated horizontal deviatoric stresses from tractions calculated by Case I, based on potentials in Figure 17. Note the large stresses near the poles.

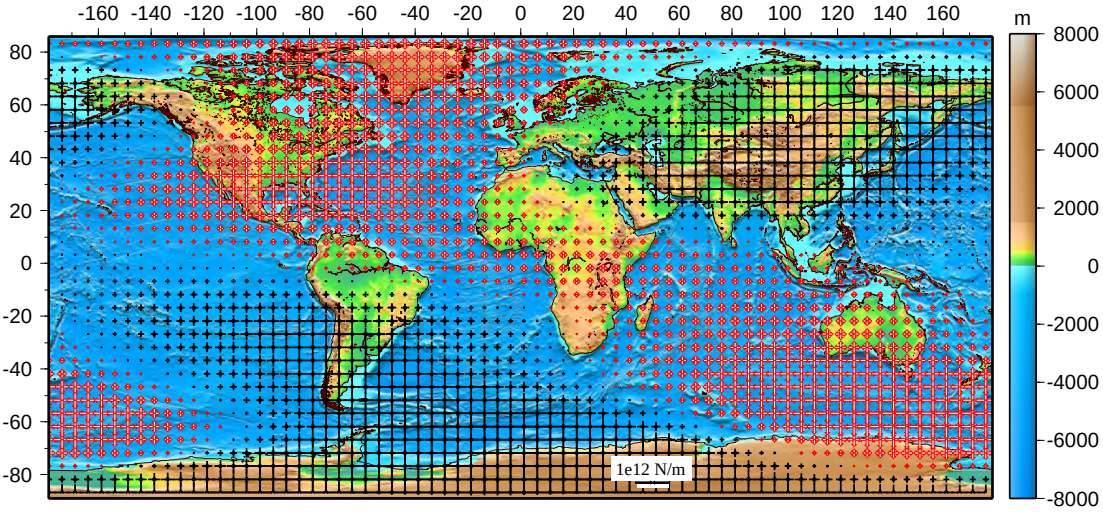

Figure 19: Global distribution of the observed potentials, $\frac{1}{3}\tau_0^{obs}$, from tractions calculated by Case II for $m = 0, 1$ for our best-fitting poloidal model.

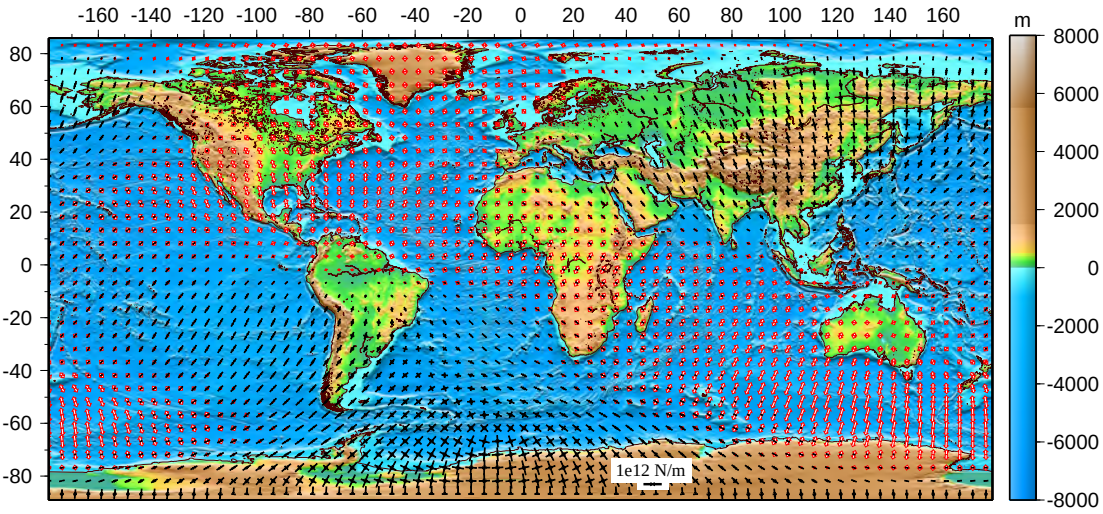

Figure 20: Global distribution of vertically integrated horizontal deviatoric stresses from tractions calculated by Case II, based on potentials in Figure 19 ($m = 0$, $m = 1$).

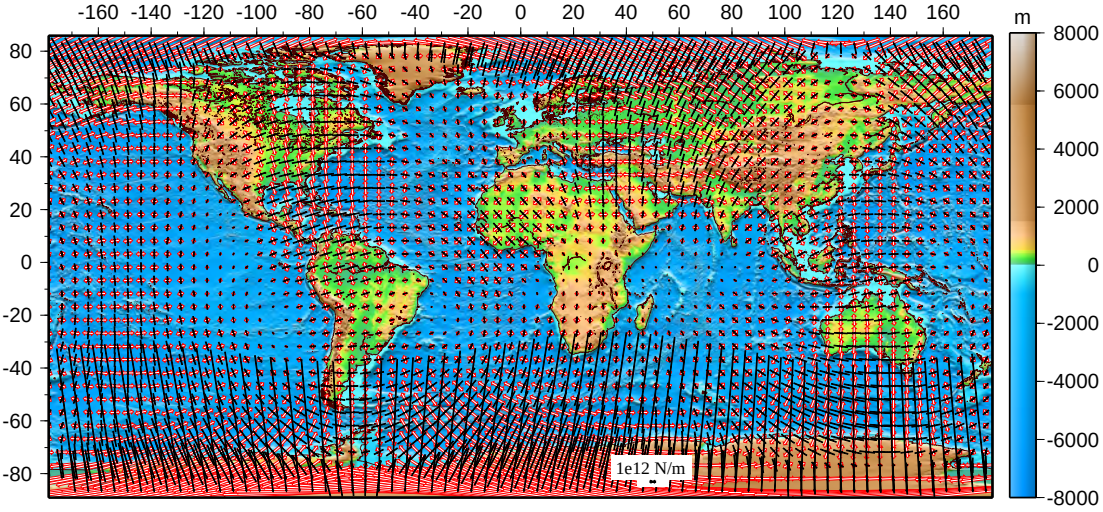

Figure 21: Global distribution of the observed potentials, $\tilde{\sigma}^{obs}_{\phi\phi}, \tilde{\sigma}^{obs}_{\phi\theta}$, from tractions calculated by Case I for all m for our best-fitting poloidal model. Note the large values for potentials contributed by $m = 0$, $m = 1$ terms near the poles.

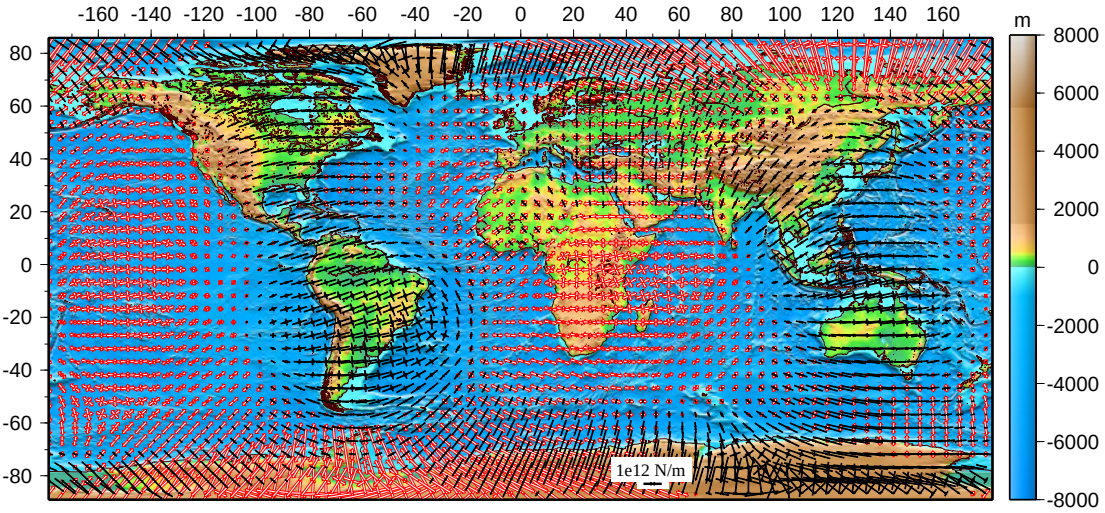

Figure 22: Global distribution of vertically integrated horizontal deviatoric stresses from tractions calculated by Case I, based on potentials in Figure 21.

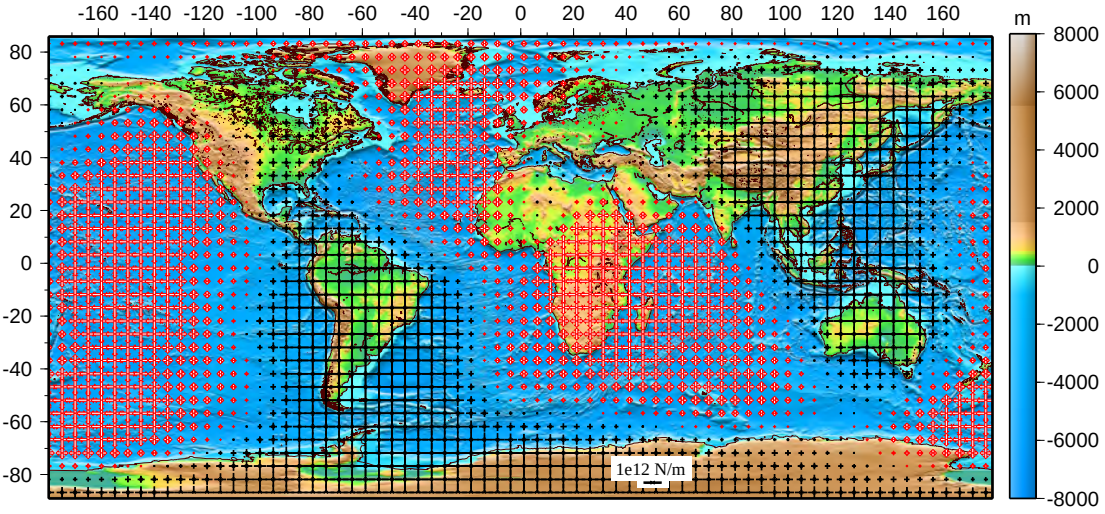

Figure 23: Global distribution of the observed potentials, $\frac{1}{3}\tau_0^{obs}$, from tractions calculated by Case II for all *m* for our best-fitting poloidal model.

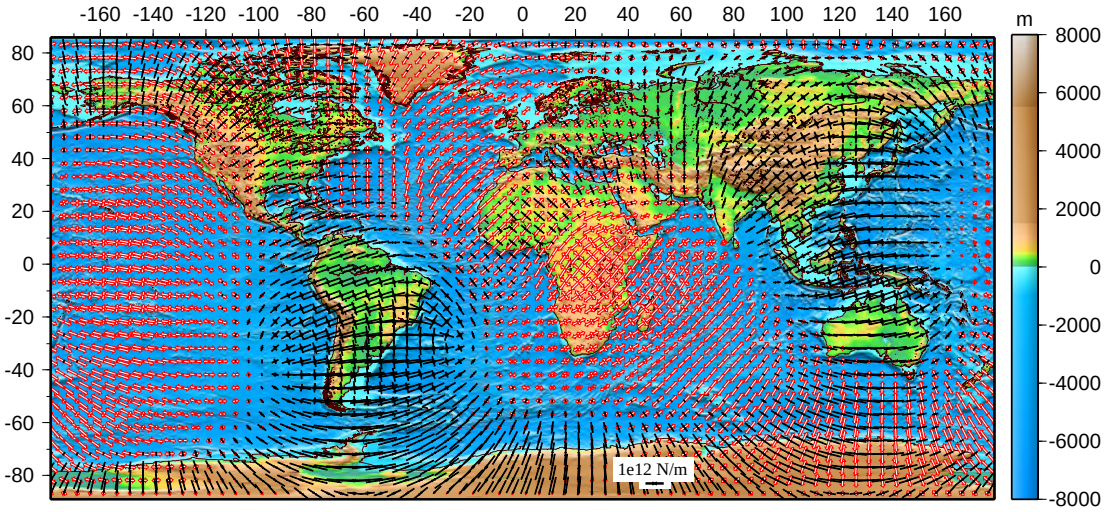

Figure 24: Global distribution of vertically integrated horizontal deviatoric stresses from tractions calculated by Case II, based on potentials in Figure 23. Differences are due to potentials that blow up at the poles for case I.

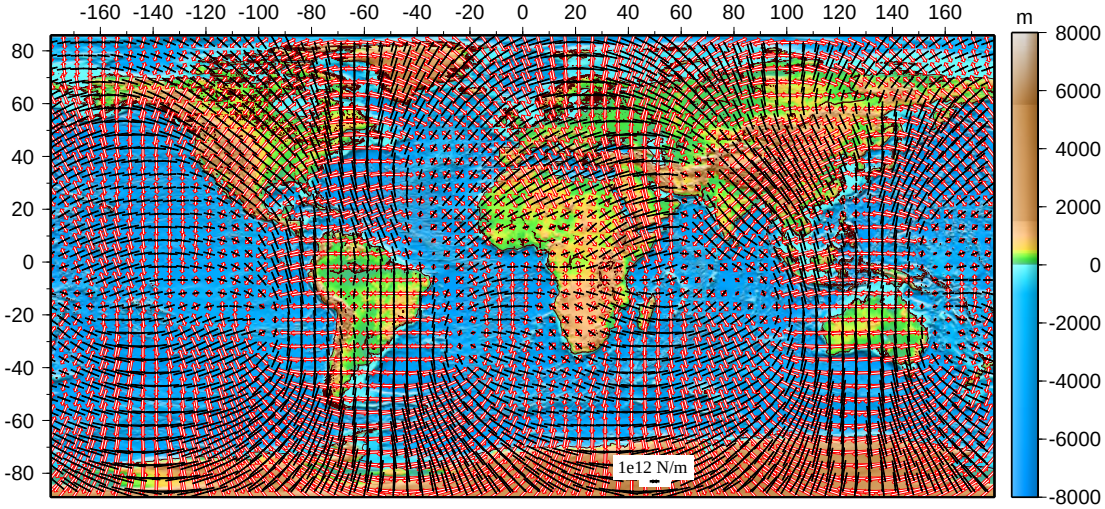

Figure 25: Global distribution of the observed potentials, $\sigma_{\phi\phi}, \sigma_{\phi\theta}$, from tractions calculated by Case I for $m \geq 2$ for one of our toroidal models.

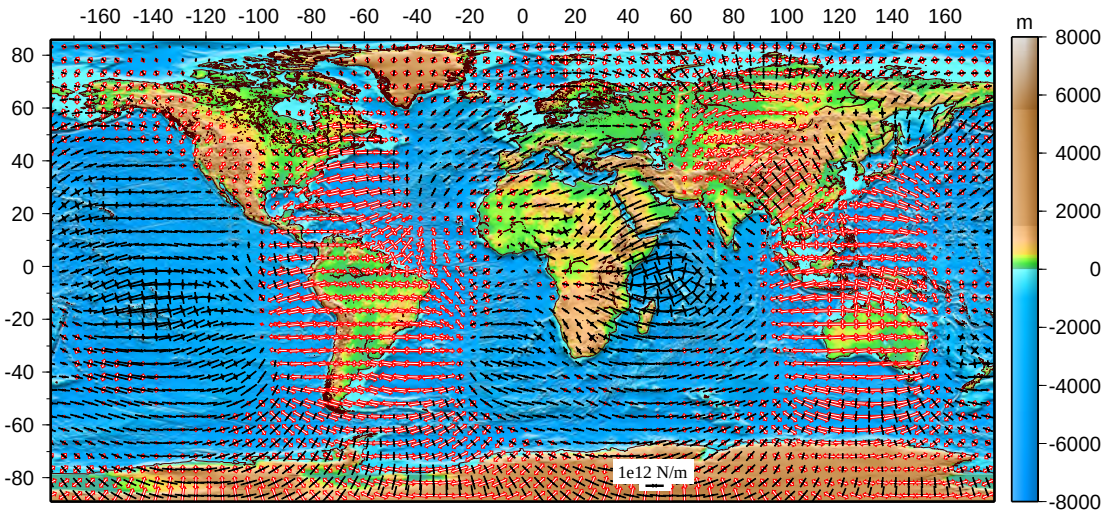

Figure 26: Vertically integrated horizontal deviatoric stresses based on potentials in Figure 25.

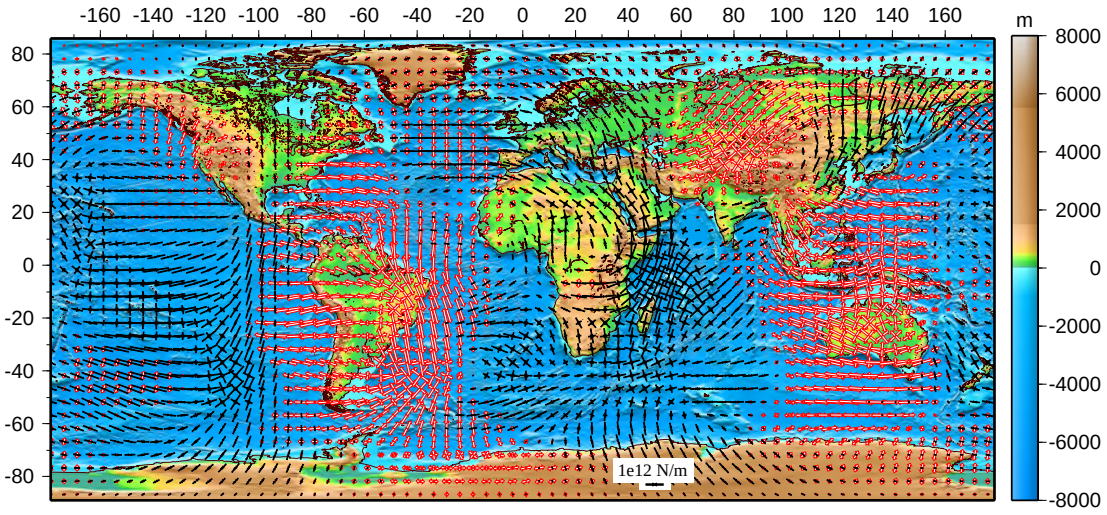

Figure 27: Observed potentials calculated by Case II (for poloidal part) and Case III (for toroidal part) based on the same toroidal model for $m \geq 2$.

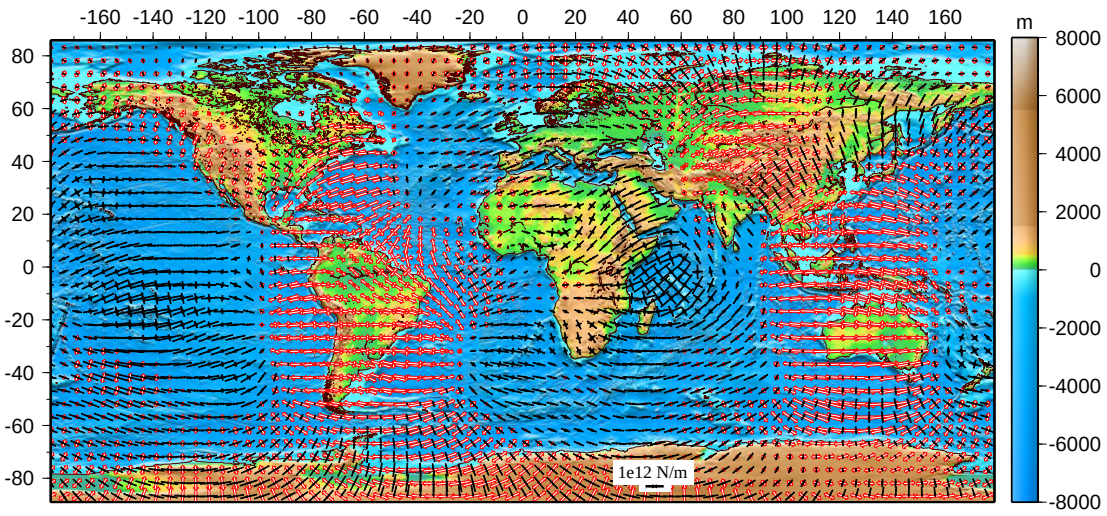

Figure 28: Vertically integrated horizontal deviatoric stresses based on potentials in Figure 27 (case II for poloidal, case III for toroidal, $m \geq 2$. Note that this deviatoric stress field is similar to the field in Figure 26 (case I, $m \geq 2$).

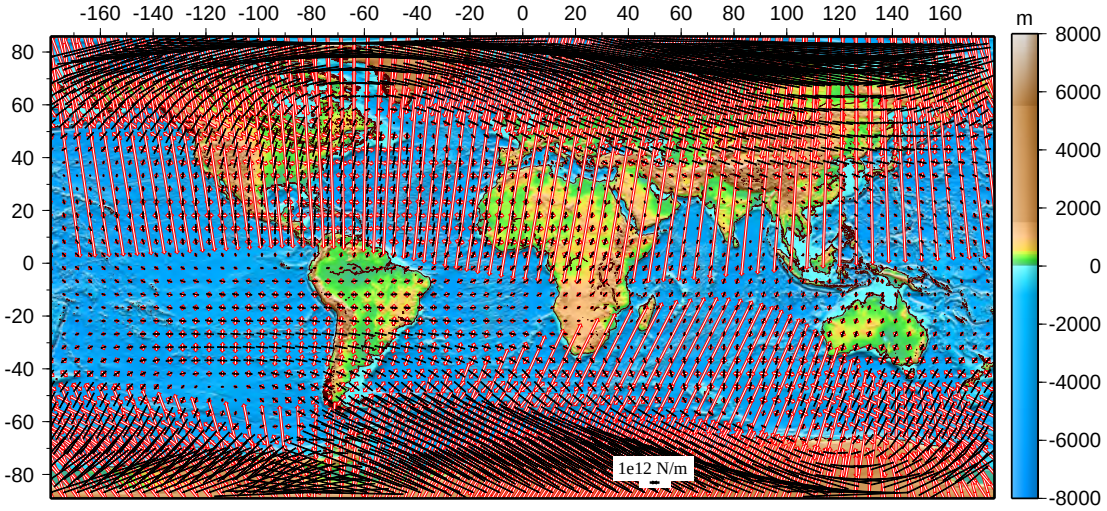

Figure 29: Observed potentials calculated by Case I based on the toroidal model for $m = 0, 1$.

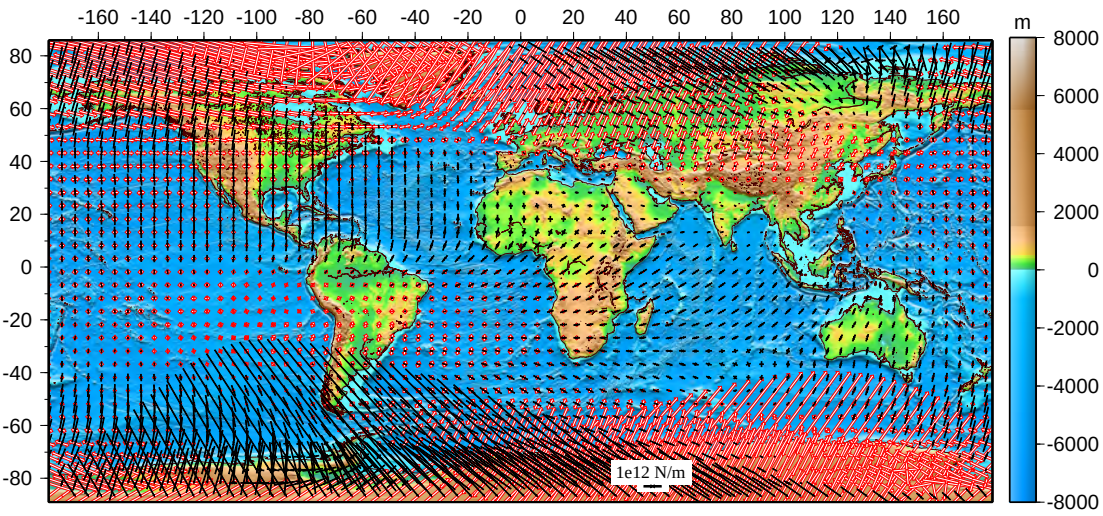

Figure 30: Vertically integrated horizontal deviatoric stresses based on potentials in Figure 29.

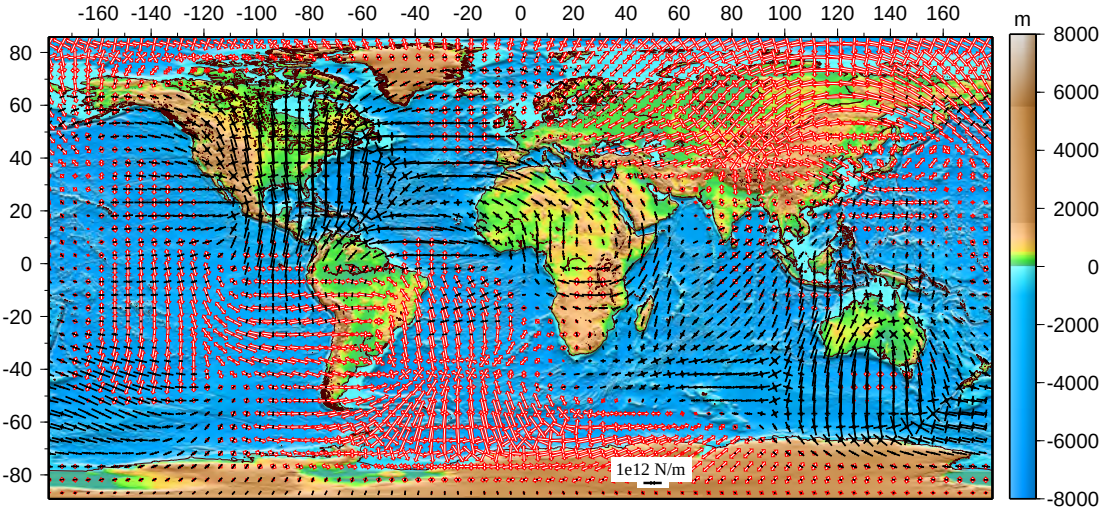

Figure 31: Observed potentials calculated by Cases II and III based on the toroidal model for $m = 0, 1$. Note that potentials are well-behaved near the poles.

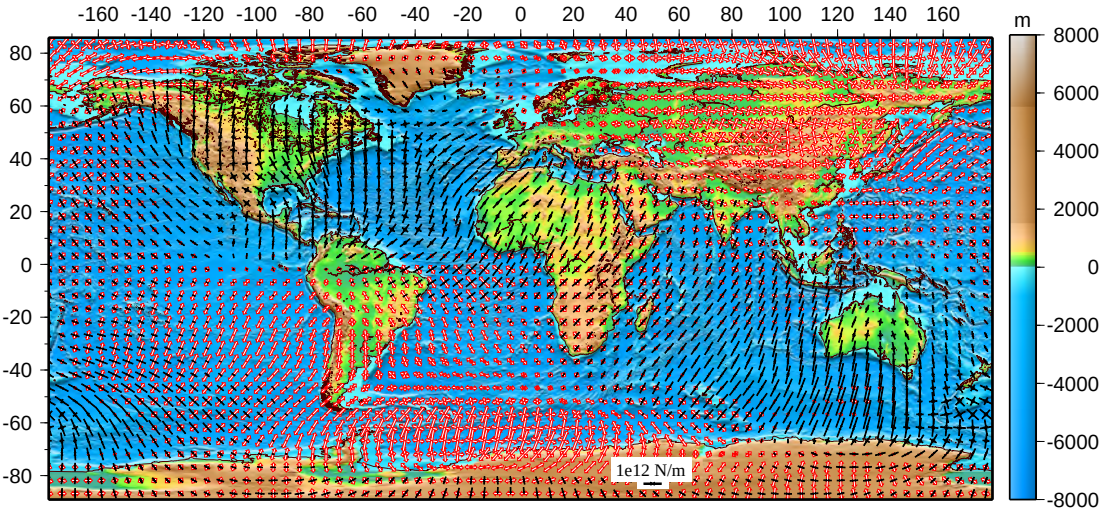

Figure 32: Vertically integrated horizontal deviatoric stresses based on potentials in Figure 31.

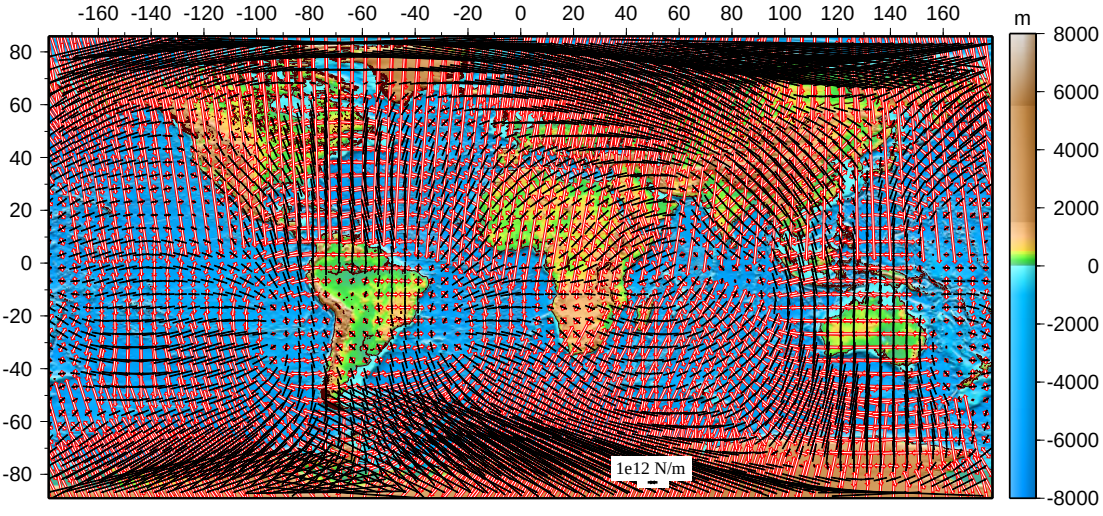

Figure 33: Observed potentials calculated by Case I based on the toroidal model for all *m*.

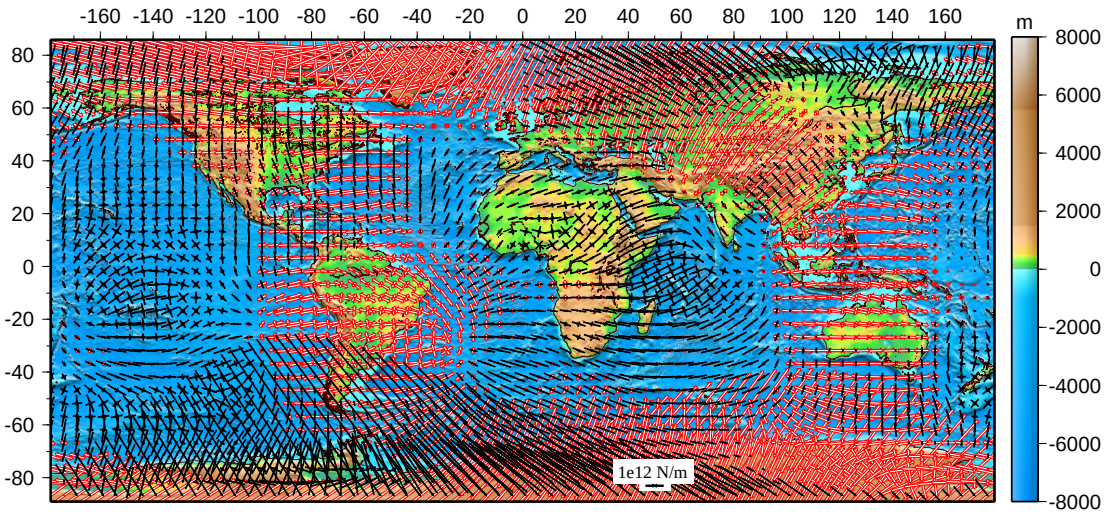

Figure 34: Vertically integrated horizontal deviatoric stresses based on potentials in Figure 33.

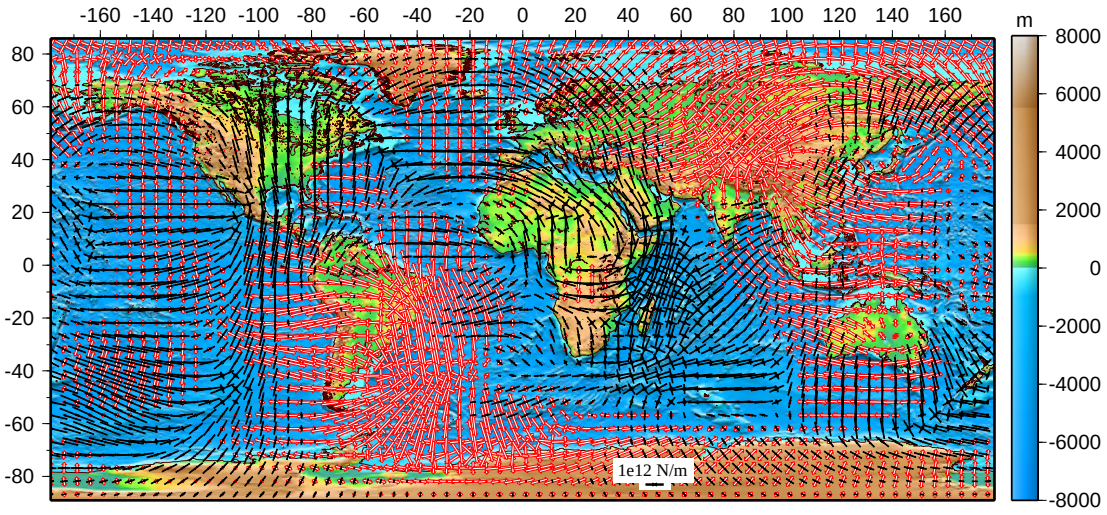

Figure 35: Observed potentials calculated by Cases II and III based on the toroidal model for all *m*. Note that potentials are well-behaved near the poles.

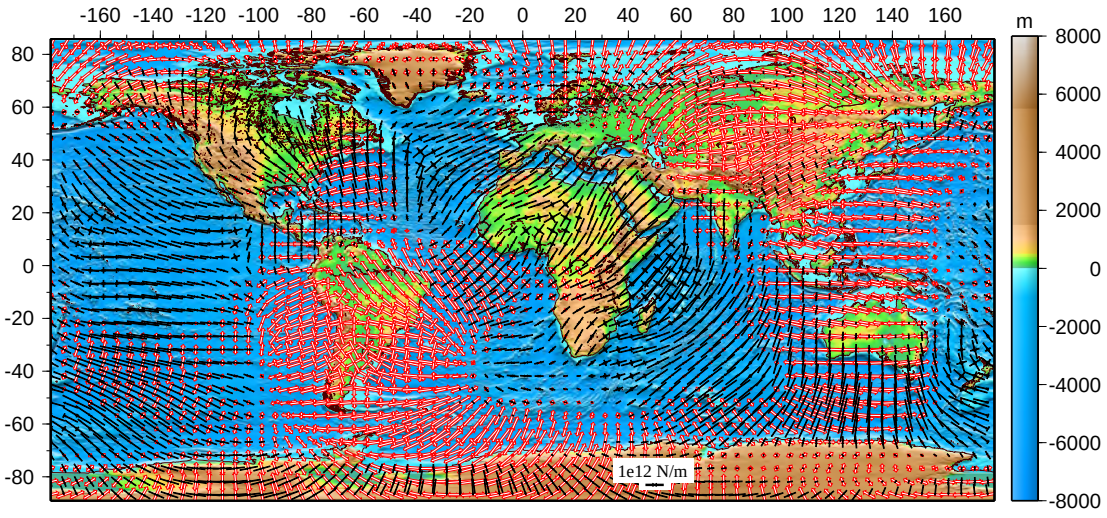

Figure 36: Vertically integrated horizontal deviatoric stresses based on potentials in Figure 35.

Chapter 7

Conclusions

Conclusions

In this dissertation I investigate the problem of how mantle flow interacts with the lithosphere in order to produce the observed lithospheric deformation. This is achieved through a global joint modeling of lithosphere dynamics and mantle convection. The lithospheric stress field is used to constrain the role of mantle convection on surface deformation. I first calculate the contribution of the gravitational potential energy per unit area (GPE) differences on the lithospheric deviatoric stress field. I perform a quantitative comparison of these predicted stresses with the velocity gradient tensor field along the deforming plate boundary zones from GSRM. Such a comparison shows that, although the deviatoric stress field generated by the buoyancy sources within the lithosphere is able to provide a good match to the strain rate observations in many areas, in certain regions, especially in regions of continental deformation, this stress field falls short of explaining the total field of observed deformation. This is also found to be true in the case of the Indian plate, where the ridge-push force, which has been invoked as the sole mechanism behind the present stability of the Tibetan Plateau, is unable to cancel out the large deviatoric N-S tension at the Tibetan Plateau that is generated by lithospheric GPE differences, as is shown in chapter 3. An additional source of stress, originating from basal tractions generated by sub-lithospheric density buoyancies is found to be necessary to explain the observed deformation.

I discuss the validity of the thinsheet method in chapter 2. I show that horizontal gradients in shear tractions applied to the base of the lithosphere at 100 km depth have to be much higher than 6MPa/10 km for them to be significant enough such that: (1) they approach values greater than one percent of magnitude of ρg, and hence (2) the thin sheet approach becomes less valid because horizontal gradients in tractions cannot be ignored. This value for gradient in tractions is much higher than horizontal gradients in tractions that are observed for long-wavelength convection models, and is likely to be higher than what may occur over short length scales within subduction zones. In the same chapter, I discuss the importance of choosing the reference level for calculating GPE differences and demonstrate that the only correct level of reference to calculate the depth integral of σ_{rr} is

the base of the lithosphere. I also talk about the assumptions involved in using the geoid dataset for calculating GPE differences and demonstrate that the geoid data can only be used under the assumption of equal pressure everywhere at the base.

A separate model of mantle convection is used to calculate the tractions acting at the base of the lithosphere. Using simple poloidal flow models, I show that addition of this component of deviatoric stress from basal tractions improves the fit to the observed deformation indicators. The poor fit in the continental deformation areas provided by GPE differences undergoes a substantial improvement when this sub-lithospheric component is considered, in addition to the contribution from lithospheric GPE differences, as I show in chapter 4. I also test the sensitivity of different radially variable viscosity models and show that those with strong (100-10,000 times) viscosity contrasts between the lithosphere and asthenosphere are required in order to fit the strain rate tensor information in GSRM. Amongst these models, those with a weak asthenosphere (10^{19} Pa-s) yield smaller basal tractions, which yield deviatoric stresses that are comparable in magnitude to those associated with GPE differences. Models where contribution from GPE differences are comparable to the contribution from basal tractions perform better at predicting stresses in sensitive areas such as Baikal region in Asia, Tibetan Plateau, western North America, and the Aegean region. Also, in chapter 4 I perform important benchmarking exercises. I generate a deviatoric stress field directly from the convection model (*Wen and Anderson*, 1997b), based on a simple viscosity structure, and compare it with the deviatoric stress field computed by the thinsheet technique. The two stress fields are found to be very similar, further justifying the suitability of the thinsheet methodology.

In chapters 2 and 4, I demonstrate the importance of lateral strength variations in the lithosphere of the thinsheet model. Comparison of deviatoric stress results from a uniform lithosphere and a laterally variable lithosphere show that the latter provides a much better fit to the deformation indicators.

I generate plate motions self-consistently in the convection models by introducing lateral viscosity variations, based on major geological features of the Earth, such as the continent-ocean divide, strength variations between old and young oceans, and the high viscosity continental keels. I test a number of viscosity structures, and using both the

constraints of plate motions and the lithospheric stress field, delineate a narrow range of viscosity structures that match both these constraints. The toroidal-poloidal velocity ratio is also used as an additional constraint. Structures with strong lateral viscosity variations within the lithosphere and a uniformly weak (10^{19} Pa-s) asthenospheric channel are necessary to yield a good fit to both the observed deformation and plate motions as demonstrated in chapter 5. The lateral viscosity variation due to the continent-ocean divide is found to play the dominant role in producing the right kind of deviatoric stresses and plate motions that match observations. The stress magnitudes associated with mantle density buoyancy generated basal tractions for the successful models are found to be comparable to the stress magnitudes from GPE differences, indicating that the relative contribution of lithosphere and mantle buoyancy sources on the lithospheric deviatoric stress field are about equal.

I also discuss at length the two new treatments developed to compute deviatoric stresses from the toroidal component of the mantle flow field in chapter 6. For spherical harmonic order 2 or greater the two methods yield similar results. However, for order 0 and 1, the deviatoric stresses become infinitely large for one method, whereas they are stable for the other. The comparison of the two different methods for $m \geq 2$ confirms that the method I use is able to recover a unique solution for deviatoric stress, given properly constructed potentials. Furthermore, I show in this chapter that care must be taken near the poles to make sure that potentials do not blow up there. This chapter shows that as long as the potentials are well behaved at the poles, the calculated deviatoric stress should be stable and uniquely determined for a given set of tractions.

Bibliography

Airy, G. B., On the computation of the effect of the attraction of mountain-masses, as disturbing the apparent astronomical latitude of stations of geodetic surveys, *Roy. Soc. of London Phil. Trans.*, *145*, 101–104, 1855.

Artyushkov, E. V., Stresses in the lithosphere caused by crustal thickness inhomogeneities, *J. Geophys. Res.*, *78*, 7675–7690, 1973.

Bai, W., C. Vigny, Y. Ricard, and C. Froidevaux, On the origin of deviatoric stresses in the lithosphere, *J. Geophys. Res.*, *97*, 11,729–11,737, 1992.

Becker, T. W., and R. J. O'Connell, Predicting plate velocities with mantle circulation models, *Geochemistry, Geophysics, Geosystems*, *2*, 2001GC000171, 2001.

Bercovici, D., A source-sink model of the generation of plate tectonics from non-newtonian mantle flow, *J. Geophys. Res.*, *100*, 2013–2030, 1995.

Bercovici, D., Generation of plate tectonics from lithosphere-mantle flow and void-volatile self-lubrication, *Earth Planet. Sci. Lett.*, *154*, 139–151, 1998.

Bercovici, D., The generation of plate tectonics from mantle convection, *Earth Planet. Sci. Lett.*, *205*, 107–121, 2003.

Bercovici, D., and Y. Ricard, The relation between mantle dynamics and plate tectonics: a primer, in *The History and Dynamics of Global Plate Motions, Geophysical Monograph*, vol. 121, pp. 5–46, 2000.

Bird, P., Testing hypotheses on plate-driving mechanisms with global lithosphere mod-

els including topography, thermal structure and faults, *J. Geophys. Res., 103*, 10,115–10,129, 1998.

Cazenave, A., A. Souriau, and K. Dominh, Global coupling of Earth surface topography with hotspots, geoid and mantle heterogeneities, *Nature, 340*, 54–57, 1989.

Christensen, U., and H. Harder, 3-d convection with variable viscosity, *Geophys. J. Int., 104*, 213–226, 1991.

Cloetingh, S., and R. Wortel, Regional stress field of the Indian plate, *Geophys. Res. Lett., 12*, 77–80, 1985.

Cloetingh, S., and R. Wortel, Stress in the Indo-Australian plate, *Tectonophys., 132*, 49–67, 1986, doi: 10.1016/0040-1951(86)90024-7.

Coblentz, D. D., and M. Sandiford, Tectonic stresses in the African plate: constraints on the ambient lithospheric stress state, *Geology, 22*, 831–834, 1994.

Coblentz, D. D., R. M. Richardson, and M. Sandiford, On the gravitational potential energy of the Earth's lithosphere, *Tectonophys., 13*, 929–945, 1994.

Coblentz, D. D., M. Sandiford, R. M. Richardson, S. Zhou, and R. Hillis, The origins of the intraplate stress field in continental Australia, *Earth Planet. Sci. Lett., 133*, 299–309, 1995.

Coblentz, D. D., S. Zhou, R. R. Hillis, R. M. Richardson, and M. Sandiford, Topography, boundary forces, and the Indo-Australian intraplate stress field, *J. Geophys. Res., 103*, 919–931, 1998, doi:10.1029/97JB02381.

Conrad, C. P., and C. Lithgow-Bertelloni, Influence of continental roots and asthenosphere on plate-mantle coupling, *Geophys. Res. Lett., 33*, L05312, doi:10.1029/2005GL025621, 2006.

Conrad, C. P., S. Bilek, and C. Lithgow-Bertelloni, Great earthquakes and slab pull: Interaction between seismic coupling and plate-slab coupling, *Earth Planet. Sci. Lett., 218*, 109–122, 2004, doi:10.1029/2005GL025621.

Dalmayrac, B., and P. Molnar, Parallel thrust and normal faulting in Peru and constraints on the state of stress, *Earth Planet. Sci. Lett.*, *55*, 473–481, 1981.

Engelder, T., Deviatoric stressitis: a virus infecting the Earth science community, *EOS Trans. AGU*, *75*, 211–212, 1994.

England, P. C., and G. A. Houseman, Finite strain calculations of continental deformation 2. comparison with the India-Eurasia collision zone, *J. Geophys. Res.*, *91*, 3664–3676, 1986.

England, P. C., and J. Jackson, Active deformation of the continents, *Ann. Rev. Earth Planet. Sci.*, *17*, 197–226, 1989.

England, P. C., and D. P. McKenzie, A thin viscous sheet model for continental deformation, *Geophys. J. R. Astron. Soc.*, *70*, 295–321, 1982.

England, P. C., and P. Molnar, Inferences of deviatoric stress in actively deforming belts from simple physical models, *Roy. Soc. of London Phil. Trans.*, *337*, 151–164, 1997a.

England, P. C., and P. Molnar, Active deformation of Asia, from kinematics to dynamics, *Science*, *278*, 647–650, 1997b.

Fleitout, L., The sources of lithospheric tectonic stresses, *Roy. Soc. of London Phil. Trans.*, *337*, 73–81, 1991.

Fleitout, L., and C. Froidevoux, Tectonics and topography for a lithosphere containing density heterogeneities, *Tectonophys.*, *1*, 21–56, 1982.

Fleitout, L., and C. Froidevoux, Tectonic stresses in the lithosphere, *Tectonophys.*, *2*, 315–324, 1983.

Flesch, L. M., W. E. Holt, A. J. Haines, and B. Shen-Tu, Dynamics of the Pacific-North American plate boundary in the western United States, *Science*, *287*, 834–836, 2000.

Flesch, L. M., A. J. Haines, and W. E. Holt, Dynamics of the India-Eurasia collision zone, *J. Geophys. Res.*, *106*, 16,435–16,460, 2001.

Flesch, L. M., W. E. Holt, A. J. Haines, L. Wen, and B. Shen-tu, The dynamics of western North America: Stress magnitudes and the relative role of gravitational potential energy, plate interaction at the boundary, and basal tractions, *Geophys. J. Int.*, *169*, 866–896, 2007.

Forsyth, D., and S. Uyeda, On the relative importance of the driving forces of plate motion, *Geophys. J. R. Astron. Soc.*, *43*, 163–200, 1975.

Forte, A. M., W. R. Peltier, A. M. Dziewonski, and R. L. Woodward, Dynamic surface topography: a new interpretation based upon mantle flow models derived from seismic topography, *Geophys. Res. Lett.*, *20*, 225–228, 1993.

Frank, F. C., Plate tectonics, the analogy with glacier flow, and isostasy, *Flow and Fracture of Rocks, Geophys. Monogr. Ser.*, *16*, 285–292, 1972, edited by H.C Heard et al., AGU, washington, D.C.

Gable, C. W., R. J. O'Connell, and B. J. Travis, Convection in three dimensions with surface plates: generation of toroidal flow, *J. Geophys. Res.*, *96*, 8391–8405, 1991.

Ghosh, A., W. E. Holt, A. J. Haines, and L. M. Flesch, Gravitational potential energy of the Tibetan Plateau and the forces driving the Indian plate, *Geology*, *34*, 321–324, 2006.

Ghosh, A., W. E. Holt, L. Wen, A. J. Haines, and L. M. Flesch, Joint modeling of lithosphere and mantle dynamics elucidating lithosphere-mantle coupling, *Geophys. Res. Lett.*, 2008, in revision.

Gripp, A. E., and R. G. Gordon, Current plate velocities relative to the hotspots incorporating the NUVEL-I global plate motion model, *Geophys. Res. Lett.*, *17*, 1109–1112, 1990.

Gung, Y., M. Panning, and B. Romanowicz, Global anisotropy and the thickness of continents, *Nature*, *422*, 707–711, 2003.

Hager, B. H., Subducted slabs and the geoid: Constraints on mantle rheology and flow, *J. Geophys. Res.*, *89*, 6003–6015, 1984.

Hager, B. H., and R. J. O'Connell, Kinematic models of large-scale flow in the earth's mantle, *J. Geophys. Res.*, *84*, 1031–1048, 1979.

Hager, B. H., and R. J. O'Connell, A simple global model of plate dynamics and mantle convection, *J. Geophys. Res.*, *86*, 4843–4878, 1981.

Hager, B. H., R. W. Clayton, M. A. Richards, R. P. Comer, and A. M. Dziewonski, Lower mantle heterogeneity, dynamic topography and the geoid, *Nature*, *313*, 541–545, 1985.

Harper, J. F., On the driving forces of plate tectonics, *Geophys. J. R. Astron. Soc.*, *40*, 465–474, 1975.

Haxby, W. F., and D. L. Turcotte, On isostatic geoid anomalies, *J. Geophys. Res.*, *83*, 5473–5478, 1978.

Holt, W. E., and A. Haines, The kinematics of northern South Island, New Zealand, determined from geologic strain rates, *J. Geophys. Res.*, *100*, 17991–18010, 1995.

Holt, W. E., N. Chamot-Rooke, X. L. Pichon, A. Haines, B. Shen-Tu, and J. Ren, Velocity field in Asia inferred from Quaternary fault slip rates and Global Positioning System observations, *J. Geophys. Res.*, *105*, 19,185–19,209, 2000.

Holt, W. E., C. Kreemer, A. Haines, L. Estey, , C. Meertens, G. Blewitt, and D. Lavallee, Project helps constrain continental dynamics and seismic hazards, *EOS Trans. AGU*, *86*, 383–387, 2005.

Houseman, G., and P. England, A dynamical model of lithosphere extension and sedimentary basin formation, *J. Geophys. Res.*, *91*, 719–729, 1986.

Huang, J., and D. Zhao, High-resolution mantle tomography of China and surrounding regions, *J. Geophys. Res.*, *111*, B09305, doi:10.1029/2005JB004066, 2006.

Humphreys, E., and D. Coblentz, North American dynamics and western U.S. tectonics, *Rev. of Geophys.*, *45*, RG3001, doi:10.1029/2005RG000181, 2007.

Jones, C. H., J. Unruh, and L. Sonder, The role of gravitational potential energy in active deformation in the southwestern United States, *Nature, 381*, 37–41, 1996.

Jordan, T. H., Composition and development of the continental tectosphere, *Nature*, *274*, 544–548, 1978.

Jordan, T. H., Structure and formation of the continental tectosphere, *J. Petrology*, pp. 11–37, 1988, Special lithosphere issue.

Karpychev, M., and L. Fleitout, Simple considerations on forces driving plate motion and on the plate-tectonic contribution to the long-wavelength geoid, *Geophys. J. Int.*, *127*, 268–282, 1996.

Kaula, W. M., Product-sum conversion of spherical harmonics with application to thermal convection, *J. Geophys. Res.*, *80*, 225–231, 1975.

Klein, E. C., L. M. Flesch, W. E. Holt, and A. J. Haines, Evidence of long-term weakness on seismogenic faults in western North America from dynamic modeling, *J. Geophys. Res.*, 2008, submitted.

Kreemer, C., W. E. Holt, and A. J. Haines, An integrated global model of present-day plate motions and plate boundary deformation, *Geophys. J. Int.*, *154*, 8–34, 2003.

Lister, C. R. B., Gravitational drive on oceanic plates caused by thermal contraction, *Nature*, *257*, 663–665, 1975.

Lithgow-Bertelloni, C., and J. H. Guynn, Origin of the lithospheric stress field, *J. Geophys. Res.*, *109*, B01408, doi:10.1029/2003JB002467, 2004.

Lithgow-Bertelloni, C., and M. Richards, Cenozoic plate driving forces, *Geophys. Res. Lett.*, *22*, 1317–1320, 1995.

Lithgow-Bertelloni, C., and P. Silver, Dynamic topography, plate driving forces and the African superswell, *Nature*, *395*, 269–272, 1998.

McKenzie, D., Active tectonics of Mediterranean region, *Geophys. J. R. Astron. Soc.*, *30*, 109–185, 1972.

Meade, B., Present-day kinematics at the India-Asia collision zone, *Geology*, *35*, doi:10.1130/G22942A.1, 2007.

Molnar, P., Continental tectonics in the aftermath of plate tectonics, *Nature*, *335*, 131–137, 1988.

Molnar, P., and H. Lyon-Caen, Some physical aspects of the support, structure, and evolution of mountain, *Spec. Paper Geol. Soc. America*, *218*, 179–207, 1988.

Molnar, P., and P. Tapponnier, Cenozoic tectonics of Asia: Effects of a continental collision, *Science*, *189*, 419–425, 1975.

Molnar, P., P. England, and J. Martinod, Mantle dynamics, uplift of the Tibetan plateau, and the Indian monsoon, *Rev. of Geophys.*, *31*, 357–396, 1993.

Morse, P. M., and H. Feshbach, in *Methods of Theoretical Physics*, pp. 257–347, McGraw-Hill, New York, 1953.

Müller, R. D., W. Roest, J. Royer, L. Gahagan, and J. Sclater, Digital isochrons of the world's ocean floor, *J. Geophys. Res.*, *102*, 3211–3214, 1997.

Panasyuk, S. V., and B. H. Hager, Models of isostatic and dynamic topography, geoid anomalies, and their uncertainties, *J. Geophys. Res.*, *105*, 28,199–28,209, 2000.

Parsons, B., and F. Richter, A relation between the driving force and geoid anomaly associated with mid-oceanic ridges, *Earth Planet. Sci. Lett.*, *51*, 445–450, 1980.

Pratt, J. H., On the attraction of the Himalaya mountains, and the elevated regions beyond them, upon the plumb line in India, *Phil. Trans. R. Soc. Lond.*, *145*, 55–100, 1855.

Reinecker, J., O. Heidbach, M. Tingay, B. Sperner, and B. Müller, The release 2005 of the World Stress Map (available online at www.world-stress-map.org), 2005.

Reynolds, S. D., D. Coblentz, and R. Hillis, Tectonic forces controlling the regional intraplate stress field in continental Australia: results from new finite-element modelling, *J. Geophys. Res.*, *107*, doi:10.1029/2001JB000408, 2002.

Ribe, N. M., The dynamics of thin shells with variable viscosity and the origin of toroidal flow in the mantle, *Geophys. J. Int.*, *110*, 537–552, 1992.

Ricard, Y., and C. Vigny, Mantle dynamics with induced plate tectonics, *J. Geophys. Res.*, *94*, 5987–6002, 1989.

Richards, M. A., and B. H. Hager, Geoid anomalies in a dynamic Earth, *J. Geophys. Res.*, *89*, 10,299–10,313, 1984.

Richardson, R. M., Ridge forces, absolute plate motions, and the intraplate stress field, *J. Geophys. Res.*, *97*, 11,739–11,748, 1992.

Richardson, R. M., S. Solomon, and N. Sleep, Tectonic stress in the plates, *Rev. of Geophys.*, *17*, 981–1019, 1979.

Rudnick, R., and A. Nyblade, The composition and thickness of Archean continental roots: constraints from xenolith thermobarometry, in *Mantle Petrology: Field Observations and High-Pressure Experimentation: A Tribute to Francis R. (Joe) Boyd*, edited by Y. Fei, C. Bertka, and B. Mysen, vol. 6, pp. 3–12, Geochemical Soc. Spec. Publ., 1999.

Sandiford, M., and D. Coblentz, Plate-scale potential-energy distributions and the fragmentation of ageing plates, *Earth Planet. Sci. Lett.*, *126*, 143–159, 1994.

Sandiford, M., D. Coblentz, and R. Richardson, Ridge torques and continental collision in the Indian-Australian plate, *Geology*, *23*, 653–656, 1995.

Sandiford, M., D. Coblentz, and W. Schellart, Evaluating slab-plate coupling in the Indo-Australian plate, *Geology*, *33*, 113–116, 2005.

Solomon, S. C., N. H. Sleep, and R. M. Richardson, On the forces driving plate tectonics: Inferences from absolute plate velocities and intraplate stress, *Geophys. J. R. Astron. Soc.*, *42*, 769–801, 1975.

Sonder, L. J., and P. England, Vertical averages of rheology of the continental lithosphere: relation to thin sheet parameters, *Earth Planet. Sci. Lett.*, *77*, 81–90, 1986.

Stein, C. A., and S. Stein, A model for the global variation in oceanic depth and heat flow with lithospheric age, *Nature, 1992*, 123–129, 1992.

Steinberger, B., H. Schmeling, and G. Marquart, Large-scale lithospheric stress field and topography induced by global mantle circulation, *Earth Planet. Sci. Lett.*, *2001*, 75–91, 2001.

Su, W. J., R. L. Woodward, and A. M. Dziewonski, Degree 12 model of shear velocity heterogeneity in the mantle, *J. Geophys. Res.*, *99*, 6945–6980, 1994.

Tackley, P., Self-consistent generation of tectonic plates in theree dimensional mantle convection, *Earth Planet. Sci. Lett.*, *157*, 9–22, 1998.

Tackley, P., Mantle convection and plate tectonics: toward an integrated physical and chemical theory, *Science*, *288*, 2002–2007, 2000.

Thatcher, W., Microplate model for the present-day deformation of Tibet, *J. Geophys. Res.*, *112*, 401, doi:10.1029/2005JB004244., 2007.

Trompert, R., and U. Hansen, Mantle convection simulations with rheologies that generate plate-like behaviour, *Nature*, *395*, 686–689, 1998.

Turcotte, D., and E. R. Oxburgh, Finite amplitude convection cells and continental drift, *J. Fluid Mechanics*, *28*, 29–42, 1967.

Turcotte, D., and G. Schubert, in *Geodynamics: Applications of Continuum Physics to Geological Problems*, p. 450, John Wiley, New York, 1982.

Wen, L., and D. L. Anderson, The fate of the slabs inferred from seismic tomography and 130 Ma subduction, *Earth Planet. Sci. Lett.*, *133*, 185–198, 1995.

Wen, L., and D. L. Anderson, Slabs, hotspots, cratons and mantle convection revealed from residual seismic tomography in the upper mantle, *Phys. Earth Planet. Int.*, *99*, 131–143, 1997a.

Wen, L., and D. L. Anderson, Present-day plate motion constraint on mantle rheology and convection, *J. Geophys. Res.*, *102*, 24,639–24,653, 1997b.

Wen, L., and D. L. Anderson, Layered mantle convection: A model for geoid and topography, *Earth Planet. Sci. Lett.*, *146*, 367–377, 1997c.

Zhang, S., and U. Christensen, Some effects of lateral viscosity variations on geoid and surface velocities induced by density anomalies in the mantle, *Geophys. J. Int.*, *114*, 531–547, 1993.

Zhong, S., and M. Gurnis, Interactions of weak faults and non-newtonian rheology produces plate tectonics in a 3D model of mantle flow, *Nature*, *383*, 245–247, 1996.

Zoback, M. L., First and second order patterns of stress in the lithosphere: the World Stress Map Project, *J. Geophys. Res.*, *102*, 11,703–11,728, 1992.

Zoback, M. L., and W. D. Mooney, Lithospheric buoyancy and continental intraplate stresses, *Int. Geol. Rev.*, *45*, 95–118, 2003.